Modeling recent trends and variability in the oceanic carbon cycle of the California Current System

Author(s):
Turi, Giuliana

Publication Date:
2014

Permanent Link:

https://doi.org/10.3929/ethz-a-010266501 →

DISS. ETH NO. 22023

Modeling recent trends and variability in the oceanic carbon cycle of the California Current System

A thesis submitted to attain the degree of
DOCTOR OF SCIENCES of ETH ZURICH
(Dr. sc. ETH Zurich)

presented by

GIULIANA TURI

M.Sc. Atmospheric and Climate Science, ETH Zurich
born on September 15th, 1984
citizen of Buochs (NW), Switzerland

accepted on the recommendation of

Prof. Dr. N. Gruber Guyan, examiner
Dr. Z. Lachkar, co-examiner
Dr. V. Garçon, co-examiner

2014

“The sea, once it casts its spell,
holds one in its net of wonder forever.”

– Jacques-Yves Cousteau

Summary

Global climate change is predicted to alter the ocean's carbonate chemistry, with the magnitude of this change being spatially heterogeneous. The California Current System (CalCS), one of the Eastern Boundary Upwelling Systems (EBUS), is a region which experiences extreme natural fluctuations in carbon fluxes on subseasonal through interannual timescales due to the upwelling of dissolved inorganic carbon (DIC) and nutrient-rich waters. Superimposed on these natural fluctuations are perturbations of the carbonate system arising from the anthropogenic emission of CO_2. Global Earth System models are too coarse to accurately simulate the upwelling dynamics of the CalCS and the associated intricate carbon fluxes between the coast, the open ocean and the atmosphere, which leads to a misrepresentation of the temporal and spatial complexity of these fluxes and an underestimation of long-term trends. To overcome this limitation, I use a regional oceanic model of the CalCS at 5 km horizontal resolution on the basis of the Regional Oceanic Modeling System (ROMS), coupled to a biogeochemical model with an integrated carbon module. With simulations from this model, I investigate the natural variability of pCO_2 and air–sea CO_2 fluxes on seasonal to interannual timescales and determine long-term trends in ocean acidification arising from the increase in anthropogenic CO_2 and from changes in the physical forcing of the CalCS, including wind-induced upwelling and temperature. Results from a climatological simulation reveal DIC and temperature to be the main drivers of seasonal pCO_2 variability, with DIC being more dominant in the nearshore 100 km due to upwelling, and seasonal variations in temperature prevailing in the offshore regions through the mechanism of CO_2 solubility. On an annual mean, the CalCS domain is an almost neutral system in terms of CO_2 fluxes, taking up only about 0.05 mol C m^{-2} yr^{-1}. Locally and on shorter timescales however, the air–sea CO_2 fluxes can range between –1.5 mol C m^{-2} yr^{-1} in the northern offshore CalCS in winter and 3.2 mol C m^{-2} yr^{-1} in the central coastal CalCS in summer, reflecting a strong onshore-offshore gradient in the combined effects of upwelling and biological productivity on seasonal variations in pCO_2. Analyses from a hindcast simulation from 1979 to 2012 demonstrate that the interannual variability of air–sea CO_2 fluxes and pCO_2 is substantial, and on the order of the magnitude of the seasonal cycle, and that this low-frequency signal is significantly correlated with several modes of climate variability, namely the El Niño/Southern Oscillation (ENSO), the Pacific Decadal Oscillation (PDO) and the North Pacific Gyre Oscillation (NPGO). These three climate variability modes have an opposing effect on pCO_2 in the nearshore 100 km compared to the regions further offshore. This seesaw pattern is due to a regional difference in the dominance of DIC and temperature, through which ENSO, PDO and NPGO act to modify pCO_2. Using the same hindcast simulation together with a simulation where only atmospheric CO_2 and lateral DIC increase between 1979 and 2012, I show that the domain-wide homogeneous increase in ocean acidification due to the rise in anthropogenic CO_2 is enhanced along the coast of Oregon and northern California by an intensification of upwelling-favorable winds. This enhancement of wind-induced upwelling locally accounts for up to 30% of the decrease in pH and 50% of the decrease in the

aragonite saturation state, and accentuates the importance of considering not only the effect of rising atmospheric CO_2 on ocean acidification but also changes in the climatic forcing in coastal upwelling regions.

Taken together, the individual studies in this PhD thesis highlight (i) the importance of using a highly resolved regional ocean model to capture the extreme spatial variability in carbon fluxes associated with the upwelling dynamics of EBUS, (ii) the tight coupling of the carbon fluxes in these regions to climatic fluctuations ranging from subseasonal to decadal timescales, and (iii) the necessity for transiently forced hindcast simulations to tease out the effects of increasing atmospheric CO_2 and changes in the physical atmospheric forcing on recent trends in the carbonate system of these regions.

Zusammenfassung

Der globale Klimawandel wird die Karbonatchemie des Ozeans in Zukunft verändern, wobei die Grösse dieser Veränderung räumlich heterogen ausfallen wird. Die Kohlenstoffflüsse aus dem und in das kalifornische Auftriebsgebiet (CalCS = California Current System), einem der Wasserauftriebsgebiete am Ostrand eines Ozeanbeckens, unterliegen starken natürlichen Fluktuationen auf monatlichen und interannuellen Zeitskalen. Diese werden primär durch den Auftrieb von gelösten organischen Kohlenstoff (DIC = dissolved inorganic carbon) und nährstoffreichem Tiefenwasser kontrolliert. Den natürlichen Fluktuationen überlagert sind Störungen des grossskaligen Kohlenstoffkreislaufs aufgrund der anthropogenen Emissionen von Kohlendioxid (CO_2). Globale Erdsystemmodelle sind gegenwärtig zu grob aufgelöst, um die Auftriebsdynamik und die zugehörigen komplizierten Kohlenstoffflüsse zwischen Küste, offenem Ozean und der Atmosphäre im CalCS korrekt zu simulieren. Dies führt zu einer fehlerhaften Darstellung der zeitlichen und räumlichen Komplexität dieser Flüsse und einer Unterschätzung deren Langzeittrends. Um diese Probleme zu überwinden, verwende ich ein regionales Ozeanmodell mit einer räumlichen Auflösung von 5 km, basierend auf dem Regional Oceanic Modeling System (ROMS), welches an ein biogeochemisches Modell mit integriertem Kohlenstoffmodul gekoppelt ist. Mit Simulationen dieses Modells untersuche ich die natürliche Variabilität von pCO_2 und Atmosphäre-Ozean-CO_2-Flüssen auf saisonalen bis interannuellen Zeitskalen. Weiter bestimme ich Langzeittrends der Ozeanversauerung, die vom Anstieg von anthropogenem CO_2 und von Änderungen physikalischer Grössen, wie windgetriebener Auftrieb und Temperatur, herrühren. Resultate von einer klimatologischen Simulation belegen, dass die saisonale pCO_2-Variabilität im CalCS von DIC und Temperatur bestimmt wird, wobei die küstennahen 100 km vom Auftrieb von DIC dominiert werden, während pCO_2 auf offener See eher von der Temperatur und deren Effekt auf die CO_2-Solubilität kontrolliert wird. Auf jährlicher Basis ist das CalCS ein beinahe neutrales CO_2-System, welches nur ungefähr $0.05\,\mathrm{mol\,C\,m^{-2}\,yr^{-1}}$ aufnimmt. In der lokalen und zeitlich höherfrequenten Betrachtung können die Atmosphäre-Ozean-CO_2-Flüsse aber zwischen $-1.5\,\mathrm{mol\,C\,m^{-2}\,yr^{-1}}$ (nördliches CalCS, offene See, Winter) und $3.2\,\mathrm{mol\,C\,m^{-2}\,yr^{-1}}$ (zentrales CalCS, küstennah, Sommer) schwanken. Diese Schwankungsbreite reflektiert den starken Gradienten zwischen offener See und Küstennähe in Bezug auf den kombinierten Effekt, den Auftrieb und biologische Produktivität auf die saisonalen pCO_2-Schwankungen haben. Analysen einer Hindcast-Simulation von 1979 bis 2012 zeigen eine substantielle interannuelle Variabilität der Atmosphäre-Ozean-CO_2-Flüsse von gleicher Grössenordnung wie der saisonale Zyklus, welche zudem signifikant mit verschiedenen Moden der Klimavariabilität korreliert, namentlich der El Niño/Southern Oscillation (ENSO), der Pacific Decadal Oscillation (PDO) und der North Pacific Gyre Oscillation (NPGO). Diese drei Moden der Klimavariabilität haben einen zum Teil gegenläufigen Effekt auf pCO_2 in Küstennähe gegenüber der offenen See. Dieses asymmetrische Muster entstammt der regional unterschiedlichen Dominanz von DIC und Temperatur, welche ihrerseits von ENSO, PDO und NPGO moduliert werden und so pCO_2 beeinflussen. Durch

die Kombination der Hindcast-Simulation mit einer Simulation über den gleichen Zeitraum, in welcher nur das atmosphärische CO_2 und das laterale DIC zunehmen - das Klima bleibt also konstant - kann ich zeigen, dass die homogene ozeanweite Versauerung durch ansteigendes anthropogenes CO_2 entlang der Küste von Oregon und Nordkalifornien durch die Intensivierung von auftriebsfördernden Winden noch verstärkt wird. Dieser verstärkte Auftrieb zeichnet sich an gewissen Stellen verantwortlich für bis zu 30% der pH-Abnahme und 50% der Erniedrigung des Aragonit-Sättigungsgrads. Dies unterstreicht die Wichtigkeit der küstennahen Klimaänderungen, welche in Untersuchungen der Ozeanversauerung durch anthropogenes CO_2 zwingend berücksichtig werden müssen.

Zusammenfassend lassen sich aus den Studien dieser Doktorarbeit folgende übergreifende Erkenntnisse ableiten: (i) Die Anwendung eines hochaufgelösten regionalen Ozeanmodells ist unabdingbar, um die extreme zeitliche und räumliche Variabilität der Kohlenstoffflüsse in Zusammenhang mit der Auftriebsdynamik der Auftriebsgebiete an Ozeanoströndern zu studieren, (ii) es existiert eine enge Kopplung von Klimavariabilität zu den Kohlenstoffflüssen in diesen Gebieten auf monatlichen bis interannuellen Zeitskalen, und (iii) um die Effekte von zunehmendem atmosphärischem CO_2 und von physikalischen Änderungen im Klimasystem auf jüngste Trends im CO_2-System dieser Gebiete zu trennen, bedarf es Hindcast-Simulationen, welche transient angetrieben sind.

Contents

Chapter 1

Introduction

1.1 The ocean in a high CO_2 world

Throughout the last 800,000 years, the atmospheric concentrations of greenhouse gases such as carbon dioxide (CO_2), methane and nitrous oxide recorded in ice cores have never been as high as they currently are (Ciais et al., 2013; Masson-Delmotte et al., 2013). Since the beginning of the industrial era around 1750, CO_2 levels have increased by roughly 40%, and reached concentrations of up to 391 ppm in the year 2011 (Fig. 1.1), due to human emissions from the combustion of fossil fuel and from cement production, but also from changes in land-use, including deforestation and biomass burning. Roughly half of this released CO_2 remains in the atmosphere, while the rest is taken up by the ocean and the land biosphere, which act as reservoirs in the global carbon cycle (Rhein et al., 2013). The ocean is by far the largest reservoir, storing about 38,000 Pg C alone in the form of dissolved inorganic carbon (DIC). In comparison, the land biosphere with about 5,500 Pg C and the atmosphere with only about 800 Pg C have much smaller carbon storage capacities (Emerson and Hedges, 2008). The interactions between the individual reservoirs are important in controlling the biogeochemical dynamics and cycling of carbon and bio-essential nutrients. According to the budgets established by Sabine et al. (2004), the ocean has taken up about 118 ± 19 Pg C between 1800 and 1994, corresponding to roughly one third of the total anthropogenic CO_2 released into the atmosphere during that time. It is estimated that in the absence of this sink, the current radiative forcing which is associated with increased atmospheric CO_2 would be about 30% higher (Sarmiento and Gruber, 2006).

Based on indirect estimates of CO_2 from the 1990's (McNeil et al., 2003; Manning and Keeling, 2006; Mikaloff Fletcher et al., 2006; Denman et al., 2007) and a set of state-of-the-art ocean biogeochemistry models (Le Quéré, 2009), Le Quéré et al. (2013) estimated the present-day global ocean CO_2 sink strength to be around -2.5 ± 0.5 Pg C yr^{-1} for the period 2002–2011, while for the year 2011 alone, the uptake was assessed to be slightly larger at -2.7 ± 0.5 Pg C yr^{-1}. As anthropogenic CO_2 emissions are anticipated to persist well throughout the twenty-first cen-

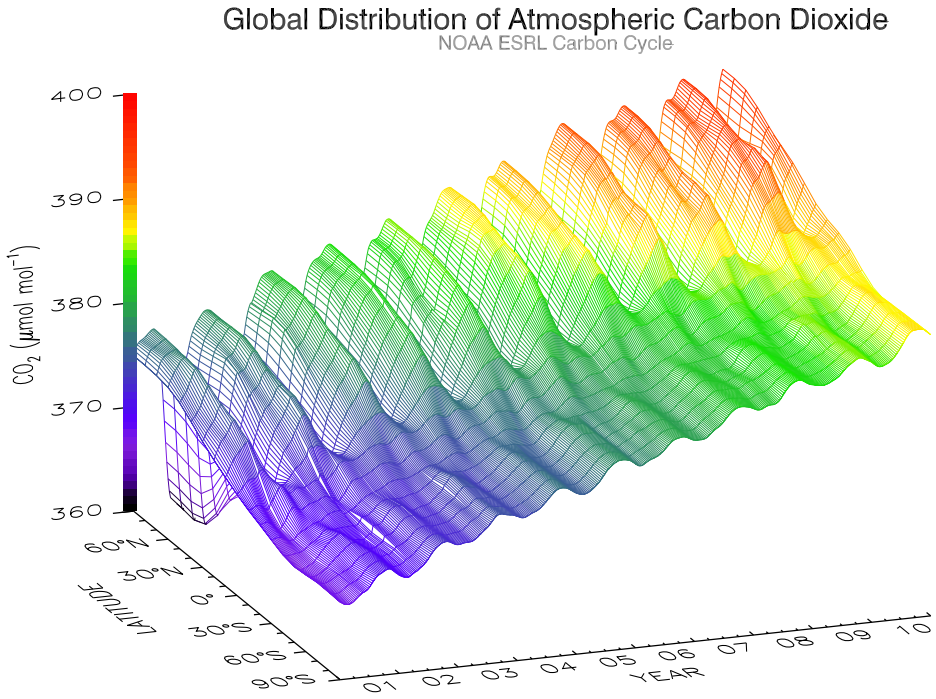

Figure 1.1 Three-dimensional representative of the latitudinal distribution of atmospheric CO_2 in the marine boundary layer from 2001 to 2010 and from 90°S to 90°N. Data is from the Carbon Cycle cooperative air sampling network (source: NOAA ESRL GLOBALVIEW-CO_2, May 2012).

tury (Ciais et al., 2013), the atmospheric CO_2 concentration and hence atmospheric pCO_2 will continue to rise, which causes the ocean to take up more CO_2 in surface waters. For a better comprehension of this human perturbation of the global carbon cycle, it is convenient to distinguish between a natural, unperturbed component and a superimposed anthropogenic component of the atmosphere-ocean carbon fluxes. Both of these components are subject to variations in Earth's climate and can lead to feedbacks between the carbon cycle and the climate system. An example of a positive feedback is the warming of the upper ocean layer due to increased surface radiation which reduces the solubility of CO_2, leading to a decreased uptake of anthropogenic CO_2 and a rise in the outgassing of natural CO_2 which was stored in the ocean reservoir. Given that the ocean carbon pool is much larger compared to the atmospheric carbon pool, an important aspect to consider is the following: if we influence the natural carbon cycle by altering processes in the ocean which involve carbon, this could have a significant additional impact on the existing atmospheric CO_2 concentration. If we want to improve our quantitative evaluation of the future atmospheric carbon pool, it is essential to gain a more profound understanding of the processes involving carbon in the ocean and their responses to global climate change.

1.1.1 CO_2 exchange at the air–sea interface and inorganic oceanic carbonate chemistry

Atmospheric CO_2 enters the ocean via the air–sea gas exchange at the surface ocean–atmosphere interface (see Eq. 2.4 in Section 2.2 for the detailed equations). When atmospheric CO_2 is taken

up by the surface ocean, it reacts with seawater to form carbonic acid (H_2CO_3), which in turn dissociates in two steps into bicarbonate (HCO_3^-) and carbonate ions (CO_3^{2-}). The equilibrium reactions for these three steps can be summarized as follows:

$$CO_{2(gas)} + H_2O \overset{K_0}{\rightleftharpoons} \overbrace{H_2CO_3 + CO_{2(aq)}}^{H_2CO_3^*} \tag{1.1}$$

$$H_2CO_3^* \overset{K_1}{\rightleftharpoons} H^+ + HCO_3^- \tag{1.2}$$

$$HCO_3^- \overset{K_2}{\rightleftharpoons} H^+ + CO_3^{2-}, \tag{1.3}$$

where H^+ is the hydrogen ion and $H_2CO_3^*$ is a hypothetical species summarizing the concentrations of H_2CO_3 and the aqueous form of CO_2 ($CO_{2(aq)}$), which are analytically nearly indistinguishable. The corresponding dissociation constants K_0, K_1 and K_2 for these three reactions are described by the following relationships:

$$K_0 = \frac{[H_2CO_3^*]}{pCO_2} \tag{1.4}$$

$$K_1 = \frac{[H^+][HCO_3^-]}{[H_2CO_3^*]} \tag{1.5}$$

$$K_2 = \frac{[H^+][CO_3^{2-}]}{[HCO_3^-]}, \tag{1.6}$$

where K_0 is the solubility of CO_2 in seawater, K_1 and K_2 are the first and second dissociation constants of carbonic acid and the brackets denote the total concentrations of the individual species. As these reactions happen at very small timescales, it is safe to assume thermodynamic equilibrium between these species.

To describe the carbonate chemistry of a seawater sample, pCO_2^{sea} and the pH value ($pH = -log[H^+]$) of the sample are typically measured. However, these parameters are not conservative to changes in temperature, salinity or pressure (changes in state), and are hence not well suited to use in modeling. Therefore, the two variables DIC and Alk, which are conservative with respect to state changes, are defined as:

$$DIC = \underbrace{[H_2CO_3^*]}_{0.5\%} + \underbrace{[HCO_3^-]}_{88.6\%} + \underbrace{[CO_3^{2-}]}_{10.9\%} \tag{1.7}$$

$$Alk = \underbrace{[HCO_3^-]}_{76.8\%} + \underbrace{2[CO_3^{2-}]}_{18.8\%} + \underbrace{[OH^-] - [H^+]}_{0.2\%} + \underbrace{[B(OH)_4^-]}_{4.2\%} + \text{minor bases}, \tag{1.8}$$

where $[OH^-]$ and $[B(OH)_4^-]$ are the concentrations of the hydroxide ion and the borate ion, respectively. The percentages denote the relative abundances of each species, determined for present-day global mean seawater properties, with a mean pH value of ∼8.2. Figure 1.2 gives an overview of the concentrations of the main inorganic carbon species as a function of oceanic pH. As both DIC and Alk are mainly determined by the concentrations of HCO_3^- and CO_3^{2-}, and only a very small fraction exists in the form of dissolved CO_2, Eqs. 1.7 and 1.8 can be approximated by:

$$DIC \approx [HCO_3^-] + [CO_3^{2-}] \tag{1.9}$$

$$Alk \approx [HCO_3^-] + 2[CO_3^{2-}], \tag{1.10}$$

where this expression for Alk is also termed “carbonate Alkalinity”. By combining Eqs. 1.9 and 1.10, the concentrations of HCO_3^- and CO_3^{2-} can then be expressed only in terms of DIC and Alk:

$$[HCO_3^-] \approx 2 \cdot DIC - Alk \tag{1.11}$$

$$[CO_3^{2-}] \approx Alk - DIC \tag{1.12}$$

1.1.2 The “soft-tissue” pump and the calcium carbonate pump

The main governing biological processes which impact DIC and Alk and hence alter pCO_2, are photosynthesis and the reverse mechanism of remineralization. During photosynthesis, inorganic carbon and nutrients in the euphotic zone (the 1% light level zone) are used by phytoplankton to produce organic matter, which then sinks to the aphotic zone, where most of it is remineralized, while a small part is buried in sediments. Through vertical transport and mixing the dissolved CO_2 and nutrients are again delivered to the surface. These processes of production, remineralization

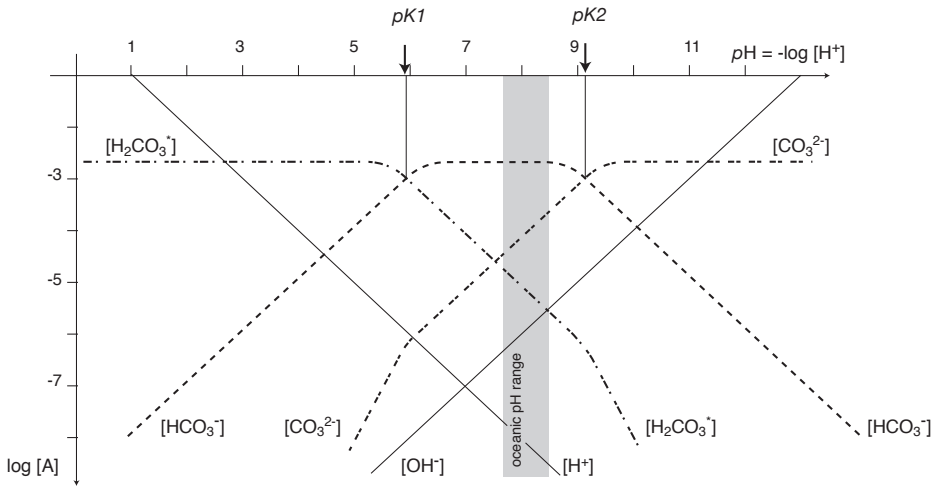

Figure 1.2 Concentrations of the carbonate species $H_2CO_3^*$, HCO_3^- and CO_3^{2-} as functions of pH (logarithmic vertical and horizontal scales). In this plot, the total DIC concentration is assumed constant at 2000 μmol kg^{-1}, while the relative contributions from each species to the DIC pool vary with increasing or decreasing pH. pK_1 is defined as the negative logarithm of the first dissociation constant from Eqs. 1.2 and 1.5 (i.e., $pK_1 = -log(K_1)$) and indicates the pH value at which the concentrations of $H_2CO_3^*$ and HCO_3^- are equal. pK_2 is calculated analogously from the second dissociation constant and refers to the pH value where $[HCO_3^-]$ is equal to $[CO_3^{2-}]$. Figure from Sarmiento and Gruber (2006).

and the vertical transport of carbon and nutrients constitute the so-called "soft-tissue" pump. Assuming constant ratios of $C : N : P : O_2 = 106 : 16 : 1 : -150$ (known as Redfield ratios; Redfield et al., 1963), these processes can be summarized as follows:

$$106CO_2 + 16NO_3^- + HPO_4^{2-} + 78H_2O + 18H^+ \underset{\text{remineralization}}{\overset{\text{production}}{\rightleftharpoons}} C_{106}H_{175}O_{42}N_{16}P + 150O_2 \tag{1.13}$$

According to this relationship, the formation of 1 mol of organic matter decreases DIC by 106 moles (-106CO_2) and increases Alk by 17 moles (-18H^+ and -HPO_4^{2-}). Its remineralization below the euphotic zone accordingly increases DIC and decreases Alk. In addition to photosynthesis and remineralization, there is a second biological reaction which impacts DIC and Alk, namely the formation and dissolution of aragonite and calcite, two mineral forms of calcium carbonate ($CaCO_3$):

$$Ca^{2+} + CO_3^{2-} \overset{K_{sp}}{\rightleftharpoons} CaCO_3, \tag{1.14}$$

In this equilibrium relationship, K_{sp} is the solubility product, defined as the product of the concentrations of the carbonate and dissolved calcium ions in equilibrium with $CaCO_3$ ($K_{sp} = [Ca^{2+}]_{sat}[CO_3^{2-}]_{sat}$). These processes of $CaCO_3$ dissolution and formation change Alk twice as

strongly as they change DIC (Eq. 1.8). Although the $CaCO_3$ cycling contributes roughly four times less to surface-to-deep DIC gradient than the "soft-tissue" pump does, the formation of $CaCO_3$ also reduces the concentration of HCO_3^- and therefore reduces Alk in the surface ocean (Eq. 1.10). Together with the sinking and dissolution of organic $CaCO_3$ in the water column, which leads to a net downward transport of DIC and Alk, the overall effect of the $CaCO_3$ cycle is therefore to increase surface ocean pCO_2.

1.1.3 Consequences of enhanced oceanic CO_2 uptake

As atmospheric CO_2 levels continue to increase, the CO_2 gas transfer across the surface ocean–atmosphere boundary will act as an equilibrator between these two mediums, leading to a concurrent rise in surface ocean pCO_2, and resulting in a drop in pH to more acidic levels, a process known as "ocean acidification". Ocean acidification has previously been referred to as "the other CO_2 problem" (Doney et al., 2009a), as it is a process impacting oceanic ecosystems and organisms that needs to be dealt with in addition to surface ocean warming due the global greenhouse effect. When atmospheric CO_2 dissolves in seawater, not even 1% of it remains as $H_2CO_3^*$, as most of it dissociates into HCO_3^- and CO_3^{2-} (Kleypas et al., 1999). At the same time, the dissolution of CO_2 in seawater leads to the formation of hydrogen ions (H^+), some of which combine with CO_3^{2-} to form more HCO_3^-. This process can be illustrated by combining Eqs. 1.1 to 1.3 into one:

$$H_2O + CO_2 + CO_3^{2-} \rightleftharpoons 2HCO_3^- \tag{1.15}$$

From this equation it follows that if CO_2 rises, CO_3^{2-} has to decrease, while concurrently, the pH of seawater is lowered. Thus any perturbation to this system in the form of added CO_2 will be adjusted by a shift in the chemical equilibrium between the carbonate species towards more HCO_3^-. This process is often referred to as the "carbonate/bicarbonate buffering system". Under average seawater conditions with pH values of 8.0 to 8.2, the concentration of HCO_3^- is roughly 6 to 10 times larger than the concentration of CO_3^{2-} (Fig. 1.2; Sarmiento and Gruber, 2006).

CO_3^{2-} is a carbon species used by calcifying organisms to build aragonite and calcite, which are essential to the formation of these organisms' shells and skeletons (Orr et al., 2005). To determine whether seawater is over- or undersaturated with respect to aragonite or calcite, a saturation state, $\Omega_{arag,calc}$, is defined as:

$$\Omega_{arag,calc} = \frac{[Ca^{2+}][CO_3^{2-}]}{K_{sp}}, \tag{1.16}$$

where $[Ca^{2+}]$ and $[CO_3^{2-}]$ are the observed concentrations of the calcium and carbonate ions.

The saturation states of aragonite and calcite are indicative of whether waters support the formation of $CaCO_3$ shells ($\Omega > 1$) or promote the dissolution of $CaCO_3$ into Ca^{2+} and CO_3^{2-} ($\Omega < 1$) (e.g., Feely et al., 2008; Gruber et al., 2012; Hauri et al., 2013b,a; Lachkar, 2014). As any variations in $[Ca^{2+}]$ are small compared to changes in $[CO_3^{2-}]$ (Sarmiento and Gruber, 2006), we can assume $[Ca^{2+}] \approx [Ca^{2+}]_{sat}$ and hence:

$$\Omega_{arag,calc} \approx \frac{[CO_3^{2-}]}{[CO_3^{2-}]_{sat}}. \tag{1.17}$$

Figure 1.3 summarizes the most important processes mentioned above by illustrating the fate of CO_2 after it has been taken up by the surface ocean.

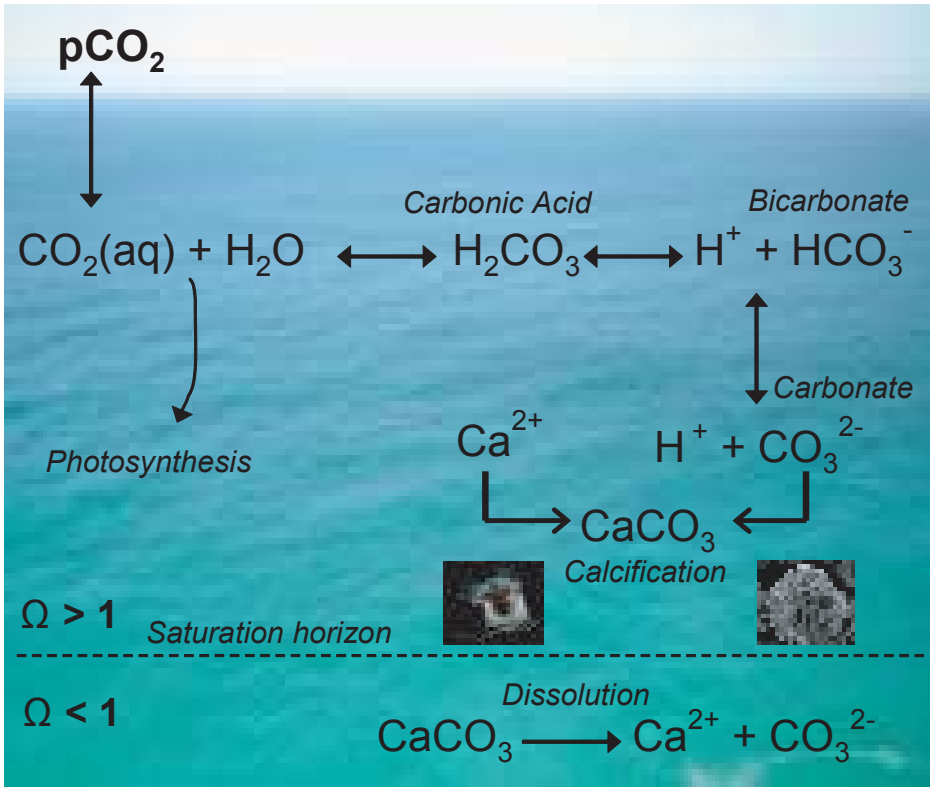

Figure 1.3 Schematic of the processes involved in ocean acidification (Courtesy of T. Frölicher; Frölicher, 2009).

There are several regions of the global ocean which are particularly sensitive to changes in their carbonate chemistry. Polar regions for instance have naturally low concentrations of CO_3^{2-} due to the cold sea surface temperature increasing the solubility of CO_2 (Orr et al., 2005). Hence, these areas are naturally closer to undersaturated conditions than tropical regions. Coastal oceans are another example of regions prone to the effects of ocean acidification. These are often areas where multiple stressors, such as eutrophication, atmospheric deposition of nutrients and river runoff (Cai et al., 2011; Doney et al., 2007; Salisbury et al., 2008, e.g.,), converge, rendering them particularly sensitive to changes in their carbonate chemistry.

1.2 The coastal ocean carbon cycle

The coastal ocean plays an important role in the global carbon cycle, as it acts as an interface between the land biosphere, the open ocean and the atmosphere, and constitutes many diverse ecosystems at different spatial scales, such as rivers, estuaries, tidal wetlands, and the continental shelf (Bauer et al., 2013). Although there is still some debate as to the present role of the coastal ocean in the global carbon cycle (Emerson and Hedges, 2008), there is a general agreement that the coastal ocean has become a net sink for CO_2 since the beginning of the industrial revolution (Mackenzie et al., 2005). Carbon cycling in these regions has been acknowledged to play an important role in the global carbon cycle and global carbon budgets (e.g., Cai, 2011; Bauer et al., 2013; Regnier et al., 2013). However, the coastal ocean has up until now been largely neglected in global carbon budget estimates, largely due to issues of undersampling and because global numerical models are often too coarse to properly resolve biogeochemical processes in coastal regions.

In the following, the focus will be laid on coastal ecosystems which are considered to contribute significantly to coastal ocean air–sea CO_2 fluxes, such as continental margins, estuaries and coastal upwelling systems.

1.2.1 Continental shelves and estuaries

In some of the earliest studies on the air–sea CO_2 exchange in continental shelves, Tsunogai et al. (1999) and Thomas et al. (2004) highlighted the importance of these regions in taking up CO_2 from the atmosphere. Tsunogai et al. (1999) introduced the term "continental shelf pump" to explain the large uptake of CO_2 in their study area, the East China Sea. The cool and dense waters over the shelf there promote the solubility of CO_2 which - together with the increased biological production - lead to an enhanced drawdown of CO_2 and increased DIC transport to the shelf floor. These dense, DIC-rich waters are then transported to the sub-surface layer of the open ocean through isopycnal mixing. Tsunogai et al. (1999) suggested that due to this continental shelf pump mechanism, the global continental shelves' sink strength could amount up to $1\,\mathrm{Pg\,C\,yr^{-1}}$, corresponding to half of the total open ocean uptake known at that time. Thomas et al. (2004) on the other hand, estimated the coastal and marginal seas to account for roughly 20% of the global CO_2 uptake. However, these estimates are based on very limited sets of observations, from the East China Sea and the North Sea, respectively, and were upscaled to the total continental shelf area (Cai and Dai, 2004). More recent studies likewise rely on upscaling methods, but base their estimates on more varied sets of observations: Borges (2005), Borges et al. (2005) and Chen and Borges (2009) used all available data on continental shelf air–sea CO_2 fluxes and inferred a global continental shelf uptake flux of –0.3 to $-0.4\,\mathrm{Pg\,C\,yr^{-1}}$. Chen and Borges (2009) also found that while most offshore areas of the global shelves act as sinks for atmospheric CO_2, many near-

shore coastal waters act as sources. Going one step further, Cai et al. (2006) split continental shelves into seven provinces and estimated air–sea CO_2 fluxes for these provinces separately. They suggest that in terms of source/sink behavior, continental margins differ latitudinally, with mid-to-high latitude shelves being sinks for CO_2 (–0.33 Pg C yr^{-1}) and low latitude shelves acting as sources (0.11 Pg C yr^{-1}). Their total mean for continental shelves hence amounted to a net sink of roughly –0.22 Pg C yr^{-1}. In a later study, Cai (2011) updated these estimates to conclude a net global continental shelf sink estimate of –0.25 Pg C yr^{-1}. Although this estimate is lower than that of Chen and Borges (2009) (–0.33 to –0.36 Pg C yr^{-1}), it agrees well with a recent study by Laruelle et al. (2010) (–0.21 $\pm$ 0.36 Pg C yr^{-1}) who used a different scaling method. Despite the many attempts to provide a reliable estimate of air–sea CO_2 fluxes in coastal oceans, it is clear from these previous studies that the coastal ocean, and in particular continental shelves, is greatly undersampled (Cai et al., 2006). Estuaries have recently been the subject of several air–sea CO_2 flux studies and have been estimated to be strong sources for CO_2 (e.g., Raymond et al., 1997; Cai and Wang, 1998; Frankignoulle et al., 1998; Borges et al., 2005, 2006). Although they only occupy about 0.3% of the global ocean surface area, while continental shelves take up roughly 7.2% of the surface area (e.g., Walsh, 1988; Cai, 2011), their integrated net outgassing flux has been found to be approximately the same as the net integrated uptake of CO_2 by continental shelves, i.e. 0.25 Pg C yr^{-1} (Cai, 2011).

Margins dominated by coastal upwelling, such as Eastern Boundary Upwelling Systems, are particularly complex coastal ecosystems in terms of carbon cycling, as they are supplied with nutrient- and DIC-rich deep water. Again, due to the lack of a sufficient sampling frequency, it is difficult to estimate precise net air–sea CO_2 fluxes for these regions. However, recent studies indicate that also in the case of EBUS, the low-latitude regions act as sources of CO_2 to the atmosphere, while mid-to-high latitude regions are CO_2 sinks (e.g., Borges et al., 2005; Cai et al., 2006).

1.2.2 Eastern Boundary Upwelling Systems

There are four major Eastern Boundary Upwelling Systems (EBUS): the California, Humboldt, Canary and Benguela Upwelling Systems (see white ovals in Fig. 1.4), which have been subject to several comparative studies (e.g., Capet et al., 2008; Chaigneau et al., 2009; Chavez and Messié, 2009; Fréon et al., 2009; Gruber et al., 2011; Lachkar and Gruber, 2012; Capone and Hutchins, 2013). All of these EBUS are associated with the subtropical oceanic gyres of the Atlantic or Pacific Ocean and include the equatorward and alongshore flowing surface currents as well as the coastal circulations which are linked to the gyres' eastern limbs. The trade winds that blow equatorwards along these eastern limbs, i.e. along the western coasts of North and South America and the northern and southern coasts of West Africa (Chavez and Messié, 2009), cause a horizontal offshore Ekman drift at the ocean's surface. In the case of the EBUS, the coastal

margins act as physical boundaries, so that the water is replaced by water from below the surface via Ekman suction (Sarmiento and Gruber, 2006). The offshore transport of CO_2 and nutrients is aided by narrow filaments which transfer the coastal water across the shelf break. Subduction of surface water occurs at the edges of such filaments and along isopycnal layers (Fig. 1.5). A further important process which promotes offshore transport is the westward propagation of mesoscale eddies which are generated by frontal instabilities (Plattner et al., 2005; Gruber et al., 2011; Nagai et al., 2014).

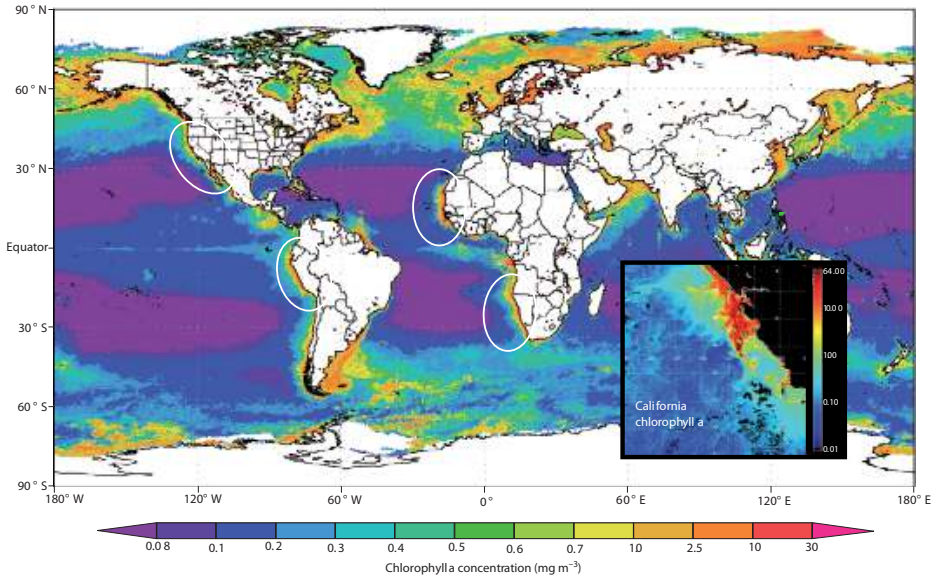

Figure 1.4 Global chlorophyll a concentrations as a false-color compilation of satellite data from the MODIS Aqua sensor for the year 2011 The white ovals indicate the approximate locations of the California, Canary, Humboldt and Benguela Current Systems. The inset shows a close-up of chlorophyll a concentrations in the California Current System. Figure adapted from Capone and Hutchins (2013).

EBUS are among the most productive large marine ecosystems, due to the wind-driven upwelling of cool water which is rich in nutrients and DIC (e.g., Chavez and Messié, 2009; Capone and Hutchins, 2013) (see background in Fig. 1.4). The upwelled nutrients support such immense phytoplankton blooms and sustain a large phytoplankton productivity that these areas support up to 20% of the global fish catch, making them indispensable as a resource to humans for harvesting biological oceanic resources (Pauly and Christensen, 1995). The range of natural variability in pCO_2 and pH in EBUS is large due to the high levels of DIC that are upwelled together with the nutrients, and is among the most extreme in the global ocean. This means that in some areas, pCO_2 can exceed values of 1000 μatm (Evans et al., 2011), a CO_2 concentration which is not projected to be reached in the atmosphere within this current century (Ciais et al., 2013). Likewise, pH values can drop to values as low as 7.6–7.7 as in the case of the California Current System (Feely et al., 2008), while the global ocean has a mean pH value of around 8.1. Phytoplankton at the surface metabolize most of the inorganic carbon through photosynthesis, so that CO_2 levels are drawn down and pH values increase in the surface ocean. Phytoplankton blooms are capable of lowering oceanic pCO_2 to values below $\sim$400 μatm, as has been observed in surface waters

in an upwelling filament off the coast of northwest Africa (Loucaides et al., 2012), where pCO_2 values were found to drop by 130 μatm in just over a week's time due to biological consumption. In some regions of certain EBUS, such as the southern California and the central Canary Current System, a comparative model study showed that biological productivity and hence CO_2 consumption increased with the intensity of wind-driven upwelling. In other parts of these EBUS however, the response to increased upwelling intensity was less clear due to factors including slower growth rates, stronger nutrient limitation and shorter surface water residence times (Lachkar and Gruber, 2013). The abundant supply of DIC to the surface also causes coastal upwelling regions to act as sources of CO_2 to the atmosphere, while further offshore, the nutrients are able to stimulate enough phytoplankton growth and reduce surface water pCO_2, so that those areas tend to act as sinks within the coastal region (e.g., Hales et al., 2005; Chavez and Messié, 2009; Turi et al., 2014a).

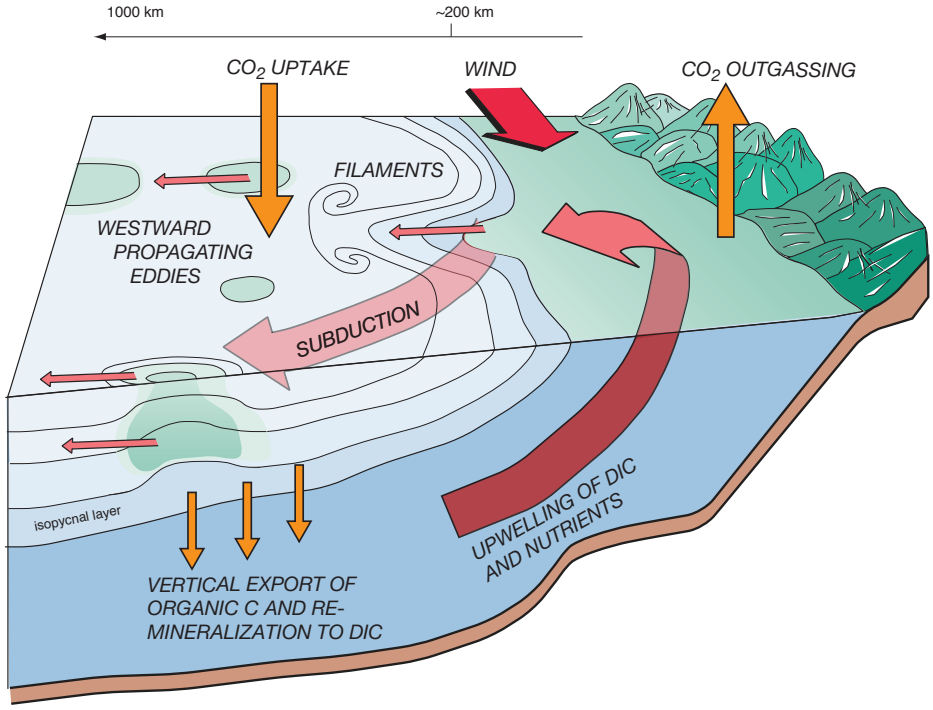

Figure 1.5 Schematic of the processes occurring in northern hemisphere EBUS: wind-induced upwelling, offshore transport and subduction (courtesy of N. Gruber).

Due to their dependence on wind strength and patterns, EBUS are subject to seasonal to interannual variability caused by the influence that oscillations of large-scale atmospheric conditions have on the basin-scale wind cycles and oceanic gyres. For instance in the California and northern Humboldt Current Systems during El Niño phases, stratification is increased and surface layers experience warm anomalies due to the weakening of westerly trade winds. The result is a deepening of the nutricline and a strong reduction in the the rate of upwelling, i.e., how much nutrients are upwelled per unit water. As a result, primary production can be reduced by a factor of 5 to 20 (Barber and Chavez, 1983). Positive phases of the Pacific Decadal Oscillation (PDO), which can last up to decades at a time and are characterized by warm anomalies in northwestern Pacific surface waters (Chavez et al., 2003; McGowan et al., 1998), have a similar impact on these

two upwelling ecosystems, in that biological productivity is greatly reduced, which demonstrates the ability of these systems to rapidly adapt to extreme circumstances or quickly return to their default state (Lavaniegos and Ohman, 2007). Another process which impacts biology in EBUS are mesoscale eddies (Capet et al., 2008; Chaigneau et al., 2009), which, in a modeling study of the California and Canary Current Systems, have been shown to have a reducing effect on phytoplankton productivity by transporting nutrients away from the nearshore to regions further offshore (Gruber et al., 2011).

Apart from natural variability, EBUS are also subject to the consequences of recent anthropogenic perturbations, such as ocean acidification, the expansion of oxygen minimum zones, long-term surface ocean warming and associated changes in stratification, changes in coastal wind intensities or increases in the nitrogen and iron input to coastal upwelling regions through atmospheric deposition and riverine input (Capone and Hutchins, 2013). Due to the abundance and proximity of coastal research facilities and measuring stations, the California Current System is the EBUS which has received the most attention, both from the observational and the modeling community. The Canary and Humboldt Current Systems have only recently been subject to more extensive investigations, both within each coastal upwelling system and comparative to other EBUS. The Benguela Current System is the least well studied and documented EBUS of the four, and has only very recently been in the focus of studies investigating air–sea N_2O and CO_2 fluxes (e.g., Gutknecht et al., 2011; Gregor and Monteiro, 2013). Despite the fact that EBUS share several key characteristics, such as the processes causing upwelling and subduction and subsequent offshore transport of surface waters, they also differ from each other with respect to issues including the intensity and timing of seasonal upwelling, the degree of primary productivity, the presence and intensity of oxygen minimum zones, the width of the continental shelf, the presence of coastally trapped waves or the influence that large-scale climate variability has on them (e.g., Liu et al., 2010; Capone and Hutchins, 2013). When comparing EBUS, it is important to consider not only these differences between the individual coastal ecosystems, but also the regional diversity within each of the EBUS (Mackas et al., 2006) and the fact that they will likely not all respond in the same manner and with the same intensity to future anthropogenic and environmental perturbations.

1.3 The California Current System

The focus of this research project is on the California Current System (CalCS), one of the four major EBUS. This is a spatially and temporally highly variable region in terms of biogeochemical cycling, with natural variations ranging from sub-seasonal through annual to interannual and interdecadal timescales (e.g., Friederich et al., 2002; Bograd et al., 2009; Hauri et al., 2013b; Turi et al., 2014a). The CalCS is considered to be one of the most vulnerable EBUS, known to be particularly sensitive to anthropogenic perturbations, and has been the focus of various studies

investigating climate change-related phenomena such as ocean acidification (e.g., Feely et al., 2008; Gruber et al., 2012; Hauri et al., 2009, 2013b,a), the expansion of oxygen minimum zones (e.g., Bograd et al., 2008; Chan et al., 2008) or the effects of global warming on the vertical water column structure of the CalCS (e.g., Rykaczewski and Dunne, 2010).

1.3.1 Geographical and physical setting

The latitudinal dimensions of the CalCS extend from around 50°N, where the east-flowing North Pacific Current approaches the north American continent, to Baja California at about 15°N (Checkley Jr. and Barth, 2009). The alongshore, equatorward blowing wind causes an offshore Ekman flow perpendicular to the direction of the wind and a resulting upwelling along the coast from British Columbia to the Baja California Peninsula (Hickey, 1979). The zone of active coastal upwelling is limited to a narrow strip along the entire coast with a width of 10–25 km, although the area influenced by the upwelling extends much further offshore (Huyer, 1983). In addition to the upwelling and offshore transport of subsurface waters, the CalCS comprises several other circulation features such as the California Current, the California Undercurrent (sometimes called California Countercurrent), the seasonal Davidson Current, the Southern California Eddy and the Coastal Jet (Fig. 1.6).

The California Current constitutes the eastern, equatorward-flowing limb of the North Pacific Subtropical Gyre, a clockwise-rotating ocean current gyre (Fig. 1.6, no. 1). This current is broad, spanning around 50 to 1000 km offshore, and occupying the topmost 300 m of the surface waters, with the strongest southward flow located approximately a few hundred kilometers off the coast and increasing strength towards the top of the water column (Hickey, 1979). Northward of around 40°N (i.e., northward of Cape Mendocino, California), the flow is oriented approximately southwards, while south of Cape Mendocino, the flow becomes increasingly southeastward, turning back towards the southwest at around 25°N. The California Current is fed in the north with cool, nutrient-rich, low-salinity subarctic waters by way of the North Pacific Current (Fig. 1.6, no. 4), while further south, the entrainment of subtropical waters increases (Tabata, 1975), with the contribution of subarctic waters being most dominant in the summer months (Hickey, 1979). South of around 35°N (i.e., south of Point Conception, California), the California Current divides into a part that travels further along Baja California, another part that turns back north to join the California Undercurrent and a part which is recirculated in the Southern California Bight and is called the Southern California Eddy (Fig. 1.6, no. 5).

The California Undercurrent is narrower than the California Current (∼10–40 km wide) and flows northward as far as Vancouver Island along the continental slope with its core at a depth of about 150–300 m (Fig. 1.6, no. 2). The Undercurrent is characterized by water masses that are fairly warm, high in salinity and phosphate and low in dissolved oxygen, as they originate from the equatorial region. North of Point Conception, the core of the California Undercurrent can

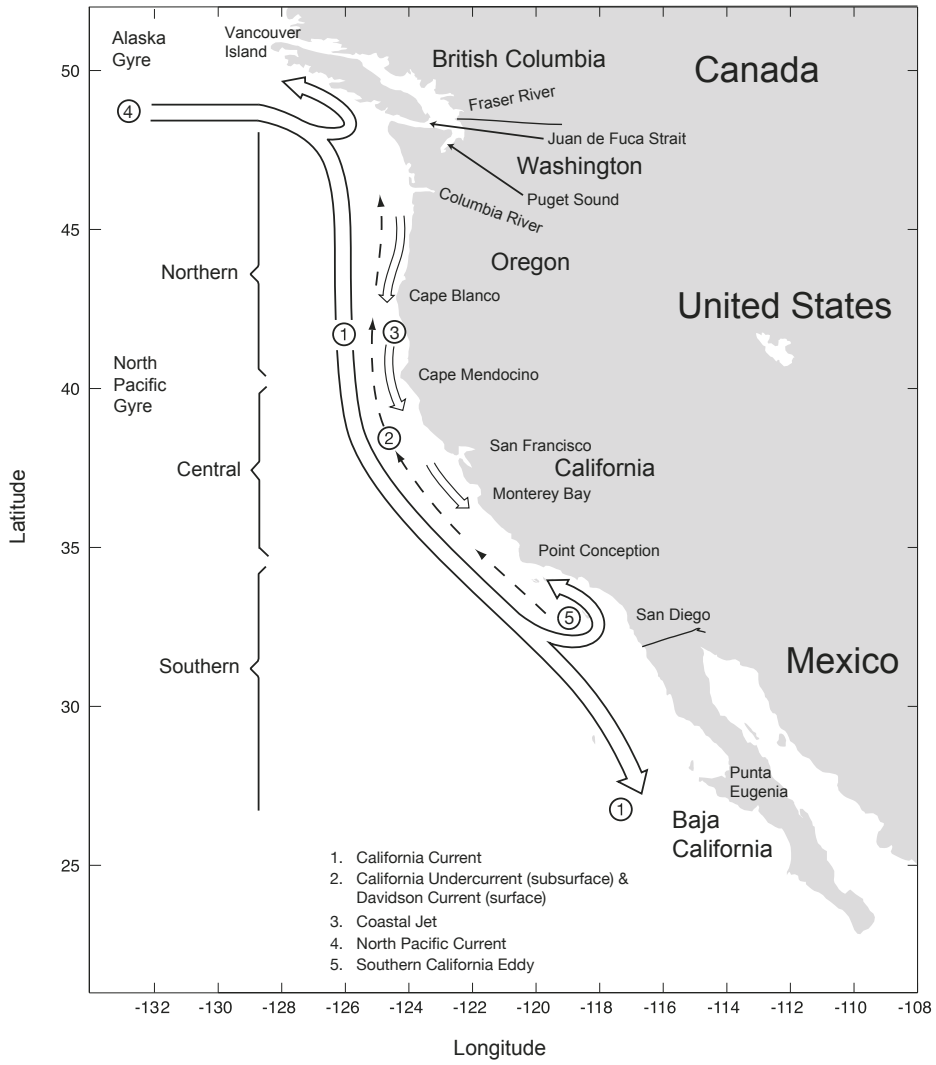

Figure 1.6 Schematic map of the California Current System with its most prominent geographical features and oceanic circulation patterns. Adapted from Checkley Jr. and Barth (2009).

reach the surface during late fall and winter, when it is known as the Davidson Current (Hickey, 1979).

The CalCS can geographically be separated into a northern, a central and a southern region (Fig. 1.6), which differ in their latitudinal seasonal wind and upwelling properties (Huyer, 1983; Checkley Jr. and Barth, 2009; Turi et al., 2014a). In the northern CalCS, the wind forcing is moderately strong and seasonally varying, while in the central CalCS, it is more persistent and equatorwards. In the southern CalCS, south of Point Conception and in particular in the southern California Bight, the seasonal variability of the wind forcing is small, with year-round, weak equatorward winds (Huyer, 1983). Due to the coastal topography, this area is shaded from the strong equatorward winds that blow along the northern and central CalCS coast. Accordingly, the coastal upwelling in the northern and central CalCS is a more seasonal event than in the southern CalCS. The central CalCS coastal regions in particular are influenced by seasonal changes in the upwelling strength. The upwelling season usually starts around early to late spring when the Aleutian low pressure system moves to the northwest, while the Pacific high-pressure system

shifts northward. These changes induce an intensification of the alongshore, equatorward wind, causing a strengthening in the coastal upwelling of CO_2- and nutrient-rich offshore waters from intermediate depths of 100 to 200 m (Feely et al., 2008). The upwelling season typically persists until late summer or fall, after which winter storms prevail and alongshore, equatorward winds weaken or even switch to northward blowing winds.

1.3.2 Biogeochemistry and carbon transport in the CalCS

The CalCS is a naturally highly variable system in terms of biogeochemistry and carbon cycling due to the extreme fluctuations in nutrients and DIC which are supplied to the surface ocean through wind-driven upwelling. Unlike the open ocean, where most of the locally produced organic matter is directly exported below the euphotic zone (Eppley and Peterson, 1979), the CalCS has been shown to be a region of spatial decoupling between new production and export production (Plattner et al., 2005). This decoupling was found to be a result of lateral offshore transport of newly produced organic matter, mainly driven by persistent mesoscale circulation features such as eddies and filaments, and less by the mean lateral Ekman-driven offshore transport. Moreoever, Nagai et al. (2014) show that the offshore transport of carbon and nutrients is not spatially uniform, but occurs in bands of alternating strong onshore and offshore transport, which supports the theory that Ekman transport is not the most dominant offshore transport mechanism. Gruber et al. (2011) suggested that westward-propagating eddies are responsible for a CalCS-wide reduction of net primary production (NPP) of 50–70% and a 35–50% decrease in the organic carbon export, where the largest reductions occur roughly between 100 and 500 km offshore. Offshore transport is also responsible for a spatial decoupling between the region of maximum upwelling and the area of highest biological productivity, which can clearly be seen in the pattern of CO_2 outgassing and uptake: by dividing the CalCS into different offshore regimes, Turi et al. (2014a) showed in a modeling study that the nearshore 100 km of the CalCS are on average a strong source of CO_2 to the atmosphere due to the excess of DIC upwelled there. The region between 100 and 400 km on the other hand acts on average as a CO_2 sink as a result of biological production being stimulated by the offshore transport of nutrients, which are not completely depleted in the nearshore upwelling zone (Fig. 1.5).

1.3.3 Large-scale climatic forcing of the CalCS

In addition to the seasonally varying equatorwards winds which induce variable degrees of upwelling all along the coast of the CalCS throughout the course of a year, the CalCS is influenced by longer-term natural variability, which has an impact on upwelling processes and hence on the ecosystem dynamics. The interannual to interdecadal variability of upwelling and related processes in the CalCS is strongly influenced by changes in the climatic forcing of this area. The

CalCS is impacted by basin-scale events such as coastally trapped Kelvin and Rossby waves, but also by more remote, large-scale climate variability modes (Fréon et al., 2009). There are three main modes of climate variability, or so-called atmospheric teleconnection patterns, which exert an important influence on the North Pacific Ocean, and in particular on the CalCS: the El Niño/Southern Oscillation (ENSO), the Pacific Decadal Oscillation (PDO) and the North Pacific Gyre Oscillation (NPGO). Each of these variability modes is associated with different atmospheric variability pattern and hence their effects on the upwelling dynamics of the CalCS vary. In order to facilitate the comparison of these climatic variability modes with data time series, monthly indices are defined for each mode, which provide a reference to the strength of a positive or negative phase of the respective mode (Fig. 1.7).

These three variability modes are not independent of each other. The different phases of the ENSO cycle are linked to the PDO and the NPGO via the North Pacific atmospheric variability, as the PDO and the NPGO can be seen as the oceanic expressions of two dominant modes of this variability, i.e., the Aleutian Low and the North Pacific Oscillation, respectively. Di Lorenzo et al. (2010) used an ensemble of simulations to demonstrate that SST anomalies associated with the Central Pacific El Niño (or "El Niño Modoki") can impact the extra-tropical atmospheric circulation. Changes in this circulation in turn drive the decadal fluctuations of the NPGO. With continuing climate change and rising atmospheric CO_2, the Central Pacific El Niño is projected to occur more frequently (Yeh et al., 2009), which could potentially have an impact on the dynamics of the NPGO as well (Di Lorenzo et al., 2010). In the following, ENSO, PDO and NPGO and their primary influences on the CalCS are explained in more detail.

1.3.3.1 El Niño/Southern Oscillation

There are several indices used to characterize the ENSO phenomenon. One of these is the Multivariate ENSO Index (MEI), which consists of a weighted average of the main oceanic and atmospheric ENSO properties in the tropical Pacific (30°S–30°N and 100°E–70°W) and is represented by the following six variables: sea-level pressure, the east-west and north-south components of the surface wind, sea surface temperature (SST), surface air temperature, and deep convection as reflected in cloud height (Wolter and Timlin, 1993, 1998, 2011). Another widely-used index is the Niño3.4 Index, which is calculated exclusively from monthly SST anomalies in the central tropical Pacific region (5°S–5°N and 170°W–120°W). The El Niño Modoki is a third climate pattern based on SST anomalies in the tropical Pacific, which is characterized by a strong positive SST anomaly in the central tropical Pacific and negative SST anomalies to the east and west of this (Ashok and Yamagata, 2009, Fig. 1.8). The teleconnection patterns associated with this pattern of warming and cooling in the tropical Pacific differ from the conventional El Niño teleconnection patterns. Hence, the the El Niño Modoki can be seen as a separate phenomenon. Furthermore, Yeh et al. (2009) found that for under global warming scenario, 8 out of 11 models projected an increased occurrence of El Niño Modoki over the classical El Niño. So far however, most studies

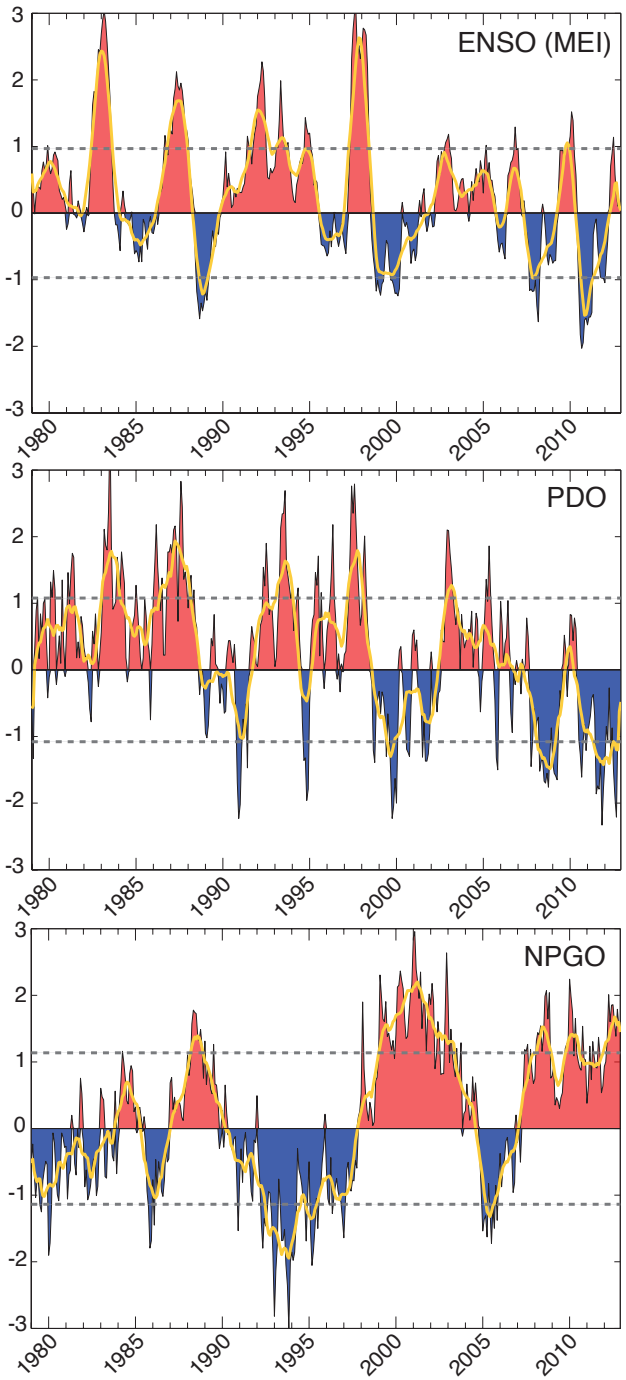

Figure 1.7 Monthly climate indices for ENSO (MEI: Multivariate ENSO Index), PDO and NPGO for the time period 1979–2012. Red shaded areas correspond to positive phases of the respective variability mode, while blue areas are negative phases. The orange lines represent the smoothed annual mean, calculated from monthly values with a 12-point moving window. The dashed lines indicate the ± 1 standard deviation thresholds, computed for each climate index separately for the period 1979–2012.

of the influence of teleconnective patterns on the CalCS have focused on the more traditional MEI and Niño3.4 Index. In these cases, positive indices represent the warm ENSO phase, or the El Niño, which is triggered by anomalous westerly winds in the equatorial Pacific that are linked to a "seesaw behavior" of the atmospheric surface pressure (Fig. 1.8). This atmospheric seesaw pattern was termed "Southern Oscillation" by Walker (1924), and its influence extends from the

eastern tropical Pacific to the western tropical Pacific and eastern Indian Ocean. The Southern Oscillation, together with the El Niño, can be seen as the atmospheric and oceanic expressions of a coupled climatic phenomenon, the ENSO (Clarke, 2014). The physical, chemical and biological responses of the equatorial Pacific to ENSO have been well-documented, particularly for the most extreme event to date during the years 1997 to 1999. For instance, combining in-situ measurements with satellite observations, Chavez (1999) investigated the response of the equatorial Pacific to the intense El Niño of 1997/1998 and found a decrease in the CO_2 outgassing strength and concurrent declines in nutrient availability and chlorophyll concentrations in the surface ocean. During the following La Niña period, the ecosystem quickly returned to a more biologically productive state, with stronger CO_2 outgassing and the largest phytoplankton blooms on record to that date.

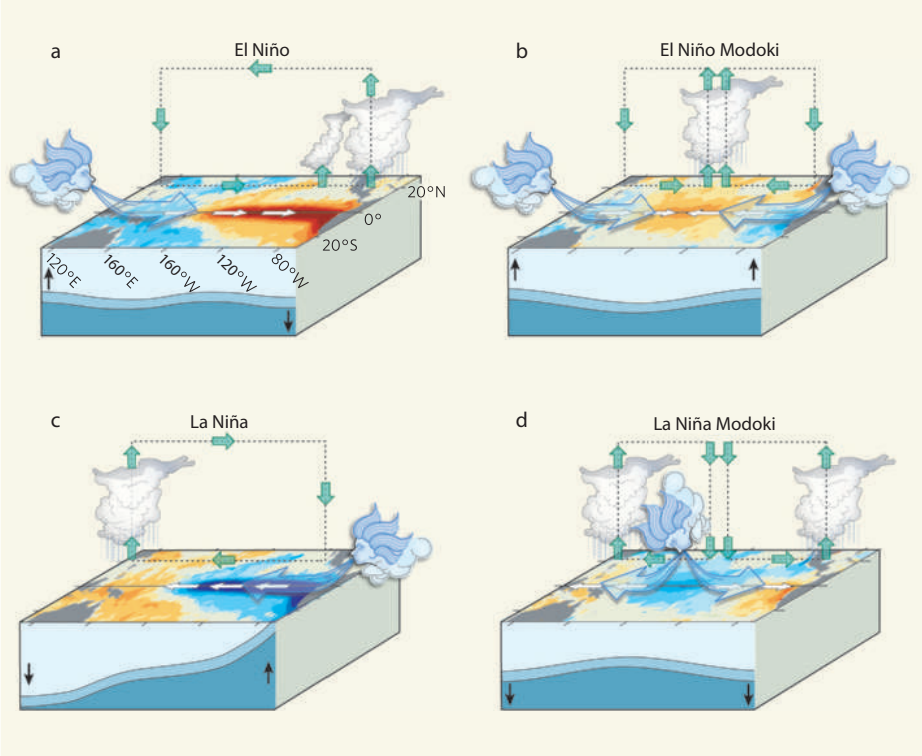

Figure 1.8 Illustration of the anomalous SST conditions in the tropical Pacific ocean during **(a)** El Niño, and **(b)** El Niño Modoki and during the respective opposite phases of **(c)** La Niña and **(d)** La Niña Modoki. The associated alterations in the atmospheric circulation and in the depth of the thermocline are also highlighted. From Ashok and Yamagata (2009).

There are also various studies investigating the more remote effects of the ENSO on the CalCS, with a particular focus on the ENSO cycle of 1997 to 1999. Bograd and Lynn (2001) for instance observed that the physical and biological response of the southern CalCS to the El Niño of 1997/1998 and the subsequent La Niña was strikingly similar to the response in the tropical Pacific, albeit with a lag of several months: during the positive ENSO phase, the nutricline deepened to below the depth from which water is typically upwelled, leading to a decline in biological production. During the ensuing negative ENSO phase, upwelling-favorable winds increased and the nutricline was found to shoal again. This study demonstrates that the influence of ENSO on

the CalCS is governed by both remote processes via the oceanic boundary (i.e., Kelvin waves) and through local atmospheric forcing (i.e., wind-driven upwelling). For the Oregon and northern California coasts, Huyer et al. (2002) suggested that the 1997 El Niño resulted in a depression of isotherms near the coast and an increased poleward flow along the coast. During the beginning of this El Niño period, warm SST anomalies were mainly associated with local conditions, while the observed subsurface warming was a result of Kelvin waves propagating the El Niño signal northwards along the coast. Towards the end of the period, warming throughout the water column was unquestionably associated with El Niño. Friederich et al. (2002) furthermore found that the ENSO cycle of 1997-1999 had a significant effect on the local air–sea CO_2 exchange in the CalCS. During the El Niño warm phase, the apparent suppression of upwelling caused oceanic pCO_2 levels to remain below atmospheric concentrations. In contrast, during the following cold period of La Niña, the intensified upwelling raised oceanic pCO_2 values to above atmospheric values, hence resulting in a release of CO_2 to the atmosphere.

1.3.3.2 Pacific Decadal Oscillation

The PDO index is derived as the leading principal component of monthly SST anomalies in the North Pacific Ocean, poleward of 20°N, and is typically connected with variations in the position and strength of Aleutian Low atmospheric pressure system (Mantua et al., 1997). The characteristics of the PDO are slightly different from those of ENSO, although they both tend to have a similar impact on the dynamics of the CalCS (Fig. 1.9). Firstly, a PDO phase can persist for several decades (20–30 years) and secondly, the climatic fingerprint of the PDO is most felt in the extratropics, in particular in the North Pacific region, with only a secondary impact felt by tropical regions (Mantua and Hare, 2002). A positive phase of the PDO is associated with warm SST anomalies in the eastern North Pacific, and hence in the CalCS region, and cold anomalies extending from Japan to the central North Pacific and with a strengthening of the Aleutian Low (Fig. 1.9). During negative phases, the opposite pattern dominates and the Aleutian Low becomes weaker (Macias et al., 2012). The effect on the upwelling in the CalCS is that a positive phase results in a shallowing of the upwelling cell, with surface waters from the north being more strongly advected. During the negative phase on the other hand, the weakening of the Aleutian Low favors alongshore, equatorward winds, hence leading to a deepening of the upwelling cell and to cooler SST anomalies (Chhak and Di Lorenzo, 2007). Chhak and Di Lorenzo (2007) suggest that during the warm PDO phase, fewer nutrients are provided to the surface ocean due to a decrease in the vertical mixing, which could lead to a drop in biological productivity, while during negative phases, enhanced vertical mixing would encourage phytoplankton growth.

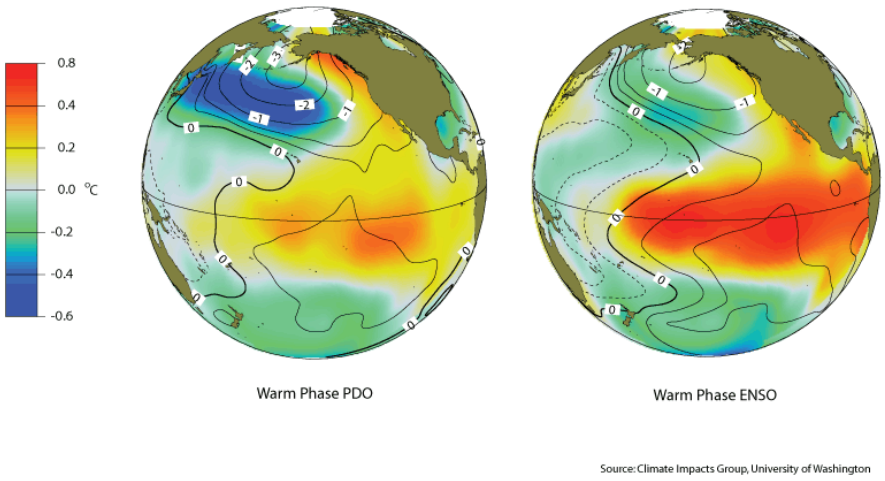

Figure 1.9 Warm phases of the PDO and of ENSO, showing SST (colored background) and sea level pressure anomalies (contour lines) for the period 1990–1992. Source: http://cses.washington.edu/cig/pnwc/aboutpdo.shtml (Climate Impacts Group, University of Washington).

1.3.3.3 North Pacific Gyre Oscillation

Di Lorenzo et al. (2008) defined the NPGO index as the second dominant mode of SSH variability in the Northeast Pacific, and showed that previously unexplained fluctuations of salinity, nutrients and chlorophyll, measured in long-term observations of the southern CalCS, were significantly correlated with the NPGO index (Di Lorenzo et al., 2009). In contrast, in the more northern areas of the CalCS, upwelling was more strongly controlled by changes in the alongshore winds, attributable to the PDO. The term "NPGO" was coined because its fluctuations reflect changes in the intensity of the central and eastern branches of the North Pacific gyre circulation. The local effects of the NPGO on the CalCS are determined by variability in surface winds, which is associated with the North Pacific Oscillation (NPO), a see-saw pattern in sea level pressure with a high pressure system over Hawaii and low pressure system in the Gulf of Alaska. In the southern CalCS, the NPGO reflects changes in alongshore winds and wind-driven upwelling, making it an ideal indicator for changes in upwelling, nutrient supply and ecosystem properties (Di Lorenzo et al., 2008). During positive NPGO phases, alongshore winds in the southern CalCS are favored, leading to deeper upwelling cell and cooler SST anomalies. In the northern CalCS however, polewards winds and a shallower upwelling cell are favored due to a strengthening of the low pressure system over the Gulf of Alaska (Chhak et al., 2009). Negative NPGO phases have the opposite effect on the CalCS (Fig. 1.10).

1.3.4 Anthropogenic perturbation of the CalCS

Superimposed on the natural fluctuations discussed above are variations arising from perturbations of the climate system due to the emission of anthropogenic CO_2 (e.g., Bakun, 1990; Ciais

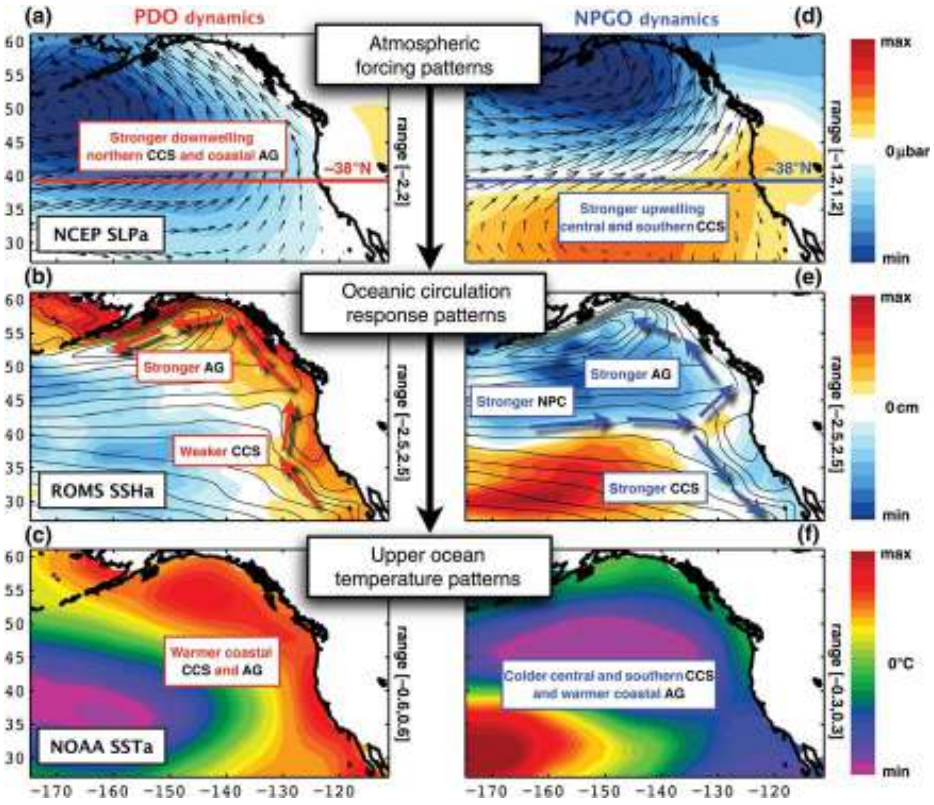

Figure 1.10 Comparison of the PDO (left column) and NPGO (right column) atmospheric forcing patterns and oceanic responses, during their respective positive phases in the Northeast Pacific. To obtain the patterns, the PDO and NPGO indices are regressed with ((**a**) and (**d**)) sea level pressure and wind stress anomalies from NCEP (National Centers for Environmental Prediction), with ((**b**) and (**e**)) sea surface height anomalies from ROMS as used by Di Lorenzo et al. (2008) and Di Lorenzo et al. (2009), and with ((**c**) and (**f**)) SST anomalies from NOAA. From King et al. (2011).

et al., 2013; Masson-Delmotte et al., 2013). Several recent studies have shown that the CalCS is particularly affected by anthropogenic perturbations: these studies have investigated the effects of rising surface ocean temperature (e.g., Di Lorenzo et al., 2005; Demarcq, 2009), of enhanced atmospheric temperature gradients between the land and the ocean, potentially resulting in a strengthening of upwelling-inducing, equatorward winds (e.g., Bakun, 1990; Schwing and Mendelssohn, 1997; Mendelssohn and Schwing, 2002; García-Reyes and Largier, 2010; Narayan et al., 2010; Song et al., 2011; Lachkar and Gruber, 2013), or of the uptake of atmospheric CO_2 by the surface ocean leading to more acidic conditions (e.g., Feely et al., 2008, 2009; Gruber et al., 2012; Hauri et al., 2013b; Leinweber and Gruber, 2013). Despite several studies investigating potential future implications for the CalCS (e.g., Snyder et al., 2003; Diffenbaugh et al., 2004; Gruber et al., 2012; Hauri et al., 2013b,a), it is not clear yet which of these mechanisms will dominate the CalCS in the future and how the upwelling dynamics and consequently the ecosystem of the CalCS will react to a combination of possible effects. The many and often contradictory studies on recent and future trends in the CalCS all vary in their temporal and geographical setting so that gaining a holistic view can be challenging. In the following, I will discuss each perturbation separately, although in reality, a clear separation of the individual processes is not strictly possible, given the interconnection between them due to their link to the increase in atmospheric

CO_2.

1.3.4.1 Changes in wind-induced upwelling and upper ocean temperature

In one of the earliest studies on the effect of global greenhouse warming on the thermal land-sea gradient, Bakun (1990) proposed that in coastal upwelling regions, an intensification of the thermal lows over the adjacent land would lead to stronger alongshore winds and enhanced coastal upwelling circulation. The result would be a cooling of the surface waters in those regions. In the case of the CalCS (24–48°N) for the time period 1945–1975, Bakun (1990) found that the strongest positive trends in upwelling were experienced for the area of 33–39°N for the upwelling season (April-September). A negative trend was only seen in areas south of 27°N. In accordance with Bakun (1990), but for a more extended time period of 1940-1990, Mendelssohn and Schwing (2002) reported for the same upwelling season increased equatorward winds and a decrease in sea surface temperature (SST) for the central region of the CalCS (32–40°N), with the strongest change experienced around 39°N (near Point Arena and Cape Mendocino, California). Regions south of 32°N experienced less of an increase in equatorward winds and even an increase in SST, and in regions north of 40°N poleward winds were found to have increased. In a modeling sensitivity study combined with in-situ measurements of SST and salinity from 1949-2000, Di Lorenzo et al. (2005) found that in the Southern California Current System, increased upwelling-favorable winds lead to a decrease in SST, which was however not strong enough to counteract the global warming-induced increase in SST. This lead to overall warmer surface waters, a deepening of the thermocline and an increased stratification. These combined effects were found to reduce the upwelling efficiency in the first 50–100 km offshore, potentially leading to a reduction in the supply of nutrients to the surface waters. This mechanisms was proposed by Di Lorenzo et al. (2005) to explain the observed decline in zooplankton (Roemmich and McGowan, 1995). Other studies support this result that surface ocean warming could lead to increased stratification, which in turn hinders the vertical mixing and hence can lead to a decrease in the supply of nutrients to the surface ocean and a resulting drop in biological productivity (e.g. McGowan et al., 2003; Palacios et al., 2004). Conversely, Chhak and Di Lorenzo (2007) demonstrate that an increase in the depth of wind-induced coastal upwelling leads to the supply of nutrients to the surface waters and hence stimulates phytoplankton growth. Satellite observations of the CalCS support this, in that they have revealed significant increases in chlorophyll concentrations and primary production in the coastal regions (Kahru et al., 2009, 2012). In their first study, Kahru et al. (2009) could detect no meaningful correlation with either SST or upwelling over the time period 1997-2007. In a follow-up study covering a more extended time period (1996–2011), Kahru et al. (2012) ascribed the positive trends in chlorophyll to either an increase in upwelling or in nutrient supply.

Concerning biological productivity in the CalCS, several studies found an inverse relationship between sea surface temperature and biological production during the last few decades (e.g., McGowan et al., 2003; Palacios et al., 2004). Warmer surface waters increase water column strat-

ification, which reduces the exchange of water across the pycnocline and acts to decrease primary production. Model simulations by Rykaczewski and Dunne (2010), however, suggest an enhancement of nitrate supply and productivity in the CalCS despite increased water column stratification. They attribute these results to an increased nitrogen enrichment of deep source waters which are upwelled in the CalCS rather than to changes in wind-driven upwelling. They do, however, also mention that the response of coastal winds to increases in greenhouse gas concentrations may be underrepresented in their model. Bakun et al. (2010) suggest that contradicting opinions on the future response of upwelling favorable winds to increasing greenhouse gases might be attributable to the chosen model resolution, which supports the use of a more highly resolved regional oceanic model.

In a modeling sensitivity study, Lachkar and Gruber (2013) investigated the response of biological production and air–sea CO_2 fluxes to increases in alongshore wind stress and upwelling intensity. They found that biological productivity responds more strongly to an increase in upwelling intensity in the southern CalCS than in the central and northern CalCS. The sensitivity of air–sea CO_2 fluxes differs between the individual regions accordingly: in the central CalCS, outgassing of CO_2 was found to be enhanced due to the decrease in biological productivity, leading to a strong sensitivity of these fluxes to increases in upwelling. In the southern CalCS on the other hand, the increase in biological efficiency supported the uptake of CO_2, which compensated the outgassing due to the upwelling increase. Hence, in this area, the sensitivity of air–sea CO_2 fluxes to an increase in upwelling is smaller.

1.3.4.2 Ocean acidification

Variables such as pCO_2 and pH are directly linked to the atmospheric concentration of CO_2. As CO_2 levels change, the CO_2 gas transfer across the surface ocean–atmosphere boundary will try to equilibrate between these two mediums. This means that on average, as atmospheric CO_2 increases, surface ocean pCO_2 will rise concurrently, resulting in a drop in pH to more acidic levels. In the context of rising atmospheric CO_2 and the associated increase in ocean acidification, Feely et al. (2004) found that the shallowest aragonite saturation horizons occur in the northeastern Pacific Ocean. Some years later, Feely et al. (2008) discovered that the whole water column shoreward of 50 m depth had become undersaturated with respect to aragonite in the CalCS, which was not predicted to occur until 2050 and was considered to be a direct consequence of elevated atmospheric CO_2 levels. Although coastal upwelling regions such as the CalCS are used to extreme fluctuations in pH values and in the saturation state of aragonite (Ω_{arag}) (Hauri et al., 2009), it is likely that the CalCS will be exposed to more frequent and prolonged events of this nature in the future (e.g. Gruber et al., 2012; Hauri et al., 2013b,a). In a modeling study, (Gruber et al., 2012) projected that by 2050, more than half the waters of the CalCS will become undersaturated with respect to aragonite. Based on the same set of simulations, Hauri et al. (2013b) simulated that by 2030, nearshore surface Ω_{arag} will have left its present-day variability envelope and aragonite

undersaturation will become widespread and almost permanent in the surface waters in the next 25 years. Hauri et al. (2013a) support this result with their findings that aragonite undersaturation events will become longer and more frequent and will gain in intensity and severity in the next 20 to 40 years. Using a set of modeling sensitivity studies, Lachkar (2014) considered the effect of upwelling intensification on ocean acidification, and found that a doubling of wind stress lead to a tripling of the volume of waters undersaturated with respect to aragonite in the CalCS. Hence, together with the ongoing increase in atmospheric CO_2 and changes to the vertical water column structure, the intensification of wind-driven upwelling contributes to the enhancement of ocean acidification in the CalCS. These results underline the difficulty in predicting the future evolution of ocean acidification in the CalCS, as many different influencing factors need to be taken into account simultaneously (Lachkar, 2014).

1.3.4.3 Expansion of oxygen minimum zones and increased nutrient input

Coastal upwelling systems are also sensitive to the input of oxygen-poor waters, which are upwelled onto the continental shelf, where respiration can further act to decrease the concentration of dissolved oxygen in the water column and therefore lead to hypoxia or anoxia. So far, there have been only a few studies investigating suboxic or anoxic events in certain regions of the CalCS. Bograd et al. (2008) observed strong declines in the oxygen content throughout the whole southern CalCS region over the period 1984–2006, with the most significant declines occurring below the thermocline. Over the same time period, they also found the hypoxic boundary ($\sim$60 mmol kg^{-1} limit) to have shoaled by up to 90 m in some areas of the southern CalCS. These results agree well with an observed surface warming and concurrent increase in thermal stratification in the same area (Bograd and Lynn, 2003; Palacios et al., 2004; Di Lorenzo et al., 2005). On the topic of oxygen minimum zones, Chan et al. (2008) found a heavy intensification of inner-shelf hypoxia and a shoaling of the anoxic layer along the central Oregon coast. This strengthening of shelf hypoxia and the change in the oxygen content of the upwelled water reflect increases in productivity-driven coastal respiration and in the strength of upwelling-favorable winds. Further warming and increased stratification could in the future further promote a decrease in oxygen levels along the CalCS coast (Stramma et al., 2008). A shoaling and expansion of oxygen minimum zones, together with ocean acidification could have deleterious effects on the benthic and pelagic ecosystems of the CalCS (Koslow et al., 2011).

1.3.5 Implications for air–sea CO_2 fluxes in the CalCS

Based on a climatological simulation of the CalCS representative of the years 2000/2001, Turi et al. (2014a) established that on average, the nearshore 100 km of the CalCS acts as a strong CO_2 source to the atmosphere, while the spatially more extensive offshore regions constitute a

weak CO_2 sink. Over the whole CalCS domain, this pattern of outgassing and uptake nearly balances out, leading to an overall weak sink of $-0.05 \pm 0.20\,\mathrm{mol\,C\,m^{-2}\,yr^{-1}}$. In a follow-up modeling study, Turi et al. (2014b, in prep.) demonstrated that an increase in upwelling-favorable winds along the coast of Oregon and northern California over roughly the last three decades lead to a significant local intensification in CO_2 outgassing, along with a rise in the surface ocean nutrient concentration and an associated enhancement of biological productivity. As Lachkar and Gruber (2013) demonstrated in their modeling sensitivity study on the effect of intensifying upwelling-favorable winds, the response of the air–sea CO_2 fluxes in the CalCS to a change in upwelling varies regionally and depends highly on how biological activity is impacted by this change. Despite the efforts of these modeling studies, it remains unclear how this CO_2 source/sink behavior will respond in detail to potential future perturbations of the CalCS such as the ones mentioned above in Subsection 1.3.4.

1.4 Thesis structure

1.4.1 Objectives and scientific questions

The main objectives of my thesis are (i) to quantify the air–sea CO_2 fluxes in the CalCS and determine the main drivers and mechanisms behind the spatiotemporal patterns of F_{CO_2} and pCO_2, (ii) to quantify recent trends in ocean acidification and carbon-related variables and determine the factors driving these changes and (iii) to investigate the interannual to decadal variability in F_{CO_2} and pCO_2 over the last 3 decades and determine the influence of large-scale climatic forcing on this variability. In order to approach these objectives, the following specific questions will be addressed in my thesis:

1. **Is the CalCS on average a source or a sink of CO_2 with respect to the atmosphere?** How do our modeled air–sea CO_2 fluxes compare to recent observational and modeling studies? (**Chapter 3**)

2. **What are the spatial and temporal variability timescales of pCO_2 in the CalCS?** How does the seasonal to annual pCO_2 variability vary spatially throughout the CalCS and are there regions where subseasonal variability becomes more important than seasonal variability? What are the most important drivers for the spatiotemporal pCO_2 variability and which mechanisms determine the spatial pattern and temporal fluctuations in pCO_2 and ultimately the air–sea CO_2 fluxes? (**Chapter 3**)

3. **How large are the trends in pCO_2, pH and Ω_{arag} over the last few decades and are there regional differences in these trends?** Are there other mechanisms, apart from the rise in atmospheric CO_2, that play an important role in driving ocean acidification in the CalCS?

If so, do these mechanisms act to accelerate or dampen ongoing ocean acidification? What role do natural fluctuations in the large-scale climatic forcing of the CalCS play compared to recent climate change-driven perturbations? (**Chapter 4**)

4. **How large is the interannual to decadal variability in $p\mathrm{CO}_2$ and air–sea CO_2 fluxes in the CalCS?** Which teleconnective modes of climate variability exert the most prominent impact on the CalCS and through which drivers does this impact manifest itself on $p\mathrm{CO}_2$ and the air–sea CO_2 fluxes? (**Chapter 5**)

1.4.2 Approach

To answer these questions, I use a regional physical oceanic model of the west coast of the US - the Regional Oceanic Modeling System (ROMS) - coupled to a simple nutrient-phytoplankton-zooplankton-detritus (NPZD) model with an implemented carbon module. The high horizontal resolution of 5 km permits the physical dynamics which are characteristic of the CalCS, i.e., upwelling and along- and offshore transport, and mesoscale structures such as eddies and larger-scale filaments to be adequately resolved. The biogeochemical NPZD model along with its carbon module allow for an adequate representation of the ecosystem and biogeochemical properties of the CalCS, which are needed to address the above questions. Using this coupled physical-biogeochemical model, I ran and analyzed two main simulations which form the basis of the results in Chapters 3, 4 and 5: the first set of simulations is forced with climatological lateral and atmospheric boundaries, meaning that the same monthly forcing is repeated for several model years and then averaged over (used in Chapter 3). The second set of simulations consists of hindcast simulations, forced with variable lateral boundary conditions with monthly values from 1979–2012, while the atmospheric forcing is daily over the same time period (Chapters 4 and 5). A more detailed description of the lateral and atmospheric boundary conditions and the model setup which was used to run the simulations can be found in Chapter 2.

1.4.3 Chapters overview

Chapter 2 provides a detailed description of the model setups and configurations that were used to run the simulations analyzed in Chapters 3, 4 and 5. Chapter 2 also offers a more extensive model evaluation with in-situ and satellite data for both the climatological and hindcast simulations.

Chapter 3 investigates the spatial and temporal variability of $p\mathrm{CO}_2$ and air–sea CO_2 fluxes in the CalCS under atmospheric CO_2 values of 370 μatm, corresponding to the years 2000/2001. The drivers and mechanisms behind the variability in oceanic $p\mathrm{CO}_2$, the main determining factor

for the spatial pattern in air–sea CO_2 fluxes in the CalCS, are identified and their relative importance in space and time is characterized. An extensive spatial and temporal evaluation of modeled versus observed pCO_2 is presented and the model's strengths and caveats are briefly discussed.

This paper was published in Biogeosciences:
Giuliana Turi, Zouhair Lachkar, and Nicolas Gruber (2014). Spatiotemporal variability and drivers of pCO_2 and air–sea CO_2 fluxes in the California Current System: an eddy-resolving modeling study. Biogeosciences, 11, 671-690.

Chapter 4 explores recent trends in ocean acidification and the climatic drivers behind these trends in the CalCS based on a hindcast simulation from 1979 to 2012. By comparing the hindcast simulation to a simulation where we keep atmospheric CO_2 and lateral DIC constant, we can separate out the effect of the physical climatic forcing alone and investigate the role of changes in upwelling-favorable winds on trends in ocean acidification. We additionally provide a detailed model evaluation with satellite observations and in-situ measurements.

This study is in preparation as:
Giuliana Turi, Zouhair Lachkar, Matthias Münnich, Nicolas Gruber, and Damian Loher. Recent climatic changes enhance ongoing ocean acidification in the California Current System.

Chapter 5 presents an extensive analysis of interannual to decadal variability of air–sea CO_2 fluxes and pCO_2 based on the same hindcast simulation as in Chapter 4. We discuss the connection of the low-frequency signal in pCO_2 to large-scale modes of climate variability. Furthermore, we make the link back to Chapter 3 by analyzing through which oceanic drivers that these climate variability modes predominantly affect interannual fluctuations in pCO_2.

This chapter is in preparation as:
Giuliana Turi, Zouhair Lachkar, Matthias Münnich, Nicolas Gruber, and Damian Loher. High interannual variability of air–sea CO_2 fluxes in the California Current System.

Chapter 6 gives a detailed overview of the main findings and conclusions of my PhD thesis and provides a discussion of the model's technical shortcomings. Finally, this last chapter offers an outlook on potential improvements and ideas for future work related to the topic of this thesis.

Chapter 2

The models and simulations

The models used in this thesis are a physical circulation model, configured to the US West Coast and based on the UCLA-ETH version of the Regional Ocean Modeling System (ROMS) (Marchesiello et al., 2003; Shchepetkin and McWilliams, 2005), coupled to a simple nitrogen-based biogeochemical model with an implemented carbon module.

2.1 The circulation model

The ROMS model domain covers a roughly 2800 km alongshore (30°N – 50°N) and 1250 km offshore section along the US West Coast and has a curvilinear, coast-following grid with an average horizontal resolution of 5 km. This horizontal grid spacing is roughly 4 to 8 times smaller than the Rossby deformation radius which varies between 20 to 40 km for the CalCS (Chelton et al., 1998), permitting an explicit resolution of most of the mesoscale eddy spectrum (Chassignet and Verron, 2006). The vertical structure of the model consists of 32 terrain-following vertical grid levels (σ-coordinates; Fig. 2.1), with increasing resolution towards the surface and the shallower nearshore regions, allowing for an improved representation of the surface boundary layer and the euphotic zone.

The model's bathymetry calculation is based on the 2' bathymetry file ETOPO2 from the National Geophysical Data Center (Smith and Sandwell, 1997), where any depths shallower than 50 m are reset to this value (Fig. 2.2). After interpolating and truncating the ETOPO2 bathymetry data, and in order to avoid large pressure gradient errors, the topography is smoothed with a selective Shapiro filter for excessive topographic slope parameter values (Beckmann and Haidvogel, 1993).

ROMS solves the primitive equations of flow using a leapfrog/Adams-Moulton predictor-corrector scheme for time stepping (Marchesiello et al., 2003), and computes the following prognostic variables: surface elevation, the barotropic and baroclinic horizontal velocity components,

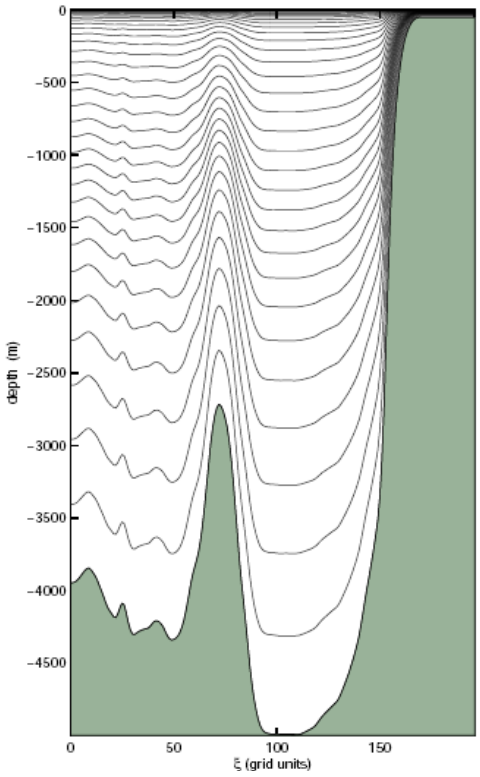

Figure 2.1 Illustration of the 32 terrain-following vertical σ-coordinate levels for depths up to 5000 m, corresponding to an offshore section of the US West Coast configuration of ROMS.

potential temperature and salinity, and the state variables of the biogeochemical model (Gruber et al., 2006). Vertical mixing in the interior of the model domain and in the boundary layer is computed using the non-local, K-Profile Parameterization scheme (KPP; Large et al., 1994). Advection parameterization uses a third order and upstream biased operator, which reduces dispersive errors and the excessive dissipation rates that are necessary to maintain smoothness (Shchepetkin and McWilliams, 1998). Density anomalies are computed using temperature and salinity, following the Jackett and McDougall (1995) relationship. The three open boundary conditions in the north, west and south of the model domain are formulated as a combination of outward radiation and flow-adaptive nudging toward prescribed external conditions (Marchesiello et al., 2001).

At the atmospheric boundary, the surface heat and freshwater fluxes are applied with a sea surface temperature (SST) and salinity (SSS) restoring, using the correction method after Barnier et al. (1995), with variable relaxation timescales. The correction terms for SST and SST are proportional to the difference between the climatological forcing values and the modeled values (Table 2.2). The SST correction term is moreover determined by the sensitivity of the latent surface ocean heat flux to changes in SST (dQ/dSST), which is dependent on the specific humidity at the air–sea interface (Barnier et al., 1995).

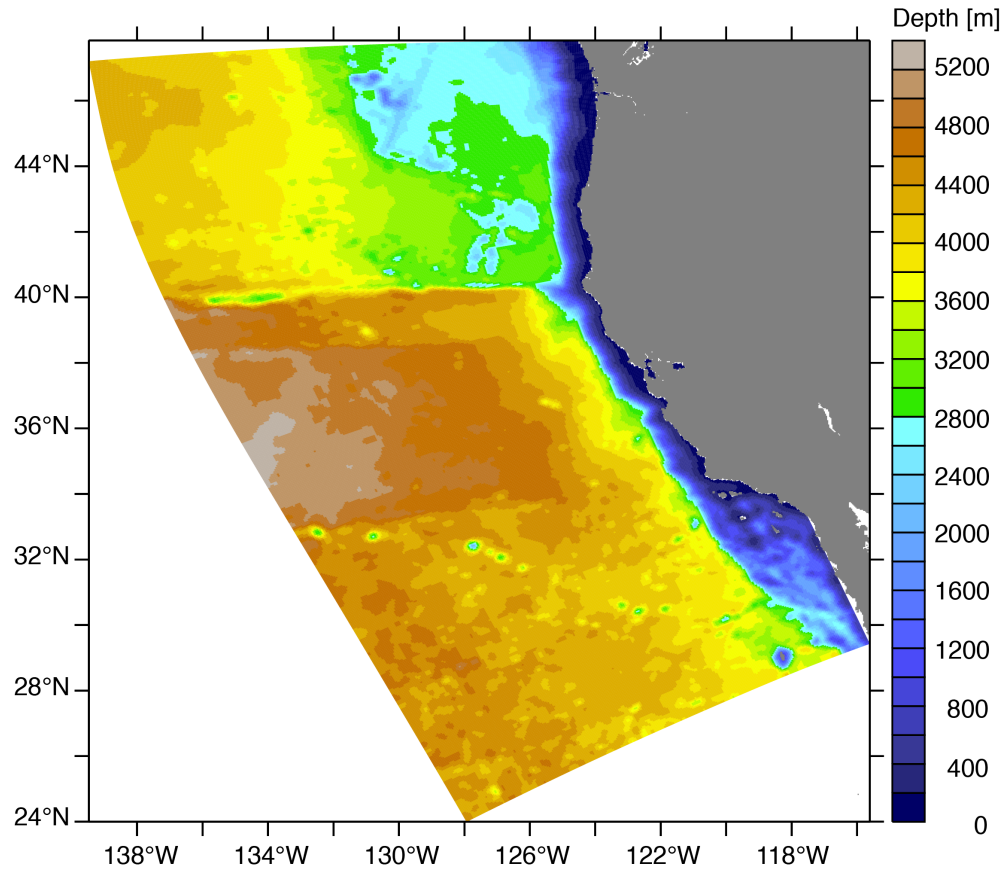

Figure 2.2 The ROMS domain showing the 2' bathymetry ETOPO2, with depths ranging from 50 m (any depths shallower than this are reset to 50 m) to deeper than 5000 m. The continental shelf is highlighted in dark blue colors.

2.2 The biogeochemical model

The biogeochemical model is a nitrogen-based nutrient-phytoplankton-zooplankton-detritus (NPZD) model. It consists of one phytoplankton and one zooplankton group and two detrital pools, with different sinking speeds. The phytoplankton group is implemented to represent a diatom-like behavior, while zooplankton is represented by one size class corresponding to meso-zooplankton. The model consists of seven non-conservative scalars or state variables, whose spatial and temporal distribution is described by a system of seven corresponding coupled partial differential equations. These state variables are nitrate (NO_3^-), ammonium (NH_4^+), phytoplankton (P), zooplankton (Z), small (D_S) and large (D_L) detritus (Fig. 2.3), and a dynamic phytoplankton chlorophyll-to-carbon ratio (θ). All of the state variables except θ represent nitrogen concentrations within the different nitrogen pools. A comprehensive description of the state variables and their partial differential equations, as well as the model's parameters is given in Gruber et al. (2006). A carbon biogeochemistry module was added to the NPZD model, representing the organic and inorganic carbon cycling within the ecosystem and at the air–sea interface, and introducing three new state variables: dissolved inorganic carbon (DIC), alkalinity (Alk) and calcium carbonate ($CaCO_3$). The organic carbon cycle is coupled to the organic nitrogen cycle via a fixed stoichiometric ratio ("Redfield" ratio; Redfield et al., 1963) of $C : N = 106 : 16$ ($r_{C:N}$). A

discussion of the limitations of using a fixed $C : N$ ratio can be found in Chapters 3 and 6 of this thesis. In the following, I will focus on the description of the model's carbon chemistry module.

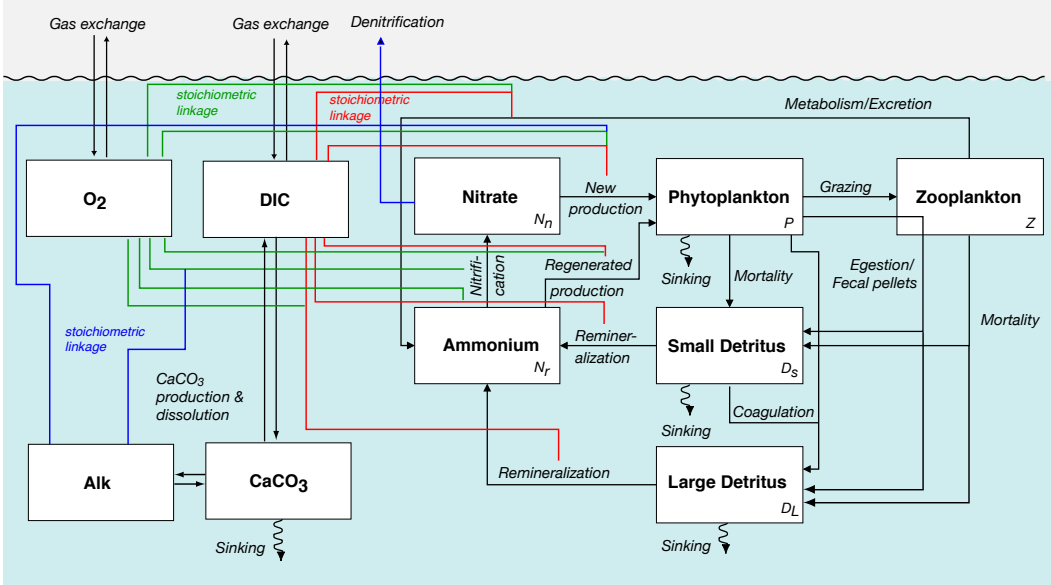

Figure 2.3 Flow diagram of the biogeochemical NPZD model. All state variables are indicated by boxes and expressed in terms of nitrogen concentrations, while the individual arrows correspond to the processes involved in the conversion of nitrogen between the individual state variables. The stoichiometric linkage between nitrogen and carbon is fixed at a ratio of $C : N = 106 : 16$ (Redfield et al., 1963). Adapted from Gruber et al. (2006).

2.2.1 The carbon chemistry module

At every grid point of the model, the concentration of any given tracer or state variable B must be conserved, and is implemented as a function of diffusion, horizontal and vertical advection, sinking and a source-minus-sink (SMS) term:

$$\frac{\partial B}{\partial t} = \underbrace{\nabla \cdot K \nabla B}_{\text{diffusion}} - \underbrace{\vec{u} \cdot \nabla_h B}_{\text{horiz. advection}} - \underbrace{(w + w^{sink}) \frac{\partial B}{\partial z}}_{\text{vert. advection + sinking}} + \underbrace{J(B)}_{\text{SMS term}}, \tag{2.1}$$

with K being the eddy kinematic diffusivity tensor and ∇ and ∇_h denoting the 3-dimensional and horizontal gradient operators. $\vec{u}$ represents the two horizontal velocities, while w stands for the vertical velocity. w^{sink} refers to the vertical sinking speed of phytoplankton and the two detrital pools. Zooplankton is not subject to sinking, as it is assumed in the model that this pool remains within the euphotic zone. The term $J(B)$ stands for the SMS term for each of the state variables. Gruber et al. (2006) lists the corresponding SMS equations for the seven basic state variables of the NPZD model, while here I will focus on the equations for the additional carbon module state variables DIC, Alk and $CaCO_3$ and on how pCO_2 is implemented in the model.

Formulation of DIC and $CaCO_3$

The concentration of DIC is altered through the SMS term by net primary production (NPP), by zooplankton respiration, by the formation and dissolution of $CaCO_3$ in the water column, by dissolution and remineralization processes in the sediments and by the air–sea CO_2 exchange (following the terminology used in Gruber et al., 2006):

$$
\begin{aligned}
J(DIC) = & - \underbrace{\mu_P^{max}(T,I) \cdot \gamma(NO_3^-, NH_4^+) \cdot P \cdot r_{C:N}}_{\text{net primary production}} + \underbrace{\eta_Z^{metab} \cdot Z \cdot r_{C:N}}_{\text{zooplankton respiration}} \\
& - \underbrace{r_{CaCO_3:C} \cdot \mu_P^{max}(T,I) \cdot \gamma(NO_3^-, NH_4^+) \cdot P \cdot r_{C:N}}_{CaCO_3 \text{ formation}} + \underbrace{k_{CaCO_3}^{diss} \cdot D_{CaCO_3}}_{CaCO_3 \text{ dissolution}} \\
& + \underbrace{k_{D_S}^{remin} \cdot D_S \cdot r_{C:N} + k_{D_L}^{remin} \cdot D_L \cdot r_{C:N}}_{\text{detritus remineralization}} \\
& + \underbrace{k_{S_D}^{remin} \cdot S_D \cdot r_{C:N}}_{\text{sediment remin. at k=1}} + \underbrace{k_{S_{CaCO_3}}^{diss} \cdot S_{CaCO_3} \cdot r_{C:N}}_{\text{sediment dissolution at k=1}} \\
& + \underbrace{J^{Gas}}_{CO_2 \text{ gas exchange}} ,
\end{aligned}
\tag{2.2}
$$

where the individual state variables (P, Z, D_S, D_L and $CaCO_3$) are either parameters in the equation or subscripts to a function or other parameter. The corresponding processes are given in the superscripts. The symbols with parentheses denote functions of the respective variables: $\mu_P^{max}(T,I)$ represents the temperature (T)-dependent, light (I)-limited growth rate of P in nutrient-replete conditions, and $\gamma(NO_3^-, NH_4^+)$ is a non-dimensional nutrient limitation factor. J^{Gas} is the air–sea CO_2 flux and is described in Eq. 2.4. $k_{D_S}^{remin}$ and $k_{D_L}^{remin}$ stand for the remineralization rates of small and large detritus in the water column, and $k_{S_D}^{remin}$ is the sediment remineralization rate at the model's bottom layer (k=1). The formation of $CaCO_3$ is linked to the formation of organic carbon by NPP via a constant proportionality factor $r_{CaCO_3:C}$. The dissolution rates of $CaCO_3$ in the water column and in the sediments are given by $k_{CaCO_3}^{diss}$ and $k_{S_{CaCO_3}}^{diss}$, respectively, with D_{CaCO_3} and S_{CaCO_3} referring to the actual $CaCO_3$ pools in the water column and in the sediments. The zooplankton basal metabolism rate is given by η_Z^{metab} and $r_{C:N}$ refers to the fixed $C:N$ ratio as mentioned above. The values for all these parameters are given in Table 2.1.

Net community production (NCP) is defined as NPP (first term in Eq. 2.2), minus heterotrophic respiration (second term in Eq. 2.2), minus detritus remineralization in the water column and sediments (fifth and sixth terms in Eq. 2.2). In our model, heterotrophic respiration refers only to zooplankton respiration, as phytoplankton and bacterial respiration are not implemented. However, as bacterial respiration is a process that leads to the remineralization of organic matter, it can be seen as the equivalent process to the remineralization of detritus in the water col-

umn and sediments. NPP, which is the sum of regenerated and new production, acts to decrease the DIC concentration. The term "regenerated production" refers to phytoplankton productivity if NH_4^+ is used, while "new production" is the term used if phytoplankton favor the uptake of NO_3^-. Phytoplankton preferentially take up NH_4^+, leading to an inhibited uptake of NO_3^-. This fact is taken into account for in the parameter $\gamma(NO_3^-, NH_4^+)$, which has a stronger limitation for NO_3^- than NH_4^+.

The formation of $CaCO_3$, which is linked to NPP via a fixed ratio ($r_{CaCO_3:C}$), also acts to decrease the DIC concentration, while the opposite mechanisms of $CaCO_3$ dissolution contributes to the increase in DIC by setting free CO_3^{2-} (see Eq. 1.14). The complete SMS equation for the concentration of $CaCO_3$ (D_{CaCO_3}) is just the third and fourth terms of Eq. 2.2 and is given by:

$$J(D_{CaCO_3}) = \underbrace{r_{CaCO_3:C} \cdot \overbrace{\mu_P^{max}(T,I) \cdot \gamma(NO_3^-, NH_4^+) \cdot P}^{\text{net primary production}} \cdot r_{C:N}}_{CaCO_3 \text{ formation}} - \underbrace{k_{CaCO_3}^{diss} \cdot D_{CaCO_3}}_{CaCO_3 \text{ dissolution}} . \tag{2.3}$$

The remineralization of the detrital pools acts to increase the DIC pool. Small and large detritus are remineralized at different rates and have different sinking speeds to account for their difference in size. This means that their remineralization length scales (i.e., sinking speed divided by remineralization rate) are substantially different from each other: D_S has a remineralization length scale of 30 m, while D_L remineralizes within 1000 m. Hence, D_S is easily transported offshore within the euphotic zone, while D_L sinks more quickly to the aphotic zone (Gruber et al., 2006).

The sediment is implemented as a simple one-layer model and added to the bottom of the physical-biogeochemical model, and it is represented by two state variables: detrital matter (S_D) and $CaCO_3$ (S_{CaCO_3}). When S_D and S_{CaCO_3} arrive at the sediment surface, they are added directly to the sediment layer. There, S_D is subjected to remineralization and S_{CaCO_3} to dissolution, and then resupplied back into the lowest model layer (k=1), from where they can gain access back into the water column through circulation processes. As is the case in the water column, the remineralization of S_D and the dissolution of S_{CaCO_3} in the sediments acts to increase the concentration of DIC.

The uptake of CO_2 by the surface ocean via gas exchange increases DIC, as this process adds HCO_3^- to the carbon pool (Eqs. 1.2 and 1.3). The CO_2 gas exchange acts to equilibrate the partial pressures of CO_2 between the atmosphere (pCO_2^{air}) and the surface ocean (pCO_2^{sea}), and is influenced by the CO_2 solubility of seawater (K_0), by the CO_2 gas transfer velocity (k_w) and by the difference in atmospheric and oceanic pCO_2 (e.g., Wanninkhof et al., 2009):

$$F_{CO_2} = -K_0 \cdot k_w \cdot \left(pCO_2^{air} - pCO_2^{sea}\right), \tag{2.4}$$

where the sign convention means that positive values of F_{CO_2} indicate an outgassing of CO_2, while negative values denote an uptake by the surface ocean. In our model, $p\mathrm{CO}_2^{sea}$ is computed using dissolved inorganic carbon (DIC), alkalinity (Alk), sea surface temperature (SST), salinity and nutrients following the standard Ocean Carbon-Cycle Model Intercomparison Project (OCMIP; Orr et al., 2005) carbonate chemistry routines (see Chapter 3 and Hauri et al. (2013b) for more details). $p\mathrm{CO}_2^{air}$ is prescribed and latitudinally averaged over our whole model domain to represent one value for the CalCS domain for each time step. The calculation of k_w for steady winds depends on the square of the wind speed and follows Eq. 3 in Wanninkhof (1992):

$$k_w = 0.31 \cdot u_{10}^2 \cdot \sqrt{\frac{660}{Sc}} \tag{2.5}$$

where u_{10} is the wind speed at 10 m height and Sc is the unit-less Schmidt number for CO_2. The proportionality constant of 0.31 is the same us used by Wanninkhof (1992) (more details on this choice of proportionality constant are given in Chapter 4). The parameterization of Sc is temperature-dependent and likewise computed as in Wanninkhof (1992). This approach allows for variability in the wind speed to affect the CO_2 gas transfer velocity.

Formulation of Alk

Alk is linked to DIC through the concentration of CO_3^{2-} (as shown in Eq. 1.12), which in turn is affected by the formation and dissolution of $CaCO_3$. The full SMS term for Alk depends on these processes, as well as on the dissolution of $CaCO_3$ in the sediments, and on the removal (new production) and formation (nitrification) of NO_3^-:

$$\begin{aligned} J(Alk) = &-2 \cdot \underbrace{r_{CaCO_3:C} \cdot \mu_P^{max}(T,I) \cdot \gamma(NO_3^-, NH_4^+) \cdot P \cdot r_{C:N}}_{\text{CaCO}_3\text{ formation}} + 2 \cdot \underbrace{k_{CaCO_3}^{diss} \cdot D_{CaCO_3}}_{\text{CaCO}_3\text{ dissolution}} \\ &+ \underbrace{\mu_P^{max}(T,I) \cdot \gamma(NO_3^-) \cdot P \cdot r_{C:N}}_{\text{new production}} - \underbrace{k^{nitr}(I) \cdot NH_4^+}_{\text{nitrification}} \\ &+ 2 \cdot \underbrace{k_{S_{CaCO_3}}^{diss}}_{\text{sediment dissolution at k=1}}, \end{aligned} \tag{2.6}$$

where $k^{nitr}(I)$ denotes the rate of nitrification, a light (I)-limited process. Table 2.1 lists the values of the individual parameters given in Eqs. 2.2, 2.3 and 2.6.

Formulation of $p\mathrm{CO}_2$

The calculation of $p\mathrm{CO}_2$ in the model is based on the definitions of DIC and Alk (Eqs. 1.7 and 1.8), on the solubility K_0 of CO_2 in seawater (Eq. 1.4) and on the first and second dissociation constants of carbonic acid, K_1 and K_2 (Eqs. 1.5 and 1.6):

$$pCO_2 = \frac{[DIC]}{K_0} \cdot \frac{[H^+]^2}{[H^+]^2 + K_1[H^+] + K_1K_2} \tag{2.7}$$

The calculation of K_0 follows the temperature-dependent formulation of Weiss (1974), while K_1 and K_2 are temperature- and salinity-dependent and are computed following Mehrbach et al. (1973), as refitted by Dickson and Millero (1987) (for a more detailed derivation of Eq. 2.7 see: Sarmiento and Gruber, 2006, p. 324).

Parameter	Symbol	Value	Units
Carbon-to-nitrogen ratio	$\mathrm{r}_{C:N}$	6.625	
Sinking parameters			
Sinking speed of P	w_P^{sink}	0.5	$\mathrm{m\,day}^{-1}$
Sinking speed of D_S	$\mathrm{w}_{D_S}^{sink}$	1.0	$\mathrm{m\,day}^{-1}$
Sinking speed of D_L	$\mathrm{w}_{D_L}^{sink}$	10.0	$\mathrm{m\,day}^{-1}$
Sinking speed of D_{CaCO_3}	$\mathrm{w}_{D_{CaCO_3}}^{sink}$	20.0	$\mathrm{m\,day}^{-1}$
Remineralization, respiration and nitrification parameters			
Remineralization rate of D_S	$\mathrm{k}_{D_S}^{remin}$	0.03	day^{-1}
Remineralization rate of D_L	$\mathrm{k}_{D_L}^{remin}$	0.01	day^{-1}
Zooplankton basal metabolism rate	η_Z^{metab}	0.1	day^{-1}
Nitrification rate (max.)	$\mathrm{k}^{nitr,max}$	0.05	day^{-1}
$CaCO_3$ formation and dissolution parameters			
CaCO_3-to-NPP ratio	$\mathrm{r}_{CaCO_3:C}$	0.03	
CaCO_3 dissolution rate	$\mathrm{k}_{CaCO_3}^{diss}$	0.0057	day^{-1}
Sediment parameters			
Sediment remineralization rate of detritus	$\mathrm{k}_{S_D}^{remin}$	0.003	day^{-1}
Sediment dissolution rate of CaCO_3	$\mathrm{k}_{S_{CaCO_3}}^{diss}$	0.002	day^{-1}

Table 2.1 Summary of the constant parameters used in the carbon module of the NPZD model, and their symbols, values and units. The same parameters were used for all the simulations described in the following Section 2.3. Note that the value for $r_{CaCO_3:C}$ (0.03) is different from the value of 0.07 used in previous studies (Gruber et al., 2006; Hauri et al., 2009; Gruber et al., 2011; Lachkar and Gruber, 2011; Gruber et al., 2012; Hauri et al., 2013b,a; Lachkar, 2014). See Section 2.5 and Chapter 3 for details on the choice of this specific value for $r_{CaCO_3:C}$.

2.3 The simulations

The analyses done in Chapter 3 are all based on climatological simulations, i.e. where the atmospheric and lateral boundary forcing is at monthly resolution and repeated for each model year, in order to simulate average conditions. The simulations used in Chapters 4 and 5 on the other hand are so-called hindcast simulations, which are forced with variable daily atmospheric values and variable monthly boundary conditions over the period 1979–2012. Table 2.2 lists the sources for all the atmospheric and lateral boundary variables used to force the model for both the climatological and hindcast simulations.

Climatological simulations

There are two types of climatological simulations used in Chapter 3. The main analyses of the spatiotemporal variability of pCO_2 and air–sea CO_2 fluxes were done using the full resolution (i.e., 5 km) setup, while the sensitivity studies, used to determine the contributions of the individual pCO_2 drivers, were done at a slightly reduced resolution of 15 km. In both cases, we started the model from rest and let it run for 12 years with monthly atmospheric and lateral forcing, and focused our analyses on years 6 through 12 of the simulations. Our analyses of seasonal variability and annual means are based on a monthly climatology over these last seven years, whereas for our mesoscale variability analysis, we used model output at 2-day resolution.

We used the same initial and boundary conditions for our simulations as are described in Hauri et al. (2013b) and Lachkar and Gruber (2013). At the atmospheric boundary, we forced our model with monthly climatologies of wind stress from the QuickSCAT-based Scatterometer Climatology of Ocean Winds (SCOW; Risien and Chelton, 2008) and of heat and freshwater fluxes from the Comprehensive Ocean-Atmosphere Data Set (COADS; da Silva et al., 1994, Table 2.2). Atmospheric CO_2 varies seasonally around a value of 370 μatm, which corresponds roughly to the concentration of the years 2000/2001. At the three lateral boundaries, we used temperature, salinity, nitrate and oxygen from the World Ocean Atlas 2005 (WOA05; Locarnini et al., 2006; Antonov et al., 2006; Garcia et al., 2006a,b). The calculation of sea surface height, and the u- and v-components of the geostrophic velocity are based on temperature and salinity from WOA05. Chlorophyll at the lateral boundaries is from the Sea-viewing Wide Field-of-view Sensor (SeaWiFS), and phytoplankton and zooplankton are linked to chlorophyll with fixed ratios (see Table 2.2 for specific values). The DIC and Alk boundary conditions are derived from the Global Ocean Data Analysis Project (GLODAP; Key et al., 2004).

A more comprehensive description of the individual simulations and the forcing and boundary conditions used in Chapter 3 can be found in there and in Hauri et al. (2013b) and Lachkar and Gruber (2013).

Hindcast simulations

The physical atmospheric forcing data - i.e., wind stress, heat and freshwater fluxes - for the simulations used in Chapters 4 and 5 are daily values spanning the time period from Janary 1979 to December 2012, based on ECMWF's ERA-Interim reanalysis (Dee et al., 2011). For atmospheric CO_2 we use monthly zonal means from the GLOBALVIEW-CO_2 data set (GLOBALVIEW-CO2, 2013), which we averaged over our model domain. At the lateral boundaries, we forced the model with observation-based climatologies, to which we added monthly anomalies from a hindcast simulation conducted by Graven et al. (2012) using the National Center for Atmospheric Research Community Climate System Model version 3.0 (CCSM3; Smith et al., 2010; Collins et al., 2006; Gent et al., 2006). The observation-based climatologies are identical to the ones we used for our climatological simulations in Chapter 3, with the exception of temperature, salinity, sea surface height and the u- and v-components of geostrophic flow, which are based on the the Simple Ocean Data Assimilation (SODA) database (e.g., Chepurin et al., 2005, Table 2.2). A more extensive explanation of the model's boundary conditions can be found in Chapters 4 and 5.

The analyses in Chapters 4 and 5 are based on two simulations, which differ from each other in their atmospheric forcing and lateral boundary conditions. Both simulations are initiated from the same model spinup, which is started from rest and run for ten years. The physical atmospheric forcing of the spinup is a climatology over the years 1979–1988, to which we added daily anomalies from the year 1985 (so-called "normal-year" forcing). The atmospheric CO_2 data were extended to cover the years 1969 to 1978, by linearly extrapolating and adding a monthly climatology to this. The lateral boundary conditions were kept climatological during the spinup, except for DIC, to which we added the CCSM3 anomalies. After the spinup, i.e., as of the beginning of 1979, we let the two simulations diverge: the first simulation - which we term "CClim" for "constant climate" - is an extension of the spinup. This means that while atmospheric CO_2 and lateral DIC continue to vary interannually until the end of 2012, the other lateral boundary conditions and the physical atmospheric forcing remain the same as in the spinup. In our second simulation - which is our true "hindcast" simulation, or "HCast" - the atmospheric forcing and the other lateral boundary conditions are also allowed to vary (with the exception of chlorophyll, phytoplankton and zooplankton which remain climatological throughout the whole simulation). The HCast and CClim simulations are both used in Chapter 4 and are explained in more detail there, while the analyses in Chapter 5 are based solely on the HCast simulation. The difference between the two simulations is essentially the effect of the physical climate alone, without the effect of increasing CO_2. More detailed information on the HCast and CClim simulations is given in Chapter 4.

Table 2.2 Summary of the model's atmospheric and lateral boundary forcing with the source of the data and the time period on which climatologies are based. The lateral boundaries are forced at monthly resolution. Atmospheric forcing is monthly only for the climatological simulations, while the ERA-Interim forcing for the hindcast simulations is daily. Atmospheric CO_2 values are monthly for all simulations.

Variable	Climatological simulations (Chapter 3)		Hindcast simulations (Chapters 5 and 4)	
	Source	Period	Source	Period
Atmospheric forcing				
CO_2	n/a$^{(\circ)}$	n/a	GLOBALVIEW-CO_2[1]	Jan. 1979–Dec. 2012
Wind stress	SCOW[2]	Sep. 1999–Aug. 2007	ERA-Interim[3]	Jan. 1979–Dec. 2012
Heat flux	COADS[4]	1945–1989	ERA-Interim	Jan. 1979–Dec. 2012
Freshwater flux	COADS	1945–1989	ERA-Interim	Jan. 1979–Dec. 2012
Surface restoring				
SST[5]	WOA05[6]	n/a$^{(*)}$	WOA05	n/a
SSS	WOA05	n/a	WOA05	n/a
dQ/dSST	COADS	1945–1989	COADS	1945–1989
Lateral boundary forcing				
Temperature (T)	WOA05	n/a	SODA[8] + CCSM anom.	Jan. 1958–Dec. 2001
Salinity (S)	WOA05	n/a	SODA + CCSM anom.	Jan. 1958–Dec. 2001
SSH	Based on T and S (WOA05)	n/a	SODA + CCSM anom.	Jan. 1958–Dec. 2001
u- and v-components	Based on T and S (WOA05)	n/a	SODA + CCSM anom.	Jan. 1958–Dec. 2001
DIC	GLODAP[7]	1972–1999	GLODAP + CCSM anom.	1972–1999
Alk	GLODAP	1972–1999	GLODAP + CCSM anom.	1972–1999
NO_3^-	WOA05	n/a	WOA05 + CCSM anom.	n/a
O_2	WOA05	n/a	WOA05 + CCSM anom.	n/a
Chlorophyll (CHL)	SeaWiFS	Sep. 1997–Feb. 2004	SeaWiFS	Sep. 1997–Feb. 2004
Phytoplankton (P)	Fixed CHL-to-P-ratio of 5 (SeaWiFS)	Sep. 1997–Feb. 2004	SeaWiFS	Sep. 1997–Feb. 2004
Zooplankton (Z)	Fixed CHL-to-Z-ratio of 1.5 (SeaWiFS)	Sep. 1997–Feb. 2004	SeaWiFS	Sep. 1997–Feb. 2004
pCO_2 (for DIC seasonal cycle)	Takahashi09	1970–2007 (normalized to year 2000)	Takahashi09	1970–2007 (normalized to year 2000)

[1] GLOBALVIEW-CO_2: NOAA-ESRL (GLOBALVIEW-CO2, 2013). [2] SCOW: QuickSCAT-based Scatterometer Climatology of Ocean Winds (Risien and Chelton, 2008). [3] ERA-Interim: ECMWF's ERA-Interim Reanalysis product (Dee et al., 2011). [4] COADS: Comprehensive Ocean-Atmosphere Data Set (da Silva et al., 1994). [5] SST and SSS restoring after Barnier et al. (1995) with variable relaxation timescales. [6] WOA05: World Ocean Atlas 2005 (Locarnini et al., 2006; Antonov et al., 2006; Garcia et al., 2006a,b). [7] GLODAP: GLobal Ocean Data Analysis Project (Key et al., 2004). [8] SODA: Simple Oceanic Data Assimilation, version 1.4.2 (e.g., Chepurin et al., 2005). $^{(\circ)}$ Climatological simulations were forced with pCO_2^{air}=370 μatm. $^{(*)}$ Data from WOA05 were averaged over various time periods for the different variables T, S, NO_3^- and O_2.

2.4 Model evaluation

The model setup and the ecological parameters used for all simulations in this study are the same as in Gruber et al. (2011), with adjustments to the $CaCO_3$ production ratio and the lateral DIC forcing as described in Chapter 3.

2.4.1 Model evaluation of climatological simulations

An extensive model evaluation for the parameters SST, chlorophyll and mixed layer depth (MLD), density structure and NPP was previously done by Gruber et al. (2011) and Lachkar and Gruber (2011). In Chapter 3, we further expanded this evaluation by including a comprehensive comparison of modeled pCO_2 with data from multiple global observational data sets and from a study by Hales et al. (2012), who used a self-organizing map approach to spatially extend a limited set of pCO_2 measurements. Hauri et al. (2013b) evaluated the model's performance in simulating DIC and Alk by comparing model output to the vertical profiles of DIC and Alk measured off Point St. George, California, by Feely et al. (2008) along their transect line 5. Hauri et al. (2013b) showed for transect line 5 that while the interior ocean patterns of DIC and Alk are relatively well reproduced by the model in the regions offshore of about 100 km, the model underestimates the steepness of the vertical gradients of both DIC and Alk in the nearshore region, resulting in too low DIC and Alk concentrations in the near-surface waters in this region. In contrast, the modeled offshore concentrations of surface ocean DIC and Alk were considerably too high.

Here, I elaborate on the model evaluation that we conducted in Chapter 3 to explain in more detail how we computed our chosen adjustment for lateral DIC. This DIC correction was done by expanding the model evaluation done by Hauri et al. (2013b) using the Feely et al. (2008) data. As the measurements from transect line 5 were sampled during a period of strong upwelling, we extended the analysis of DIC and Alk to include transect line 9 just north of Point Conception. The comparison yielded similar results, meaning that both DIC and Alk are underestimated by the model in the nearshore surface waters and overestimated in the surface waters offshore of roughly 100 km, albeit the underestimation was lower than for transect line 5. To quantify these biases in the surface layer, we computed mean DIC and Alk from Feely et al. (2008) measurements within the first 5 m depth from transect lines 4 to 11, which lie within the ROMS model domain (Figs. A.1 to A.4). Then we compared this to mean surface DIC and Alk from the model, sampled in the same locations. We found that the model on average overestimated DIC by roughly 16 mmol C m^{-3} and Alk by about 6 mmol C m^{-3} in the top 5 m of the surface layer. The resulting underestimation of the difference Alk$-$DIC of about 9 mmol C m^{-3}, which is a good approximation of the concentration of the carbonate ion (Sarmiento and Gruber, 2006), leads to an overestimation of pCO_2 of about 20 μatm. Thus the surface ocean biases in DIC and Alk that we identified based on this limited number of observations explained nearly all the positive bias

in surface ocean $p\mathrm{CO}_2$.

We ran a series of sensitivity simulations to determine the impact of a reduction in the lateral boundary DIC concentrations on the nearshore and domain-wide $p\mathrm{CO}_2$ and air–sea CO_2 fluxes (Fig. 2.4). Furthermore, we wanted to test our choice of using a CaCO_3 production ratio ($\mathrm{r}_{CaCO_3:C}$) of 0.03 rather than 0.07, as used previously by Gruber et al. (2011) and Hauri et al. (2013b) and to investigate the impact of doubling the parameters for phytoplankton light sensitivity (p_α) and phytoplankton mortality (t_{Pmort}) to values of 2 and 0.048, respectively (as specified in Gruber et al. (2011); rather than values of 1 and 0.024, as used previously by Gruber et al. (2006)). As a reference, we ran a control run ("CTRL"; square symbol in Fig. 2.4), where we used the original values for $\mathrm{r}_{CaCO_3:C}$, p_α and t_{Pmort} of 0.07, 1 and 0.024. In the first sensitivity study, we simultaneously changed these three values to 0.03, 2 and 0.048, respectively ("Adjusted biology"; diamond symbol in Fig. 2.4). In the following sensitivity studies, we additionally reduced the DIC concentration at the lateral boundaries, either by a constant offset of –15 mmol C m^{-3} throughout the whole water column or by an offset of –15 mmol C m^{-3} and –8 mmol C m^{-3}, tapering linearly off with increasing density to a maximum depth of 350 m (star and circle symbols in Fig. 2.4). From each of these sensitivity studies, we computed the average air–sea CO_2 fluxes for the nearshore 100 km and for the whole domain, and calculated the bias in $p\mathrm{CO}_2$ compared to observational data sets for the same regions. This sensitivity study revealed that a tapering offset of -8 mmol C m^{-3}, which we used in Chapter 3 to correct our DIC boundary conditions, yielded the best results in terms of the $p\mathrm{CO}_2$ bias for the whole domain, although the nearshore 100 km still had a small positive bias of roughly 10 μatm (filled circle in Fig. 2.4).

2.4.2 Model evaluation of hindcast simulations

In Chapter 4, we present a model evaluation of the hindcast simulation (HCast) with available in-situ and satellite observations. We focus on evaluating the model's performance in simulating trends over different time periods between 1979 to 2012, depending on the respective time frames of the observations. We show that in comparison to nearshore buoy measurements from the National Oceanic and Atmospheric Administration's (NOAA) National Data Buoy Center, the model has good skills in reproducing SST and upwelling trends north of 38°N for the time periods 1982–2008 (García-Reyes and Largier, 2010) and 1980–2010 (Seo et al., 2012) (Figs. 4.6 and 4.7). To the south of this however, the model underestimates the strength of wind-induced upwelling and simulates a weaker cooling than was measured at the buoy stations over both time periods.

This underestimation of cooling can also be seen in Fig. 4.8 of Chapter 4, where we compare our modeled data to satellite observations from NOAA's AVHRR Pathfinder Version 5 SST Project for the time frame from 1988 to 2009 (see Table 2.3 for a list of satellite-related acronyms). Compared to AVHRR, the model simulates a weaker cooling throughout the entire

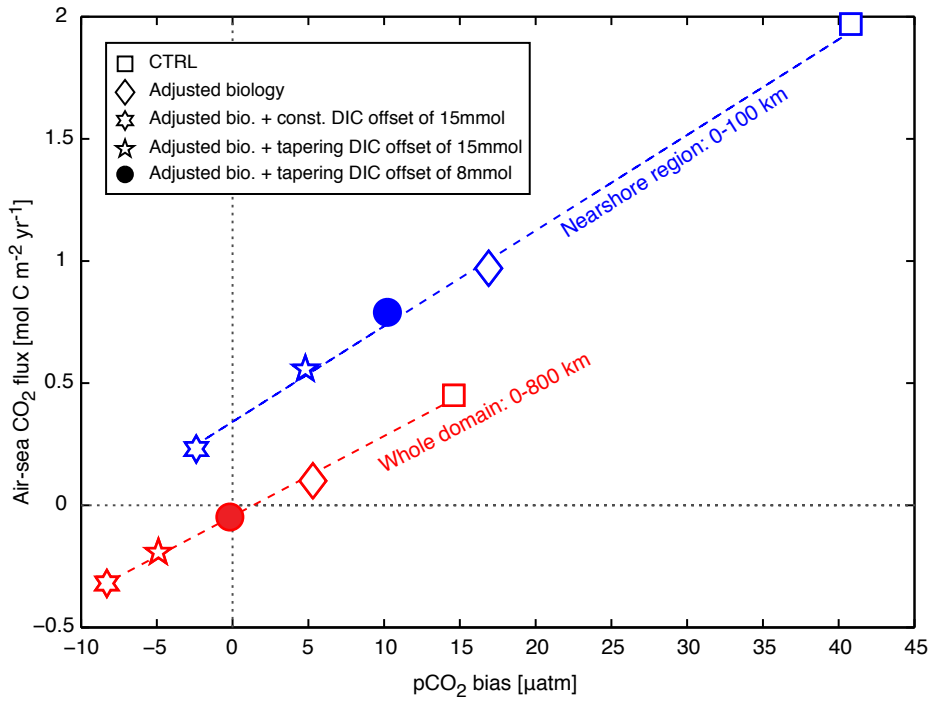

Figure 2.4 Comparison of averaged air–sea CO_2 fluxes and pCO_2 biases from four sensitivity simulations and one control run (CTRL) for the nearshore 100 km and the whole analysis domain (0–800 km). These sensitivity studies were in Chapter 3 to determine which values for $CaCO_3$ production ratio, phytoplankton light sensitivity and phytoplankton mortality to use and by how much to reduce the lateral boundary DIC concentrations. "Constant DIC offset" means that we applied the same offset to the whole water column, while "tapering DIC offset" indicates that the adjustment of either –15 mmol C m^{-3} or –8 mmol C m^{-3} tapers linearly off from the surface with increasing density to a maximum depth of 350 m, below which the offset is zero. The pCO_2 biases were computed in comparison to a combined pCO_2 data set including measurements from the Surface Ocean CO_2 Atlas (SOCAT Version 2; Pfeil et al., 2013), the global surface pCO_2 database (Takahashi et al., 2013) and the MBARI/CalCOFI Line 67 (Collins et al., 2003).

100 km nearshore region and even suggests an increase in SST south of 38°N, where the satellite data indicate a negative SST trend. Offshore of 100 km, the model simulates a uniform cooling, whereas the measurements from AVHRR show a warming in the northern half of the model domain. Compared to chlorophyll observations from the European Space Agency's (ESA) GlobColour Project, our model underestimates the positive, observed chlorophyll trends throughout most of the domain, with the strongest underestimation in the nearshore 100 km (Fig. 4.8). Despite these caveats, we conclude in Chapter 4 that the trends in ocean acidification in the CalCS are not significantly affected by this misrepresentation by the model. A more detailed discussion of the implications of the model's weaknesses for our results can be found in Chapter 4.

Here, I expand on the hindcast model evaluation from Chapter 4 to include a more extensive comparison with the same satellite data and with measurements of SST, salinity and pCO_2 from an in-situ mooring located in Santa Monica Bay, California (Leinweber et al., 2009; Leinweber and Gruber, 2013). I focus here on the model's abilities in capturing the mean and the temporal variability over different time periods.

Comparison with satellite observations

Compared to satellite observations, the model has good skills in simulating the long-term mean north-south gradient in SST as well as the onshore-offshore gradient in chlorophyll (Fig. 2.5a and d). However, it also has several weaknesses, which emerge particularly in the coastal areas. The model has a tendency to overestimate the long-term mean SST throughout the whole model domain by about 0.4°C, and simulates particularly high values in the nearshore 100 km around Point Conception, California and in the Southern California Bight, where the overestimation is up to 1°C (Fig. 2.5c). Chlorophyll is also overestimated by the model, especially in the coastal areas around Cape Mendocino, California, where it simulates values that are up to 50% too high compared to the observed chlorophyll (Fig. 2.5f). The nearshore-offshore gradient in sea surface height is slightly underestimated by the model, which tends to simulate higher values in the very northern and southern nearshore areas compared to satellite observations (Fig. 2.5i). The overestimation of SST by the model in the southern CalCS could lead to higher $p\mathrm{CO}_2$ values in those regions, whereas the too high chlorophyll values in the central/northern CalCS could cause $p\mathrm{CO}_2$ to be underestimated there, creating an artificial north-south gradient in $p\mathrm{CO}_2$ along the coast. In the case of SST, the overestimation by the model can be partially explained by the simulation of too strong trends in the same regions, as can be seen in Fig. 4.8a-c of Chapter 4. For chlorophyll however, the overestimation cannot be explained by a shortcoming in the modeled trends, as the model tends to underestimate chlorophyll trends all along the coast compared to satellite data (see Fig. 4.8d-f). Other possible explanations for the model's overestimation of mean chlorophyll around Cape Mendocino include ...

The model has very good skills in capturing the temporal variability for SST, chlorophyll and SSH, both in terms of standard deviations and correlations with the observed data (Figs. 2.6 and 2.7). It has a tendency to overestimate the long-term variability in SST and chlorophyll in the same regions as it overestimates the long-term means, i.e., around and south of Point Conception for SST and around Cape Mendocino for chlorophyll (Fig. 2.6c and f). Generally, the variability is more strongly overestimated in the nearshore regions, which could be due to an overestimation of the strength of wind-induced upwelling events. The temporal variability of SSH is fairly well represented, with only a slight overestimation throughout the whole model domain (Fig. 2.6i).

In general, the temporal correlations of modeled versus observed data are very high for all three variables. SST correlations are particularly high, with values up to 0.9 in widespread parts of the offshore regions and a domain-wide average of roughly 0.8 (Fig. 2.7a). In the nearshore region around Cape Mendocino, the SST correlations are slightly lower, but nevertheless significant (significance not shown). Correlations for chlorophyll and SSH are slightly lower than those for SST, with the highest correlation being around 0.8 for both (Figs. 2.7b and c). The correlations for chlorophyll are even negative in the southern offshore regions, which corresponds to the area of lowest chlorophyll concentrations and standard deviations (Figs. 2.5e and 2.6e).

In conclusion, the overestimation of SST is consistent with the model evaluation done in

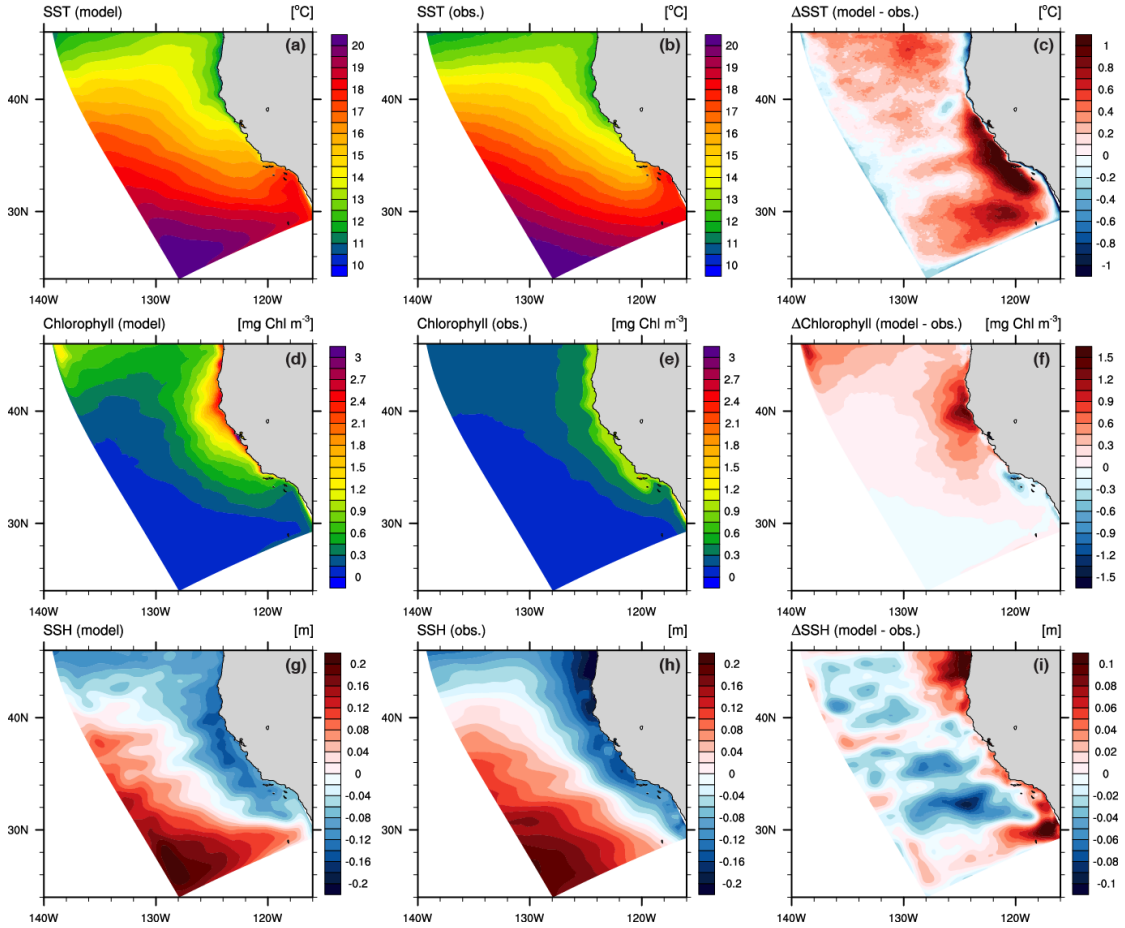

Figure 2.5 Temporal means of monthly SST (panels **(a)** to **(c)**), chlorophyll (panels **(d)** to **(f)**) and sea surface height (SSH; panels **(g)** to **(i)**) from the ROMS hindcast simulation (left column) and satellite observations (center column) and the difference between the modeled and observed means (right column). SST observations are from NOAA's AVHRR Pathfinder Version 5 SST Project at 4 km horizontal resolution and span the time period from June 1988 to December 2009. Chlorophyll data are from ESA's GlobColour Project (0.25° horizontal resolution), which includes measurements from SeaWiFS, MODISA and MERIS and covers the time period from September 1997 to December 2012. The SSH measurements are from AVISO's Rio05 mean dynamic topography (MDT) product at a horizontal resolution of 0.5° from 1993 to 1999 (Rio and Hernandez, 2004). The modeled data were averaged over the same time periods as the respective satellite observations to be directly comparable.

Chapter 4, where we found that upwelling trends are likely underestimated south of around 38°N. This implies that the long-term mean upwelling might also underestimated in this region, leading to warmer SST anomalies in the surface waters around Point Conception. Furthermore, the region where chlorophyll is most overestimated by the model coincides with the area where we found the strongest increase in upwelling, potentially suggesting that the wind-induced upwelling strength could be overestimated by the model in this region. However, one needs to be cautious when interpreting these model evaluation results and comparing them to the long-term trends between 1979 and 2012 presented in Chapter 4, as the individual satellite observations all span different, shorter time periods than the whole simulation and thus mainly serve as a validation of the model's skills in reproducing the mean state and variability rather than a verification of the trends computed in Chapter 4.

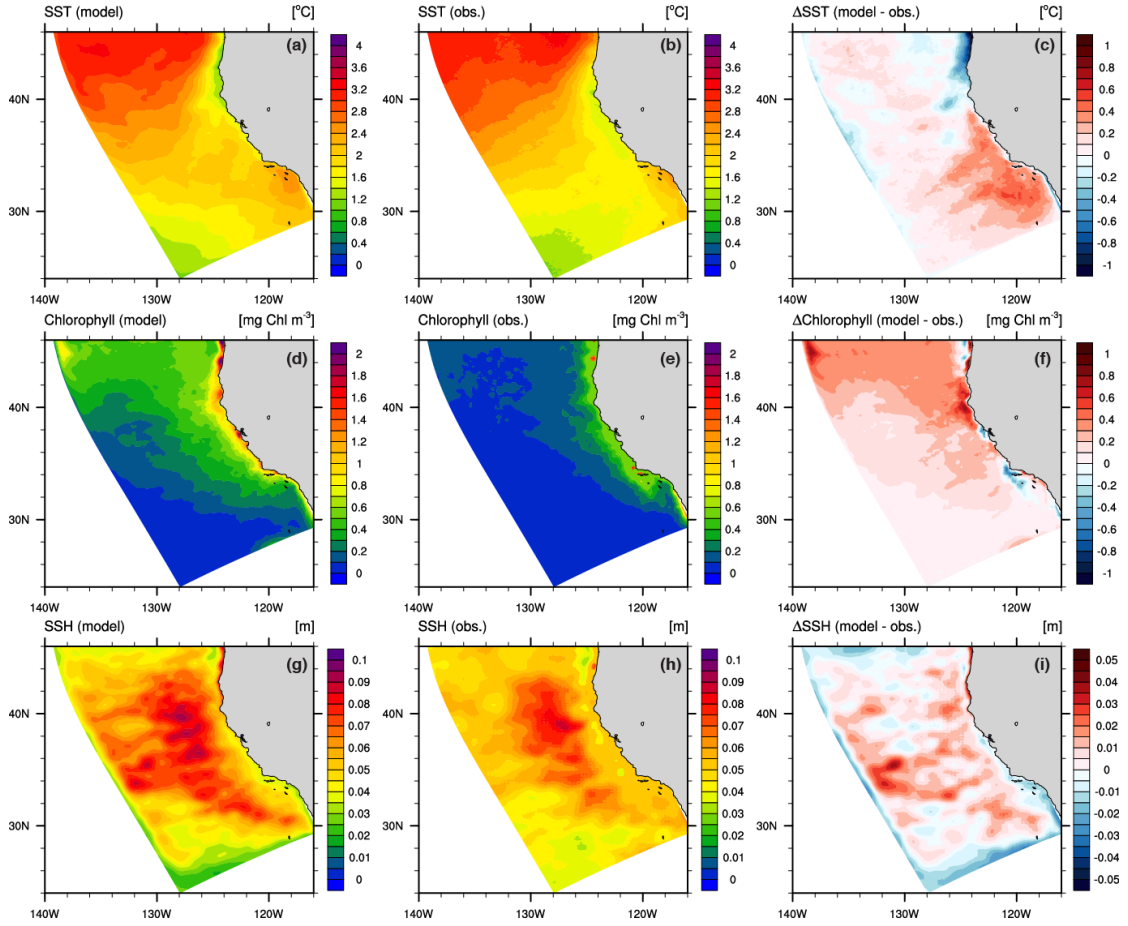

Figure 2.6 Standard deviations of monthly SST (panels **(a)** to **(c)**), chlorophyll (panels **(d)** to **(f)**) and sea surface height (SSH; panels **(g)** to **(i)**) from the ROMS hindcast simulation (left column) and satellite observations (center column) and the difference between the modeled and observed standard deviations (right column). SST observations are from NOAA's AVHRR Pathfinder Version 5 SST Project at 4 km horizontal resolution and span the time period from June 1988 to December 2009. Chlorophyll data are from ESA's GlobColour Project (0.25° horizontal resolution), which includes measurements from SeaWiFS, MODISA and MERIS and covers the time period from September 1997 to December 2012. The SSH measurements are from AVISO's Ssalto/Duacs gridded sea level anomalies product at a horizontal resolution of $\frac{1}{3}^\circ$ from December 1992 to December 2012. The standard deviations of the modeled data were computed over the same time periods as the respective satellite observations to be directly comparable.

Comparison with in-situ measurements

In addition to the comparisons with satellite observations, I used SST, salinity and pCO_2 in-situ data from the mooring in Santa Monica Bay (Leinweber et al., 2009; Leinweber and Gruber, 2013) to validate the model's performance over the last decade of the hindcast simulation (2003–2012). The mooring is situated roughly 10–20 km from the coast, at ∼33.9°N and 118.7°W. Figure 2.8a highlights that the model has good skills in simulating the seasonal cycle and the absolute values of SST, with an almost negligible negative bias of –0.2°C and a very high correlation of 0.8 (Fig. 2.8d). The magnitude of the temporal variability in SST is also captured very well, with a standard deviation comparable to that of the observations. The temporal variability of salinity is slightly less well simulated, with a correlation of roughly 0.6 and a standard that is roughly half of that of the observations (normalized standard deviation is 0.6). The model also

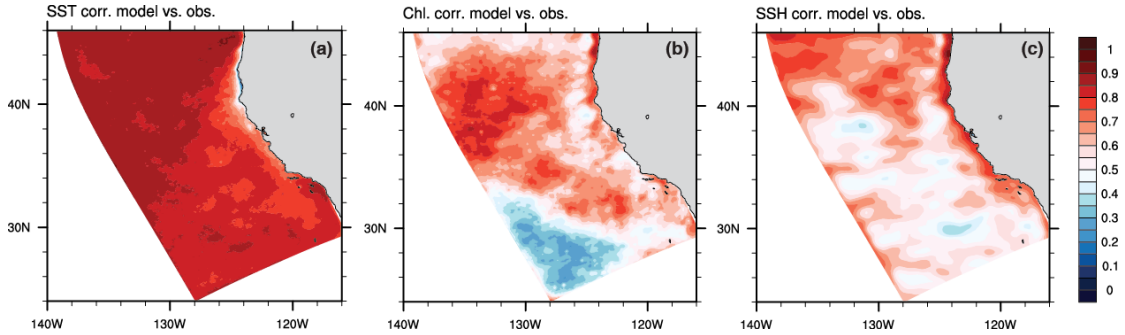

Figure 2.7 Correlations of monthly modeled versus observed **(a)** SST, **(b)** chlorophyll and **(c)** sea surface height (SSH). The modeled data are from the ROMS hindcast simulation. SST observations are from NOAA's AVHRR Pathfinder Version 5 SST Project at 4 km horizontal resolution and span the time period from June 1988 to December 2009. Chlorophyll data were measured by ESA's GlobColour Project (0.25° horizontal resolution), which includes measurements from SeaWiFS, MODISA and MERIS and covers the time period from September 1997 to December 2012. The SSH measurements are from AVISO's Ssalto/Duacs gridded sea level anomalies product at a horizontal resolution of $\frac{1}{3}^\circ$ from December 1992 to December 2012. Simple least-squares linear trends were removed from both modeled and observed data before the correlations were computed. The modeled data were sampled over the same time periods as the respective satellite observations to be directly comparable.

Table 2.3 List of satellite product acronyms and their respective webpages.

Acronym	Meaning	Webpage
AVHRR	Advanced Very High Resolution Radiometer	http://noaasis.noaa.gov/NOAASIS/ml/avhrr.html
AVISO	Archiving, Validation and Interpretation of Satellite Oceanographic Data	http://www.aviso.altimetry.fr/en/home.html
GlobColour	(European Node for) Global Ocean Colour	http://www.globcolour.info/
SeaWiFS	Sea-viewing Wide Field-of-view Sensor	http://oceancolor.gsfc.nasa.gov/SeaWiFS/
MODISA	Moderate Resolution Imaging Spectroradiometer on NASA Aqua Satellite	http://aqua.nasa.gov/about/instrument_modis.php
MERIS	Medium Resolution Imaging Instrument on ESA Envisat Satellite	https://earth.esa.int/web/guest/missions/esa-operational-eo-missions/envisat/instruments/meris

slightly underestimates salinity on average over the whole time period by –0.2 (Fig. 2.8b). However, the model strongly overestimates pCO_2 by on average 76 μatm, and has great difficulties in reproducing the temporal variability of pCO_2 (Fig. 2.8c). The modeled data show a clear seasonal cycle in pCO_2, reflecting the seasonality in SST, whereas the measured pCO_2 show a much more variable temporal behavior and stronger decrease in summertime pCO_2, implying that the model is missing a process that would decrease DIC in summer (personal communication with A. Leinweber, UCLA). Several studies suggest that including nitrogen (N_2) fixation in models could serve as a remedy and lead to the desired decrease in DIC and pCO_2 (e.g., Hood et al., 2001; Leinweber et al., 2005). Hamersley et al. (2011) showed that N_2 fixation indeed exists in

Santa Monica Bay, although not to the extent that it could account for the pCO_2 difference seen in comparison to our modeled data. Another process, whose absence in the model could be a plausible explanation for the model's overestimation of pCO_2, is the diurnal, vertical migration of zooplankton such as dinoflagellates (personal communication with A. Leinweber, UCLA). If zooplankton regularly migrate to depths below the euphotic zone, they increase the DIC pool at this depth, due to respiration processes and remineralization after their death. The model however assumes that they constantly remain within the euphotic zone, and thus would overestimate the DIC pool at the surface compared to in-situ measurements.

Furthermore, the buoy's proximity to land ($\sim$10–20 km) means that it could be affected by coastal influences, such as riverine input of nutrients. A higher nutrient concentration would stimulate higher biological productivity, potentially resulting in a drop in pCO_2. This effect would not show up in the modeled data due to the lack of a parameterization for riverine input (see discussion on model shortcomings in Chapter 6).

In summary, the comparison of the model with the in-situ data is complicated by the paucity of observations within one month, so that monthly means could be biased towards individual measurements. In addition, towards the end of the time series ($\sim$2010–2012), measured data become increasingly sparse, further impeding the comparison with the modeled data. This highlights the urgent need for an expansion of the observational network and for temporally more complete time series of pCO_2 in the Southern California Bight, in order to constrain the model and aim to improve its representation of the complex carbon cycle dynamics in that region.

2.5 Technical model improvements

Several technical improvements to the model have been made in this study compared to previous modeling work done with ROMS on the carbon cycle in the CalCS. In the following, the most important model developments that have been made in this work are highlighted.

Correction of lateral boundary DIC

In Chapter 3, we established that reducing the model's lateral DIC boundary conditions provided by GLODAP by –8 mmol C m^{-3} at the surface, with this adjustment tapering off to a depth of 350 m, significantly improved the model's overall positive bias in surface pCO_2 compared to a set of observational data sets. Although the nearshore 100 km still showed a positive bias of roughly 10 μatm compared to the observations after this correction, the domain-wide pCO_2 bias had been reduced to almost zero (Fig. 2.4). The sensitivity simulations conducted in Fig. 2.4 demonstrate the high sensitivity of the modeled pCO_2 and associated air–sea CO_2 fluxes to the choice of the model's DIC boundary conditions. Furthermore, they highlight the importance of a solid model evaluation with available in-situ data. Given that this correction of –8 mmol C m^{-3} lies within

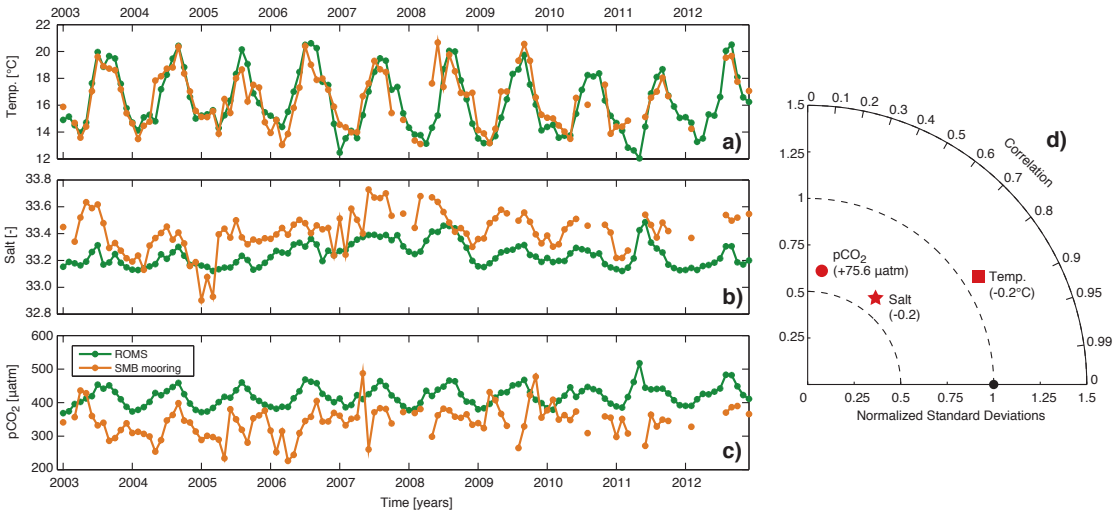

Figure 2.8 Monthly timeseries of observed and modeled **(a)** SST, **(b)** salinity and **(c)** $p\mathrm{CO}_2$ from 2003 to 2012. The in-situ data are from a mooring located in Santa Monica Bay (SMB), California ($\sim$33.9°N, 118.7°W; Leinweber et al., 2009; Leinweber and Gruber, 2013) and are courtesy of A. Leinweber, UCLA. Individual, daily in-situ measurements were averaged to produce monthly means. The modeled data are also monthly means and were averaged for a radius of roughly 50 km around the location of the mooring. Panel **(d)** shows a Taylor diagram (Taylor, 2001) of modeled vs. observed data, where the modeled data's normalized standard deviation is the distance to the origin point, indicated by the dashed lines (a value of 1 means a perfect agreement with the temporal variability of the observed data). The temporal correlation between modeled and observed data is represented by the angle between each model point and the vertical axis (Pearson correlation coefficient). The values in parentheses are the mean biases for each of the variables compared to the observed data.

the error estimates given by GLODAP for the CalCS region, we were able to confirm that this adjustment was a reasonable choice.

Adjusting the CaCO_3 formation ratio, phytoplankton light sensitivity and phytoplankton mortality

Furthermore in Chapter 3, we determined that using a CaCO_3 formation ratio ($\mathrm{r}_{CaCO_3:C}$) of 0.03, rather than the previously used value of 0.07 (Gruber et al., 2011, 2012; Hauri et al., 2013b,a), yielded a CaCO_3-to-organic-carbon ratio at 100 m depth of 0.09, which was more comparable to the global mean export ratio of 0.06–0.11 (Lee, 2001; Sarmiento et al., 2002; Jin et al., 2006). The previously used value yielded a too high, unrealistic CaCO_3-to-organic-carbon ratio of 0.25, hence producing too much CaCO_3 per unit organic carbon formed. As a consequence of adjusting our ratio to 0.03, our surface ocean $p\mathrm{CO}_2$ and hence the positive bias in comparison to observations decreased.

In addition, we adopted the the same values for the parameters phytoplankton light sensitivity and phytoplankton mortality as used by Gruber et al. (2011) of 2 and 0.048, which are twice as large as the values used previously by Gruber et al. (2006). Together with the choice of $\mathrm{r}_{CaCO_3:C}$ this further reduced the model's positive $p\mathrm{CO}_2$ bias compared to observations (Fig. 2.4). These adjustments in $\mathrm{r}_{CaCO_3:C}$ and various ecosystem parameters highlights the need for a tuning of the

ecosystem model to a specific site, in this case to the coastal upwelling conditions of the CalCS, and underlines the importance of re-evaluating the model's performance with available in-situ data. For the hindcast simulations in Chapters 4 and 5, we continued using the same ecological parameters and correction to the lateral DIC that were established in Chapter 3.

High-frequency, transient atmospheric forcing

The hindcast simulations performed in Chapters 4 and 5 were forced from 1979 to 2012 with daily values for u- and v-momentum wind stress, surface heat and freshwater fluxes and shortwave solar radiation from ECMWF's ERA-Interim Reanalysis product (Dee et al., 2011). To date, the highest temporal resolution of simulations used for instance by us in Chapter 3 or by Gruber et al. (2012) and Hauri et al. (2013b) was monthly. The use of high-frequency atmospheric forcing for the hindcast simulations explicitly permits the resolution of processes which persist for timescales shorter than one month, such as short-term variations in the upwelling related to changes in weather patterns and in the alongshore wind stress. Particularly the inclusion of high resolution wind stress is a crucial improvement, as this permits us to capture strong, short-lived upwelling events, which have an effect on surface $p\mathrm{CO}_2$, pH and Ω_{arag}. The analyses presented in Chapters 4 and 5 focus on monthly or longer-term variability only, and it remains to be seen whether the inclusion of daily wind forcing has an important impact on the average monthly upwelling behavior and circulation patterns. Together with the analysis of sub-monthly variability based on these hindcast simulations, this will be the subject of future studies which will expand on the work presented in this PhD thesis (see Section 6.3).

Furthermore, forcing the model with transient as opposed to climatological atmospheric values allowed for the inclusion of phenomena occurring on interannual to decadal timescales between 1979 to 2012. So far, in the studies mentioned above, any interannual variability had been based on the model's internal stochastic fluctuations only. With the new hindcast simulations, it became possible to include atmospheric forcing associated with longer-term climatic fluctuations, such as the teleconnective patterns ENSO, PDO and NPGO (Chapter 5). Another consequence of having transient atmospheric forcing was that in Chapter 4, we were able to perform a set of simulations which allowed us to investigate separately the effects of rising atmospheric CO_2 concentrations and of changes in the physical forcing on the progression of ocean acidification in the CalCS, which to date had not been possible with the previous simulations. With this we were able to show that changes in upwelling-favorable winds can account for up to 30% of pH trends and 50% of the trends in Ω_{arag} and highlight the importance of considering not only changes in anthropogenic CO_2 but also changes in the physical climatic forcing.

Transient lateral boundary forcing

In addition to the daily, transient atmospheric forcing, the hindcast simulations from Chapters 4 and 5 were forced at the lateral boundaries with transient data at monthly resolution, based on

model output from a CCSM hindcast simulation performed by Graven et al. (2012). Together with the transient atmospheric forcing, this allowed by way of the oceanic boundaries for a full representation of interannual to decadal events, which is an important improvement in comparison to previous studies which were forced with climatological values at the lateral boundaries. A study by Rykaczewski and Dunne (2010) using an Earth System Model (GFDL ESM 2.1) projected that over the 21st century, nitrate supply to and biological productivity in the CalCS will increase, despite an increase in stratification and only minor changes in upwelling. They attributed these changes to a nitrate enrichment of source waters entering the CalCS region. This result emphasizes the importance of forcing regional oceanic models, such as ROMS in the CalCS, with variable lateral boundary conditions, rather than using climatological values at the boundaries, to assure that for instance changes in lateral circulation and advection are captured in addition to changes driven solely through the atmosphere. In Section 6.2, I discuss the drawback of having only monthly boundary conditions rather than higher resolution and the implications for the carbon cycle in the CalCS.

Chapter 3

Spatiotemporal variability and drivers of pCO_2 and air-sea CO_2 fluxes in the California Current System: an eddy-resolving modeling study

G. Turi, Z. Lachkar, and N. Gruber

Environmental Physics, Institute of Biogeochemistry and Pollutant Dynamics, ETH Zürich, Zürich, Switzerland

This manuscript was published under the same title in Biogeosciences, 2014, Volume 11, Issue 3, pages 671-690. It is used here with copyright permissions from Copernicus Publications.

Abstract

We quantify the CO_2 source/sink nature of the California Current System (CalCS) and determine the drivers and processes behind the mean and spatiotemporal variability of the partial pressure of CO_2 (pCO_2) in the surface ocean. To this end, we analyze eddy-resolving, climatological simulations of a coupled physical–biogeochemical oceanic model on the basis of the Regional Oceanic Modeling System (ROMS).

In the annual mean, the entire CalCS within 800 km of the coast and from $\sim 33°$N to 46°N is essentially neutral with regard to atmospheric CO_2: the model simulates an integrated uptake flux of -0.9 ± 3.6 Tg C yr^{-1}, corresponding to an average flux density of -0.05 ± 0.20 mol C m^{-2} yr^{-1}. This near zero flux is a consequence of an almost complete regional compensation between (i) strong outgassing in the nearshore region (first 100 km) that brings waters with high concentrations of dissolved inorganic carbon (DIC) to the surface and (ii) and a weaker, but more widespread uptake flux in the offshore region due to an intense biological reduction of this DIC, driven by the nutrients that are upwelled together with the DIC.

The air–sea CO_2 fluxes vary substantially in time, both on seasonal and sub-seasonal timescales, largely driven by variations in surface ocean pCO_2. Most of the variability in pCO_2 is associated with the seasonal cycle, with the exception of the nearshore region, where sub-seasonal variations driven by mesoscale processes dominate. In the regions offshore of 100 km, changes in surface temperature are the main driver, while in the nearshore region, changes in surface temperature, as well as anomalies in DIC and alkalinity (Alk) owing to changes in circulation, biological productivity and air–sea CO_2 fluxes dominate. The prevalence of eddy-driven variability in the nearshore 100 km leads to a complex spatiotemporal mosaic of surface ocean pCO_2 and air–sea CO_2 fluxes that require a substantial observational effort to determine the source/sink nature of this region reliably.

3.1 Introduction

The coastal ocean often has not been appropriately taken into account in global carbon budget estimates, despite the fact that the associated carbon fluxes are disproportionately large with respect to the small fraction of the global ocean area that coastal oceans occupy (e.g., Liu et al., 2000; Borges et al., 2005; Chavez et al., 2007; Liu et al., 2010; Regnier et al., 2013). Global ocean models tend to be too coarse to resolve important coastal processes and observational data are often limited in space and time (e.g., Laruelle et al., 2010). Therefore, coastal air–sea CO_2 fluxes are currently still relatively poorly quantified, with considerable regional and global uncertainties.

Coastal upwelling regions are particularly dynamic in terms of carbon cycling as they experience extreme temporal and spatial variability in carbon fluxes (e.g., Friederich et al., 2002; Cai et al., 2006; Leinweber et al., 2009; Evans et al., 2011), further adding to the uncertainty in the coastal carbon budget. As the upwelled water is rich in dissolved inorganic carbon (DIC), its partial pressure of CO_2 (pCO_2) is very high and can often exceed atmospheric levels, hence leading to an outgassing of CO_2. At the same time, the upwelled nutrients stimulate phytoplankton productivity, which supports a large fixation and export of organic carbon (e.g., Muller-Karger et al., 2005). This leads to a decrease in surface ocean pCO_2 and enhances the drawdown of atmospheric CO_2 (e.g., Hales et al., 2005, 2012; Chavez and Messié, 2009). These opposing mechanisms and the highly variable ocean circulation with a large amount of mesoscale variability render coastal upwelling systems extremely complex with regard to carbon cycling.

The California Current System (CalCS), one of the four major eastern boundary upwelling systems, exhibits an intricate interplay of physical and biological controls on lateral and air–sea CO_2 fluxes. On the one hand, its relatively high level of eddy activity reduces biological productivity to levels below those expected on the basis of its rate of upwelling, leading also to a reduced vertical export of fixed carbon (Gruber et al., 2011; Lachkar and Gruber, 2011). On the other hand, filaments and other meso- and submesoscale structures cause a substantial lateral export of organic carbon (Nagai et al., 2014), thereby leading to a strong decoupling between biological production and vertical carbon export (Plattner et al., 2005).

The CalCS has been the subject of many studies investigating a variety of different aspects ranging from ecosystem vulnerability to global anthropogenic perturbations such as ocean acidification (e.g., Feely et al., 2008; Gruber et al., 2012; Hauri et al., 2013b) and the emergence of areas of hypoxic oxygen concentrations (e.g., Chan et al., 2008), to more process-related topics such as the phenology of coastal upwelling (e.g., Bograd et al., 2009) and the impacts of different processes on biological production (e.g., Gruber et al., 2011; Lachkar and Gruber, 2011, 2013). However, only a few studies have so far dealt with the source/sink nature of the CalCS with regard to atmospheric CO_2 or quantified the contribution of the CalCS to the global carbon budget (Borges et al., 2005; Cai et al., 2006; Chavez et al., 2007; Hales et al., 2012).

The published studies have come to rather different conclusions with regard to whether the entire CalCS is a source or a sink of atmospheric CO_2 (see Table 3.1). Friederich et al. (2002) found that the area off Monterey Bay, California, switched from being a sink of roughly $-0.5\,\mathrm{mol\,C\,m^{-2}\,yr^{-1}}$ during weak upwelling years (El Niño) to outgassing CO_2 at a rate of around $1.9\,\mathrm{mol\,C\,m^{-2}\,yr^{-1}}$ during strong upwelling years (La Niña). Based on this very limited set of observations used by Friederich et al. (2002) and other studies of temperate coastal upwelling systems, Borges et al. (2005) suggested that upwelling systems from 30 to 60°N act on average as weak sources with a mean flux density of $0.11\,\mathrm{mol\,C\,m^{-2}\,yr^{-1}}$. In contrast, Cai et al. (2006) argued that midlatitude upwelling shelves (also 30–60°N) are sinks with a mean flux density of $-1\,\mathrm{mol\,C\,m^{-2}\,yr^{-1}}$. Hales et al. (2005), whose estimates are included in those of Cai et al. (2006), found that the Oregon coast had a particularly strong sink strength of $-7.3\,\mathrm{mol\,C\,m^{-2}\,yr^{-1}}$, based on 120 days of measurements in 2001. More recent observations from the Oregon coast by Evans et al. (2011) support the conclusion of this region being a sink, but they also showed that the air–sea CO_2 fluxes in this area are highly variable. In particular, they found very high pCO_2 with values exceeding 1000 μatm in late summer to early fall, while waters in that area were almost consistently undersaturated with respect to the atmosphere in winter and spring. This led to a small annual uptake with a mean flux density of $-0.3 \pm 6.8\,\mathrm{mol\,C\,m^{-2}\,yr^{-1}}$. A similar small uptake flux was reported for the Santa Monica Bay, using a limited duration, but high frequency time series (Leinweber et al., 2009).

In the first attempt to provide a CalCS-wide estimate without relying on the extrapolation of measurements from one site to the entire region, Chavez et al. (2007) collected all available pCO_2 observations from the Lamont–Doherty Earth Observatory (LDEO) database, and inferred an essentially neutral CalCS with an outgassing flux density of $0.03\,\mathrm{mol\,C\,m^{-2}\,yr^{-1}}$. This corresponds to a total loss of $0.5\,\mathrm{Tg\,C\,yr^{-1}}$ to the atmosphere over the entire west coast of the US and extending ~ 300 km offshore (first three $1^\circ \times 1^\circ$ grid boxes). Using a large set of zonal cruises offshore of Monterey Bay, Pennington et al. (2010) confirmed the nearly balanced air–sea CO_2 budget for the central part of the CalCS, but also emphasized the existence of large onshore–offshore gradients in the fluxes, with a tendency towards outgassing in the more nearshore areas and year-round uptake offshore of ~ 52 km. The sink nature in the offshore region is also supported by the LDEO surface ocean CO_2 climatology of Takahashi et al. (2009), which reports a net sink of $-0.8\,\mathrm{mol\,C\,m^{-2}\,yr^{-1}}$ for the nine $4^\circ \times 5^\circ$ grid boxes that are located roughly between 400 and 800 km offshore of the west coast of the US.

Most recently, Hales et al. (2012) refined the estimate by Chavez et al. (2007) using the same data but employing a self–organizing map approach to extrapolate the observations in time and space. For the same region, i.e. the area of the central North American Pacific continental margin (22–50°N, within 370 km from the coast), they came to a rather different result, i.e. a moderate sink of $-14\,\mathrm{Tg\,C\,yr^{-1}}$ for the period from 1997 to 2005, corresponding to a flux density of $-0.66\,\mathrm{mol\,C\,m^{-2}\,yr^{-1}}$. They confirmed the strong onshore–offshore differences in pCO_2 and CO_2 fluxes pointed out by Pennington et al. (2010), both in terms of the annual mean and the

Table 3.1 Summary of studies contributing to air–sea CO_2 flux (F_{CO_2}) quantification in the CalCS. F_{CO_2} has been converted to flux densities for better intercomparison. Positive F_{CO_2} values indicate a source to the atmosphere, while negative values mean an uptake by the surface ocean.

Study	Type of data	Spatial coverage	Temporal coverage	F_{CO_2} [mol C m^{-2} yr^{-1}]
This study	Modeled	$\sim$ 33–46°N, 0–800 km offshore	Climatological simulation, representative of 2000/2001	-0.05 ± 0.20 (-0.9 ± 3.6Tg C yr^{-1})
Hales et al. (2012)	Neural network analysis of underway (LDEO database)	North American Pacific continental margin: 22–50°N, 0–370 km offshore	1997–2005	-0.66 ± 0.66 (-14 ± 14Tg C yr^{-1})
Evans et al. (2011)	Underway and mooring	Central Oregon midshelf: 44.5–44.8°N, 124.4–124.2°W	Aug 2007–May 2010	-0.3 ± 6.8[1]
Pennington et al. (2010)	Underway and mooring	Central California: Monterey Bay and along CalCOFI Line 67	1997–2001	-0.08 (0–20 km)[2] $+0.75$ (20–52 km)
Takahashi et al. (2009)	Underway (LDEO database)	30–46°N, 120–135°W: nine $4^\circ \times 5^\circ$ grid boxes	1970–2007, reference year 2000	-0.8
Leinweber et al. (2009)	Mooring	Southern California, S. Monica Bay: 33.1°N, 118.7°W	Aug 5–Oct 4 2002	-0.76
Chavez et al. (2007)	Underway (LDEO database)	Entire west coast of the US extending $\sim$ 300 km offshore: first three $1^\circ \times 1^\circ$ grid boxes	1979–2004, reference year 1995	$+0.03$
Cai et al. (2006)	Underway	Midlatitude upwelling shelves: 30–60°N	Various	-1.0[3]
Borges et al. (2005)	Underway	Temperate coastal upwelling systems: 30–60°N	Various	$+0.11$[4]
Hales et al. (2005)	Underway	Oregon coast: 44–45°N	May–Aug 2001: 120 days	-7.3
Friederich et al. (2002)	Underway and mooring	Central California: Monterey Bay and along CalCOFI Line 67	Jul 1997–Jul 1998: El Niño Jul 1998–Jul 1999: La Niña	-0.3 to -0.7 (El Niño) $+1.5$ to $+2.2$ (La Niña)

[1] pCO_2^{air} is assumed constant at 392 μatm. [2] Pennington et al. (2010) infer a near zero flux for the central California area (34.4–40.5°N). [3] Estimates for Northern and Central California and Oregon are based on Friederich et al. (2002) and Hales et al. (2005). [4] Estimates for the Californian coast are based on Friederich et al. (2002).

level of variability.

While these previous studies document the direction and magnitude of the air–sea CO_2 fluxes in different locations of the CalCS and reveal their subseasonal to interannual variability, their lack of consistent geographic settings, the absence of sufficiently dense and spatially extended observational coverage and their differing temporal coverage hinders the emergence of a synthetic view of the CalCS acting as a source or a sink of atmospheric CO_2. This provides an opportunity for numerical models to complement the observational studies as they can provide a synoptic and more complete view of the spatiotemporal variability of the air–sea CO_2 fluxes. The models further offer the opportunity to investigate the processes underlying the mean fluxes and their variability in considerably greater depth than currently possible with the in situ data.

In this study, we use a series of eddy-resolving simulations from a coupled physical–biogeochemical oceanic model on the basis of the Regional Oceanic Modeling System (ROMS) to quantify (i) the climatological mean air–sea CO_2 fluxes and their drivers, (ii) the spatiotemporal variability of these fluxes, and (iii) the key drivers and processes behind the variability of these fluxes, i.e. the drivers and processes affecting surface ocean pCO_2. Our study shows that although the CalCS as a whole acts on average as a very weak carbon sink with respect to the atmosphere, the air–sea CO_2 fluxes are locally large and highly variable in space and time.

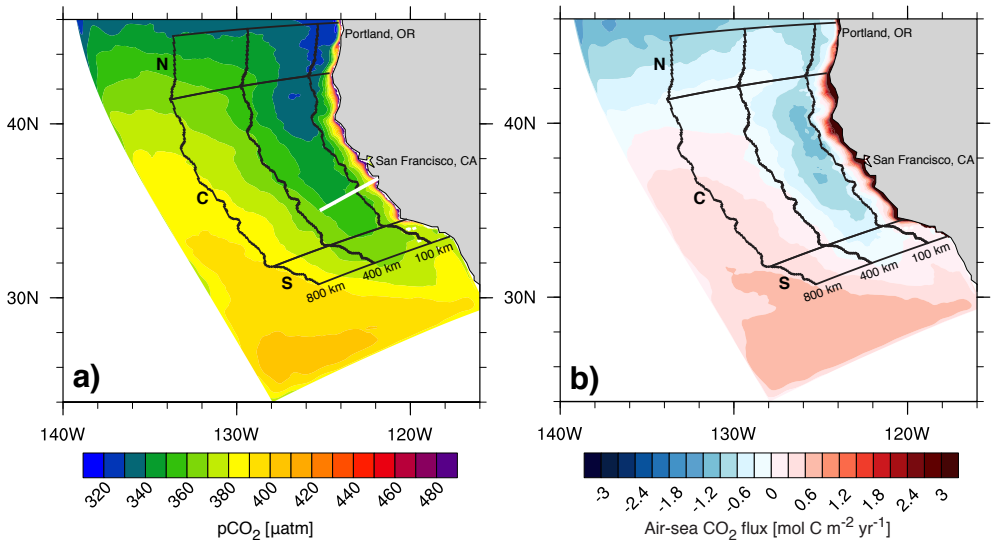

Figure 3.1 Annual mean surface pCO_2 **(a)** and air–sea CO_2 flux **(b)** as simulated in the CalCS. Positive air–sea fluxes denote an outgassing of CO_2. The superimposed black lines indicate the nine subdomains, where the northern (N), central (C) and southern (S) subdomains are all split into a nearshore (0–100 km), a near-offshore (100–400 km) and a far-offshore (400–800 km) subdomain. The white line in panel **(a)** indicates the approximate location of the MBARI/CalCOFI Line 67.

Furthermore, the present work highlights the fundamental contrasts in the dynamics of the carbon cycle that exist between the nearshore areas dominated by the effects of upwelling and biological production and the regions further offshore where variations induced by temperature play a more prominent role. Finally, our investigation reveals that mesoscale eddies contribute substantially to surface pCO_2 variability in the nearshore central CalCS, making it challenging to derive a synoptic and representative view of the CO_2 fluxes on the basis of the sparse observations currently available.

3.2 Methods

3.2.1 Model details

The model used in this study is an eddy-resolving, coupled physical–biogeochemical oceanic model of the west coast of the US based on ROMS. The model domain covers roughly 2800 km alongshore (30°N–50°N) and 1250 km offshore (Fig. 3.1), and has a curvilinear, coast-following grid with an average grid spacing of 5 km. The model's vertical grid consists of 32 depth levels with increasing resolution towards the surface and in the shallower nearshore regions. The physical model is based on the UCLA-ETH version of ROMS (Marchesiello et al., 2003; Shchepetkin and McWilliams, 2005).

The biogeochemical model is a nitrogen-based nutrient-phytoplankton-zooplankton-detritus (NPZD) model and includes a single phytoplankton group, implemented to mimic diatom-like

behavior. A comprehensive description of the NPZD model can be found in Gruber et al. (2006). We use the same model setup and ecological parameters as Gruber et al. (2011).

An interactive carbon module was additionally implemented in the model and introduces three new state variables: dissolved inorganic carbon (DIC), alkalinity (Alk) and calcium carbonate ($CaCO_3$) (Gruber et al., 2012; Hauri et al., 2013b; Lachkar and Gruber, 2013). All of these state variables are subject to physical transport and mixing, while $CaCO_3$ is furthermore allowed to sink at a constant rate of 20 m day^{-1}. The organic carbon cycle is linked to the organic nitrogen cycle with a fixed stoichiometric $C : N$ ratio of $106 : 16$ (Redfield et al., 1963). DIC concentrations are altered by the air–sea CO_2 flux, the precipitation and dissolution of $CaCO_3$ and the net community production, which is defined as net primary production (NPP) minus heterotrophic respiration. The Alk concentration is modified by the formation and removal of nitrate as well as the precipitation and dissolution of $CaCO_3$. The precipitation of $CaCO_3$ is linked to NPP via a constant proportionality factor of 0.03, meaning that for each formed mole of organic carbon, 0.03 mol of $CaCO_3$ are produced. $CaCO_3$ dissolves at a rate of 0.0057 day^{-1} in the water column and 0.002 day^{-1} in the sediments.

We lowered the production ratio for $CaCO_3$ from the value of 0.07 used previously by Gruber et al. (2011) and Hauri et al. (2013b) to account for the fact that their resulting $CaCO_3$ to organic carbon export ratio of 0.25 at 100 m depth was substantially larger than expected, while our new value of 0.09 is consistent with the global mean export ratio of about 0.06–0.11 (Lee, 2001; Sarmiento et al., 2002; Jin et al., 2006). In addition, we found that lowering the production ratio also yielded model-simulated pCO_2 that compared better to observations.

The surface ocean carbonate chemistry is calculated following the standard Ocean Carbon-Cycle Model Intercomparison Project (OCMIP) carbonate chemistry routines[1]. For all our simulations, atmospheric pCO_2 (pCO_2^{air}) oscillates seasonally around a mean value of 370 μatm, which corresponds approximately to the atmospheric concentration in the years 2000 and 2001, with a seasonal amplitude of 2.9 μatm, which was taken from the NOAA Marine Boundary Layer Reference[2] for the mean latitude of our domain.

With the partial pressures of CO_2 of atmosphere (pCO_2^{air}) and surface ocean (pCO_2^{sea}), the air–sea CO_2 flux is computed using the standard bulk formula:

$$F_{CO_2} = -K_0 \cdot k_w \cdot \left(pCO_2^{air} - pCO_2^{sea}\right), \tag{3.1}$$

where K_0 denotes the solubility of CO_2, computed using the temperature- and salinity-dependent formulation of Weiss (1974), and k_w is the CO_2 gas transfer (piston) velocity. The calculation of the piston velocity for steady (short-term) winds assumes a quadratic dependence on the wind speed (Wanninkhof, 1992), using the coefficient for long-term winds. pCO_2^{sea} is calculated using

[1] http://ocmip5.ipsl.jussieu.fr/OCMIP/phase3/simulations/NOCES/HOWTO-NOCES-3.html
[2] http://www.esrl.noaa.gov/gmd/ccgg/mbl/mbl.html

DIC, Alk, temperature (T), salinity (S) and nutrients, employing the first and second dissociation constants of carbonic acid of Millero (1995), with original reference to Mehrbach et al. (1973) and as refitted by Dickson and Millero (1987). Our sign convention is that positive values of F_{CO_2} denote an outgassing of CO_2, while negative values indicate an uptake by the surface ocean.

3.2.2 Initial and boundary conditions

The model was started from rest and run for 12 yr with monthly climatological forcing. As our model simulations require about 5 yr for the spinup, we use model years 6–12 for analysis. For our annual mean and seasonal analyses in Sects. 3.3, 3.4, 3.5 and 3.6.1, we used model output at monthly resolution and averaged this to obtain a climatology over 7 yr. For the analysis of mesoscale processes in Sect. 3.6.2, we used 2-day model output and looked at all analysis years without averaging.

The initial and boundary conditions for our runs are as described in Hauri et al. (2013b) and Lachkar and Gruber (2013). In particular, the DIC and Alk initial and boundary conditions were derived from the Global Ocean Data Analysis Project (GLODAP; Key et al., 2004). A seasonal cycle was added to Alk in the surface ocean, using the regression approach of Lee et al. (2006) and employing surface ocean T and S. Similarly, a seasonal cycle of surface DIC was constructed using the monthly pCO_2 climatology of Takahashi et al. (2006), and monthly surface Alk, T and S. The seasonal cycles of DIC and Alk are then modeled to penetrate into the upper thermocline, assuming that these variations are proportional to the seasonal amplitude of T at the different depths.

We slightly modified the upper ocean lateral boundary conditions of DIC inferred from GLODAP (Lee et al., 2006; Takahashi et al., 2006) in order to improve upon our model-simulated pCO_2, DIC and Alk fields relative to observations (see more on model evaluation in Sect. 3.3). The modification consisted of adjusting the vertical profile of DIC with an offset starting value of $-8\,\mathrm{mmol\,C\,m^{-3}}$ at the surface, and then tapering off linearly with density to a depth of 350 m, below which the adjustment is zero. We determined the magnitude of this correction from the model-simulated positive DIC bias of about $10\,\mathrm{mmol\,C\,m^{-3}}$ in the first 10 m relative to data collected from a coast-wide survey cruise undertaken from May to June 2007 by Feely et al. (2008). The most likely reason for the bias in our uncorrected boundary conditions is that they were computed from the gridded products of GLODAP and Takahashi et al. (2006), with particularly the former being based on relatively sparse observations in the eastern North Pacific. The magnitude of the correction is small relative to the uncertainties of GLODAP's DIC gridded product, with the gridding error alone exceeding $10\,\mathrm{mmol\,C\,m^{-3}}$ for the CalCS (Key et al., 2004).

Table 3.2 Summary of the sensitivity studies used to determine the contributions of air–sea CO_2 flux, biological production, CO_2 solubility and circulation to total pCO_2 from the control simulation.

Simulation	Properties
CTRL	Control simulation
S1	No air–sea CO_2 flux
S2	No air–sea CO_2 flux, no biological production
S3	No air–sea CO_2 flux, no biological production, constant CO_2 solubility
Calculation	**Implication**
CTRL − S1	Contribution of air–sea CO_2 flux to total pCO_2
S1 − S2	Contribution of biological production to total pCO_2
S2 − S3	Contribution of CO_2 solubility to total pCO_2
S3	"Pure circulation": pCO_2 if only circulation existed

3.2.3 Drivers and processes

We employ two complementary approaches to quantify and understand the causes of the spatial and temporal variability in surface ocean pCO_2 in Sects. 3.5 and 3.6.

In the first approach we aim to identify the role of four different drivers, namely the state variables DIC, Alk, T and S, in causing variations in pCO_2. To this end, we used a first-order Taylor expansion to decompose pCO_2 into four individual components representing the contributions from changes in these four drivers. We neglect the very small contribution arising from variations in nutrients. Following Lovenduski et al. (2007) and Doney et al. (2009b), we separated the DIC and Alk changes into a part driven by freshwater (FW) fluxes and one driven by other processes, and combined the FW flux-induced changes in DIC and Alk with the changes in S to form a FW flux term, thus

$$\Delta pCO_2 \approx \underbrace{\frac{\partial pCO_2}{\partial \mathrm{DIC^s}} \cdot \Delta \mathrm{DIC^s}}_{\Delta pCO_2^{DIC,S}} + \underbrace{\frac{\partial pCO_2}{\partial \mathrm{Alk^s}} \cdot \Delta \mathrm{Alk^s}}_{\Delta pCO_2^{Alk,S}} + \underbrace{\frac{\partial pCO_2}{\partial T} \cdot \Delta T}_{\Delta pCO_2^{T}} + \underbrace{\frac{\partial pCO_2}{\partial \mathrm{FW}} \cdot \Delta \mathrm{FW}}_{\Delta pCO_2^{FW}}, \qquad (3.2)$$

where $\mathrm{DIC^s}$ and $\mathrm{Alk^s}$ are the salinity-normalized concentrations of DIC and Alk (normalized to a domain mean salinity of 35), and where the partial derivatives describe the sensitivities of pCO_2 to small changes in DIC, Alk, T and FW (after Sarmiento and Gruber, 2006, p. 329). These partial derivatives were determined by adding a small perturbation to each driver and recalculating pCO_2 four times with these new values using an offline carbonate chemistry calculating tool based on the OCMIP routines. The Δ terms are the temporal or spatial anomalies from an annual or domain mean, respectively.

The second approach goes one step further by focusing on the actual processes, i.e. the processes that alter the state variables, namely the air–sea CO_2 flux, biological production, CO_2 solubility and ocean circulation. In order to identify these processes we ran a series of sensitivity studies where we consecutively removed their contributions. In addition, we ran a control

simulation (CTRL) with no perturbations to be used as a reference (Table 3.2).

We thus separate the model-simulated pCO_2 of the control run (pCO_2^{Control}) into the following four components:

$$\underbrace{pCO_2^{\text{Control}}}_{\text{CTRL}} = \underbrace{pCO_2^{\text{Gas ex.}}}_{\text{CTRL}-\text{S1}} + \underbrace{pCO_2^{\text{Biology}}}_{\text{S1}-\text{S2}} + \underbrace{pCO_2^{\text{Solubility}}}_{\text{S2}-\text{S3}} + \underbrace{pCO_2^{\text{Circulation}}}_{\text{S3}}. \tag{3.3}$$

In the first sensitivity study (S1) we set the air–sea CO_2 flux coefficient in the model to zero, thereby preventing any exchange of CO_2 between the surface ocean and the atmosphere. The difference in pCO_2 between this simulation and the control simulation, i.e. CTRL $-$ S1, is thus the impact of the air–sea CO_2 flux on pCO_2. In the second sensitivity study (S2), we started from S1, but additionally set incoming solar radiation in the model to zero, thereby inhibiting phytoplankton growth and hence eliminating biological production of organic and inorganic carbon. The difference S1 $-$ S2 is then the impact of biological production on pCO_2. In the third sensitivity study (S3) we eliminated the impact of solubility, i.e. of surface ocean T and S, by setting the CO_2 solubility to a constant value. This was achieved by setting T and S within the solubility equations to domain mean values of 15 °C and 33.1, respectively. The difference S2 $-$ S3 is then the impact of surface ocean T and S on pCO_2. We end up with a simulation S3, whose only remaining mechanism impacting pCO_2 is circulation acting upon the boundary conditions of DIC and Alk, i.e. transporting and mixing these values from the boundaries into the interior of the domain and then also to the surface, where they impact surface ocean pCO_2.

Due to computational resource limitation, we undertook these simulations at a slightly coarser horizontal resolution of 15 km, using the same initial conditions and running them for the same length as the full-resolution simulations. Despite the degradation in resolution, the model still manages to represent well the major mesoscale features.

In this second approach, we implicitly make the assumption that the contributions of the different processes are linearly additive. Given the nonlinearities of the ocean carbonate system (Sarmiento and Gruber, 2006), this is strictly speaking not the case. This sequential removal of processes is at best an approximate method that allows the estimation of the magnitude of each term in Eq. 3.3. However, our experience with a permuted sequence where we first inhibited biological production and then set the air–sea CO_2 flux to zero, showed little difference, indicating that these nonlinearities are not substantial enough to alter our results. Moreover, this kind of approach has previously been used to great effect to investigate similar questions (e.g., Murnane et al., 1999; Schmittner et al., 2013).

3.3 Model evaluation

A thorough model evaluation of sea surface temperature (SST), chlorophyll, mixed layer depth (MLD), density structure and NPP for the CalCS was presented by Gruber et al. (2011) and Lachkar and Gruber (2011). They found that the model reproduces the annual mean and seasonal patterns of chlorophyll and MLD reasonably well, but that the model has a cold bias of roughly 1 °C compared to satellite data. Further, Gruber et al. (2011) found an underestimation of NPP by the model of about 41 % within 1000 km and 30 % within 100 km from the coast between 34 and 42°N compared to satellite-based estimates from Kahru et al. (2009).

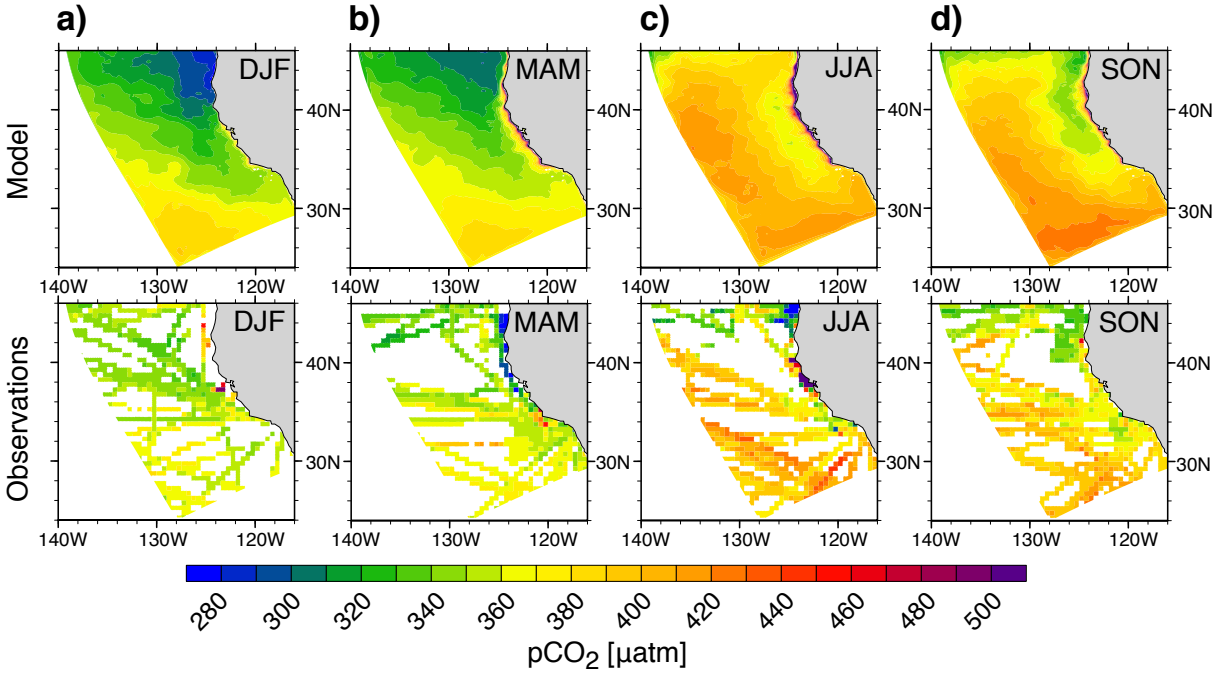

Figure 3.2 Seasonally averaged modeled (upper row) and observed (lower row) surface pCO_2 for winter (**a**; DJF), spring (**b**; MAM), summer (**c**; JJA) and fall (**d**; SON). Observations are pCO_2 computed from the Surface Ocean CO_2 Atlas (SOCAT Version 2; Pfeil et al., 2013), the global surface pCO_2 database (Takahashi et al., 2013) and the MBARI/CalCOFI Line 67 (Collins et al., 2003). The data were first binned to $0.5° \times 0.5°$ grid boxes to compute a climatology, normalized to the year 2000 and then regridded to match the ROMS grid. The lower row shows all the grid boxes with observations in them, i.e. before we applied our elimination criteria.

We extend these evaluations by comparing the model's simulated sea surface pCO_2 to observations from three different in situ data sources: (i) measurements of the fugacity of CO_2 (fCO_2) from the Surface Ocean CO_2 Atlas (SOCAT Version 2; Pfeil et al., 2013), which spans the time period from 1970 to 2011 and includes more than 220 000 observations within our model domain; (ii) pCO_2 measurements from the global surface pCO_2 (LDEO) database (Takahashi et al., 2013), spanning the period from 1957 through 2013 for our model domain and consisting of roughly 534 000 measurements; and (iii) pCO_2 data collected by the Naval Postgraduate School and the Monterey Bay Research Aquarium Institute (MBARI) along the California Cooperative Fisheries Investigations' (CalCOFI) Line 67 with more than 7000 data points in our domain for the years

from 1997 through 2001 (Collins et al., 2003). To facilitate the comparison with the model, we first converted all data to pCO_2, then binned them into $0.5^\circ \times 0.5^\circ$ grid boxes and finally normalized them to the year 2000 assuming a mean annual pCO_2 increase rate of 1.5 μatm yr^{-1} as used by Takahashi et al. (2006, 2009). We then regridded these binned and normalized data to match our ROMS curvilinear grid and averaged pCO_2 over each grid box. If there were any grid boxes containing observations from different databases, we gave preference to the SOCAT database. We evaluated our model's performance for nine subdomains separately, namely a nearshore (0–100 km), a near-offshore (100–400 km) and a far-offshore (400–800 km) subdomain (see contour lines in Fig. 3.1). The choice of these specific subdomains is based on the magnitude and offshore extent of upwelling, as well as the distinct meridional differences in the structure of the CalCS.

Figure 3.2 highlights that the model has reasonable to good skills in reproducing the observed near- to offshore gradient of pCO_2 for all seasons, and does particularly well in the summer months when it captures the seasonal upwelling signal near the coast (Fig. 3.2c). The model also captures the north–south gradients and its seasonal progression, particularly in the offshore regions (Fig. 3.2a, b, d). However, it does have a tendency to overestimate pCO_2 in the nearshore regions, which is especially noticeable in the northern and central subdomains in spring and summer (Fig. 3.2b, c).

A more quantitative assessment of the model's successes and challenges in reproducing the observed pCO_2 is offered by the Taylor diagrams in Fig. 3.3, which provide a summary of how well the observed and modeled pCO_2 patterns match in terms of their spatial correlation, their root-mean-square difference and the ratio of their standard deviations. Additionally, the diagrams show the difference between modeled and observed pCO_2 as a color-coded bias. For this analysis, we used only those data that fulfilled the following criteria: (i) for the annual mean analysis, only grid boxes containing at least two observations from opposite seasons were considered (i.e. DJF/JJA or MAM/SON) and (ii) for the seasonal analysis, only grid boxes with two observations taken in two different months within a season were retained. This reduced the number of grid boxes considerably, particularly in the nearshore region in winter and spring and offshore of 100 km. For the annual mean analysis, the number of available grid boxes is reduced by about 27% to a total of 38 477 grid boxes with averaged pCO_2 observations in them.

The annual mean correlations of the spatial pattern range between about 0.3 and 0.7 and are therefore slightly lower than the values achieved for chlorophyll (Lachkar and Gruber, 2011). Furthermore, the overall poorer performance of the model with regard to the seasonal cycle is reminiscent of the generally lower seasonal correlations found for chlorophyll, SST and mixed layer depth. However, while the variability of chlorophyll is underestimated everywhere, the model captures it fairly well for pCO_2: normalized standard deviations for all regions range between 0.4 and 2.0 with annual means of 0.6 for the nearshore region (Fig. 3.3c) and around 0.8 for the offshore regions (Fig. 3.3a, b). There exist substantial seasonal differences in the degree to which the spatial variability is captured: while the model underestimates the pCO_2 variability

Table 3.3 Regional variability of annual mean surface pCO_2 and air–sea CO_2 fluxes in the CalCS. The pCO_2 difference in the last column is pCO_2 from our study minus pCO_2 from Hales et al. (2012).

Domain	Surface area	Air–sea CO_2 flux density	Integrated air–sea CO_2 flux	pCO_2	pCO_2 difference to Hales et al. (2012)
	[km^2]	[mol C m^{-2} yr^{-1}]	[Tg C yr^{-1}]	[μatm]	[μatm]
Nearshore					
north	33 781	+0.01	<0.01	350.7	33.6
central	112 973	+1.11	+1.5	385.2	3.3
south	21 681	+0.26	+0.1	366.5	25.4
total	168 435	+0.78	+1.6	375.9	11.6
Near-offshore					
north	108 403	−0.49	−0.6	338.0	3.2
central	351 808	−0.53	−2.2	349.2	−8.4
south	65 365	−0.15	−0.1	365.0	4.9
total	525 576	−0.47	−3.0	348.9	−4.3
Far-offshore					
north	174 720	−0.53	−1.1	352.7	n/a
central	531 430	+0.19	+1.2	374.7	n/a
south	92 230	+0.36	+0.4	381.3	n/a
total	798 380	+0.05	+0.5	370.6	n/a
CalCS total	1 492 391	-0.05 ± 0.20	-0.9 ± 3.6	363.5	n/a

in the offshore regions in three out of four seasons, it overestimates it in spring and fall in the nearshore region.

Furthermore, the Taylor diagrams in Fig. 3.3 reveal substantial regional and temporal differences in the magnitude of the bias in surface ocean pCO_2. The magnitude of over- and underestimation is on average largest in the nearshore 0–100 km with values ranging between -22 μatm for winter and 43 μatm for summer. Between 100 and 400 km offshore, the bias varies between -24 μatm in winter and 14 μatm in summer. Similarly in the 400–800 km offshore region, the biases range between -13 μatm for spring and 14 μatm for fall. In the annual mean, the model has a pCO_2 bias of 7 μatm in the nearshore subdomain, and biases of -6 and 4 μatm in the near- and far-offshore subdomains, respectively.

The comparison of our model to the ungridded pCO_2 data from CalCOFI Line 67 (Fig. 3.4), provides us with more detailed information about our model's performance in simulating the onshore–offshore gradient. In accordance with our results for the whole domain, the model mean pCO_2 of each season has a positive bias with respect to the mean observed pCO_2 in the first 100 km, where the model overestimates pCO_2 by up to 300 μatm (summer), but on average agrees very well with the data offshore of 100 km. For all four seasons, the maximum value of modeled pCO_2 peaks closer to the coast than the observed pCO_2, i.e. in the first 10–20 km,

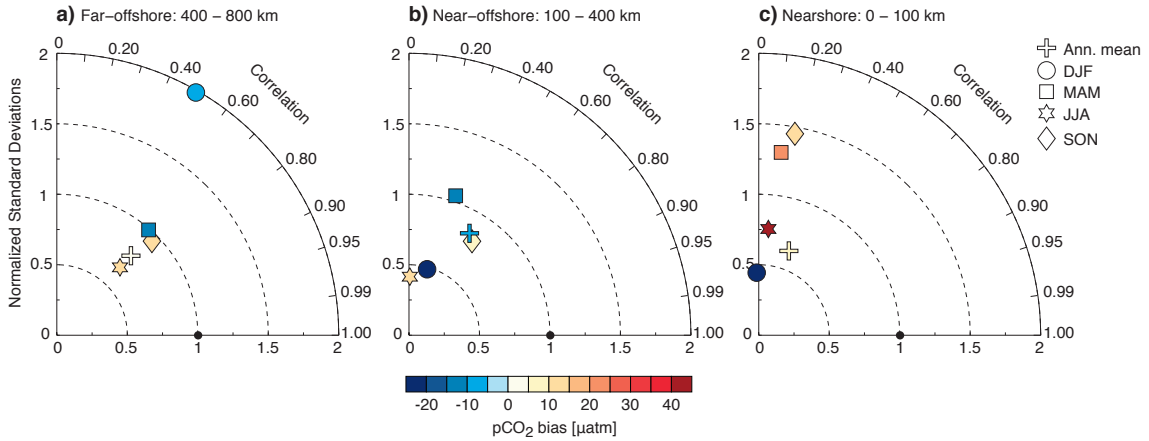

Figure 3.3 Taylor diagrams (Taylor, 2001) of modeled vs. observed pCO_2 for the far-offshore **(a)**, near-offshore **(b)** and nearshore **(c)** subdomains. Observations are from the Surface Ocean CO_2 Atlas (SOCAT Version 2; Pfeil et al., 2013), the global surface pCO_2 database (Takahashi et al., 2013) and the MBARI/CalCOFI Line 67 (Collins et al., 2003). The distance to the origin point (dashed lines) indicates the modeled field's normalized standard deviation (i.e. a value of 1 would mean a perfect agreement with the observed spatial variability). The angle between each model point and the vertical axis represents the spatial correlation coefficient ("Pearson correlation") for the model vs. the observations. The distance from the observation reference point (black dot) to the model point is that model field's central pattern root-mean square. The color code indicates the bias of the modeled vs. the observed pCO_2: positive values mean the model overestimates pCO_2 and vice versa.

and decreases with increasing distance to the coast. The observed pCO_2 reaches a maximum, on average, between 20 and 50 km offshore.

To further check the model's performance, we compared our modeled surface ocean pCO_2 to pCO_2 data predicted by the neural network model of Hales et al. (2012) (Table 3.3). As this data was pregridded at $0.25° \times 0.25°$, we regridded it to match our ROMS grid. Furthermore, we compared pCO_2 only for the 6 subdomains within 400 km of the coast, as the Hales et al. (2012) data extend only to about 370 km offshore. The results confirm that in the annual mean, our model consistently overestimates pCO_2 in the first 100 km, while between 100 and 400 km, the pCO_2 difference is almost negligible, with a slight underestimation by our model. This is consistent with our model evaluation with the SOCAT, LDEO and MBARI data for our whole analysis domain (Fig. 3.3). Over all of these six subdomains however, the model has a nearly negligible pCO_2 bias of -0.3 μatm compared to data from Hales et al. (2012) (not listed in Table 3.3).

In conclusion, our model has very good skills in modeling the domain-wide mean pCO_2 and captures the observed spatial and temporal variability of pCO_2 well. In particular, our regional model, although benefiting from the additional constraints provided by the lateral boundary conditions, tends to simulate the observed pCO_2 considerably better than any typical global-scale ocean biogeochemistry model, which often have domain-wide biases of several tens of μatm (e.g., Wanninkhof et al., 2013). However, the model consistently overestimates pCO_2 in the nearshore 100 km, which we verified with various independent databases. We believe this overestimation to be mainly due to deficiencies in our forcing: first, due to the relatively coarse resolution of

our wind forcing ($0.25° \times 0.25°$), the wind speed may be overestimated in the nearshore areas (Capet et al., 2004), which would favor more intense coastal upwelling and elevate nearshore pCO_2 levels. Second, our use of climatological forcing results in a nearly continuous upwelling along the coast, while, in reality, periods of intense upwelling are followed by relaxation periods, when ocean biology can reduce surface ocean pCO_2. Errors in our lateral boundary conditions, the model's too low levels of NPP and biases in the nutrient distributions may also help explain the nearshore pCO_2 biases.

3.4 Sources and sinks for atmospheric CO_2

We model the whole CalCS as a nearly balanced system with regard to atmospheric CO_2, annually taking up only about $-0.9\,\mathrm{Tg\,C\,yr^{-1}}$ over the analysis domain (0–800 km and $\sim$33–46°N). This corresponds to an average uptake flux density of $-0.05\,\mathrm{mol\,C\,m^{-2}\,yr^{-1}}$ (Table 3.3). This near zero flux hides the presence of strong regional sources and sinks (Figs. 3.1b, 3.5): the whole northern subdomain acts as a net sink of $-0.46\,\mathrm{mol\,C\,m^{-2}\,yr^{-1}}$ (Fig. 3.5a), while the central and southern subdomains are on average sources with flux densities of 0.04 and $0.16\,\mathrm{mol\,C\,m^{-2}\,yr^{-1}}$, respectively (Fig. 3.5b, c). In the offshore direction, the nearshore 100 km is the strongest source, losing CO_2 to the atmosphere with a flux density of $0.78\,\mathrm{mol\,C\,m^{-2}\,yr^{-1}}$ (Table 3.3). In contrast, the area between 100 and 400 km is the most important contributor to the overall sink with a flux density of $-0.47\,\mathrm{mol\,C\,m^{-2}\,yr^{-1}}$. Further offshore of 400 km, the surface ocean is nearly neutral in the annual mean, outgassing on average only $0.05\,\mathrm{mol\,C\,m^{-2}\,yr^{-1}}$. Of the individual subdomains, the central nearshore CalCS between Pt. Conception, California, and Cape Blanco, Oregon, is the strongest CO_2 source, with an average flux density of $1.11\,\mathrm{mol\,C\,m^{-2}\,yr^{-1}}$, whereas the central area between 100 and 400 km is one of the strongest sink areas with $-0.53\,\mathrm{mol\,C\,m^{-2}\,yr^{-1}}$.

In terms of seasonal variability, the strongest outgassing occurs in summer (during the upwelling season) in the nearshore central CalCS (Fig. 3.5b), while further offshore in summer outgassing is substantially reduced and there is even an uptake in fall. This pattern is also simulated in the northern area, but to a lesser degree (Fig. 3.5a). Nearly the whole analysis domain acts as a sink for CO_2 in winter and spring, except for the central and southern nearshore domains, which are sources from spring until fall (Fig. 3.5b, c).

We have not undertaken a systematic investigation of the uncertainties associated with our modeled pCO_2 and air–sea CO_2 fluxes. We did however run additional sensitivity simulations, where we varied either the boundary conditions or some of the model's parameters within their uncertainty to get an indication of the order of magnitude of this error. Altering the model's DIC boundary conditions by $\pm 10\,\mathrm{mmol\,C\,m^{-3}}$, which corresponds to the model's bias in surface DIC that we established in Sect. 3.3 by comparing to data from the Feely et al. (2008) cruise, resulted in a domain-wide pCO_2 change of approximately $\pm 5\,\mu$atm, with a corresponding air–sea CO_2

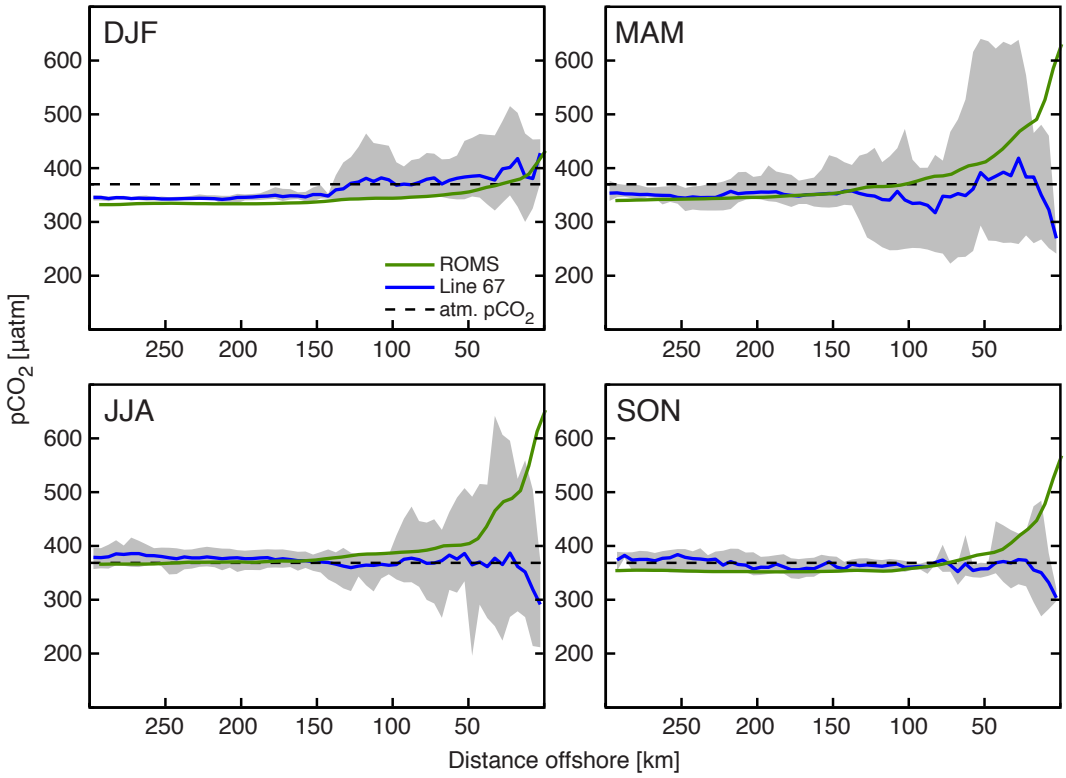

Figure 3.4 Seasonally averaged pCO_2 from our model (green line) and from MBARI/CalCOFI Line 67 (blue line) as a function of distance offshore. The gray shaded area represents the range of observed pCO_2 within each season. The dashed black line indicates our model's annual mean atmospheric pCO_2 of 370 μatm.

flux change of about $\pm 0.2\,\mathrm{mol\,C\,m^{-2}\,yr^{-1}}$. Changing the $CaCO_3$ production ratio from 0.07 to 0.03 and the use of the set of biological parameters of Gruber et al. (2011) instead of those of Gruber et al. (2006) resulted in domain-wide flux changes within the same uncertainty range. Thus, we estimate that the uncertainty associated with our modeled annual mean flux for the whole domain is at least $\pm 0.20\,\mathrm{mol\,C\,m^{-2}\,yr^{-1}}$, corresponding to an integrated flux uncertainty of $\pm 3.6\,\mathrm{Tg\,C\,yr^{-1}}$ (Table 3.3). This estimate does not include the effect of potential pCO_2 biases of our model, particularly those in the nearshore regions. The nearshore bias of around 10 μatm causes roughly an error in the CO_2 flux of $0.4\,\mathrm{mol\,C\,m^{-2}\,yr^{-1}}$. Thus, if we were to subtract this bias uniformly from our model simulated pCO_2, our net outgassing in the nearshore 100 km would be nearly halved to around $0.4\,\mathrm{mol\,C\,m^{-2}\,yr^{-1}}$. However, we do not apply such a correction given the substantial uncertainty associated with the determination of the model bias.

Our uncertainty estimate also does not include the potential impact of variable stoichiometric $C:N$ ratios for phytoplankton growth. Martiny et al. (2013) showed that these ratios may vary systematically, with oligotrophic gyres having larger than Redfield ratios and nutrient-replete systems having lower than Redfield ratios. While we do not expect a substantial effect of such systematic variations in the $C:N$ ratios on the overall budget of the CalCS, they will nevertheless quite certainly affect the local fluxes. We would expect a larger outgassing in the nearshore regions, as the tendency for lower than Redfield $C:N$ ratio in such nutrient replete systems would cause a lower carbon drawdown, permitting a larger fraction of the upwelled carbon to

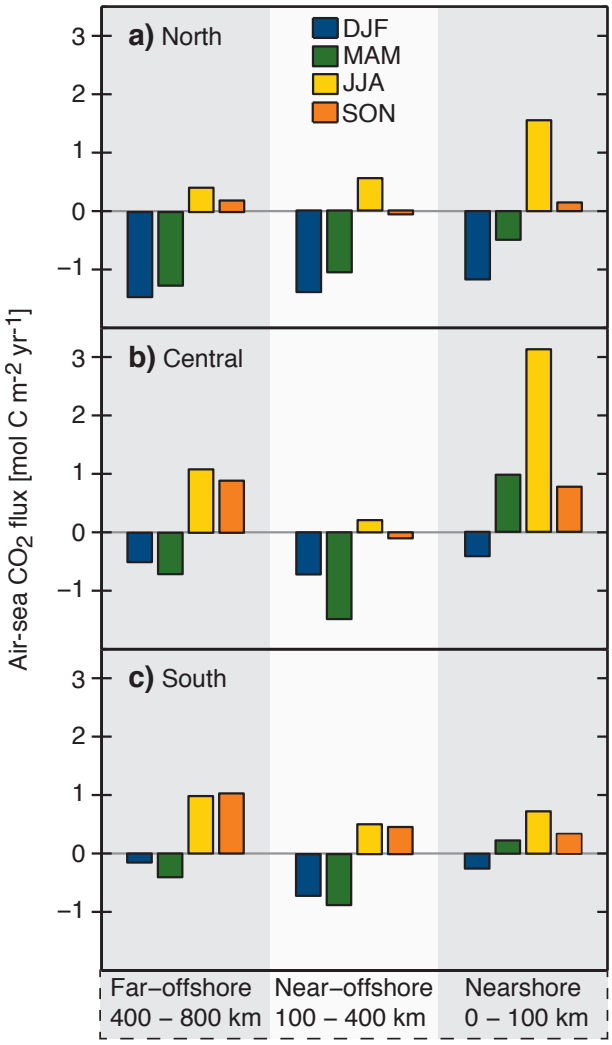

Figure 3.5 Seasonally averaged air–sea CO_2 flux for the northern **(a)**, central **(b)** and southern **(c)** subdomains in the nearshore, near-offshore and far-offshore regions. Positive values denote an outgassing of CO_2, negative values an uptake by the surface ocean.

escape to the atmosphere. In contrast, in the oligotrophic offshore regions, we would expect a stronger uptake of CO_2 from the atmosphere, as the higher than Redfield $C : N$ ratio would tend to lead to lower pCO_2. Overall, we would expect a stronger onshore–offshore gradient, but not a large change in the net flux over the entire study region. A more quantitative assessment of the effect of using a variable $C : N$ ratio would require a more detailed, separate analysis with additional sensitivity simulations.

Our domain's mean flux density of $-0.05 \pm 0.20\,\mathrm{mol\,C\,m^{-2}\,yr^{-1}}$ agrees best with the results of Chavez et al. (2007), who suggested the whole west coast of the US to act as a nearly balanced, small source of $0.03\,\mathrm{mol\,C\,m^{-2}\,yr^{-1}}$. However, the flux densities of the individual subdomains agree more with the findings of Evans et al. (2011), who showed that the Oregon coast (which is to the largest part included in our northern subdomain) acts as an annual net sink of $-0.3\,\mathrm{mol\,C\,m^{-2}\,yr^{-1}}$, and with the results of Pennington et al. (2010), who found that the central California region is nearly balanced. All of the subdomains experience a sign change in CO_2 fluxes during the course of a year, which is consistent with the findings of Hales et al. (2012).

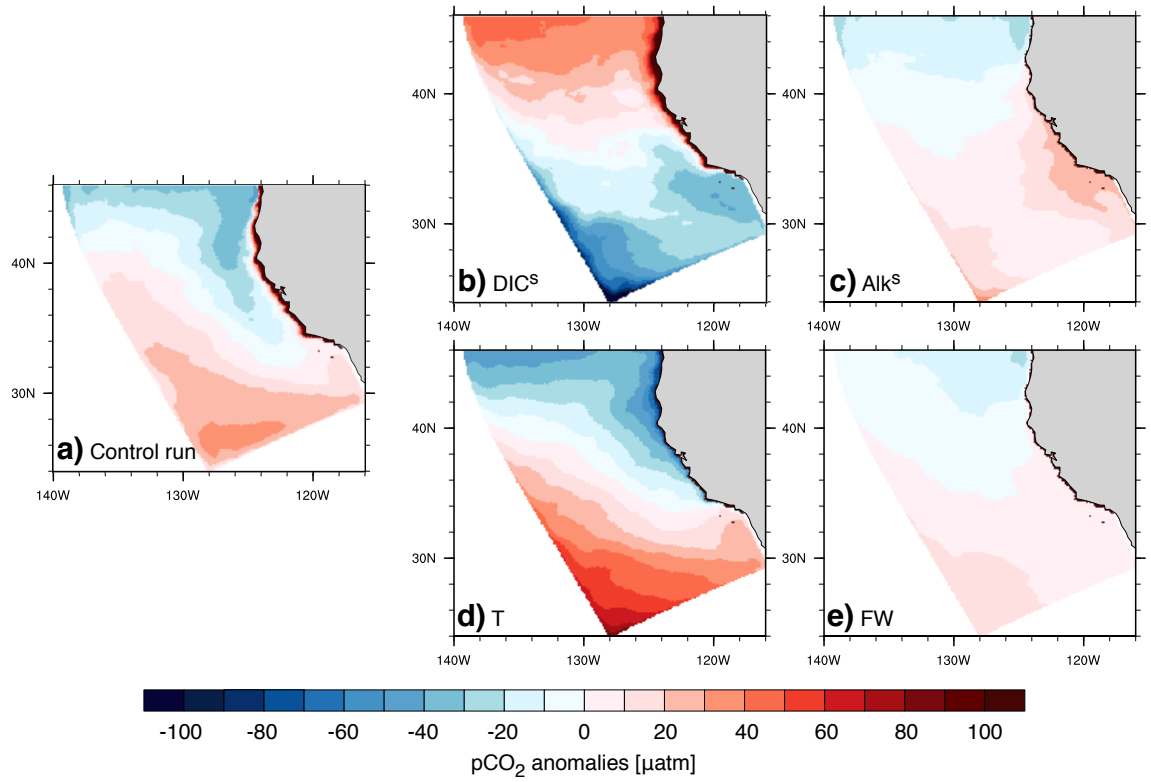

Figure 3.6 Spatial pCO_2 anomalies computed as the difference between in situ and domain mean pCO_2. Panel **(a)** shows total pCO_2 anomalies in the control simulation and panels **(b–e)** show the contributions of the four drivers DIC^s, Alk^s, T and FW to the total.

In order to compare our air–sea CO_2 fluxes more directly to Hales et al. (2012), we average our results over only the first 0–400 km. This yields an average uptake flux density of $-0.17\,\mathrm{mol\,C\,m^{-2}\,yr^{-1}}$, which is smaller than their result of $-0.66\,\mathrm{mol\,C\,m^{-2}\,yr^{-1}}$ over a similar region. However, given the sizable errors in the estimate by Hales et al. (2012) as well as ours, the two estimates are actually statistically indistinguishable. They both agree that the CalCS is essentially neutral with regard to atmospheric CO_2 or a small sink at best.

These comparisons demonstrate that while the net CO_2 flux over the entire CalCS is relatively small, the fluxes vary strongly in space and time, in accordance with findings from several of the previous studies (e.g., Hales et al., 2005; Chavez et al., 2007; Evans et al., 2011; Hales et al., 2012).

The air–sea CO_2 flux pattern is almost entirely driven by surface ocean pCO_2, which exhibits strong regional differences (Fig. 3.1a, Table 3.3). Compared to surface ocean pCO_2, variations in atmospheric pCO_2 are very small (e.g., Komhyr et al., 1985; Conway et al., 1994) and variations in the gas transfer velocity and in the CO_2 solubility are of secondary importance, as they only tend to modulate the magnitude of air–sea CO_2 fluxes without influencing their sign (Eq. 3.1).

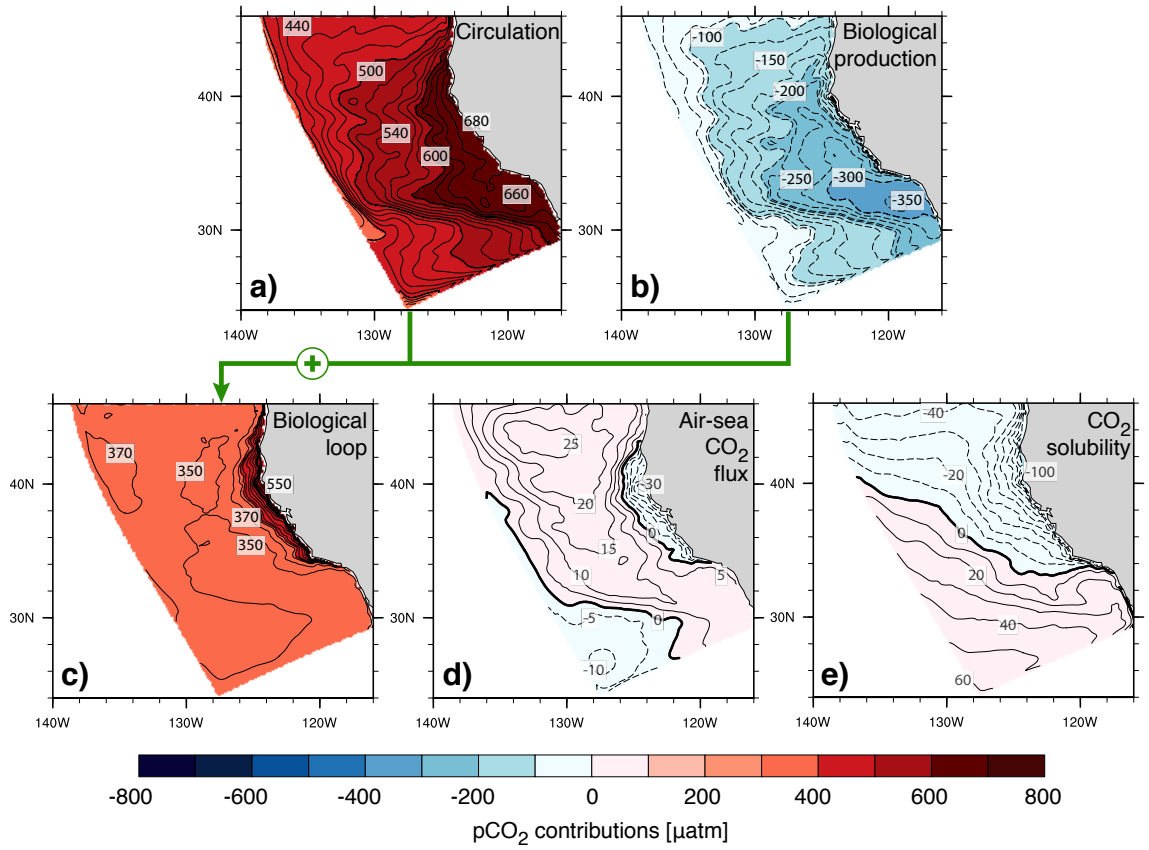

Figure 3.7 Contributions of ocean circulation **(a)**, biological production **(b)**, air–sea CO_2 flux **(d)** and CO_2 solubility **(e)** to annual mean pCO_2 as simulated in the control simulation. Panel **(c)** represents the contribution of the biological loop, i.e. the sum of **(a)** and **(b)** (indicated by the green line). Positive contributions are displayed as solid lines, negative contributions as dashed lines.

3.5 Spatial variability of annual mean pCO_2

To highlight the spatial variability of the annual mean surface ocean pCO_2, we subtract its domain average and consider spatial anomalies only (Fig. 3.6a). Two distinct features can be identified in Fig. 3.6a, which is very close to the pattern of the air–sea pCO_2 difference (not shown), given that the domain average pCO_2 differs little from atmospheric pCO_2: (i) large positive anomalies are found in the upwelling area along the coast of the central CalCS, and (ii) there is a division around 38°N between the northern part of the model domain, which tends to have negative anomalies, and the southern part with positive anomalies.

The analysis of the drivers behind this pattern reveals that this pattern is largely a result of strong spatial gradients in DIC^s and T (Fig. 3.6b, d), with Alk^s having a smaller role and FW fluxes being unimportant (Fig. 3.6c, e). The strong north–south gradients induced by DIC^s and T tend to cancel each other substantially, so that the largely unopposed onshore–offshore gradient of DIC^s becomes a prominent feature in the annual mean distribution of pCO_2. An exception to this general pattern is the Southern California Bight, where the contribution of Alk^s is important, tending to oppose the effect of DIC^s.

The identification of the processes underlying the spatial pattern in pCO_2 permits us to better understand what drives these gradients, in particular those of the key driver DIC^s (Fig. 3.7). This process-based separation based on the sensitivity studies (Table 3.2) reveals that the most important contributions to the spatial gradients of annual mean pCO_2 are circulation and biological production (Fig. 3.7a, b), both of which act upon DIC and Alk. Circulation, i.e. the transport of high DIC and Alk from the boundaries into the domain's interior and then to the surface, leads to high surface ocean pCO_2 values far exceeding atmospheric pCO_2 over most of the domain (Fig. 3.7a). The high DIC in the upwelled waters pushes surface pCO_2 up to values around 700 μatm in the upwelling area and between 400 and 600 μatm further offshore. In the central domain, high pCO_2 values extend particularly far offshore: values of 550 μatm can still be found around 400–500 km offshore. This large offshore extent is caused by the intense offshore Ekman and eddy-driven transport in the central CalCS (Nagai et al., 2014), which is not strongly opposed by the biological removal of DIC. The upwelled waters are also enriched in Alk, which acts to reduce the impact of the upwelling of DIC on surface ocean pCO_2, but this effect is substantially smaller (not shown).

The biological fixation of CO_2 and the subsequent transport of the fixed carbon to depth opposes the circulation effect and acts to decrease pCO_2 nearly everywhere by around 160 μatm on average (Fig. 3.7b). This biologically induced pCO_2 drawdown is generally largest in the nearshore region. Yet, unlike physical circulation, whose effects are largest in the upwelling area of the central CalCS and decrease with increasing distance to the coast, the biologically driven pCO_2 drawdown is highest between 50 and 100 km offshore in the central CalCS and extends farther offshore than the physical circulation-driven maximum. This results in the biological compensation of circulation effects being much weaker in the first 50 km nearshore region of the central CalCS in comparison to the rest of the domain. The spatial decoupling between the area of maximum upwelling and the region of maximum biological production has been documented in previous studies of the CalCS and was linked to the large upwelling-driven offshore fluxes of nutrients, which are not fully utilized in the coastal upwelling zone (Gruber et al., 2011; Lachkar and Gruber, 2011). The combined effect of circulation and biological production, which we will refer to here as the "biological loop", is hence largest in the first 50–100 km, with values of 500–650 μatm (Fig. 3.7c). Offshore of 100 km, the contribution of the biological loop is nearly homogeneous at around 350 μatm, i.e. below atmospheric CO_2.

In contrast to circulation and biology, the contribution by the air–sea CO_2 flux is comparatively small, contributing ± 30 μatm (Fig. 3.7d). This pattern is directly tied to the regions where the CalCS acts as a source or sink for atmospheric CO_2 (see Fig. 3.1b). The contribution by the processes affecting the solubility of CO_2 is somewhat larger, amounting to spatial gradients in pCO_2 of up to ± 50 μatm (Fig. 3.7e). This contribution very closely resembles that associated with the T driver (compare with Fig. 3.6d). This is because variations in T dominate the variations in the CO_2 solubility, while the contribution of FW is very small.

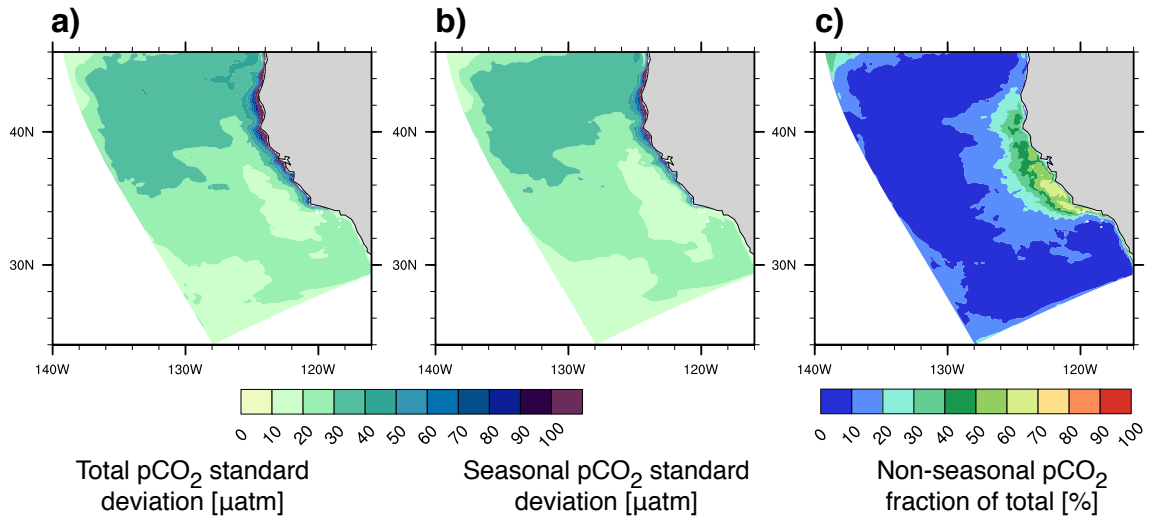

Figure 3.8 Total pCO_2 standard deviation **(a)** computed from 2–day output spanning seven consecutive model years, and seasonal pCO_2 standard deviation **(b)** derived from a fitted mean over the same seven years. Panel **(c)** shows the fraction of the total pCO_2 variance (square of the standard deviation) attributable to nonseasonal variability, i.e. the difference between total and seasonal pCO_2 variance divided by the total variance (shown in percent).

In summary, the net effect of circulation and biological productivity, i.e. the contribution of the biological loop, controls to a large extent the distribution of pCO_2, with small differences in the spatial pattern between these two opposing tendencies explaining much of the onshore–offshore gradient. This is because these small differences explain the spatial distribution of DIC^s, the most important driver for the spatial distribution of pCO_2. This also explains the very high pCO_2 values found in the 50 km wide coastal strip in the central CalCS as well as the rapid decrease of pCO_2 with increasing distance to the coast in that region (see Fig. 3.1a). The processes affecting solubility, i.e. primarily surface ocean T, explain most of the north–south gradient in surface ocean pCO_2, since the combined effect of circulation and biology shows nearly no spatial gradient in the offshore regions, and the air–sea CO_2 flux is largely unimportant.

As pCO_2 and the air–sea CO_2 fluxes vary not only on a spatial scale but show also high temporal variability, we next investigate the drivers and processes behind the seasonal and nonseasonal components of pCO_2 variability.

3.6 Temporal pCO_2 variability

3.6.1 Seasonal variability

Surface ocean pCO_2 in the CalCS varies substantially in time with a standard deviation of up to $\pm 100\,\mu$atm in the nearshore 0–100 km (Fig. 3.8a). The standard deviation tapers off quite quickly with increasing offshore distance with typical values of about 10–40 μatm in the regions further offshore. A good part of this variability is driven by the seasonal cycle (Fig. 3.8b), especially in

the offshore region, where it accounts for almost all of the variability.

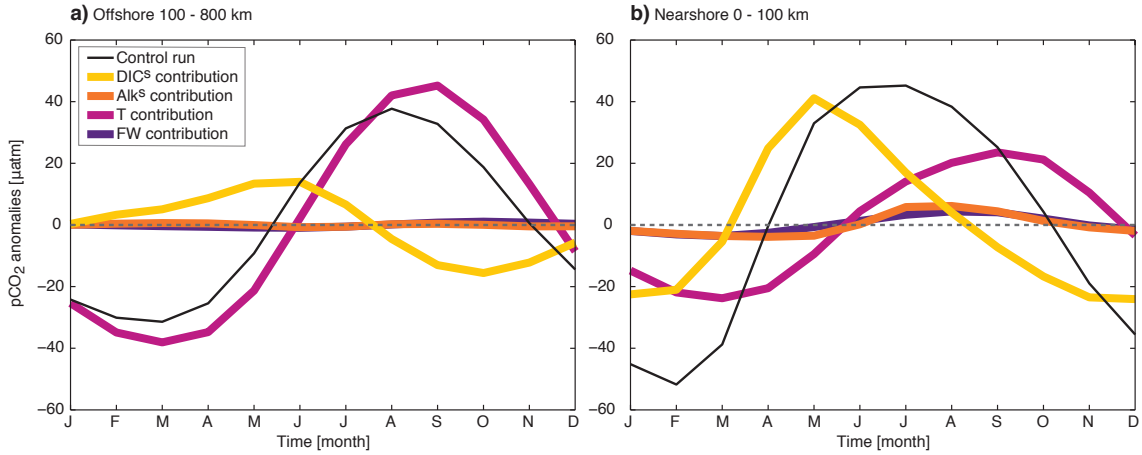

Figure 3.9 Monthly mean pCO_2 anomalies for the offshore **(a)** and the nearshore **(b)** domains: the colored lines represent the contributions of the four drivers DIC^s, Alk^s, T and FW to monthly mean pCO_2 anomalies from the control simulation (black line).

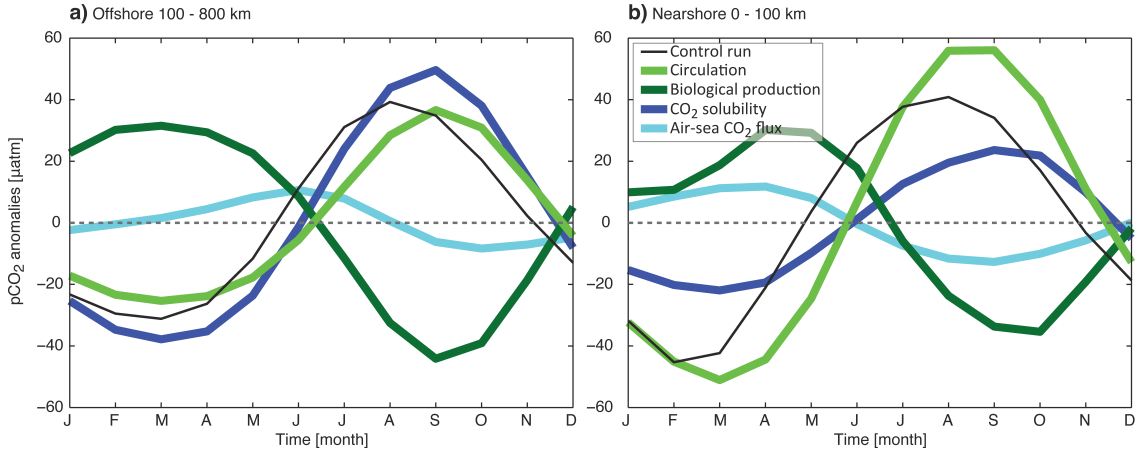

Figure 3.10 Monthly mean pCO_2 anomalies for the offshore **(a)** and the nearshore **(b)** domains: the colored lines represent the contributions of ocean circulation, biological production, CO_2 solubility and air–sea CO_2 flux to monthly mean pCO_2 anomalies from the control simulation (black line).

To investigate the seasonality of surface ocean pCO_2, we subtract the annual mean pCO_2 from the simulated monthly climatology and consider pCO_2 seasonal anomalies and their drivers following the same approach used for studying the spatial pattern. To capture the contrasting features of pCO_2 seasonality between the coastal and open ocean regions, we analyze nearshore-averaged (less than 100 km offshore) and offshore-averaged temporal anomalies separately. In both the nearshore and offshore regions, positive anomalies of pCO_2 prevail during summer and early fall whereas negative anomalies are observed during the winter and in early spring (black lines in Figs. 3.9 and 3.10).

The decomposition of the pCO_2 seasonal anomalies into individual contributions associated with changes in DIC^s, Alk^s, T and FW (Fig. 3.9) shows that the seasonal variability of pCO_2 in the two regions is driven by distinctly different combinations, whose relative contributions to the

seasonal cycle are similar to the contributions discussed for the spatial pattern. In the offshore region, the seasonal cycle is to a very large extent caused by the seasonality of T, i.e. by the seasonal cycle of warming and cooling (Fig. 3.9a). The pCO_2 variations driven by DIC^s tend to have an opposing seasonal cycle, thereby flattening the simulated pCO_2 relative to that purely driven by T. In contrast, the pCO_2 seasonality in the nearshore region is caused by variations in both T and DIC^s – and to a lesser degree variations in Alk^s and in the FW fluxes (Fig. 3.9b). Here, the DIC^s-driven variations are about four months out of phase with those of T, causing primarily a phase shift of the pCO_2 seasonality relative to the purely T-driven seasonal cycle. The seasonal cycle of the Alk^s-driven component is characterized by higher modes, i.e. further modifying the modeled seasonal cycle of pCO_2.

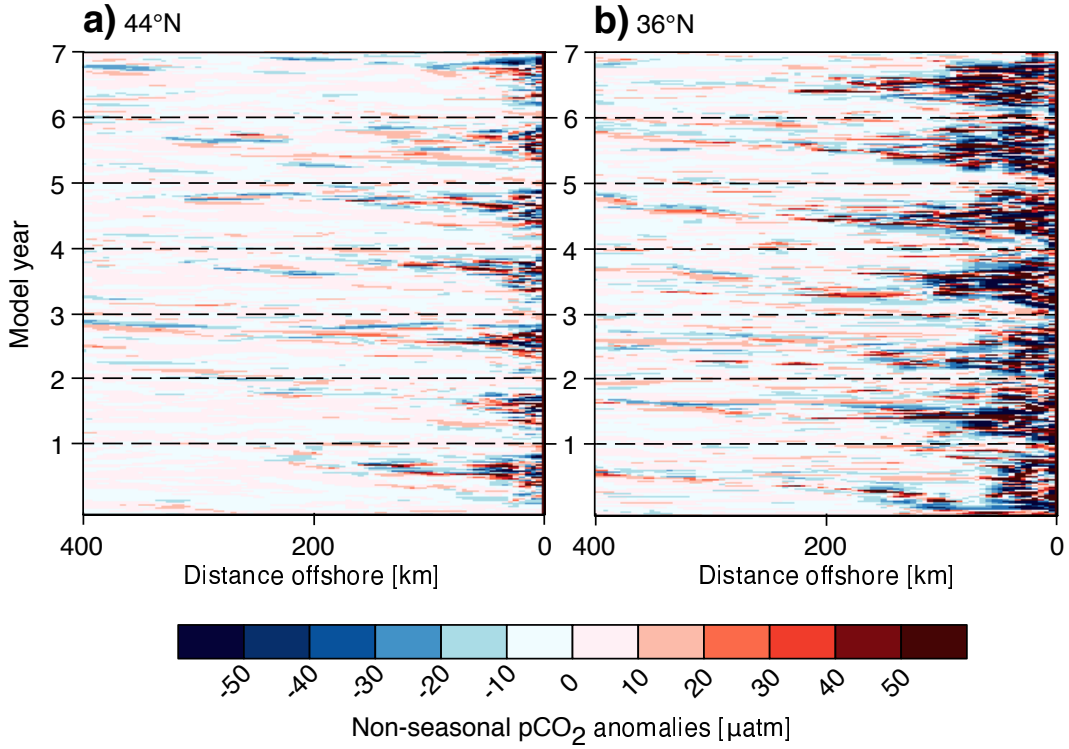

Figure 3.11 Hovmöller diagrams representing nonseasonal pCO_2 anomalies as a function of distance offshore, based on 2–day output spanning seven consecutive model years. The anomalies were computed as the difference between the total pCO_2 over the seven analysis years and a seasonal fitted mean over the same seven years. Panel **(a)** shows a transect at around 44°N, while panel **(b)** depicts a transect at around 36°N. The transects run roughly along the midlines of the northern and central subdomains, respectively.

As was the case for the spatial distribution of pCO_2, we can gain further insight into the working of the seasonal cycle of pCO_2 by analyzing the processes behind it, i.e. by determining the contributions of the air–sea CO_2 flux, ocean biology, CO_2 solubility, and ocean circulation.

In the offshore domain, the processes controlling CO_2 solubility contribute most to the seasonal pCO_2 variability (Fig. 3.10a). In this region, the contributions of circulation and biology tend to nearly perfectly balance each other, whereas the air–sea CO_2 flux acts to slightly reduce the overall amplitude of the pCO_2 seasonal cycle. In contrast, in the nearshore region, circula-

tion, i.e. essentially upwelling, is the most important driver of pCO_2 seasonality (Fig. 3.10b). Biological production tends to counteract the circulation effect particularly in spring and early summer. Yet, this biological compensation is only partial, especially during winter when biology has little effect on pCO_2. The seasonal variations in CO_2 solubility also play an important role in the nearshore region, but are less prominent than in the offshore region. Finally, similarly to its role in the offshore region, the air–sea CO_2 flux acts throughout the year to dampen the seasonal cycle of pCO_2.

In conclusion, the simulated seasonality of pCO_2 emerges from the degree of compensation between the solubility-driven pCO_2 variations associated with the seasonal cooling and heating of the surface waters as well as the combined circulation- and biology-driven variations affecting surface ocean DIC^s and hence pCO_2. In the offshore region, the solubility-driven variations clearly dominate, while circulation/biology can only dampen the seasonality somewhat. In the nearshore regions, the circulation/biology-driven variations are of nearly the same amplitude, but out of phase, leading to a complex seasonal cycle in pCO_2.

3.6.2 Mesoscale variability

Figure 3.8 highlights that although the seasonal component accounts for most of the total pCO_2 variability in the offshore regions, a substantial fraction of the total variability in the nearshore regions is driven by the nonseasonal component (Fig. 3.8c, shown in percent). Our model results demonstrate that the nonseasonal component is the dominant variability mode in the first 100–200 km offshore of the central CalCS, explaining up to 70 % of the total pCO_2 variability (Fig. 3.8c). Most of this variability is driven by mesoscale activity, which is more intense in the upwelling regions due to stronger baroclinic instabilities. To further investigate the eddy-driven component of our modeled pCO_2 variability, we analyze the nonseasonal pCO_2 component as a function of time and offshore distance (Fig. 3.11): a comparison of the northern and central offshore transects confirms that the activity attributable to mesoscale and nonseasonal processes is much more prominent in the central area (Fig. 3.11b), which displays year-round strong eddy activity often reaching out up to 200 km offshore, whereas in the north (Fig. 3.11a) the eddy activity is detectable only on a seasonal timescale, starting in late summer or early fall. In general, for both domains, strong offshore transport occurs most frequently around the middle of the year. We do not show any transects for the southern subdomain, as any activity attributable to mesoscale eddies was negligible there compared to the other two subdomains.

This high variability associated with eddy activity, which is especially pronounced in the nearshore area, leads to relatively short temporal and spatial decorrelation scales, requiring relatively dense sampling in time and space in order to fully capture the true pCO_2 signal. In the open ocean, Jones et al. (2012) showed that pCO_2 can be correlated over distances of several hundred kilometers, but pointed out that these scales are much shorter in the coastal ocean, perhaps as

short as a few tens of kilometers in space and from a few days to weeks in time.

Without a full Observing System Simulation Experiment, we are not in the position to make accurate recommendations with regard to how the current network would have to be expanded to capture the mean flux and its variability with good confidence. Nevertheless, we can make some qualitative, general statements, based on our model-based experience. First, the presently available observations are likely sufficient to estimate the domain-wide climatological annual mean air–sea CO_2 flux, as indicated by the relatively good agreement between the most recent estimates. Second, the current network is with good confidence insufficient to determine variability in time and space around this mean flux. In order to achieve this, the network would mainly need to be expanded in the first 100 km, where the short temporal and spatial decorrelation length scales require a denser coverage of pCO_2 and air–sea CO_2 flux measurements. It would furthermore be highly desirable to have a more complete latitudinal coverage of the nearshore area of the entire west coast of the US, whose current observational coverage is at best fragmentary. To this end, alongshore underway cruises, rather than moored stations, may provide the most adequate means of measuring pCO_2 within this extended area of interest.

Given that our model is forced with monthly climatologies at the surface and at the lateral boundaries, the fraction of nonseasonal variability is likely underestimated in our simulations. This is because neither long-term variability such as interannual or -decadal variability nor very high frequency variability associated with weather systems are included in our forcing. Submesoscale processes like filaments and fronts, which cannot be properly resolved at our model resolution, may further lead to an underestimation of the level of nonseasonal pCO_2 variability in our model. We thus refer to a future study for a more detailed assessment of the required sampling density in order to fully capture the true variability of pCO_2 and the associated air–sea CO_2 fluxes.

3.7 Discussion

Several questions emerge from our finding that the strong sources and sinks within the CalCS sum up to a nearly balanced system overall with regard to atmospheric CO_2. First, does this near complete spatial compensation occur by chance, or are there some underlying mechanisms at play? Second, if such underlying mechanisms exist, how might they control the air–sea CO_2 balance under future climate change? Third, what is the contribution of the oceanic uptake of anthropogenic CO_2 to the overall source/sink balance? Fourth, how do the air–sea CO_2 fluxes within the CalCS compare to fluxes elsewhere, and in particular, how do these results fit into the global picture?

Our analysis of the mechanisms underlying the annual mean air–sea CO_2 fluxes reveals that the near complete spatial compensation is a result of ocean productivity very closely compensat-

ing the effect of ocean circulation on the air–sea CO_2 flux. This compensation is not fortuitous, as these two processes are fundamentally linked to each other. This is because they represent the two components of the biological loop, i.e. the downward component, which is usually referred to as the biological pump (Volk and Hoffert, 1985) and is largely caused by the downward export of organic matter, and the upward component driven by the upward mixing and transport of the DIC- and Alk-rich deeper waters to the surface (Gruber and Sarmiento, 2002; Sarmiento and Gruber, 2006). As the upward component tends to control also the supply of the limiting nutrient to the near surface ocean, and hence also determines to a large degree the magnitude of biological productivity, the upward and downward components of the biological loop are strongly coupled with each other. The efficiency of the biological pump, i.e. the efficiency with which the upward supplied limiting nutrient is biologically taken up and exported downward again, is a good indicator of the strength of this linkage (Sarmiento and Gruber, 2006). In the CalCS, where nitrate tends to be the limiting nutrient (Eppley and Peterson, 1979), the nitrate use efficiency turns out to be very high, as evidenced by the near complete consumption of nitrate in the offshore region. This implies also a very high efficiency of the biological pump, and hence a tendency for an overall near complete compensation between the effects of biology and circulation. This does not occur regionally: in the very nearshore, the nutrient use efficiency is relatively low, allowing a part of the upwelled DIC to escape into the atmosphere. However, as these waters "age" while they are being transported further offshore, the biological pump operates so efficiently that all nitrate is fully utilized, creating the conditions for some of the escaped CO_2 to be taken up again by the surface ocean (e.g., Hales et al., 2005; Feely et al., 2008; Pennington et al., 2010; Fassbender et al., 2011).

These arguments depend, of course, critically on the near constancy of the stoichiometric $C : N$ ratio of phytoplankton growth. Any carbon over- or underconsumption relative to our assumed Redfield ratio of $106 : 16$ would permit the biologically driven component of the air–sea CO_2 fluxes to decouple from the efficiency of the biological pump. But as we argued above, we expect the potentially systematic tendencies of this ratio to have a relatively small effect on the whole domain air–sea CO_2 fluxes. While the nearshore carbon underconsumption makes the biological pump less efficient there, the tendency for carbon overconsumption in the offshore, which enhances the efficiency, may largely compensate for it, resulting in little overall change. This is rather speculative, and a more thorough assessment of the effect of systematic variations in the stoichiometric ratios on the air–sea CO_2 fluxes is clearly needed. But our current understanding of the underlying processes controlling these ratios is poor, preventing us from following this path.

Regardless of the uncertainty arising from the stoichiometric ratios, the efficiency of the biological pump might change in the future under climate change-driven perturbations such as upwelling-favorable wind intensification and increased stratification. For example, Lachkar and Gruber (2013) show that increasing upwelling-favorable winds results in a decrease in the biological pump efficiency, and hence an increase in the CO_2 outgassing. This is because the large

increase in outgassing associated with the upwelling intensification outweighs the effects of the concurrent increase in productivity on surface $p\mathrm{CO}_2$.

It is important to recognize that the anthropogenic perturbation of atmospheric CO_2 has perturbed the air–sea CO_2 fluxes in the CalCS. By comparing our simulations to one where we had set atmospheric CO_2 to a preindustrial value of 280 μatm (Gruber et al., 2012; Hauri et al., 2013b), we estimate the domain mean uptake flux of anthropogenic CO_2 in the CalCS to be about $-1\,\mathrm{mol\,C\,m^{-2}\,yr^{-1}}$, which is about twice as large as the global mean (e.g., Mikaloff Fletcher et al., 2006; Gruber et al., 2009; Wanninkhof et al., 2013). This is not unexpected given that upwelling regions tend to be places of stronger than normal uptake of anthropogenic CO_2 from the atmosphere, largely as a consequence of them transporting waters to the surface that have not seen the atmosphere for some time. This substantial uptake flux of anthropogenic CO_2 implies that the entire CalCS in preindustrial times was a small to moderate net source of CO_2 to the atmosphere.

The different processes controlling surface ocean $p\mathrm{CO}_2$ operate in the CalCS in a manner that is similar to how they impact surface ocean $p\mathrm{CO}_2$ on the global scale, as also there the interaction of ocean circulation and biology is a primary determinant of the spatial distribution of the air–sea CO_2 fluxes (e.g., Gruber and Sarmiento, 2002; Toggweiler et al., 2003; Sarmiento and Gruber, 2006; Gruber et al., 2009). Globally, circulation in the absence of biology tends to increase $p\mathrm{CO}_2$ everywhere, with the efficiency of the biological pump ultimately determining how strong the opposing effect of biology ends up being, i.e. whether a particular region becomes a source or a sink of CO_2, with regard to the biological loop. In the CalCS, the high degree of nutrient utilization and the implied high efficiency of the biological pump suggests that this region operates more like the temperate to subpolar North Atlantic, where the biologically induced fluxes are overall small, and very unlike the North Pacific, where a low nutrient utilization leads to a substantial net outgassing of CO_2 associated with the biological loop (Gruber et al., 2009). We expect also the Canary Current System to operate very similarly to the CalCS given the observed complete nutrient utilization there. In contrast, we expect the Humboldt Current System, where nitrate is often not very efficiently used due to iron limitation, to have a strong net outgassing caused by the inefficient biological pump.

3.8 Summary and outlook

We used a series of eddy-resolving simulations of the CalCS (i) to assess the climatological mean air–sea CO_2 fluxes and their spatiotemporal variability and (ii) to determine the drivers and processes behind the variability of these fluxes and ultimately surface ocean $p\mathrm{CO}_2$.

Our model results demonstrate that the CalCS is essentially balanced in terms of air–sea CO_2 fluxes, with a very small net uptake flux density of $-0.05 \pm 0.20\,\mathrm{mol\,C\,m^{-2}\,yr^{-1}}$. The fluxes

vary strongly locally and on a seasonal timescale, with the nearshore 100 km losing a substantial amount of CO_2 to the atmosphere, which is largely compensated by biologically driven uptake in the regions offshore of 100 km. We interpret this strong spatial compensation to be the result of a highly efficient biological pump, as indicated by the complete utilization of the upwelled limiting nutrient, nitrate. The CalCS acts also as a substantial sink for anthropogenic CO_2, taking up approximately $-1\,\mathrm{mol\,C\,m^{-2}\,yr^{-1}}$, implying that the CalCS was a weak source of CO_2 to the atmosphere in preindustrial times.

Nearly all of the variability in air–sea CO_2 fluxes is caused by surface ocean pCO_2, whose seasonal variability dominates over most of the offshore areas, while in the nearshore 100 km most of the variability is determined by subseasonal, mesoscale activity. The variability in the nearshore is mostly associated with circulation and biological production, which affect DIC, Alk and T, while air–sea CO_2 fluxes, CO_2 solubility and FW fluxes play a minor role. However, offshore of 100 km, changes in T are the most important drivers of pCO_2 variability.

One of the main caveats of our model study is that we neither include high frequency forcing associated with weather-related events, nor longer-term interannual variability. We aim to address this issue in a future study by adding such forcing to our model. We also plan to include an analysis of spatial and temporal decorrelation length scales in order to assess the required sampling density for accurately determining the source/sink nature of the CalCS.

Although we made through our model-based study substantial progress in determining the source/sink nature of the CalCS and the mechanisms underlying it, it would be highly desirable to verify this with observations. Clearly, the current network is largely inadequate for this purpose, and would have to be substantially strengthened. Furthermore, accurate quantification of the net air–sea CO_2 fluxes in the CalCS is also becoming increasingly important in the context of CO_2 inversion studies that aim to verify the emissions of anthropogenic CO_2 in California through measurements of atmospheric CO_2. This is because the large and highly variable air–sea CO_2 fluxes leave a substantial imprint on atmospheric CO_2, which has to be well quantified before the emissions can be inferred. Together with the observations, the models need to be further developed and refined, as they permit us to put the observations into a spatiotemporal context, and help assess the relevant processes.

Acknowledgements This research was financially supported by the Swiss Federal Institute of Technology Zürich (ETH Zürich) and through EU FP7 project CARBOCHANGE – Changes in carbon uptake and emissions by oceans in a changing climate – which received funding from the European Commission's Seventh Framework Programme under grant agreement no. 264879. All simulations were performed at the central computing cluster of ETH Zürich, Brutus. We are grateful to the ROMS and NPZD developers in general, and thank in particular M. Münnich, D. Loher and L. Kropuenske-Artman from ETH Zürich for their invaluable help and support, and

G.-K. Plattner for some of the initial analyses. We also thank B. Hales for kindly providing us with his $p\mathrm{CO}_2$ data, F. P. Chavez for sharing $p\mathrm{CO}_2$ measurements from the MBARI/CalCOFI Line 67, R. A. Feely for granting us access to his cruise database (doi:10.3334/CDIAC/otg.CLIVAR_NACP_West_Coast_Cruise_2007) and the SOCAT and LDEO teams for making their global $f\mathrm{CO}_2$ and $p\mathrm{CO}_2$ data sets available to us. The authors are also grateful to two anonymous referees for their valuable comments and suggestions, which have helped improve the quality and clarity of this manuscript.

Edited by: L. Cotrim da Cunha

Chapter 4

Recent climatic changes enhance ongoing ocean acidification in the California Current System

G. Turi, Z. Lachkar, M. Münnich, N. Gruber, and D. Loher

Environmental Physics, Institute of Biogeochemistry and Pollutant Dynamics, ETH Zürich, Zürich, Switzerland

This manuscript is in preparation.

Abstract

Using a set of eddy-resolving hindcast simulations, we quantify the progression of ocean acidification in the California Current System (CalCS) from 1979 to 2012 and determine the climatic drivers behind recent regional changes in $p\mathrm{CO}_2$, pH and the aragonite saturation state (Ω_{arag}). Overall, we model a domain-wide increase in $p\mathrm{CO}_2$ and concurrent decreases in pH and in the saturation state of aragonite (Ω_{arag}), which can be directly attributed to the rise in atmospheric CO_2 over the last three decades. Furthermore, we model a shoaling of the aragonite saturation horizon to depths shallower than 200 m and an expansion of the fraction of undersaturated water in the top 400 m of the water column, with the layer between 200 to 400 m becoming on average completely undersaturated with respect to aragonite during the last eight years of the simulation. Modifications to the spatial pattern of purely atmospheric CO_2-driven ocean acidification are particularly evident in the nearshore 0–100 km around Cape Mendocino, California ($\sim$39-43°N), where an intensification of wind-driven upwelling has lead to a significant increase in $p\mathrm{CO}_2$ of up to 100 μatm and decreases in pH and Ω_{arag} of up to –0.08 and –0.5 over the 34 years, respectively. These wind-driven modifications account for roughly one third of the total trends in $p\mathrm{CO}_2$ and pH and up to half of the trend in Ω_{arag} for the nearshore region between San Francisco Bay and the USA/Canada border. Further offshore of 100 km, an increase in biological productivity and a decrease in sea surface temperature have dampened the signal in ocean acidification, leading to a slightly reduced increase in $p\mathrm{CO}_2$ and reduced decrease in pH and Ω_{arag}. Due to the brevity of the simulation, it remains a matter of debate whether the nearshore increase in upwelling-favorable winds is due to natural, interannual to decadal fluctuations in the climatic forcing of the CalCS or whether it is mainly driven by an intensification of the thermal land-sea gradient due to climate warming.

4.1 Introduction

The California Current System (CalCS) has recently been the subject of several studies investigating the progression of ocean acidification and its implications for this region (e.g., Feely et al., 2008, 2009; Hauri et al., 2009; Gruber et al., 2012; Hauri et al., 2013b,a; Leinweber and Gruber, 2013; Lachkar, 2014; Bednarsek et al., 2014). It has been suggested that the main driver for the recent intensification of ocean acidification is the observed increase in atmospheric CO_2 over the last decades (e.g., Feely et al., 2008; Gruber et al., 2012), which directly impacts oceanic pCO_2, and hence pH and the saturation state of aragonite (Ω_{arag}), through the air–sea CO_2 gas exchange. It is however unclear whether this observed rise in CO_2 can explain all of the ongoing and projected ocean acidification in the CalCS or whether other recent perturbations in the climatic forcing of the CalCS play a crucial role as well. In this study, we use a set of eddy-resolving hindcast simulations of the US West Coast on the basis of the Regional Oceanic Modeling System (ROMS) to show that recent changes in the physical climatic forcing of the CalCS have led to regionally significant modifications of purely CO_2-driven ocean acidification from 1979 to 2012.

During a cruise in May and June 2007 in the CalCS, Feely et al. (2008) observed an increase in the spatial extent of surface waters undersaturated with respect to aragonite ($\Omega_{arag} < 1$), and that in some coastal regions undersaturated waters even shoaled into the top 20 m of the water column. Although coastal upwelling regions such as the CalCS are accustomed to extreme fluctuations in pCO_2, pH and Ω_{arag} due to the seasonality and episodicity of wind-driven upwelling (e.g., Feely et al., 2008; Hauri et al., 2009), it is very likely that these regions will become exposed to more frequent, prolonged and intense events of this nature in the near future (Gruber et al., 2012; Hauri et al., 2013b,a). Variations in oceanic pCO_2 and thus pH and Ω_{arag} are also influenced from the oceanic side by changes in sea surface temperature (SST), dissolved inorganic carbon (DIC), alkalinity (Alk) and to a lesser extent by variations in salinity (Turi et al., 2014a). Hence changes in these driving variables due to changes in biological productivity, circulation, wind-driven upwelling or surface ocean warming, could have an additional impact on the carbonate chemistry by either enhancing or dampening any trends that arise solely from the rise in atmospheric CO_2.

Recent in situ- and satellite-based studies have demonstrated that upwelling-favorable winds have indeed increased in the CalCS in the last decades (e.g., Bakun, 1990; Schwing and Mendelssohn, 1997; Mendelssohn and Schwing, 2002; Demarcq, 2009; García-Reyes and Largier, 2010; Narayan et al., 2010; Seo et al., 2012). This intensification of wind-driven upwelling has been suggested by Bakun (1990) to be linked to an increase in the thermal land-sea gradient driven by global surface warming, and is hence expected to continue in the future (e.g., Snyder et al., 2003; Diffenbaugh et al., 2004). The effect of increased upwelling-favorable winds on the biogeochemistry of the CalCS has been investigated by Lachkar and Gruber (2013) and Lachkar (2014) using a series of modeling sensitivity studies.

A doubling of alongshore wind stress was found to lead to an overall increase in net primary production (NPP) (Lachkar and Gruber, 2013), and to a tripling of the volume of water undersaturated with respect to Ω_{arag} (Lachkar, 2014). A modeling study by Chhak and Di Lorenzo (2007) supports the results of Lachkar and Gruber (2013), by demonstrating that an increase in the depth of wind-induced upwelling in the CalCS leads to a stronger supply of nutrients to the surface waters and hence stimulates biological productivity. Indeed, satellite observations have revealed significant increases in chlorophyll concentrations and primary production in the CalCS since the end of the 1990's (Kahru et al., 2009, 2012). However, it is not clear what the primary driving mechanisms for these increases are. Several studies indicate that surface ocean warming, and the associated increase in stratification, have led to a decrease in the supply of nutrients to the surface ocean due to a hindering of vertical mixing, hence resulting in a decrease in NPP (e.g., McGowan et al., 2003; Palacios et al., 2004). There remains some uncertainty about the counteracting effect of the increase in upwelling-driven cooling of surface waters on the overall observed increase in SST due to global surface warming and the implications for the biogeochemistry of the CalCS. Using a modeling sensitivity study combined with in situ measurements of SST and salinity, Di Lorenzo et al. (2005) proposed that from 1949 to 2000, the increase in SST due to surface warming in the southern CalCS was the dominant effect, which lead also to a deepening of the thermocline and increased stratification. These combined effects were found to reduce the efficiency of coastal upwelling in supplying nutrients to the surface and could hence serve as a possible explanation for a decline in zooplankton which had been observed from 1951 to the early 1990's (Roemmich and McGowan, 1995). For the period of 1998–2007, Demarcq (2009) demonstrated that there was a significant relationship between the increase in equatorward wind and phytoplankton biomass, whereas changes in SST were not significantly correlated to changes in biomass due to a masking from the continuous surface ocean warming. This makes it difficult to use SST trends as an indicator of changes in upwelling intensity in the light of continuous warming.

The many and often contradictory studies on recent trends and their driving mechanisms in the CalCS all vary in their temporal and geographical setting so that gaining a holistic view is challenging. So far, none of these studies have investigated the relative importance of the increase in atmospheric CO_2 versus changes in other climatic forcing on ongoing ocean acidification in the CalCS. Gruber et al. (2012), Hauri et al. (2013b) and Hauri et al. (2013a) ran their future simulations under increasing atmospheric CO_2, but assuming present-day climatic forcing for the whole simulation period. We expand on these previous studies by providing a spatially and temporally synoptic view of the recent progression of ocean acidification in the CalCS over the last three decades (1979–2012) and tease out its individual drivers. We propose that the main mechanism behind the non-homogeneous spatial pattern of ocean acidification trends is an increase in coastal wind-driven upwelling in the first 100 km, which accelerates the increase in oceanic pCO_2 and the decrease in pH and Ω_{arag}.

4.2 Model and methods

4.2.1 Model details and simulations

In this study, we use an eddy-resolving coupled physical-biogeochemical oceanic model on the basis of ROMS to simulate the CalCS from 1979 to 2012. The model has an average horizontal grid spacing of 5 km and 32 depth levels (σ-levels), covering roughly 30–50°N and extending $\sim$1250 km offshore (Turi et al., 2014a). The physical model is based on the UCLA-ETH version of ROMS (Marchesiello et al., 2003; Shchepetkin and McWilliams, 2005). Coupled to the physical model is a nitrogen-based nutrient-phytoplankton-zooplankton-detritus (NPZD) model, with single phytoplankton and zooplankton groups and two detrital pools with different sinking speeds. For a more comprehensive description of the NPZD model, the reader is referred to Gruber et al. (2006). The model setup and ecological parameters are the same as used in Turi et al. (2014a).

An interactive carbon module was added to the biogeochemical model, introducing three state variables: dissolved inorganic carbon (DIC), alkalinity (Alk) and calcium carbonate ($CaCO_3$). The organic carbon cycle is linked to the organic nitrogen cycle via a fixed stoichiometric C:N ratio of 106:16 (Redfield et al., 1963). A discussion of the limitations of using a fixed C:N ratio is included in Turi et al. (2014a) and a more detailed description of the implementation of the relevant carbon variables can be found in Turi et al. (2014a) and Hauri et al. (2013b).

The model spinup is started from rest, i.e., without any initial momentum, and spun up for 10 years, corresponding to the time period 1969–1978, with varying atmospheric CO_2 and lateral DIC boundary conditions. The other lateral boundary variables and the physical atmospheric forcing are climatological. Starting from the beginning of the year 1979, we output the modeled variables at monthly frequency and use the period from January 1979 to December 2012 for our analyses.

We ran two simulations, which start from the same initial conditions in January 1979, but which differ from each other in their physical atmospheric and lateral boundary forcing. The first simulation can essentially be seen as a continuation of the spinup: atmospheric CO_2 and lateral DIC increase until the end of the year 2012, while for the same time period, the remaining lateral boundary variables and the physical atmospheric forcing are kept climatological, as in the spinup. The purpose of this "constant climate" (or "CClim") simulation is to separate out the effect of increasing carbon (i.e., increasing atmospheric CO_2 and lateral DIC) versus the effect of the remaining climatic forcing on potential trends in ocean acidification in the CalCS. Our second simulation branches off from the CClim simulation after the spinup at the beginning of January 1979: in this case, instead of keeping the physical atmospheric forcing and most of the lateral boundary variables climatological (except for DIC), we allow the model to be forced transiently

at all of its boundaries. Just as in the CClim simulation, atmospheric CO_2 increases until the end of 2012. This simulation is termed "hindcast" (or "HCast"), as its purpose is to reproduce as accurately as possible the atmospheric and oceanic conditions in the CalCS over the last 34 years. The difference between the HCast and the CClim simulations is thus just the contribution of variable climatic forcing.

4.2.2 Atmospheric and lateral boundary conditions

The physical atmospheric boundary conditions (i.e., u- and v-momentum wind stress, surface heat and freshwater fluxes and shortwave solar radiation) used in the HCast simulation, are daily values from 1979 to 2012 from ECMWF's ERA-Interim Reanalysis product at a horizontal resolution of $\sim$79 km (Dee et al., 2011). For the atmospheric forcing of the CClim simulation, we computed a monthly climatology based on the daily ERA-Interim data from 1979 to 1988, and added to this daily anomalies from the year 1985 for all variables (so-called "normal-year" forcing). The same climatology over the first ten years of ERA-Interim is used during the spinup. We chose this period, in order to assure a smooth transition from the spinup to the forcing of 1979.

Our atmospheric CO_2 forcing is based on monthly CO_2 concentrations from the ESRL GLOBALVIEW-CO_2 data set (GLOBALVIEW-CO2, 2013) from January 1979 to December 2012, corresponding to the same period as the ERA-Interim data. We averaged latitudinally from 24°N to 48°N and used domain-mean monthly values. To convert GLOBALVIEW's mole fraction of CO_2 to pCO_2, we used monthly atmospheric surface pressure, temperature and relative humidity data from ERA-Interim. As the GLOBALVIEW-CO_2 data only exist as of January 1979, we extended this time series to cover the years 1969–1978 by computing a linear trend based on the period 1979 to 2012 and adding to this a monthly climatology calculated over the same time period.

The lateral initial and boundary conditions for the CClim simulation for temperature and salinity are climatologies derived from the Simple Ocean Data Assimilation (SODA) database, whereas nutrients and oxygen are taken from the World Ocean Atlas 2005. Chlorophyll, phytoplankton and zooplankton lateral initial and boundary conditions are climatologies derived from SeaWiFS, while the DIC and Alk initial and boundary conditions are taken from the Global Ocean Data Analysis Project (GLODAP; Key et al., 2004). A more extensive explanation of the model's lateral DIC and Alk forcing can be found in Turi et al. (2014a). In order to obtain transient conditions for DIC in the spinup and in the CClim simulation and for DIC, Alk, nitrate, oxygen, temperature and salinity for the HCast simulation (phytoplankton, zooplankton and chlorophyll are climatological), we added monthly anomalies from a hindcast simulation performed by Graven et al. (2012) to our monthly climatological boundary conditions. The simulations were done using the National Center for Atmospheric Research Community Climate System Model version 3.0 (CCSM3; Smith et al., 2010; Collins et al., 2006; Gent et al., 2006) and were forced with

the Common Ocean-ice Reference Experiments - Corrected Inter-Annual Forcing (CORE-CIAF; Large and Yeager, 2004). As the CCSM3 simulation by Graven et al. (2012) only spans the period from 1760 to 2007, we extended this simulation until the end of 2009 (i.e., until the end of the CORE-CIAF data period), and repeated the forcing of the year 2009 three times to match the ERA-Interim period, which ends in 2012.

4.2.3 Additional methods

As our model computes $p\mathrm{CO}_2$ and pH only for the surface layer and does not include an online calculation of Ω_{arag}, we employed an offline carbonate chemistry calculating tool based on the Ocean Carbon-Cycle Model Intercomparison Project (OCMIP) routines (Orr et al., 2005) to recompute $p\mathrm{CO}_2$, pH and Ω_{arag} to our model's 32 depth levels, using the input variables temperature (T), salinity (S), DIC and Alk provided by our model. In this study, we focus only on aragonite rather than calcite, as the former is the less stable mineral form of CaCO_3 and hence seawater will become undersaturated with respect to aragonite first (e.g., Mucci, 1983; Gruber et al., 2012).

We calculate all of our trends as least-squares linear regressions of monthly or annual mean values from 1979 to 2012. For the computation of the significance of trends, we use the p-value from a Student's t-test and account for autocorrelation by reducing the degrees of freedom according to the equivalent sample size (after Zwiers and von Storch, 1995). We limit our analyses to three regions (see inset in Figs. 4.2 and 4.3): a northern and a southern nearshore region coastwards of 100 km with a division around 38°N near the San Francisco Bay (Regions 1 and 2) and an offshore region between 100 km and 800 km distance to the coast (Region 3). The latitudinal dimensions of the two nearshore domains cover the coastal area roughly from the USA/Mexico border ($\sim$33°N) to just south of the Columbia river mouth ($\sim$46°N).

For our analysis of upwelling strength, we defined a monthly upwelling index from 1979 to 2012, as the alongshore wind stress component divided by the latitudinally dependent Coriolis parameter. This index represents the magnitude of offshore (positive values) or onshore (negative values) water transport, integrated for increments of 100 m along the coast and is given in units of $[\mathrm{m}^3\,\mathrm{s}^{-1}(100\mathrm{m})^{-1}]$ (as calculated in Macias et al., 2012). To compute the alongshore wind component, we used monthly averaged u- and v-momentum wind stress from ERA-Interim and our model's coastal angle due north, which was smoothed using the "LOESS" method based on a weighted quadratic least squares regression in order to account for the coarser resolution of ERA-Interim's wind product. We analyze only the first 100 km along the coast, as the influence of alongshore wind stress on coastal upwelling is largest in this area and becomes less significant further offshore.

4.3 Results

4.3.1 Progression of ocean acidification over the last three decades

Over the whole model analysis domain and from 1979 to 2012, we model in our HCast simulation an average shoaling of the saturation horizon of aragonite (i.e., the depth at which Ω_{arag} drops below a value of 1) of roughly 25 m dec^{-1} (dec = decade), corresponding to a total shoaling of 85 m over the whole time period (Fig. 4.1; model analysis domain highlighted by black frame). This shoaling is most pronounced in the nearshore 200–500 km, where values between 30 to 40 m dec^{-1} are widespread, with a maximum shoaling of 43 m dec^{-1} offshore of Cape Mendocino, California. The average depth of the saturation horizon during the first five years of the simulation from 1979 to 1983 lies around 325 m, while during the last 5 years the domain mean saturation horizon depth shoaled to an average depth of 240 m (not shown). In wide parts of the nearshore area up to roughly 300 km offshore, the saturation horizon remained on average in the top 200 m of the water column during the last five simulation years (red stippled area in Fig. 4.1). In certain coastal regions, such as offshore of San Francisco Bay, between Cape Mendocino and Cape Blanco and along the Oregon coast north of Cape Blanco, the saturation horizon even remained on average in the top 100 m during the last five simulation years, with an average depth of 187 m throughout the whole nearshore 100 km strip (not shown).

Seeing as the nearshore 100 km strip is particularly affected by changes in the depth of the aragonite saturation horizon, we take a closer look at the temporal evolution of the saturation horizon and the volume fraction of water undersaturated with respect to aragonite (i.e., the volume percentage of water with $\Omega_{arag} < 1$) for these three regions separately (Fig. 4.2a and b). It becomes apparent that the temporal progressions of the saturation horizon and the volume fraction of undersaturated water have distinct regional characteristics. In the case of the saturation horizon, the initial state is inherently different for the three regions (Fig. 4.2a): at the beginning of the time period in the offshore region, the saturation horizon is quite deep at around 340 m during the first five years and shoals by around 100 m to an average depth of about 240 m by the end of 2012. In the nearshore regions on the other hand, the saturation horizon is on average naturally shallower at the beginning of the simulation, with initial depths of around 300 m. Over the 34 years, the saturation horizon in the southern region shoals by about 90 m to an average depth of around 210 m, whereas in the northern region, the change is largest with a shoaling of about 130 m to a depth of 170 m on average over the last five years. There are also clear regional differences in the change in the amount of undersaturated water over time, with the change in the northern nearshore region being again the most noticeable both for depths between 200 and 400 m and for the top 200 m of the water column (Fig. 4.2b). At the beginning of the simulation, the amount of water undersaturated with respect to aragonite occupies about half of the total water volume between 200 to 400 m depth for both the northern and southern nearshore regions, while in the offshore region, the initial volume fraction is slightly lower at about 30%. However, from the year 2005

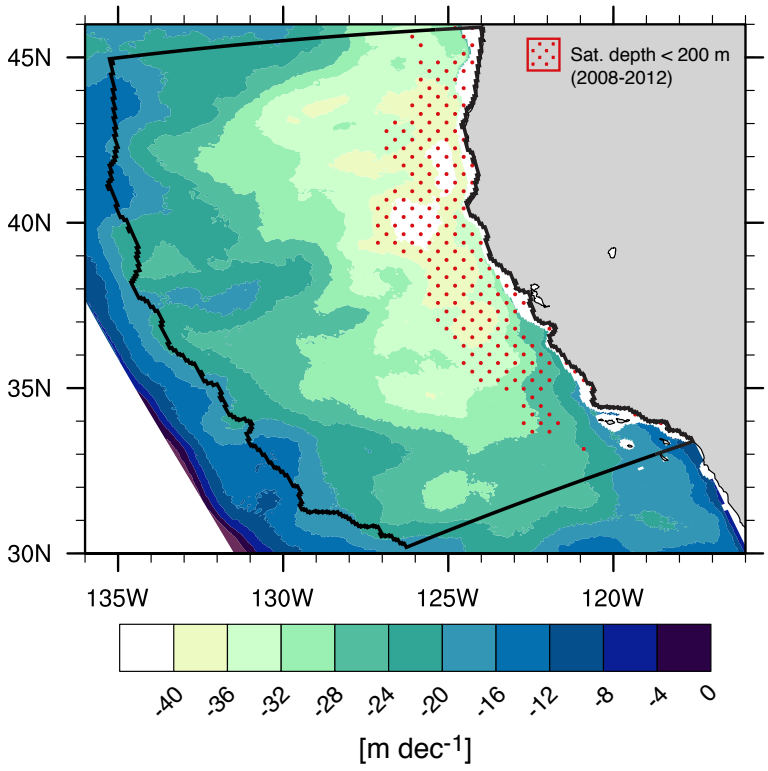

Figure 4.1 Change per decade in the saturation horizon of aragonite, i.e., the depth at which Ω_{arag} drops below a value of 1, from 1979 to 2012, calculated as the least squares linear trend of the data. The black frame indicates the whole model domain which we used for our analyses. The red stippling indicates the area where the saturation horizon remained on average within the top 200 m of the water column during the last five years of the simulation (2008–2012).

onward, the whole water column between 200 to 400 m has become completely undersaturated in the northern nearshore region, and undersaturated water occupies about 90% and 75% of the total volume in the southern nearshore and the offshore regions, respectively. Similarly, in the top 200 m of the water column the amount of undersaturated water increases from zero for all regions, to about 10% in the northern nearshore region and 3% in the other two regions.

To investigate whether this regional peculiarity is evident for other variables as well, we compute trends in pCO_2, pH and Ω_{arag} for the top 60 m of the water column (Fig. 4.3). This depth is consistent with the analyses of Gruber et al. (2012) and corresponds approximately to the average depth of the euphotic zone in the CalCS. Computing these trends from our HCast simulation for 1979–2012, we obtain a domain-wide increase in pCO_2 of 18 μatm dec^{-1} and concurrent decreases in pH and Ω_{arag} of –0.018 dec^{-1} and –0.104 dec^{-1} (top row of Fig. 4.3). Over the same time period, atmospheric CO_2 increased on average by a total of approximately 57 μatm or by roughly 16 μatm dec^{-1}. The CalCS-wide increase in pCO_2 and decreases in pH and Ω_{arag} show similar clear regional differences as were apparent in Fig. 4.2. The strongest change in pCO_2 is experienced by the nearshore area within roughly 100 km of the coast around Cape Mendocino, or, more broadly, between Point Arena, California and Cape Blanco, Oregon (∼39–43°N), with trends of up to 30 μatm dec^{-1}, or a total change of around 100 μatm over 34 years. Further offshore between about 200–600 km and to the south of Point Arena, the change is noticeably

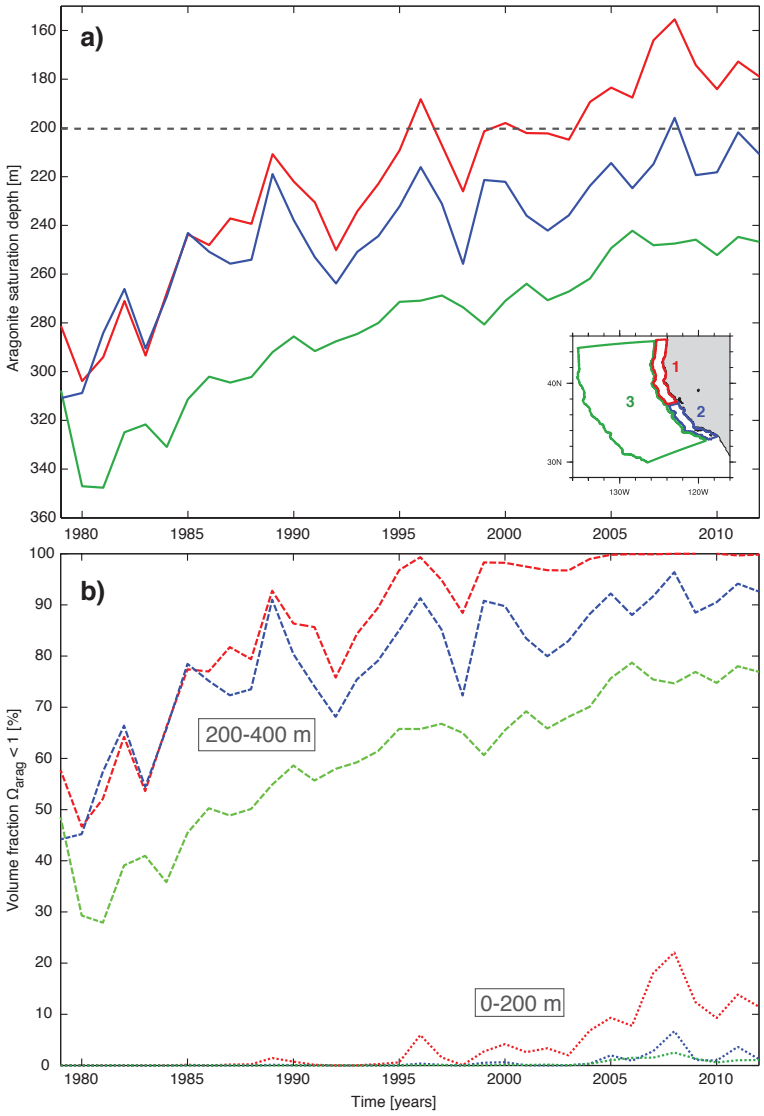

Figure 4.2 **(a)** Aragonite saturation depth (or "saturation horizon"), i.e., the depth at which Ω_{arag} drops below a value of 1, and **(b)** volume fraction of water undersaturated with respect to aragonite ($\Omega_{arag} < 1$) for the top 200 m (dotted lines) of the water column and for the 200-400 m layer (dashed lines) as a function of time from 1979 to 2012. The inset indicates the three regions for which the volume fraction was computed. The monthly model output was smoothed to show annual mean values.

smaller, but nevertheless significant, with values around 15 μatm dec^{-1}. A similar pattern can be seen in pH (Fig. 4.3b): the largest negative trends appear around the same "hotspot" near Cape Mendocino with trends of up to –0.025 dec^{-1}. This "hotspot" is also visible in the trends pattern of Ω_{arag}, where negative trends reach values of –0.15 dec^{-1} (Fig. 4.3c). Further offshore though, the Ω_{arag} pattern does not resemble the patterns of pCO$_2$ and pH: larger negative trends are also experienced in areas up to 800 km offshore. What the trends patterns of these three variables have in common though is a distinct north–south gradient in the first 100 km, with the largest domain-wide changes found in the Cape Mendocino "hotspot" area and the smallest changes to the south between Point Arena and Point Conception, with a regional separation around 38°N.

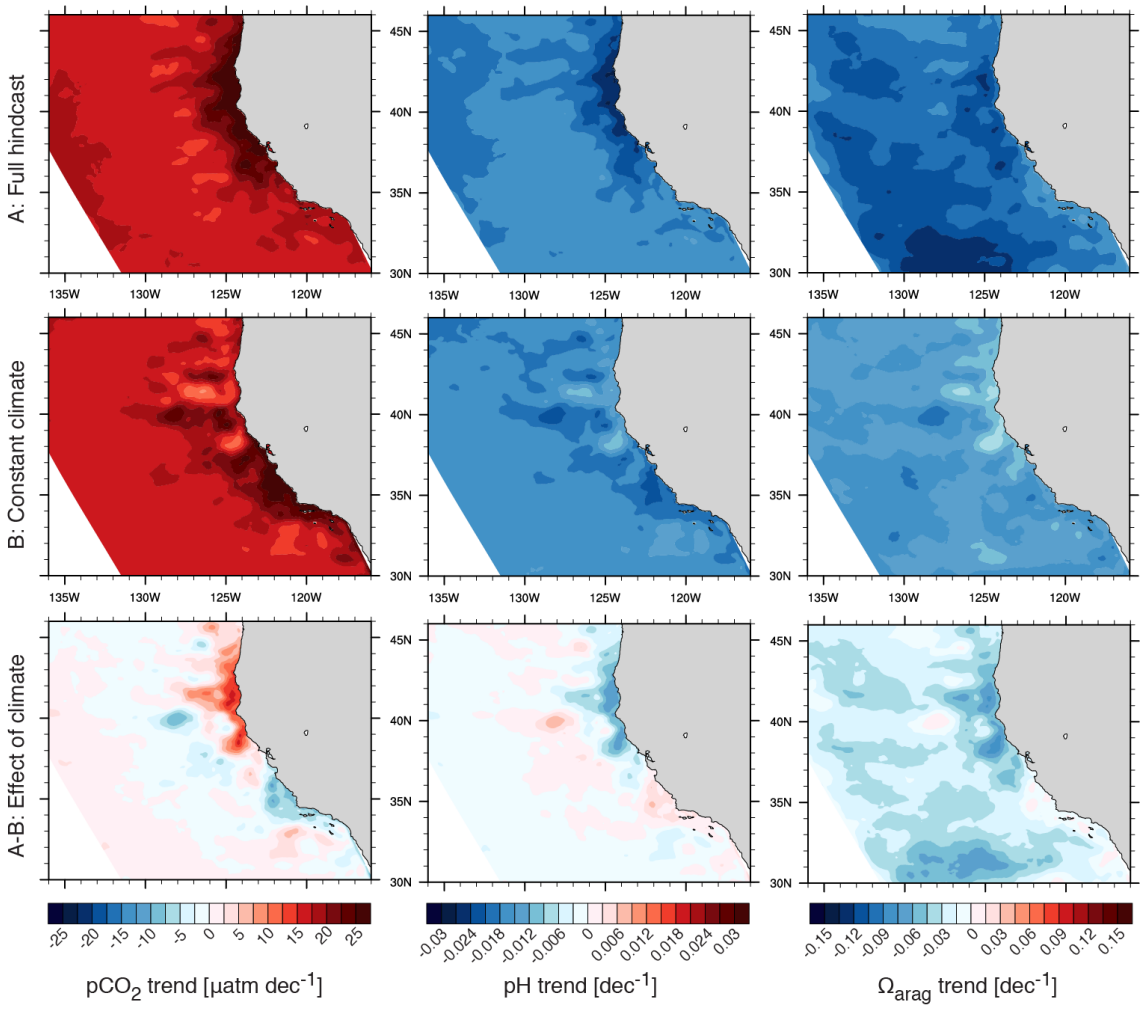

Figure 4.3 Changes per decade in pCO_2, pH and Ω_{arag} from 1979 to 2012 for the HCast (top row) and the CClim (center row) simulations, calculated as the least squares linear trends of the data averaged over the top 60 m of the water column. The bottom row is the difference between the HCast and the CClim trends (HCast–CClim). All trends calculated for the HCast and the CClim simulations were significant at the 95% significance level (calculated as the p-value from a Student's t-test; not indicated).

4.3.2 Contribution of recent climatic changes to ocean acidification

In order to separate the influence of increasing carbon from the influence of changes in the physical atmospheric forcing on trends in pCO_2, pH and Ω_{arag}, we calculate the same linear trends from 1979 to 2012 for the CClim simulation for these variables (center row of Fig. 4.3). By prescribing atmospheric CO_2 and lateral DIC, but keeping the physical atmospheric forcing and the remaining lateral boundary variables climatological in this simulation, the trends patterns that emerge for pCO_2, pH and Ω_{arag} are purely driven by the increases the atmospheric and lateral carbon. To tease out the effect of the climatic forcing alone and eliminate the influence of increasing carbon, we subtract the trends computed from the CClim simulation from the trends obtained from the HCast simulation (bottom row of Fig. 4.3). This reveals that the strongest changes due to climatic forcing alone are felt by the nearshore region around Cape Mendocino, with maximum changes of 15 μatm dec^{-1} for pCO_2, and –0.01 dec^{-1} in pH and –0.05 dec^{-1} in

Ω_{arag}. However, what this difference also reveals is that in the nearshore regions south of roughly 38°N and offshore between roughly 200 to 500 km, the climatic forcing leads to a slight decrease in $p\mathrm{CO}_2$ (up to –10 μatm dec^{-1}) and an increase in pH (up to 0.01 dec^{-1}). For a more quantitative assessment of the the total changes in these three variables over the 34 years, we average over the same three regions as in Fig. 4.2 (Fig. 4.4). The northern nearshore region experiences the largest total changes in $p\mathrm{CO}_2$ (88 μatm) and pH (–0.08) compared to the other two regions. The total change in Ω_{arag} of around –0.35 is roughly the same in the northern nearshore region and the offshore region, while it is slightly smaller in the southern region. The most apparent difference between the three regions however is that in the northern nearshore region, the contribution of the climatic forcing alone explains about 31% and 34% of the total changes in $p\mathrm{CO}_2$ and pH, while it is responsible for almost half of the total change in Ω_{arag}. Averaged over the whole offshore region, the effect of the climatic forcing is negligible for $p\mathrm{CO}_2$ and pH, while it accounts for roughly 30% of the total change in Ω_{arag}. In the southern nearshore region, the effect of climate on trends in $p\mathrm{CO}_2$ and pH is of the opposite sign than in the other two regions, in that the climatic forcing decrease $p\mathrm{CO}_2$ by about 16μatm and increases pH by 0.05. The effect on Ω_{arag} is the same as in the other two regions, albeit smaller.

4.3.3 How does climate variability influence ocean acidification?

Changes in the climatic forcing can affect coastal ocean acidification through several different factors. Alterations in the upwelling strength and changes in the upper ocean temperature, which in turn impact the water column stability, both have an effect on the rate of DIC supply to the surface. For instance, surface ocean warming could lead to an increase in stratification and reduced vertical mixing, while an increase in wind-induced upwelling could lead to more DIC being transported to the surface. Changes in the vertical mixing and the upwelling strength also alter biological productivity and the rate of remineralization, which in turn directly affect ocean acidification. Yet, Lachkar (2014) demonstrated that coastal acidification in the CalCS is mainly a consequence of upwelling of waters with low carbonate ion concentrations ([CO_3^{2-}]) to the surface, while the local biological productivity plays a minor role. Moreover, Turi et al. (2014a) highlighted that in the nearshore 100 km, circulation is the main driver of $p\mathrm{CO}_2$ variability, while biological activity is much less important. To verify this, we computed trends in temperature, nitrate (NO_3) and net primary production (NPP) for the top 60 m of the water column (Fig. 4.5a-c). We model a domain-wide average upper ocean cooling trend of about –0.25°C dec^{-1}, corresponding to a total temperature change of –0.85°C over 34 years (Fig. 4.5a). A cooling of the surface ocean leads to a destabilization of the vertical structure of the water column, hence to a decrease in stratification and a concurrent increase in the depth of the mixed layer. Indeed, we model a domain-wide deepening of the mixed layer of around 1 m dec^{-1} (not shown). At the same time, our model suggests a significant increase in the NO_3 concentration throughout the upwelling zone along the coast from San Francisco Bay to the USA/Canada border and up

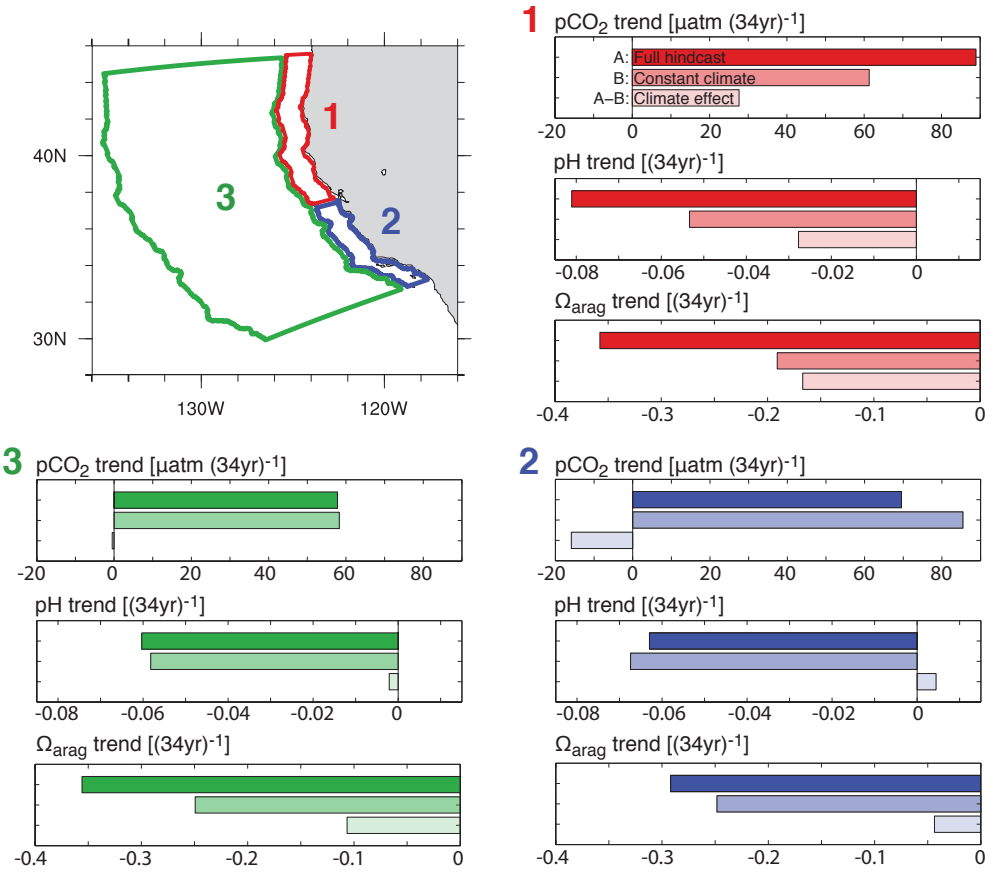

Figure 4.4 Total changes (per 34 years) in $p\mathrm{CO}_2$, pH and Ω_{arag} from 1979 to 2012 averaged over the top 60 m of the water column for our two simulations and for the same three regions as analyzed in Fig. 4.2. Changes are calculated as the least squares linear trends of the data. The top bar is output from the HCast simulation, the center bar represents trends from the CClim simulation and the bottom bar is the difference between the two (HCast-CClim), i.e., the contribution of climatic forcing other than the increase in atmospheric CO_2.

to roughly 300 km offshore, with values up to 1.2 mmol N m^{-3} dec^{-1} (Fig. 4.5b). The northern nearshore region experiences the largest increase with an average of 0.8 mmol N m^{-3} dec^{-1}. The trend in NO_3 shows a very strong nearshore-offshore gradient, with the increase in NO_3 quickly diminishing with increased distance to the coast. Offshore of roughly 300 km, there is nearly no detectable or significant trend, which is most likely due to biological activity efficiently utilizing the abundant supply of nutrients. Accordingly, a positive trend is modeled for NPP, with a similar, but more widespread pattern of increase (Fig. 4.5c). The largest increase in NPP with values of up to 1.6 mol C m^{-2} yr^{-1} dec^{-1} is located roughly 200 to 300 km offshore of central California, and not immediately close to the coast, as in the case of NO_3. Furthermore, the same division around San Francisco Bay as could be seen for $p\mathrm{CO}_2$ and pH between the northern nearshore and southern nearshore regions is visible both in NPP and NO_3, which show positive average trends in the north and negative trends in the south. This regional difference is again most likely ascribed to the spatial difference between the increase in upwelling-favorable wind to the north of roughly 38°N and the decrease to the south.

The domain-wide cooling trend in Fig. 4.5a, which can be seen as a proxy for a decrease in

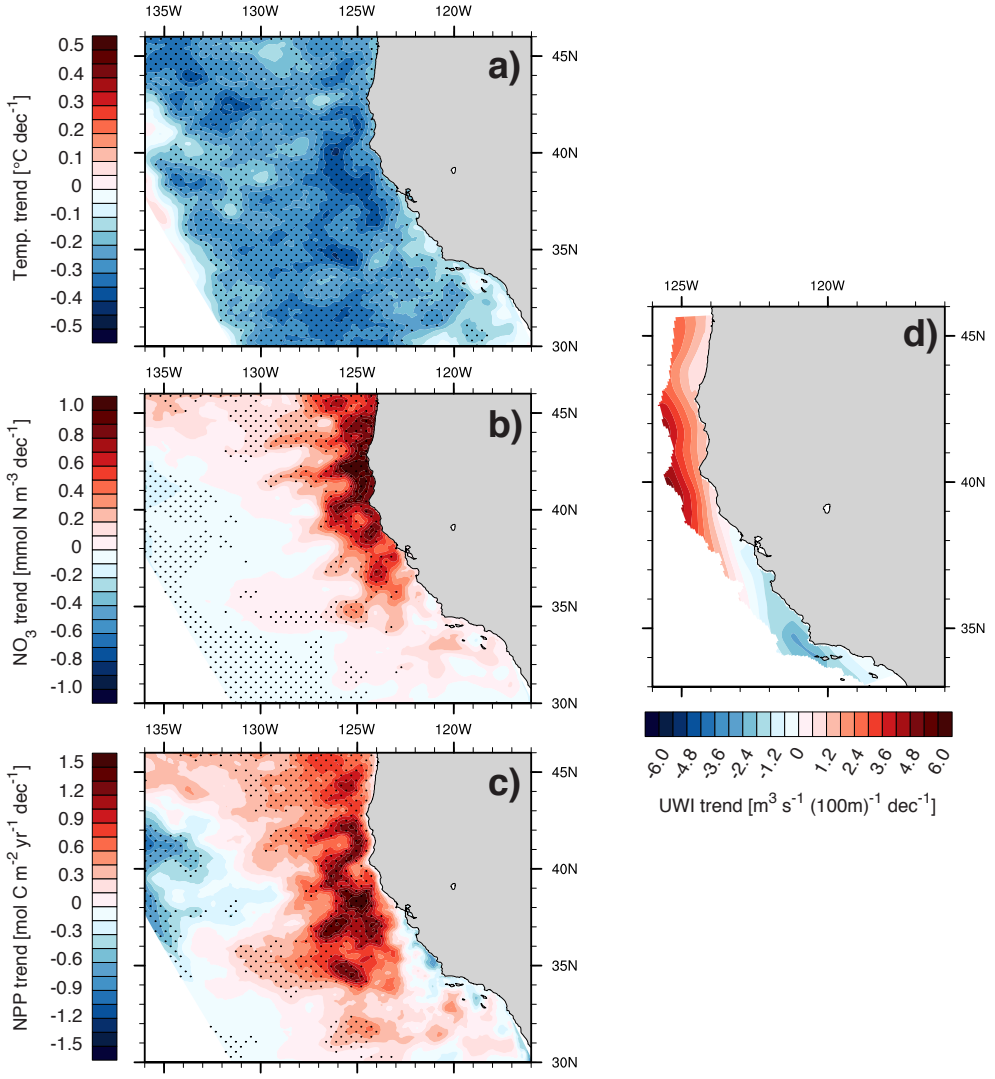

Figure 4.5 Changes per decade in **(a)** temperature, **(b)** NO_3, **(c)** NPP and **(d)** upwelling index (UWI) from 1979 to 2012 from our HCast simulation, calculated as the least squares linear trends of the data. Temperature, NO_3 and NPP were averaged over the top 60 m of the water column. Note the different geographical extent of panel (d), as we only show UWI for the first 100 km along the coast. The black stippling indicates trends significant at the 95% level (calculated as the p-value from a Student's t-test).

stratification and increased vertical mixing, shows a too uniform pattern over the whole analysis domain to serve as an explanation for the local enhanced decrease in pH and Ω_{arag} around Cape Mendocino in Figs. 4.3h and 4.3i and the shoaling of the aragonite saturation horizon in Fig. 4.2a. As biological productivity acts to increase $[CO_3^{2-}]$, the strong positive trends in NPP from Fig. 4.5c can also be ruled out as a possible explanation for this local enhancement of ocean acidification. Therefore, we conclude that only a change in the upwelling strength, affecting the rate of DIC supply to the surface, can explain this strong local pattern.

To detect whether there were any apparent changes in upwelling over the simulation time period, we computed our upwelling index (UWI) based on the alongshore component of our wind forcing (Fig. 4.5d). Indeed, we find an increase in wind-driven upwelling around Cape Mendocino, with values as large as 5.1 $m^3\,s^{-1}\,(100m)^{-1}\,dec^{-1}$. There is a regional separation

in the UWI trend around 38°N, which corresponds roughly to the division between our northern and southern nearshore regions. Averaging over these two regions yields an increase in UWI of around 2.2 $m^3\,s^{-1}\,(100m)^{-1}\,dec^{-1}$ in the northern region and a slightly less pronounced average decrease of –1.0 $m^3\,s^{-1}\,(100m)^{-1}\,dec^{-1}$ in the south. The approximate location of this separation between increase and decrease in wind-driven upwelling coincides with the spatial division in the nearshore trends patterns for pCO_2, pH and Ω_{arag} discussed above. This spatial agreement, together with our results for the volume fraction of undersaturated water and the saturation horizon leads us to the conclusion that wind-driven upwelling is the main driver for changes in these variables and for the regional enhancement of ocean acidification in the nearshore 100 km around Cape Mendocino.

4.4 Discussion and model evaluation

There are several caveats and uncertainties in this study which need to be addressed. Firstly, our alongshore wind stress trend is likely underestimated in the coastal regions south of Cape Mendocino (∼38°N), due to the coarse horizontal resolution of the ERA-Interim wind forcing data in comparison to our model's horizontal resolution (∼79 km vs. 5 km). In these areas, we computed a decrease in upwelling strength based on alongshore winds (Fig. 4.5d), although several previous studies have demonstrated that upwelling has increased over the last few decades in regions south of about 38°N. Based on a set of buoy measurements from the National Oceanic and Atmospheric Administration's (NOAA) National Data Buoy Center, García-Reyes and Largier (2010) found a significant increase at the 90% significance level in equatorward, alongshore wind speed for five out of nine buoys located in the area from roughly 35°N to 42°N, averaged for the upwelling season from March to July for the years 1982 to 2008 (Fig. 4.6a). This increase in wind speed was confirmed separately by Seo et al. (2012), who demonstrated for the same set of buoys, but for the time period 1980–2010, that three buoys showed a significant increase in meridional wind speed for the months June through August (Fig. 4.7a). As nearshore upwelling is primarily determined by the alongshore wind component, we compare our model's wind forcing to the buoy measurements of García-Reyes and Largier (2010). Figure 4.6a shows that north of around 38°N, the trends are well represented in the ERA-Interim wind product over the same time period as García-Reyes and Largier (2010) (upwelling season means for 1982–2008) and also for the entire simulation time period from 1979 to 2012. South of 38°N however, the trend in the ERA-Interim alongshore wind speed is significantly smaller, with values around 0.01 $m\,s^{-1}\,yr^{-1}$ compared to 0.05 $m\,s^{-1}\,yr^{-1}$ further north. Furthermore, although the signs of the ERA-Interim wind speed trends agree with García-Reyes and Largier (2010), none of the ERA-Interim trends are significant at the 90% significance level. Therefore, the positive upwelling strength trend, which enhances ocean acidification, may even extend further south than than 38°N, leading us to conclude that this wind-driven enhancement of ocean acidification is possibly much more widespread

along the US West Coast than simulated in our study.

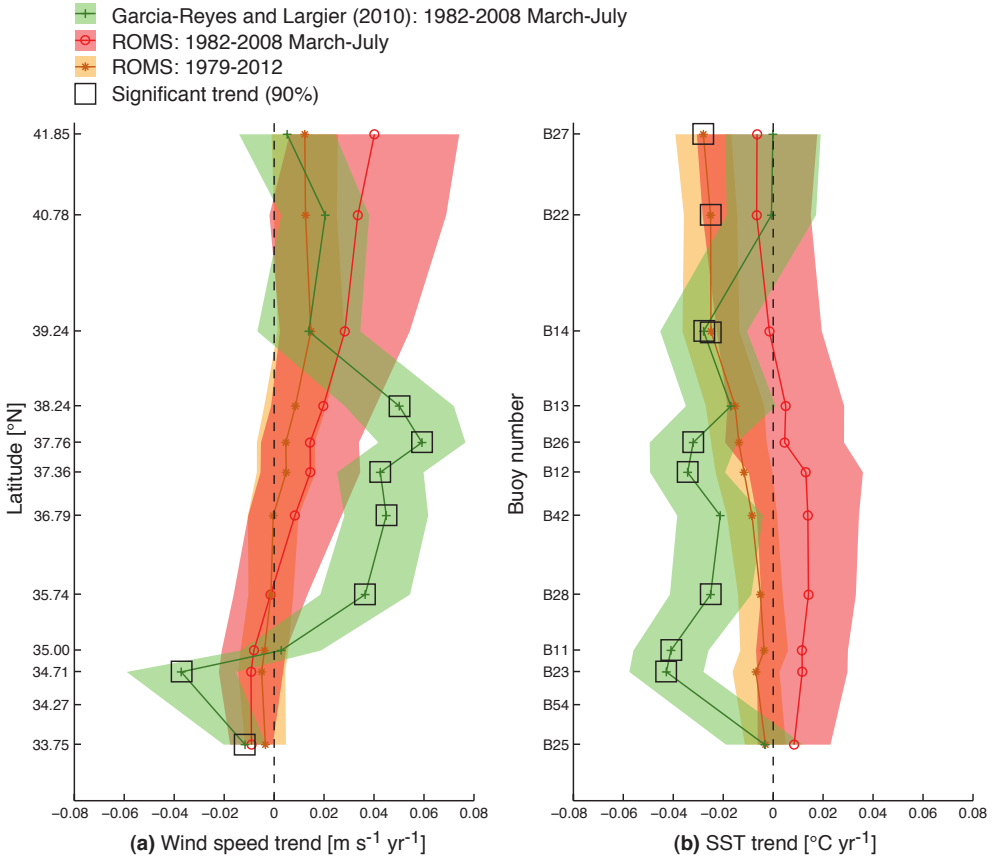

Figure 4.6 Comparison of trends in **(a)** alongshore wind speed from ERA-Interim and from García-Reyes and Largier (2010) and in **(b)** SST from our model and from García-Reyes and Largier (2010) for 11 buoys from NOAA's National Data Buoy Center. Positive wind speed values indicate increased equatorward winds, while negative values represent a decrease. The ERA-Interim and the modeled data were sampled in the same locations as the buoys, and averaged for a radius of roughly 50 km around each buoy location. Data from García-Reyes and Largier (2010) were provided directly to us and are averaged over the upwelling season (March-July) of each year from 1982 to 2008 (green line). We averaged our model data over the same time period for the same months to be directly comparable to the observational data (red line). As a comparison, we included trends of annual mean data over our whole simulation time period from 1979 to 2012 (orange line). Trends which are significant at the 90% significance level are highlighted by black boxes. We computed trends in the modeled and observational data using ordinary least squares linear regressions. Standard errors were calculated on annual mean data, accounting for autocorrelation by reducing the degrees of freedom according to the equivalent sample size.

Secondly, the underestimation of upwelling south of 38°N becomes again apparent when comparing the modeled SST trends with results from both García-Reyes and Largier (2010) and Seo et al. (2012) (Figs. 4.6b and 4.7b). North of roughly 38°N, the model performs quite well compared to the observations. However, to the south of this, the model consistently simulates a surface warming during the upwelling seasons defined by García-Reyes and Largier (2010) and Seo et al. (2012), although the in-situ observations show a surface cooling. In addition, Fig. 4.8a-c displays the comparison of modeled SST to satellite SST observations from NOAA's Advanced Very High Resolution Radiometer (AVHRR) Pathfinder Version 5 SST Project over the time period from June 1988 to December 2009, and shows that indeed the model underestimates the

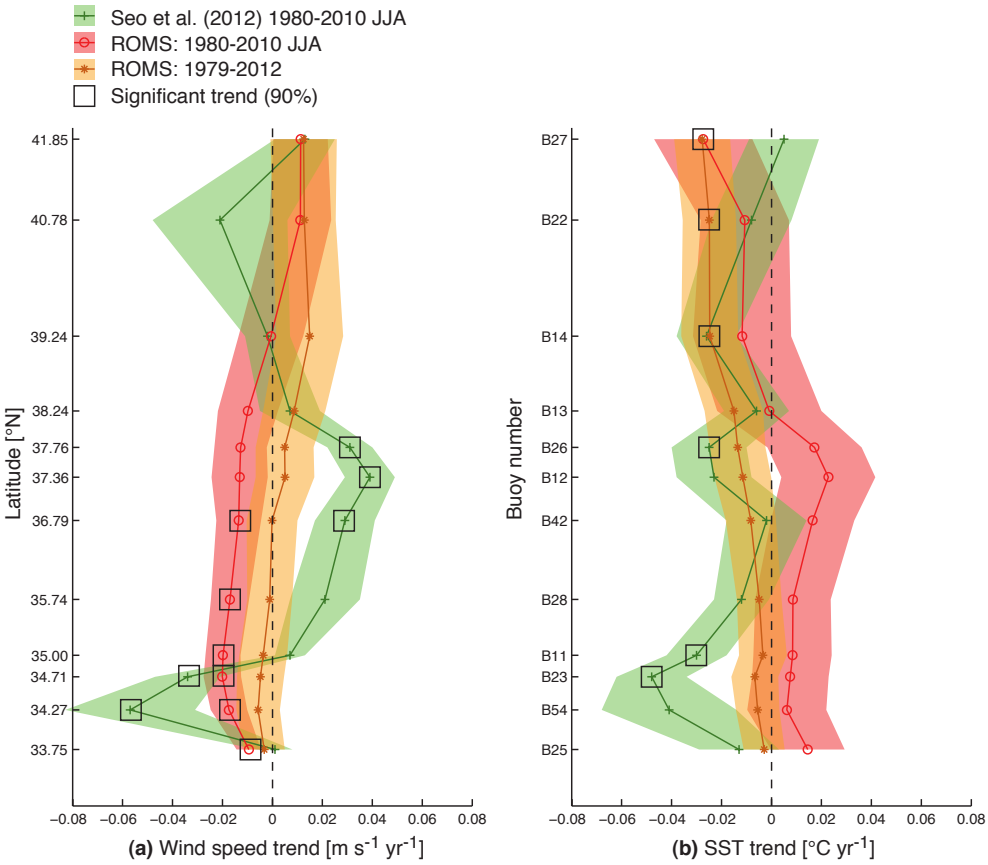

Figure 4.7 Comparison of trends in **(a)** alongshore wind speed from ERA-Interim and meridional wind speed from Seo et al. (2012) and in **(b)** SST from our model and from Seo et al. (2012) for 12 buoys from NOAA's National Data Buoy Center. Positive wind speed values indicate increased equatorward winds, while negative values represent a decrease. As wind speed from Seo et al. (2012) is meridional, it is hence not directly comparable to our alongshore wind speed in absolute terms, but nevertheless gives an indication of the sign. The modeled data were sampled in the same locations as the buoys, and averaged for a radius of roughly 50 km around each buoy location. Observational data were taken from Table 1 of Seo et al. (2012) and are averaged over June to August of each year from 1980 to 2010 (green line). We averaged our model data over the same time period for the same months to be directly comparable to the observational data (red line), and we adjusted their trends, which were given per decade, to match our per year trends. As a comparison, we included trends of annual mean data over our whole simulation time period from 1979 to 2012 (orange line; same as in Fig. 4.6). Trends which are significant at the 90% significance level are highlighted by black boxes. We computed trends in the modeled data using ordinary least squares linear regressions and standard errors were calculated on annual mean data, accounting for autocorrelation by reducing the degrees of freedom according to the equivalent sample size.

cooling particularly in the nearshore 0–200 km south of 38°N. The fact that the model simulates a domain-wide uniform cooling with no clear nearshore-offshore gradient (Fig. 4.5a), combined with a possible underestimation of the upwelling strength, suggests that the model is unable to capture a change in the depth of the upwelling, which would emerge as a clear stronger nearshore cooling signal. It is however likely that the change in the strength of upwelling is accurately modeled, which affects the rate of DIC and nutrients supplied to the surface, but does not alter surface ocean temperatures. This can clearly be seen as a signal in NO_3 in Fig. 4.5b. However, if there were an additional increase in the depth of the upwelling, this would further exacerbate

ocean acidification by reducing Ω_{arag} due to a decrease in $[CO_3^{2-}]$ (Lachkar, 2014), and would therefore change our results only in a quantitative way, while the qualitative conclusions would remain the same.

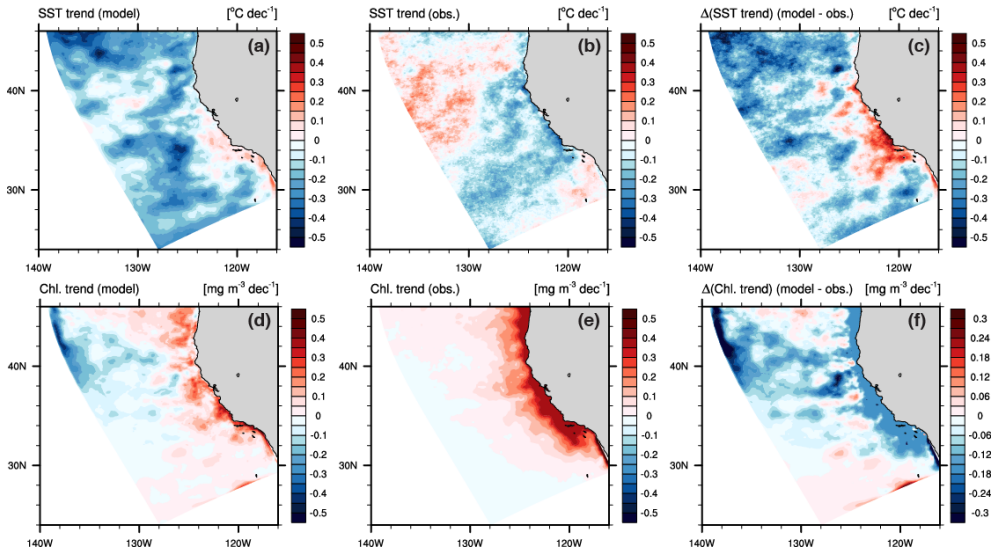

Figure 4.8 Comparison of modeled versus satellite-observed trends in (**(a)** to **(c)**) SST and (**(d)** to **(f)**) chlorophyll, computed as the least squares linear trends of the data. SSTs are monthly data from NOAA's AVHRR Pathfinder Version 5 SST Project (4 km horizontal resolution) spanning the period from June 1988 to December 2009 and chlorophyll data are from the European Space Agency's (ESA) GlobColour Project (0.25° horizontal resolution), with monthly values from September 1997 to December 2012, including observations from the Sea-viewing Wide Field-of-view Sensor (SeaWiFS), the Moderate Resolution Imaging Spectroradiometer on NASA Aqua Satellite (MODISA) and the Medium Resolution Imaging Instrument on ESA Envisat Satellite (MERIS). We sampled our model output over the same time periods to be directly comparable to the satellite observations. Panels **(a)** and **(d)** are the modeled trends, **(b)** and **(e)** are trends computed from the observations and **(c)** and **(f)** are the difference in the trends, i.e., modeled minus observed trends.

Finally, a comparison with satellite observations of chlorophyll from the European Space Agency's (ESA) GlobColour Project for the time period from September 1997 to December 2012, shows that the model underestimates the increase in chlorophyll particularly throughout the whole nearshore region by up to 50% (Fig. 4.8d-f), which can be seen as an indicator for an underestimation of nearshore NPP. As biology acts to increase pH and Ω_{arag} and hence dampen ocean acidification, a further increase in NPP would result in less ocean acidification in the nearshore region. Thus, the uncertainties associated with the underestimation of both the upwelling and the chlorophyll act to compensate each other. However, as Lachkar (2014) demonstrated, the local biological productivity is less important for determining coastal acidification in the CalCS compared to the control of circulation, i.e., upwelling. Hence, we conclude that in total, the wind-driven ocean acidification signal presented here is likely underestimated and the uncertainty in the magnitude of these trends does not affect our conclusion.

4.5 Conclusions and outlook

We used two simulations from an eddy-resolving oceanic model of the US West Coast to (i) investigate trends in ocean acidification from 1979 to 2012 in the CalCS and (ii) determine the drivers behind the regional modifications of these trends which cannot be explained solely by the increase in atmospheric CO_2.

We find a domain-wide increase in oceanic pCO_2 and concomitant decreases in pH and Ω_{arag} in the top 60 m of the water column over the last 34 years. Moreover, the whole CalCS experiences a shoaling of the aragonite saturation horizon and a domain-wide expansion of the volume fraction of water undersaturated with respect to aragonite ($\Omega_{arag} < 1$) in the upper 200 m of the water column. The most severe changes occur in an area limited to the first 100 km along the coast, roughly between San Francisco Bay and Cape Blanco, Oregon ($\sim$39–43°N). From the year 2005 to the end of the simulation, waters with undersaturated aragonite conditions in this area occupy 100% of the total water mass in the layer between 200 and 400 m depth, while in the top 200 m, the fraction of undersaturated water is roughly 10% by the end of the simulation. In the same area, our model results suggest pCO_2 to have increased by up to 100 μatm and pH and Ω_{arag} to have decreased by as much as –0.08 and –0.5, respectively. A maximum shoaling of the aragonite saturation horizon of 100 m from 1979 to 2012 was found to occur offshore of Cape Mendocino and Cape Blanco, roughly between 100–300 km from the coast.

We found this extreme regional enhancement in coastal ocean acidification trends to be driven to a significant extent by changes in the climatic forcing alone, which can explain up to 30% of the trends in pCO_2 and pH and 50% of the trends in Ω_{arag} in the coastal region around Cape Mendocino. We propose that in the nearshore 100 km, an increase in wind-driven upwelling north of 38°N is the main driver for the local enhancement in ocean acidification. In the same region, we see a significant increase in NO_3 by up to 1.2 mmol N m^{-3} dec^{-1}, accentuating that this region is particularly affected by wind-driven upwelling intensification. Stimulated by the increased supply of nutrients, biological productivity likewise experiences an increase, albeit with a maximum at around 200 to 300 km offshore of central California. In the offshore regions, this intensification of biological productivity is likely responsible for a dampening in the ocean acidification trend, which can be seen in the slight decrease in pCO_2 and increase in pH and Ω_{arag}. Over the whole model domain, we model a cooling of –1 to –1.2 °C, which decreases the vertical stability of the water column and leads to a uniform enhanced vertical supply of nutrients and DIC to the surface.

Previous modeling studies of the CalCS using ROMS by Gruber et al. (2012), Hauri et al. (2013b) and Hauri et al. (2013a) were conducted under increasing atmospheric CO_2 only, with repeat present-day climatic forcing. This modeling study is the first to investigate separately the effects of increasing atmospheric CO_2 and of changes in the physical forcing on ocean acidification in the CalCS. Our model results however show a clear connection between a local increase

in wind-induced upwelling and a significant acceleration of ocean acidification in the nearshore 100 km around Cape Mendocino. As this local change in the climatic forcing alone can explain up to 50% of the decrease in Ω_{arag} and 30% of the negative trends in pH, it is important to take this climatic effect into account when investigating current and future changes in ocean acidification - in the CalCS as well as in other coastal upwelling regions (Lachkar, 2014).

Despite the significance of these climatic trends, it is challenging to answer the question whether they are driven primarily by interannual to decadal fluctuations in the climatic forcing of the CalCS (Turi et al., 2014c), or whether they are indeed fingerprints of ongoing anthropogenic climate change, as has been alluded to in a number of studies in recent decades (e.g., Bakun, 1990; Diffenbaugh et al., 2004; Narayan et al., 2010). These studies propose that an increased thermal gradient due to the asynchronous warming of land and sea should intensify alongshore winds and thereby increase coastal upwelling to the north of the Southern California Bight, while weakening upwelling in the south. An analysis of 33 simulations from the Coupled Model Intercomparison Project 5 (CMIP5; 1979–2012: historical simulations were extended with the respective Representative Concentration Pathway emission scenario 8.5 (RCP 8.5) member; Taylor et al., 2012), indeed reproduces a trend, as was seen in this study, towards increased upwelling-favorable winds in the northern CalCS and reduced alongshore winds to the south, being indicative of a forced component in the recent wind trends over the CalCS (see Fig. B.1 in the Appendix). This intensification in alongshore winds is, however, underestimated considerably in the coupled models. Consequently, these models fail to capture the pronounced sea surface cooling trend induced by increased upwelling, primarily owing to their coarse spatial resolution of roughly 1°. This leads to a smaller trend in the thermal land-sea gradient in historical coupled model simulations as compared to observations and therewith likely to an underestimation or misrepresentation of the observed dynamics in coupled models.

Further, given the shortness of our investigated time period, significant modulations of these trends due to large-scale teleconnective patterns such as the El Niño/Southern Oscillation (ENSO), the Pacific Decadal Oscillation (PDO), or the North Pacific Gyre Oscillation (NPGO) cannot be excluded (e.g., Chhak and Di Lorenzo, 2007; Di Lorenzo et al., 2008; Macias et al., 2012; Turi et al., 2014c). In particular, the superposition of strong positive or negative phases of these three modes of climate variability can cause anomalous upwelling conditions (see Fig. B.2 in the Appendix), which potentially obscure a long-term climate change-driven trend (e.g., Boyd et al., 2008; Henson et al., 2010).

These results imply that the hypothesis by Bakun (1990) is to be interpreted with care in the CalCS, as ENSO, PDO, NPGO or other climate oscillations in the North Pacific could be the main drivers of these trends. Furthermore, strong recent trends in the larger-scale circulation in the equatorial Pacific (e.g., England et al., 2014) complicate the isolation of regional land-sea-atmosphere feedbacks in observations and reanalyses over this period. In addition, in CMIP5 projections under the RCP 8.5, large-scale changes in circulation appear to mask a potential

continuation of the regional land-sea-atmosphere feedback throughout the end of the 21st century (Fig. B.1 in the Appendix). Given the biases in global models, a coupling of regional climate model projections (e.g., Mearns et al., 2012) to ROMS may shed more light on the future of the CalCS under increasing atmospheric CO_2. It is however undeniable that amplified local ocean acidification, as simulated in this study, has a deleterious impact on calcifying organisms by reducing the saturation state of Ω_{arag} to a point of waters being corrosive to the organisms' shells and skeletons (e.g., Feely et al., 2008; Bednarsek et al., 2014). Moreover, this acceleration of ocean acidification reduces the time that these organisms have to adapt to such changes and can therefore pose an increased risk to the success of local ecosystem services (e.g., Soto, 2002).

Acknowledgements This research was funded by the Swiss Federal Institute of Technology Zürich (ETH Zürich) and through the EU FP7 projects CARBOCHANGE and GEOCARBON, which received financial support from the European Commission's Seventh Framework Programme (FP7/2007-2013) under grant agreement n^{o} 264879 and 283080, respectively. All the simulations in this study were performed at the central computing cluster of ETH Zürich, Brutus. The ECMWF ERA-Interim Reanalysis data used in this study were downloaded from the ECMWF Data Server (http://www.ecmwf.int/research/era/do/get/era-interim). We are grateful to M. García-Reyes for sharing the buoy measurements used in García-Reyes and Largier (2010), which were obtained from NOAA's National Data Buoy Center (http://www.ndbc.noaa.gov/). We thank F. Lehner and D. Byrne for their helpful comments on the manuscript.

Chapter 5

High interannual variability of air–sea CO_2 fluxes in the California Current System

G. Turi, Z. Lachkar, M. Münnich, N. Gruber, and D. Loher

Environmental Physics, Institute of Biogeochemistry and Pollutant Dynamics, ETH Zürich, Zürich, Switzerland

This manuscript is in preparation.

Abstract

The rise in anthropogenic CO_2 is predicted to alter the ocean's carbonate chemistry. In regions where the variability of carbon fluxes is naturally high, such as in Eastern Boundary Upwelling Regions (EBUS), trends may be masked by this variability, making it difficult to distinguish between the climate-change driven component of the total variability and the part driven by natural fluctuations in the climate system. In this study, we analyze the interannual to decadal variability of air–sea CO_2 fluxes and pCO_2 in the California Current System (CalCS). To this end, we use a highly-resolved regional oceanic model of the US West Coast to simulate the biogeochemistry and carbon dynamics in the CalCS between 1979 and 2012. Analyses from this hindcast simulation reveal that the magnitude of the low-frequency ($>$1 year) signal in air–sea CO_2 fluxes is roughly of the same magnitude as the seasonal cycle, and in the nearshore 100 km it can act to enhance the seasonal cycle by up to 70% during years of extreme climate variability. Correlations of the air–sea CO_2 fluxes with three indices of climate variability (ENSO, PDO and NPGO) highlight the strong control of these climate variability modes on the source/sink behavior of the CalCS on interannual timescales, with an opposing pattern in the effect on the outgassing and uptake of CO_2 between the nearshore 100 km and the regions further offshore. We determine that the sensitivity of pCO_2 to interannual fluctuations in these three modes of climate variability is largest in the nearshore 100 km and is linked to changes in the supply of dissolved inorganic carbon (DIC) to the surface ocean. Further offshore, climate variability acts to influence pCO_2 mainly through changes in temperature and alkalinity, with their effects being opposite to those of DIC.

5.1 Introduction

Climate variability modes whose fingerprints are felt in the Northern Pacific Ocean, such as the El Niño/Southern Oscillation (ENSO), the Pacific Decadal Oscillation (PDO) and the North Pacific Gyre Oscillation (NPGO), have been shown to exert an important influence on the biogeochemistry and upwelling properties of the California Current System (CalCS) (e.g., Bograd and Lynn, 2001; Friederich et al., 2002; Chhak and Di Lorenzo, 2007; Di Lorenzo et al., 2008, 2009). Through changes in circulation and upwelling, in surface ocean temperature, and in the vertical structure of the water column in the CalCS, the local carbon fluxes and biology are indirectly influenced through these modes of climate variability. The individual modes of climate variability - ENSO, PDO and NPGO - are not completely independent of each other. Studies have shown that the PDO and NPGO are linked to ENSO through the atmospheric variability of the North Pacific, as these two modes of climate variability are considered to be the oceanic expressions of the Aleutian Low (the low pressure system over the Gulf of Alaska) and the North Pacific Oscillation, respectively (e.g., Di Lorenzo et al., 2010; Furtado et al., 2011). During positive phases of both ENSO and PDO, the CalCS experiences positive sea surface temperature (SST) anomalies due to a shallowing of the upwelling cell. It has been shown that due to the decrease in vertical mixing during warm PDO phases, fewer nutrients are upwelled to the surface, causing a reduction in biological productivity (Chhak and Di Lorenzo, 2007). In general, the NPGO phases tend to have an opposite effect on the CalCS than ENSO and PDO, with cooler SSTs during positive phases and a general intensification of upwelling-favorable winds south of around 38°N, causing a deepening of the upwelling cell (Chhak et al., 2009; King et al., 2011). North of 38°N though, positive NPGO phases lead to a strengthening of the Aleutian Low, which favors a shallower upwelling cell in those regions. Di Lorenzo et al. (2008) concluded that in the southern CalCS, the positive influence of the NPGO on the alongshore, equatorwards wind made it an ideal indicator for changes in upwelling and nutrient supply to the surface and Di Lorenzo et al. (2009) found that in that region previously unexplained fluctuations in salinity, nutrients and chlorophyll correlated significantly with the NPGO.

So far, no study has investigated the interannual variability of air–sea CO_2 fluxes and pCO_2 in the CalCS and to what extent this variability is controlled by different modes of climate variability such as ENSO, PDO and NPGO. The goal of this study is to quantify this interannual variability, as it may mask long-term trends in the air–sea CO_2 fluxes. Furthermore, we aim to shed light on the sensitivity of air–sea CO_2 fluxes and pCO_2 to fluctuations in large-scale climatic forcing patterns, so as to understand to what degree these patterns drive the interannual variability of carbon fluxes in the CalCS. In addition, we explore through which oceanic drivers that these forcing patterns ultimately determine pCO_2 and the air–sea CO_2 fluxes in the CalCS. There are four main oceanic drivers which determine surface ocean pCO_2, namely dissolved inorganic carbon (DIC), alkalinity (Alk), temperature (T) and salinity (S). Turi et al. (2014a) showed that the importance of these drivers in determining the seasonal variability of pCO_2 varies locally: in the

nearshore 100 km changes in DIC, and to a lesser extent T, were found to play the most important role in driving the seasonal cycle of pCO_2. In the offshore 100–800 km however, T was found to be the crucial driver, whereas the contributions of DIC, Alk and S tended to cancel each other out. The driving mechanisms behind the changes in these drivers were found to be a combination of upwelling and biological productivity. It is unclear what effect ENSO, PDO and NPGO have on these drivers and mechanisms and ultimately on pCO_2 in the CalCS and whether there is a local difference between their influence in the nearshore versus the offshore regions of the CalCS. Here, we use a hindcast simulation from 1979 to 2012 from the same regional oceanic model (ROMS) as used by Turi et al. (2014a) to demonstrate that these three variability modes indeed have an important influence on the carbonate system of the CalCS.

5.2 Methods

We use a coupled physical-biogeochemical oceanic model to simulate the biogeochemistry and carbon cycling in the CalCS over the time period 1979 to 2012. The physical model is based on the UCLA-ETH version of ROMS (Marchesiello et al., 2003; Shchepetkin and McWilliams, 2005), while coupled to this is a simple nitrogen-based nutrient-phytoplankton-zooplankton-detritus (NPZD) model. The NPZD model includes an interactive carbon module, which is linked to the organic nitrogen cycle with a fixed stoichiometric Redfield ratio of $C : N = 106 : 16$ (Redfield et al., 1963), and provides three state variables: DIC, Alk and calcium carbonate ($CaCO_3$). The NPZD model is described in more detail in Gruber et al. (2006), while Turi et al. (2014a) and Hauri et al. (2013b) provide an extensive description of how the carbon variables are implemented in the model.

With an average horizontal grid spacing of 5 km, the model is capable of resolving mesoscale eddy structures and filaments as well as important upwelling-related circulation features of the US West Coast. The model's vertical structure consists of 32 σ-levels with increased resolution towards the surface and the nearshore areas, and its spatial extent covers roughly the region from 30 to 50°N and extends up to 1250 km offshore (Turi et al., 2014a,b).

All analyses done in this study are based on the same model simulations as used in Turi et al. (2014b) and are described in detail there. Here, we focus only on the hindcast simulation with increasing atmospheric CO_2, daily varying physical atmospheric forcing and monthly varying lateral boundary condition (simulation termed "HCast" in Turi et al., 2014b). A detailed description of the initial conditions and of the atmospheric and lateral boundary conditions used force the model, as well as an extensive model evaluation can be found in Turi et al. (2014b). Our modeled data is averaged over roughly three days, from which we compute monthly or annual means for further analyses.

For the analyses of the climate indices, we used (i) the monthly Multivariate ENSO Index

(MEI) from NOAA's Earth System Research Laboratory (ESRL) as an indicator of the El Niño/La Niña cycle (e.g., Wolter and Timlin, 1993), (ii) the monthly PDO index from the Joint Institute for the Study of Atmosphere and Ocean (JISAO; Mantua et al., 1997) and (iii) the monthly NPGO index as first introduced and distributed by Di Lorenzo et al. (2008).

5.3 Results

5.3.1 Temporal scales of variability in air–sea CO_2 fluxes and pCO_2

We begin by analyzing the different frequency modes of the air–sea CO_2 fluxes in the CalCS for a nearshore (0–100 km) and an offshore (100–800 km) domain separately, based on model output averaged over three days (Fig. 5.1; analysis domains indicated by contour lines in Fig. 5.3). The temporal variability of air–sea CO_2 fluxes in the nearshore 100 km is clearly larger than in the offshore area, with extreme peaks in outgassing with values of up to 13 mol C m^{-2} yr^{-1} (e.g., in 1996, 2002 and 2008), occurring mainly during the upwelling season ($\sim$April to September; not shown explicitly). Clear seasonal signals emerge both for the nearshore and the offshore domains (Fig. 5.1a), with the magnitude, mean and timing of the seasonal cycles differing between the two regions (Fig. 5.1b): the nearshore area loses on average 1.26 mol C m^{-2} yr^{-1} to the atmosphere, while the offshore area outgasses a net 0.34 mol C m^{-2} yr^{-1} over the time period 1979–2012. In addition, the peak in outgassing is reached roughly one month earlier in the nearshore area compared to the offshore (July vs. August), which is likely due to a combination of a lag in the timing of upwelled DIC reaching the offshore regions and the local biology there drawing down surface ocean pCO_2 levels.

To determine the different variability modes in the air–sea CO_2 fluxes, we isolate the low- from the high-frequency variability. To this end, we use a fast Fourier transform (FFT) on the detrended and deseasonalized data with a cutoff frequency of one year (Fig. 5.1c, d and e). This analysis reveals that the interannual variability is substantially higher in the nearshore 100 km than between 100 to 800 km. This low-frequency amplitude is roughly of the order of the mean CO_2 fluxes for both the nearshore and the offshore regions (compare with Fig. 5.1b). However, compared to the amplitude of the seasonal cycle, the nearshore signal is more important than the offshore signal. Superimposed on the seasonal cycle, the interannual fluctuations in the nearshore region can act to enhance the seasonal amplitude by up to 70%, such as during the year 2008, thus accounting together for up to roughly 30% of the maximum total variability during that year. The high-frequency component of pCO_2 variability (Fig. 5.1e) shows a signal which emerges from the mean white noise and is indicative that interannual forcing of the CalCS also affects the short-term variability of pCO_2. However, in the following, we will focus our analyses exclusively on low-frequency variability on the order of one year or longer.

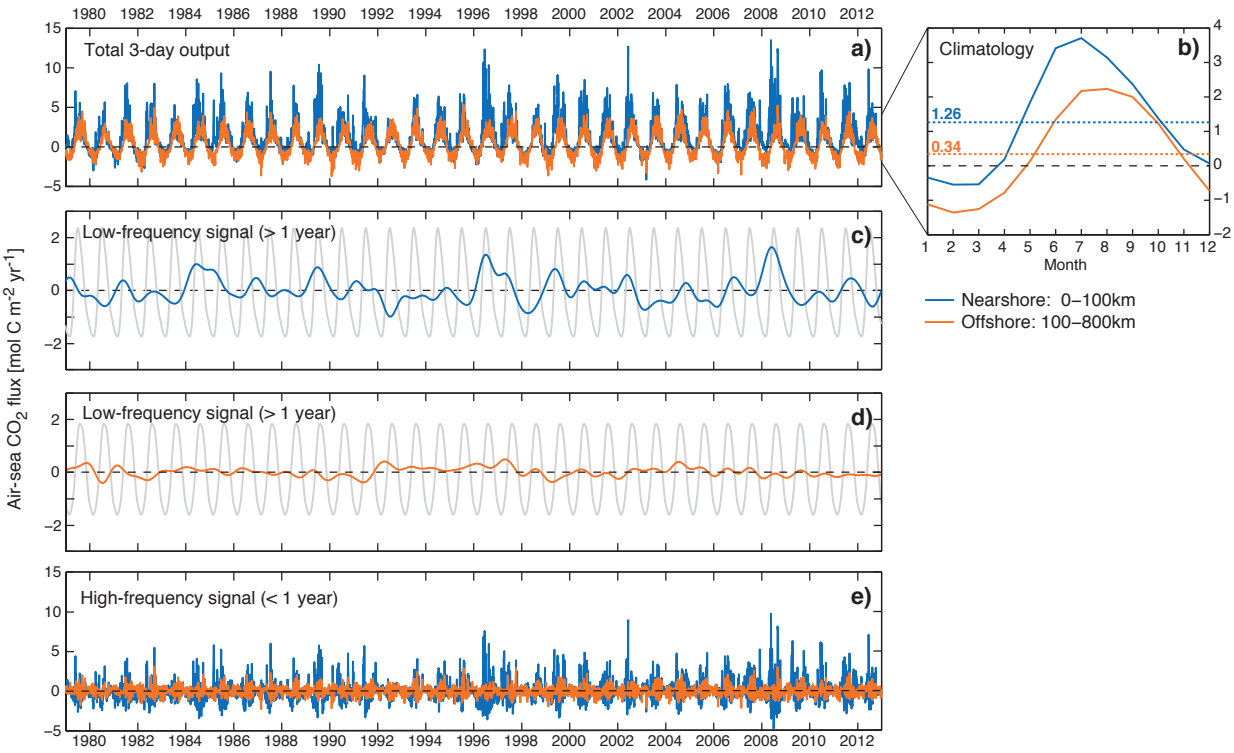

Figure 5.1 Temporal evolution of nearshore- and offshore averaged air–sea CO_2 fluxes from 1979 to 2012 for **(a)** 3-day averages, **(c)** the nearshore low-frequency, **(d)** the offshore low-frequency and **(d)** the high-frequency components of these 3-day averages. The separation into a low- and a high-frequency component was performed on detrended and deseasonalized 3-day averages with a fast Fourier transform (FFT) filter, using a cutoff frequency of one year. Any linear trends in the data were removed prior to the FFT analysis. Panel **(b)** shows the long-term monthly climatologies of the nearshore- and offshore-averaged air–sea CO_2 fluxes and their respective long-term means (dotted lines). The light gray lines in panels **(c)** and **(d)** are the respective seasonal cycles for the nearshore and the offshore regions, with long-term means removed. Positive values of air–sea CO_2 fluxes indicate an outgassing, while negative values are an uptake by the surface ocean.

5.3.2 Relationship of air–sea CO_2 fluxes and pCO_2 to large-scale climate variability modes

To determine whether this low-frequency signal can be explained by mechanisms of remote forcing in the CalCS, we correlate the nearshore- and offshore-averaged air–sea CO_2 fluxes with the ENSO, PDO and NPGO indices (Fig. 5.2). From this analysis we can gain initial insight into the influence of these three climate variability modes on the CalCS: all three of them oppositely correlate with the air–sea CO_2 fluxes for the nearshore versus the offshore region, while the NPGO has an opposite effect on pCO_2 in the CalCS to those of ENSO and PDO. In general, the PDO and NPGO correlate slightly better with the air–sea CO_2 fluxes in the offshore region, whereas for ENSO the correlation is higher in the nearshore 100 km. In the nearshore region, the correlations with ENSO and PDO are both negative and on the order of –0.4, while the NPGO positively correlates with the mean air–sea CO_2 flux at around 0.3 (Fig. 5.2a). Conversely, in the offshore region, the correlation with NPGO is negative at –0.43, while the ENSO and the PDO correlate with the opposite sign with values of 0.24 and 0.51, respectively (Fig. 5.2b). As was the case

for the total air–sea CO_2 flux variability in Fig. 5.1a, the variability of the low-frequency air–sea CO_2 fluxes is also roughly twice as high in the nearshore compared to the offshore region (Fig. 5.2). It should be noted that these correlations between the air–sea CO_2 fluxes and the individual climate indices were computed at zero lag. We tested correlations for a sequence of increasing lags at monthly resolution and found that they did not differ dramatically from the correlation at zero lag (maximum deviation of ± 0.01; not shown).

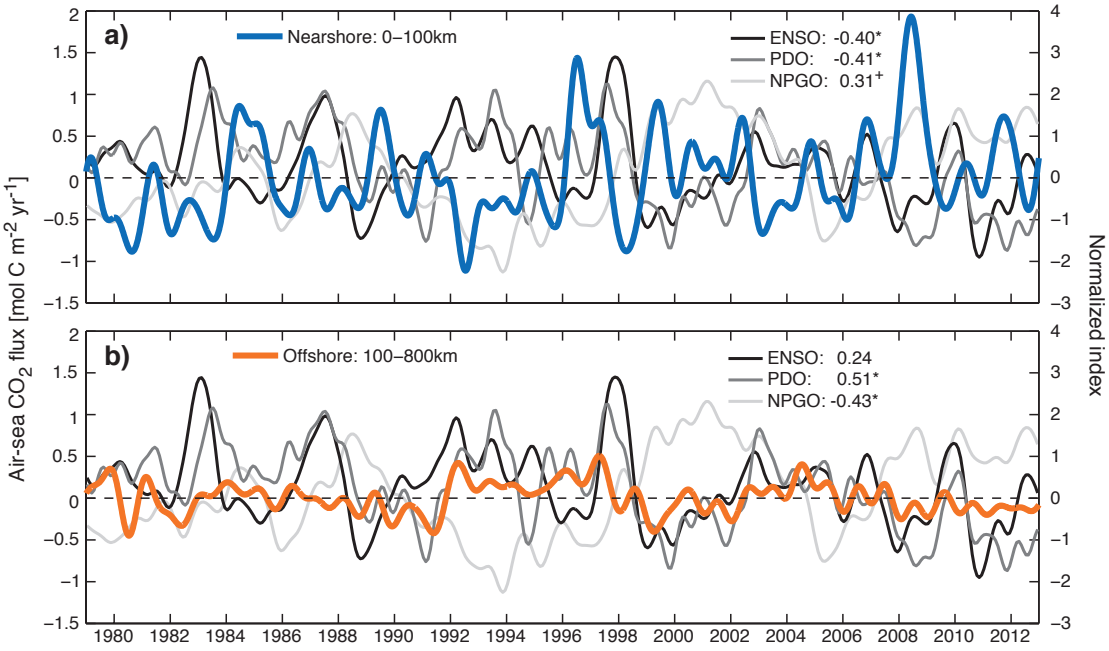

Figure 5.2 Temporal evolution of low-frequency **(a)** nearshore- and **(b)** offshore-averaged air–sea CO_2 fluxes from 1979 to 2012 (the blue and orange lines are identical to the ones in Fig. 5.1c and d). The lag zero correlations of the air–sea CO_2 fluxes with the ENSO (black lines), PDO (dark gray lines) and NPGO (light gray lines) indices are indicated, with correlations at the 90% confidence interval (CI) marked with a plus sign and at the 95% CI with a star sign. The low-frequency signals for the CO_2 fluxes and the three climate indices were computed with a fast Fourier transform (FFT) filter, with a cutoff frequency of one year. The original temporal resolution of the air–sea CO_2 fluxes is 3-day averages, while the original climate indices are monthly values. Any linear trends in the air–sea CO_2 fluxes were removed prior to the FFT analysis. Positive values of air–sea CO_2 fluxes indicate an outgassing, while negative values are an uptake by the surface ocean.

The magnitude and sign of the air–sea CO_2 fluxes are determined to the largest extent by the difference between atmospheric and oceanic pCO_2, with the magnitude of the fluxes being further modified by the CO_2 solubility (K_0) of seawater and the gas transfer velocity (k_w) at the air–sea interface (see Eq. 1 in Turi et al., 2014a). As variations in atmospheric pCO_2 are small compared to oceanic pCO_2 and fluctuations in K_0 and k_w are of lesser importance in determining the absolute CO_2 fluxes, we concentrate our following analyses on oceanic pCO_2 rather than the air–sea CO_2 fluxes. Figure C.1a highlights that - as was the case for the air–sea CO_2 fluxes - the total pCO_2 variability is highest in the nearshore 100 km, and decreases quickly to half of the total variability already at 200 km from the coast. Performing the same FFT analysis as for the air–sea CO_2 fluxes confirms that the high-frequency variability explains a major part of this high nearshore variability, although the low-frequency signal nevertheless shows a distinct nearshore-

offshore gradient in pCO_2 variability (Fig. C.1b and c). In the following, we will focus our analyses on pCO_2 as an indicator of air–sea CO_2 fluxes.

To investigate whether there is a difference in the influence of ENSO, PDO and NPGO on pCO_2 for individual seasons, we correlate pCO_2 with the three climate indices for each season separately (Fig. 5.3). The seesaw pattern in the sign change of the correlations between the nearshore and the offshore region which was already hinted at in Fig. 5.2, is clearly visible also on a seasonal timescale, and emerges particularly in spring (MAM) and summer (JJA) for all three climate indices (Fig. 5.3). Furthermore, there is a distinct difference in how well the climate indices correlate with pCO_2 for the individual seasons. In the case of PDO, the largest absolute correlations with the clearest spatial patterns between nearshore and offshore are found in winter (DJF), spring and summer with correlations of up to ± 0.6. For ENSO and NPGO on the other hand, the correlations tend to be best in spring and summer, with values lying between –0.5 and 0.5. The spatial correlation patterns for fall (SON) are less distinct for all three climate indices, although a nearshore signal around Cape Mendocino ($\sim$40°N) does emerge for ENSO and PDO and correlations lie between –0.4 and 0.4.

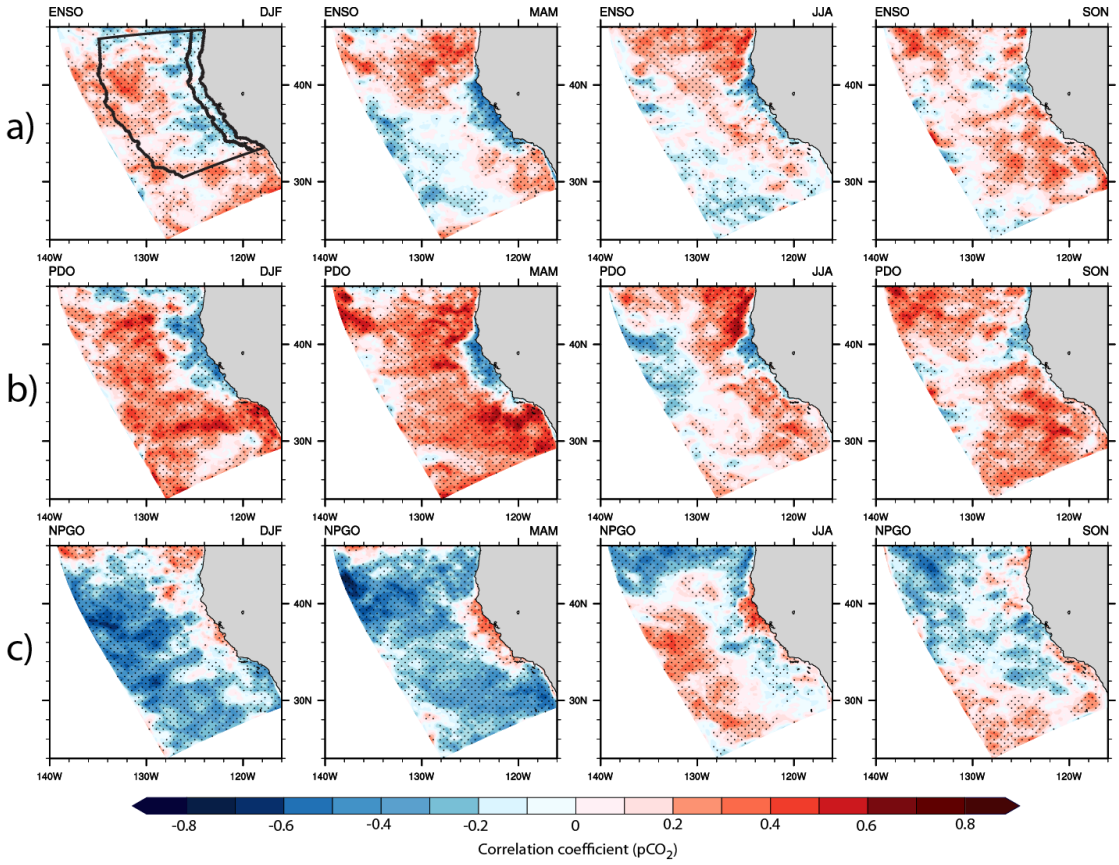

Figure 5.3 Correlations at lag zero of individual seasons on an annual basis between surface ocean pCO_2 and **(a)** ENSO, **(b)** PDO and **(c)** NPGO. The stippling indicates correlations that are significant at the 95% confidence level.

From these correlations between pCO_2 and the individual climate indices, we cannot yet deduce the absolute magnitude of changes in pCO_2 related to a change in the climate indices.

To determine to what degree a change in each index can actually predict a change in pCO_2, we additionally investigate the sensitivity of pCO_2 to per unit changes in the three indices (Fig. 5.4). This analysis reveals that the sensitivity of pCO_2 is much larger in the nearshore 100 km, compared to the offshore 100–800 km (see Fig. 5.5 for nearshore- and offshore-averaged pCO_2 sensitivities). The sensitivity of pCO_2 is particularly high for ENSO and PDO in spring in the nearshore region, where an increase by one index unit can result in a decrease in pCO_2 of up to –36 μatm (Fig. 5.5a and b). The effect of ENSO on pCO_2 in the nearshore region is nearly as important in summer (up to 31 μatm), while PDO also exerts a strong influence on pCO_2 during winter (up to 29 μatm) As we established previously in Figs. 5.2 and 5.3, the sensitivity of pCO_2 to changes in the NPGO is opposite in sign to its response to ENSO and PDO, with an increase in the NPGO index leading to a maximum increase in pCO_2 in the nearshore region of up to 20 μatm (spring and summer). Averaged over the nearshore and the offshore regions, the sensitivities of pCO_2 to the climate indices are dramatically decreased, and only on the order of a few μatm, highlighting that magnitude of interannual variability varies strongly locally.

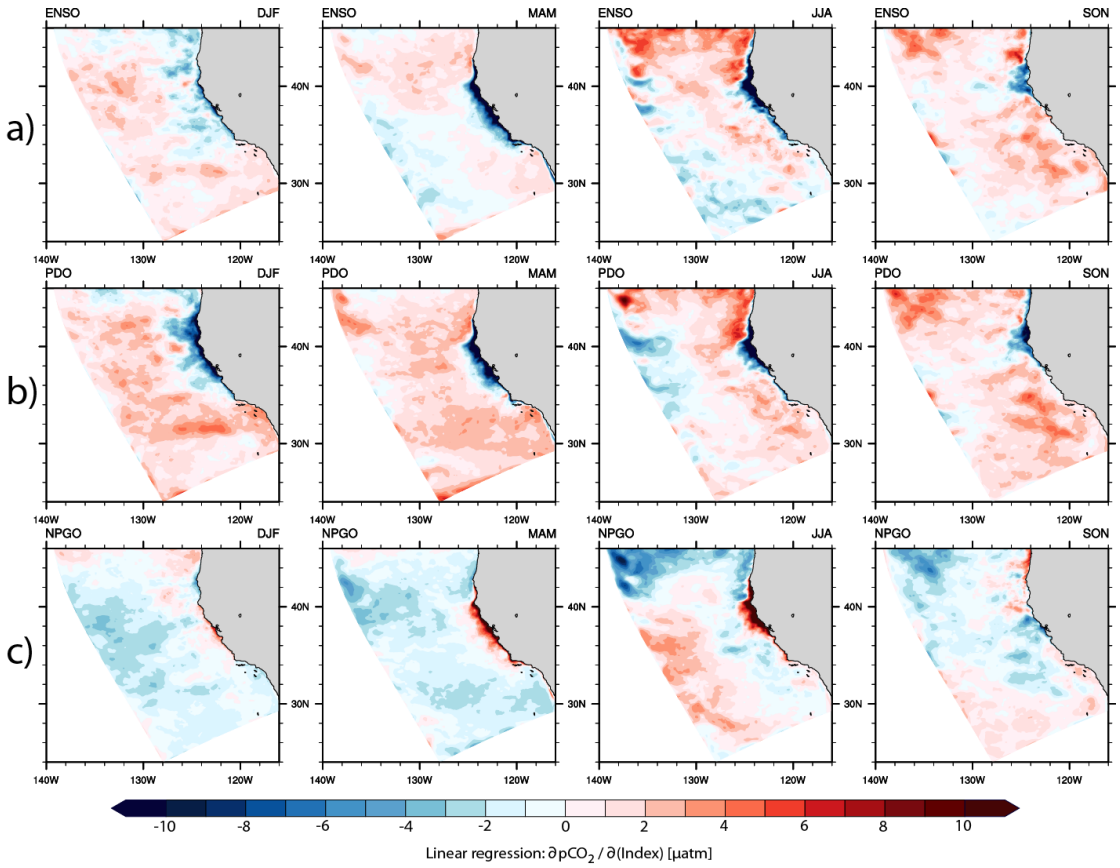

Figure 5.4 Sensitivity of pCO_2 to per unit index changes in **(a)** ENSO, **(b)** PDO and **(c)** NPGO, calculated as the linear regression slopes of individual seasons on an annual basis.

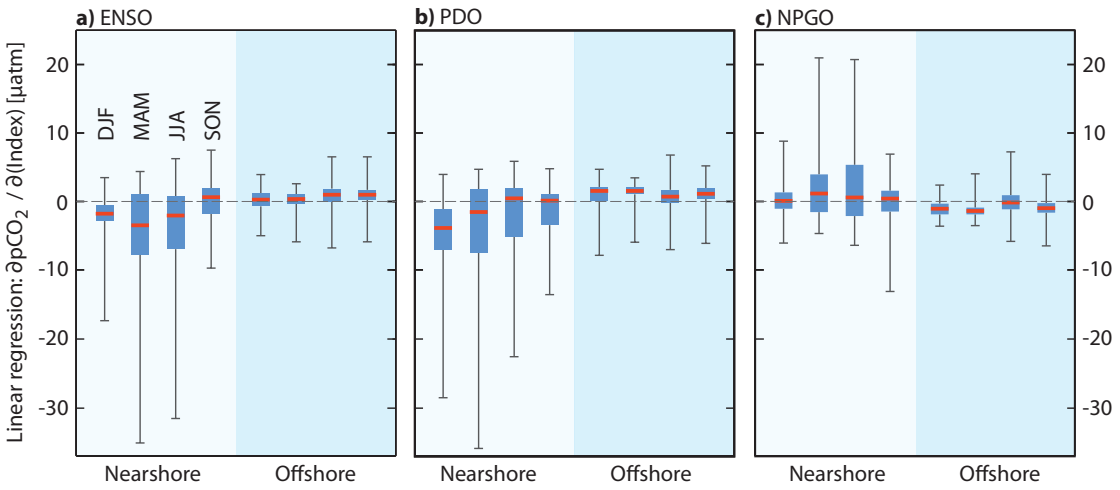

Figure 5.5 Nearshore- and offshore-averaged sensitivities of pCO_2 to per unit index changes in **(a)** ENSO, **(b)** PDO and **(c)** NPGO, calculated as the linear regression slopes of individual seasons on an annual basis. See black contour lines for the extent of the nearshore 0–100 km and offshore 100–800 km domains. The red lines indicate the mean pCO_2 sensitivities, while the extent of the blue boxes represents the interquartile range. The minima and maxima of the boxes' arms correspond to the range of possible pCO_2 sensitivities within each domain and season.

5.3.3 Through which drivers do large-scale climate variability modes modulate pCO_2?

Oceanic pCO_2 is influenced by four main drivers, namely DIC, Alk, T and S (Turi et al., 2014a). By affecting any of these four drivers, ENSO, PDO and NPGO can act to indirectly alter pCO_2. In Fig. 5.4 we established the sensitivity of pCO_2 to changes in these three climate indices. To determine through which of these four drivers ENSO, PDO and NPGO affect pCO_2, we use a first-order Taylor expansion approach to separate the sensitivity of pCO_2 to a change in the individual climate indices into four components which correspond to changes in pCO_2 arising from the sensitivities of DIC, Alk, T and S to changes in the three climate indices (following Lovenduski et al., 2007; Doney et al., 2009b; Turi et al., 2014a). As Turi et al. (2014a) did, we disregard the small contribution of the indices via nutrients to changes in pCO_2. The following equation explains our procedure for any given climatic index ("Index"):

$$\frac{\partial pCO_2}{\partial Index} \approx \underbrace{\frac{\partial pCO_2}{\partial DIC} \cdot \frac{\partial DIC}{\partial Index}}_{DICterm} + \underbrace{\frac{\partial pCO_2}{\partial Alk} \cdot \frac{\partial Alk}{\partial Index}}_{Alkterm} + \underbrace{\frac{\partial pCO_2}{\partial T} \cdot \frac{\partial T}{\partial Index}}_{Tterm} + \underbrace{\frac{\partial pCO_2}{\partial S} \cdot \frac{\partial S}{\partial Index}}_{Sterm}, \tag{5.1}$$

where the sensitivity of pCO_2 to each driver was computed using the definitions from Sarmiento and Gruber (2006) (p. 329). The individual terms in Eq. 5.1 then represent the sensitivity of pCO_2

to changes in each driver induced by either ENSO, PDO or NPGO, which add up to the total sensitivity of pCO_2 to changes in these three climate indices as shown in Fig. 5.4. The derivatives of the four drivers with respect to the indices (second factor of each term in Eq. 5.1) are just the slopes of the linear regressions of the drivers with the indices (see Figs. C.2 to C.5 in the Appendix). This separation into four individual terms, corresponding to the four principal drivers of pCO_2, reveals that the strong nearshore signals in pCO_2 that can be seen for most seasons in Fig. 5.4 are driven to the largest extent by the DIC term from Eq. 5.1 (Fig. 5.6). The sensitivity of pCO_2 to changes in DIC shows the strongest nearshore-offshore gradient in spring and summer for all three climate variability modes, although the influence of PDO on pCO_2 through DIC is also clearly visible in winter all along the coast from California to Oregon. In fall, the sensitivity of pCO_2 to changes in DIC is less pronounced and shifted more towards the north, along the coast of Oregon for all three climate variability modes. The influence of the three climate indices on pCO_2 through changes in T and Alk is fairly homogeneous throughout the whole domain (Figs. 5.7 and 5.8), although the Alk term does tend to slightly counteract the effect of the DIC term in the nearshore 100 km in spring and summer. Increases in both ENSO and PDO act to increase pCO_2, while the effect of NPGO on pCO_2 through changes in Alk and T is negative. Changes in S are too small to contribute significantly to the total changes in pCO_2 and are not shown here (see Fig. C.6 in the Appendix).

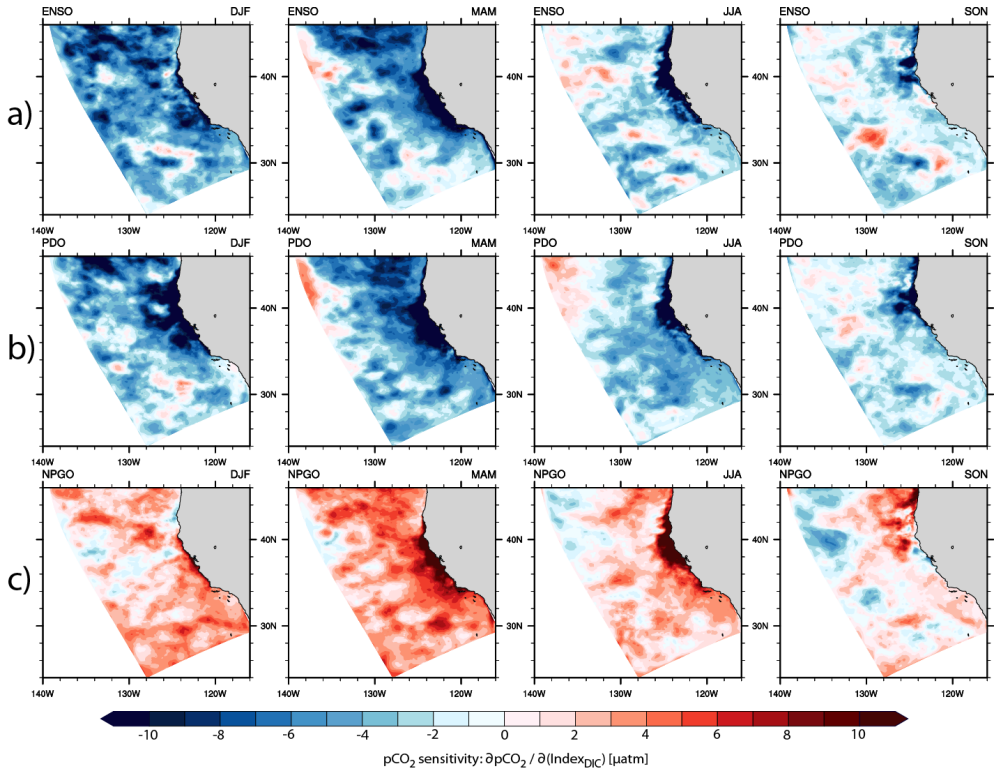

Figure 5.6 Sensitivity of pCO_2 to surface ocean DIC fluctuations induced by changes in **(a)** ENSO, **(b)** PDO and **(c)** NPGO (first term of Eq. 5.1).

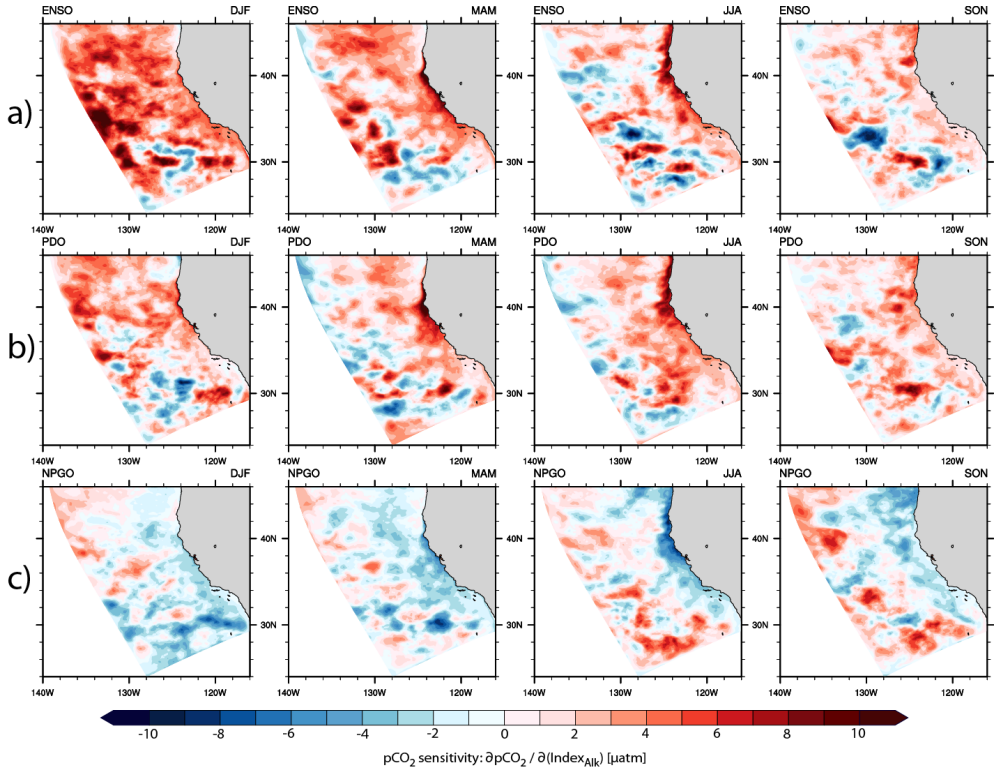

Figure 5.7 Sensitivity of pCO_2 to surface ocean Alk fluctuations induced by changes in **(a)** ENSO, **(b)** PDO and **(c)** NPGO (second term of Eq. 5.1).

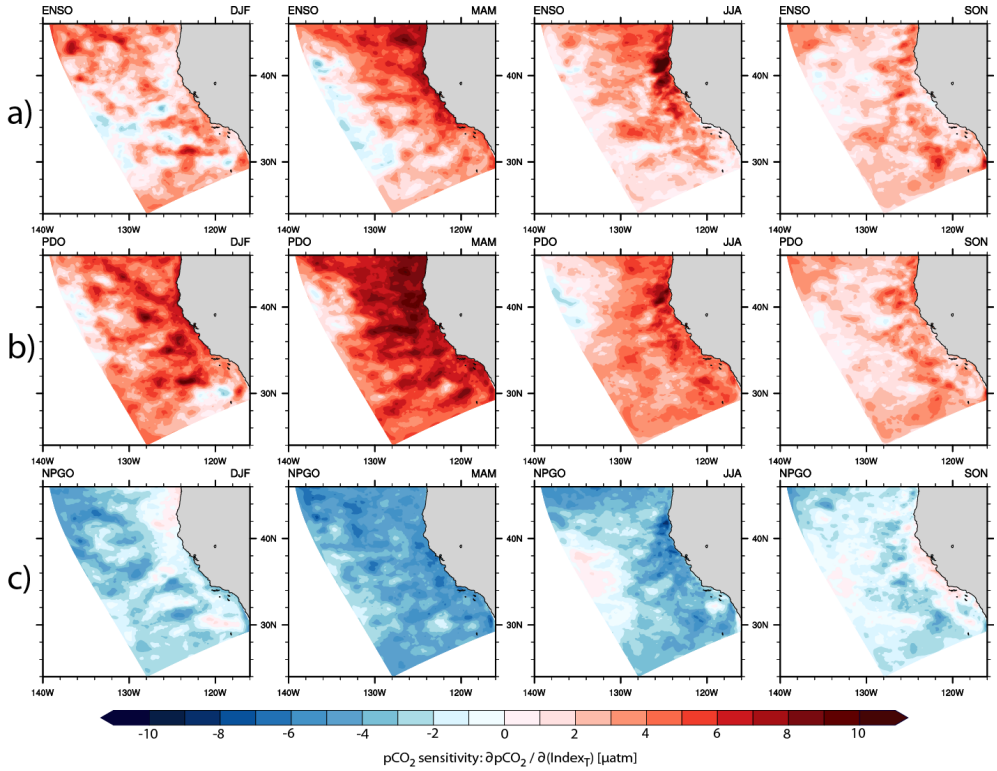

Figure 5.8 Sensitivity of pCO_2 to surface ocean T fluctuations induced by changes in **(a)** ENSO, **(b)** PDO and **(c)** NPGO (third term of Eq. 5.1).

5.4 Discussion and outlook

Several questions arise from our results: firstly, through which mechanisms do ENSO, PDO and NPGO affect DIC, Alk and T and ultimately drive pCO_2? And secondly, how do the changes in pCO_2 driven by interannual to decadal variations in ENSO, PDO and NPGO, as seen in Fig. 5.4, compare to (i) shorter-term fluctuations in pCO_2 and (ii) long-term pCO_2 trends?

To answer the first question, we refer to Turi et al. (2014a), who demonstrated that there are two main mechanisms which govern changes in pCO_2 in the near- and the offshore regions, namely upwelling and biological productivity. The patterns in Figs. 5.6 and 5.7, which indicate a stronger contribution of DIC and to some extent Alk in the nearshore regions, suggest that upwelling is the main process through which ENSO, PDO and NPGO can affect the surface concentration of DIC and Alk and hence alter pCO_2. Indeed, Turi et al. (2014b) demonstrate that strong negative or positive phases of these three climate indices can substantially alter the mean upwelling strength in the CalCS (see Fig. B.2 in the Appendix). Previous studies have shown that all three modes of climate variability affect the strength and depth of the upwelling cell (e.g., Chhak and Di Lorenzo, 2007; Chhak et al., 2009; Di Lorenzo et al., 2008, 2009; King et al., 2011). Consequently, the supply of nutrients to the surface is affected which in turn determines the degree of biological productivity. In order to quantify the relative responses of biological productivity and circulation to changes in ENSO, PDO and NPGO, we plan to do an extreme year composite analysis of the different carbon fluxes and pools in the CalCS.

To address the second question, we compare our results to findings from Turi et al. (2014a) and Turi et al. (2014b). Based on a climatological simulation with ROMS, representative of the years 2000–2001 in terms of atmospheric CO_2, Turi et al. (2014a) showed that the seasonal pCO_2 cycle has an amplitude of roughly $\pm 50\,\mu$atm in the nearshore 100 km, while in the offshore 100–800 km, the seasonal fluctuations are slightly smaller around $\pm 30\,\mu$atm (Figs. 9 and 10 in Turi et al., 2014a). Using a hindcast simulation from 1979 to 2012 with constant atmospheric CO_2, Turi et al. (2014b) demonstrated that trends in pCO_2 in the nearshore 100 km due to changes in the wind forcing alone can be as large as $20\mu\text{atm}\,\text{dec}^{-1}$ or 68μatm over the 34 years of the simulation (Fig. 4.3 in Turi et al., 2014b). We showed that the sensitivity of pCO_2 to changes in ENSO, PDO and NPGO can be locally very high, with values of up to 36μatm per unit of index change (e.g., ENSO and PDO in spring; Fig. 5.5). The locally high values are comparable to the amplitude of the pCO_2 seasonal cycle and the long-term trends, considering that during extreme years these climate indices can reach values of up to 3–4 units (Fig. B.2), resulting in a change in pCO_2 of up to 100–150 μatm for individual locations in the CalCS. This suggests that the interannual variability in pCO_2 and air–sea CO_2 fluxes is large enough to potentially mask any climate change-driven trends, making it challenging to recognize them among the natural variability of the carbon fluxes (e.g., Boyd et al., 2008; Henson et al., 2010; Keller et al., 2013).

Several shortcomings and uncertainties from this study need to be addressed in further detail.

For instance, due to the temporal resolution of our lateral boundary forcing being only monthly, any individual events occurring on shorter timescales cannot not be resolved at our lateral boundaries. This means that our model likely underestimates the influence of remote forcing by way of the oceanic lateral boundaries. Such events include incoming Kelvin waves from the eastern equatorial region, which manifest themselves in the CalCS as a northward propagation of a depression in the thermocline and a concurrent rise in sea surface height (Brown et al., 2001; Chavez et al., 2002). The speed of Kelvin waves along the North American Coast has been estimated to be around 222–268 km day^{-1} (Frischknecht et al., 2014), meaning that such a signal passes through our CalCS domain within roughly 1–2 weeks. This time frame is too short for individual events to be accurately resolved by our boundary forcing. It is possible that a sequence of individual events which affect the mean sea surface height and thermocline depth could be captured in our boundary forcing. However, any individual remote signals occurring on timescales shorter than one month can hence only be felt by way of the atmospheric boundary, as the temporal resolution of our forcing there is daily.

Furthermore, we found that on average, both the nearshore 0–100 km and the offshore 100–800 km are sources of CO_2 to the atmosphere, with mean flux densities of 1.26 and 0.34 mol C m^{-2} yr^{-1}, respectively (Fig. 5.1). This result is slightly different from what Turi et al. (2014a) found in their climatological simulations. There, the nearshore region was found to be a net source of CO_2 to the atmosphere of 0.78 mol C m^{-2} yr^{-1}, while the offshore region was a net sink of –0.16 mol C m^{-2} yr^{-1} (Table 3 of Turi et al., 2014a). Hence the air–sea CO_2 fluxes from our hindcast simulation have a tendency towards stronger outgassing compared to fluxes from previous climatological simulations. The most likely reason for this is that the hindcast simulations are forced with daily wind stress data, while the atmospheric forcing of the climatological simulations is only monthly, implying that using higher-frequency forcing has an impact on the mean state of the air–sea CO_2 fluxes. This does however not affect our conclusions in this study, as we focus on the long-term variability around detrended data and hence do not consider the mean state.

In addition, to account for changes in DIC and Alk due to freshwater input to the surface ocean, it would be more precise to apply a salinity-normalization to DIC and Alk in Eq. 5.1, and include an additional term accounting for the pCO_2 sensitivity to freshwater, as was done previously by Turi et al. (2014a).

5.5 Conclusions

We used a highly resolved regional ocean model of the US West Coast to model the interannual variability of air–sea CO_2 fluxes and pCO_2 in the CalCS from 1979 to 2012. We found a substantial interannual variability particularly in the nearshore 100 km, which can act to increase the

magnitude of the seasonal in air–sea CO_2 fluxes by up to 70% during years of extreme climatic fluctuations. This is for instance the case in 2008, a year during which ENSO and PDO were in strongly negative phases and NPGO in a strongly positive phase. It is known that negative ENSO and PDO phases as well as positive NPGO phases all act to intensify coastal upwelling in the CalCS, thus supplying the surface ocean with more DIC, which could explain the anomalous positive outgassing during such years. The nearshore- and offshore-averaged low-frequency air–sea CO_2 fluxes correlate well with all three modes of climate both in the nearshore and the offshore regions. The correlations of the air–sea CO_2 flux with PDO and NPGO are slightly higher in the offshore region, while ENSO correlates better with the CO_2 flux in nearshore 100 km. The low-frequency signal of pCO_2 shows a similar behavior to the one of the air–sea CO_2 fluxes: the sensitivity of pCO_2 to changes in these three indices shows a clear nearshore-offshore seesaw pattern, with the sensitivity being up to 7 times higher in the nearshore region (e.g., ENSO and PDO in spring). This clear onshore-offshore signal is determined by the different dominance of DIC in then nearshore versus Alk and T in the offshore region. The combined effects of DIC, Alk and T are thus responsible for the seesaw pattern between the nearshore and the offshore regions in the pCO_2 response to changes in ENSO, PDO or NPGO. There are no clear differences between the three modes of variability in their influence on the absolute magnitude of pCO_2 sensitivity to per unit changes in their indices. When looking at individual seasons, the sensitivity of pCO_2 to changes in the three climate variability modes tends to be largest in spring and summer and to some extent in winter in the case of PDO, whereas in fall, the nearshore signal is less pronounced. This indicates that the effect of the three climate indices on pCO_2 is most felt during the upwelling season (roughly April to September), whereas the influence of PDO on pCO_2 is important also during winter.

A study by Keller et al. (2013) on the time of emergence for climate change-driven trends versus natural variability, suggests that for carbon variables such as DIC, pCO_2 or pH - an indicator for ocean acidification - is on the order of 10 to 30 years for the Northeastern Pacific Ocean. Similarly, Henson et al. (2010) suggested that time series of chlorophyll and primary production should be on of $\sim$40 years before a climate change-driven trend can be detected. Here, as was the case in Turi et al. (2014b), our analyses are based on 34 simulation years from 1979 to 2012. Especially in system such as the CalCS, which we have shown here to be subject of extreme fluctuations in pCO_2 and air–sea CO_2 fluxes, this time period might be too short to significantly distinguish between long-term trends and high natural variability. Turi et al. (2014b) demonstrated that the trends in ocean acidification due to the rise in atmospheric CO_2 alone are undoubtedly significant and are easily distinguished from natural fluctuation. The trends due to changes in other physical climatic forcing however, such as changes in upwelling-favorable winds, are less prominent and thus more easily masked by natural variability. More work is called for to determine the timing at which such trends might escape from the natural "variability envelope" (e.g., Henson et al., 2010; Hauri et al., 2013a). Nonetheless, we have made substantial progress in quantifying the interannual variability of pCO_2 and air–sea CO_2 fluxes in the CalCS,

which will help in the detection and quantification of climate change-driven trends.

Acknowledgements The research leading to these results has received funding from the Swiss Federal Institute of Technology Zürich (ETH Zürich) and through the European Union's Seventh Framework Programme (FP7/2007-2013) under grant agreement n^o 283080, project GEOCARBON, and grant agreement n^o 264879, project CARBOCHANGE. The simulations used in this study were performed at the central computing cluster of ETH Zürich, Brutus. The ECMWF ERA-Interim Reanalysis data used to force our model at the atmospheric boundary were obtained from the ECMWF Data Server (http://www.ecmwf.int/research/era/do/get/era-interim). The Multivariate ENSO Index was obtained from http://www.esrl.noaa.gov/psd/enso/mei/, the PDO index from http://jisao.washington.edu/pdo/ and the NPGO index from http://www.o3d.org/npgo/. We are grateful to F. Lehner and D. Byrne for their invaluable comments on the manuscript.

Chapter 6

Synthesis

EBUS are regions which experience extreme fluctuations in biogeochemistry and carbon fluxes due to their natural setting: the wind-induced upwelling provides the surface ocean with an abundance of cool, nutrient- and DIC-rich water, which in turn impacts biological productivity, the offshore transport of carbon and the exchange of CO_2 with the atmosphere. It has been shown that EBUS are roughly ten times more productive than the open ocean and together account for up to 20% of the global fish catch, making them key regions for commercial fisheries. Hence, any perturbations of these system that have a lasting effect on organisms and their habitats would have important consequences for commercial fishing revenues (Cooley and Doney, 2009). Indeed, superimposed on the natural fluctuations occurring in EBUS are perturbations arising from recent changes in human activities, which include surface ocean warming, ocean acidification and deoxygenation, changes in primary production and increased eutrophication due to enhanced riverine input of nutrients (Bopp et al., 2013). These multiple stressors, along with other perturbations such as marine pollution, habitat destruction and overfishing, pose an ongoing threat to the organisms and ecosystems that are dependent on these coastal upwelling regions. However, it can be challenging to recognize climate change-driven trends in systems which show a high natural variability of carbon and biogeochemical fluxes, as is the case in EBUS (Henson et al., 2010). In order to separate the climate change-driven component from variability which arises from natural, subseasonal to interannual fluctuations, it is necessary to quantify the different variability modes and their spatial and temporal length scales.

In this PhD thesis, I used a set of eddy-resolving simulations of the US West Coast on the basis of ROMS to investigate the carbonate dynamics of the CalCS, which serves here as a case study for the other three EBUS. The CalCS is the EBUS with the most readily available carbon chemistry data, hence observational and modeling studies together can be used to progressively monitor the influence of multiple stressors on the carbon fluxes and biogeochemistry of the CalCS.

Specifically, I addressed the following questions in this thesis:

- Is the CalCS a source of a sink of CO_2 with respect to the atmosphere? How large is the seasonal variability of pCO_2 and air–sea CO_2 fluxes and what are the most important drivers behind this seasonal variability? (**Chapter 3**)

- How large are the trends in ocean acidification over the last few decades and does the magnitude of these trends differ within the CalCS? What other mechanisms, apart from the rise in atmospheric CO_2, are drivers of trends in ocean acidification? (**Chapter 4**)

- How does the interannual to decadal variability in pCO_2 and air–sea CO_2 fluxes compare to the seasonal variability and long-term trends? What modes of climate variability exert the most prominent impact on pCO_2 in the CalCS and through which drivers? (**Chapter 5**)

By investigating these questions, I was able to shed light on the different modes of variability in carbon fluxes in the CalCS on a seasonal to interannual timescale and determine trends in the carbonate system of the CalCS over the last three decades.

6.1 Major scientific findings

Our studies are the first to use a highly resolved regional oceanic model such as ROMS to investigate pCO_2 and the air–sea CO_2 fluxes in the CalCS. Furthermore, our use of hindcast simulations forced with daily ERA-Interim data from 1979 to 2012 to investigate the progression of ocean acidification and the interannual variability of carbon fluxes in the CalCS is a state-of-the-art development in regional ocean carbonate system modeling. In the following, I summarize the major scientific findings from Chapters 3, 4 and 5.

- **pCO_2 and the associated air–sea CO_2 fluxes in the CalCS exhibit a strong spatiotemporal heterogeneity (Chapter 3).** The highest pCO_2 values and strongest CO_2 outgassing occur in the coastal 100 km strip. Further offshore of 100 km, the CalCS is on average a weak sink of CO_2. The high variability in air–sea CO_2 fluxes is mainly driven by the seasonal cycle in pCO_2, although in the nearshore 100 km the subseasonal component plays an additional important role. This implies that in order to characterize the region in terms of CO_2 fluxes, data sampling must be spatially and temporally sufficiently resolved to capture this high variability. This has implications for the observational community, as the spatial representativeness of pointwise measurements decreases dramatically with increasing distance from an individual station. In the studies of this thesis, we have made use of several in-situ databases for our model evaluation, including DIC and Alk measurements from the Feely et al. (2008) cruise, pCO_2 measurements from the CalCOFI Line 67 (courtesy of F. Chavez) and from a mooring in Santa Monica Bay, California (courtesy of A. Leinweber), as well as measurements from several global databases such as SOCAT (Pfeil et al., 2013)

and the global surface pCO_2 database (Takahashi et al., 2013). However the spatial and temporal coverage of the combination of all these measurements is still lacking, particularly in the nearshore 100 km, where a denser sampling frequency is particularly important due to the high variability of carbon fluxes there. Therefore, it would be highly desirable to expand the current observational network to include more moorings and underway cruises or to make potential existing measurements more readily available to the global carbon community. Based on preliminary analyses of spatial and temporal correlation length scales (Fig. A.5), I suggest for the nearshore region that the sampling density should be increased to measurements roughly every 20–25 km and one within 1–2 weeks. For the region offshore of 100 km, this could be increased to 120–150 km and every month. In the meantime, our model simulations can provide a spatially and temporally more synoptic view on the variability of CO_2 fluxes and thus provide guidance for a potential strengthening of the observational network.

- **The present CalCS is an almost neutral system in terms of air–sea CO_2 fluxes (Chapter 3).** This is due to the spatial compensation between strong outgassing in the nearshore 100 km and a weak, but widespread uptake of CO_2 in the offshore domains. This spatial compensation was found to be a combination of several driving mechanisms: in the nearshore regions, the upwelling of DIC-rich waters is responsible for elevating pCO_2 levels to above atmospheric values. In the offshore regions on the other hand, the concurrent upwelling of nutrients stimulates enough biological productivity to draw down CO_2 levels below those of the atmosphere. In Chapter 4 we showed that the trends in the uptake and outgassing of CO_2 from 1979 to 2012 can vary locally between –0.6 and 1.2 mol C m^{-1} yr^{-1} dec^{-1} (Fig. B.3a). On the one hand, due to the increase in atmospheric CO_2 alone, the whole CalCS between 0–800 km becomes a slightly stronger CO_2 sink, with an average uptake trend of –0.02 mol C m^{-1} yr^{-1} dec^{-1} (Fig. B.3b). On the other hand, the anomalously strong outgassing trend along the coast of Oregon and northern California, attributable to an increase in upwelling-favorable winds, acts to compensate this domain-wide uptake strengthening (Fig. B.3c). Taken together, these effects account for an overall slight increase in the outgassing strength of $\sim$0.01 mol C m^{-1} yr^{-1} (or 0.12 Pg C yr^{-1}) over the whole 34 years. The question remains how the CO_2 source/sink behavior of the CalCS will react to in the future to a combination of multiple stressors, such as the continuing rise in atmospheric CO_2 and changes in the physical climatic forcing and whether this spatial compensation between strong outgassing in the nearshore and uptake in the offshore will still hold. Based on the hindcast simulation it seems that an increase in upwelling outweighs the effect of rising atmospheric CO_2 and suggest that if these effects continue linearly in the future, the CalCS will become a stronger outgassing region. However, due to non-linearities in the carbonate system and the limited predictability of future CO_2 emissions, this conclusion is possibly too simplistic. To address the fate of the source/sink behavior of the CalCS, I propose to run a set of future simulations, which will be discussed in more

detail in Section 6.3.

- **Temperature and DIC are the most important drivers for seasonal fluctuations in $p\mathbf{CO_2}$ (Chapter 3).** Temperature is the more dominant driver in the offshore regions, while DIC is the major determinant of $p\mathrm{CO_2}$ in the nearshore 100 km. With future climate change, the importance of these individual drivers will likely be affected due to changes in upwelling, surface ocean warming or cooling or changes to the vertical structure and mixing of the water column and hence their combined effects on $p\mathrm{CO_2}$ and the air–sea $\mathrm{CO_2}$ fluxes will change. In Chapter 4 we model a domain-wide decrease in temperature and increase in biological productivity in the offshore regions over the last 3 decades. Both of these processes act to reduce surface ocean $p\mathrm{CO_2}$ and hence increase the $\mathrm{CO_2}$ sink strength in the CalCS. In Section 6.3 I discuss plans for running a set of future simulations to investigate whether these trends will continue throughout the 21$^{\mathbf{st}}$ century and to determine the relative contributions of changes in biology and temperature to the source/sink behavior of the CalCS.

- **The rise in atmospheric $\mathbf{CO_2}$ from 1979 to 2012 of roughly 60μatm is responsible for a domain-wide increase in surface ocean $p\mathbf{CO_2}$ and decreases in pH and Ω_{arag} in the CalCS (Chapter 4).** Over the same time period, we model a domain-wide shoaling of the aragonite saturation horizon and a spreading of the volume of waters undersaturated with respect to aragonite. All of these changes are particularly pronounced in the nearshore 100 km along the coast of Oregon and northern California, with a center of action offshore of Cape Mendocino ($\sim$40°N). This change in the carbonate chemistry of the CalCS has a direct impact on the physiological health of organisms which use aragonite or calcite to synthesize their shells and skeletons. This comprises a myriad of organisms across different trophic levels, including many shellfish, such as oysters, clams, mussels and crabs, but also sea urchins, pteropods and gastropods (e.g., Orr et al., 2005; Fabry et al., 2008; Cooley and Doney, 2009; Hauri et al., 2009; Bednarsek et al., 2014). If Ω_{arag} drops below a value of one, aragonite and calcite start to dissolve (e.g., Kleypas et al., 2006). This has been shown to happen to live pteropods in laboratory experiments (Orr et al., 2005) but has also been observed to occur presently for pteropods in their natural environment along the Washington-Oregon-California coast (Bednarsek et al., 2014). Together with other stressors that are expected to occur as a consequence of climate change, such as upper ocean warming, the expansion of oxygen minimum zones or changes in nutrient inputs (Bopp et al., 2013), ocean acidification poses an ongoing threat to coastal ecosystems such as the CalCS. We have shown in this study that this threat has increased over the last three decades due to rising atmospheric $\mathrm{CO_2}$ and is therefore likely to continue in the near future, as has been alluded to by various other modeling studies (e.g., Gruber et al., 2012; Hauri et al., 2013b,a). In Section 6.3 we discuss how to address this complex problem of the future effects of multiple stressors on the CalCS.

- **An intensification of upwelling-favorable winds around Cape Mendocino, California, is the main driver for the local acceleration of ocean acidification in the CalCS (Chapter 4).** An in-situ study by García-Reyes and Largier (2010) confirms the increase in alongshore wind speed north of ∼38°N which we see in our ERA-Interim wind forcing. However, several questions remain to be addressed. Firstly, is this increase in upwelling-favorable winds due to a climate change-driven intensification of the thermal land-sea gradient along the coast in the CalCS, as has been suggested by several previous studies (e.g., Bakun, 1990; Diffenbaugh et al., 2004; Narayan et al., 2010), or are trends in the different modes of climate variability such as ENSO, PDO or NPGO over the time period from 1979 to 2012 responsible for these anomalous winds? And secondly, will alongshore winds continue to intensify in the future and if so, what are the driving mechanisms behind these changes? In Chapter 4 we highlighted the strong connection between these three climate variability modes and coastal upwelling (Fig. B.2), suggesting that our trends over the last three decades could indeed be mainly influenced by transitions between strong negative or positive phases of these modes throughout our simulation time period. However, the shortness of the simulation period (34 years) makes a clear distinction between climate change-driven trends and natural, interannual variability challenging (Henson et al., 2010). This highlights again the need for a future simulation of the CalCS over the 21st century (see Section 6.3) and for the continuous future monitoring of wind data along the coast of the CalCS, as has already been done in the past by NOAA's National Data Buoy Center (analyzed for instance by: García-Reyes and Largier, 2010; Seo et al., 2012). Furthermore, Song et al. (2011) demonstrated that the representation of upwelling in the CalCS in ROMS is highly dependent on the horizontal resolution of the wind forcing product and that with increasing resolution of the forcing product upwelling becomes stronger. This underlines the importance of using a highly resolved wind forcing product to accurately represent coastal upwelling intensity, variability and long-term trends. A discussion of whether our ERA-Interim wind forcing product with a horizontal resolution of ∼79 km is satisfactory can be found in Section 6.2.

- **A widespread decrease in sea surface temperature and increase in biological productivity act to slightly dampen the progression of ocean acidification (Chapter 4).** However, these effects are not strong enough to compensate the local acceleration of ocean acidification in the nearshore 100 km due to the increase in upwelling-favorable winds. The overall effect of this strengthening of upwelling is that the nearshore region experiences an increase in pCO_2 and concurrent decreases in pH and Ω_{arag}. The results from our study imply that from the multiple stressors that the CalCS is subject to, i.e. an increase in upwelling and biological productivity and a decrease in temperature, it is the upwelling which prevails in the nearshore 100 km and hence drives the progression of ocean acidification there. Our results are confirmed by Lachkar and Gruber (2013) and Lachkar (2014), who used a series of sensitivity studies with ROMS to demonstrate that an increase in upwelling-favorable

winds in the CalCS leads to an increase in biological productivity but also to an expansion of water undersaturated with respect to Ω_{arag}. On the one hand, this nearshore acceleration of ocean acidification has potentially far-reaching and destructive consequences for benthic calcifying organisms such as foraminifera, pteropods or planktonic life stages of bivalves and echinoderms and could lead to a shift in species compositions or a disappearance of certain types of organisms (e.g., Orr et al., 2005; Fabry et al., 2008; Hauri et al., 2009; Bednarsek et al., 2014). On the other hand, an increase in primary production has implications for economic yields in the CalCS and could potentially support local fisheries industries. It has been shown that although all EBUS together occupy only about 1% of the total global surface ocean area, they sustain up to 20% of the global fish harvest (Pauly and Christensen, 1995), making them essential as coastal resources regions. However, it is difficult to assess what impact a shift in ecosystem properties could have on the success of local services dependent on a thriving CalCS ecosystem, as one would need to take into consideration multiple stressors such as ocean acidification, deoxygenation, ocean warming and changes in biological productivity (Bopp et al., 2013). A future simulation of the CalCS would help shed more light on the relative contributions of multiple stressors and will be addressed in Section 6.3.

- **The interannual variability of air–sea CO_2 fluxes and pCO_2 is on the order of seasonal fluctuations or long-term trends (Chapter 5).** During extreme years of climate variability, the low-frequency signal in the air–sea CO_2 fluxes can enhance the amplitude of the seasonal cycle by up to 70% in the nearshore 100 km, thus accounting for a substantial fraction of the total variability. In the offshore regions, the contribution of the low-frequency signal to the total variability is less important. Indeed, we show that the sensitivity of pCO_2 to changes in the ENSO, PDO and NPGO indices is highest in the nearshore 100 km and can reach values of up to 36 μatm (e.g., for ENSO and PDO in spring). Hence if PDO or ENSO decrease by 3–4 index units, as can be the case during extreme years, pCO_2 will concurrently increase by up to 100–150 μatm. This value is substantially larger than the trends in pCO_2 of maximum 20 μatm dec^{-1} attributable to an intensification of wind-induced upwelling (see Chapter 4). Due to the confounding effect of this substantial interannual variability, a clear distinction between truly climate change-driven trends and modulations through natural variability becomes challenging (e.g., Boyd et al., 2008). Climate change-driven trends only become important when they escape from the natural variability envelope (e.g., Hauri et al., 2013a), and a recent study has suggested that time series for highly variable systems such as the CalCS, should be at least ~40 years long to be able to recognize climate change-driven trends (Henson et al., 2010).

6.2 Model shortcomings and caveats

In the different studies of this PhD thesis, we have made substantial progress in modeling recent trends and variability in the carbonate system in the CalCS. Nevertheless, there are some drawbacks to the current setup of the model which I will highlight in the following. I discuss the implications of these drawbacks for the findings in Chapters 3 to 5, and where applicable, I suggest improvements that could be made.

Resolution of model and wind product

Several studies have demonstrated that the resolution of the wind forcing plays an important role for accurately modeling the upwelling dynamics in the CalCS (e.g., Capet et al., 2004; Bakun et al., 2010; Song et al., 2011; Fiechter et al., 2014). Most recently, using a series of coupled physical-biogeochemical simulations of the CalCS based on ROMS, Fiechter et al. (2014) compared the effects of using a coarse wind product (NCEP; $1.9° \times 1.9°$) to using a highly resolved wind product (COAMPS; 3–27 km for the CalCS) on upwelling and air–sea CO_2 fluxes in the CalCS. They found that the coarse product fails to capture the local impact of coastal topography on the wind field, thus leading to a substantial underestimation or even vanishing of upwelling centers along the coast, which are located leeward (equatorward) of capes. Because of this misrepresentation of upwelling, outgassing of CO_2 is also underestimated in these regions. Fiechter et al. (2014) furthermore addressed the issue of horizontal resolution of the ocean circulation model by using different model setups: one at a coarse resolution of 1/3°, and two eddy-resolving setups at 1/10° and 1/30° (our model has a horizontal resolution of roughly 1/20° and is thus comparable to their eddy-resolving setups). They suggest that the importance of horizontal resolution primarily plays a role in the atmosphere rather than in the underlying ocean, assuming that the ocean circulation model is sufficiently highly resolved to accurately simulate the upwelling dynamics. In our climatological simulations we used wind forcing from the QuickSCAT-based Scatterometer Climatology of Ocean Winds (SCOW; Risien and Chelton, 2008) at a horizontal resolution of roughly $0.25° \times 0.25°$. Our hindcast simulations on the other hand are forced with wind data from ECMWF's ERA-Interim Reanalysis product (Dee et al., 2011), which has a resolution of roughly 79 km in the CalCS domain. Given the fact that these resolution lie roughly between the those of the two wind products used by Fiechter et al. (2014), one can assume that upwelling along the coast of the CalCS is underestimated to some extent in our simulations as well, thus leading to an underestimation of CO_2 outgassing. This underestimation is probably larger in the case of our hindcast simulation, as they are forced with the coarser wind product. Thus it would be important to test for the magnitude of a possible underestimation of air–sea CO_2 fluxes by running a set of sensitivity simulations using different wind forcing, e.g. ERA-Interim, SCOW and COAMPS for our model setup of the CalCS.

Simple biogeochemical model

The NPZD model which we used for the studies in this thesis, is a simplified ecosystem model with one generalized phytoplankton and one generalized zooplankton representation (Section 2.2 and Fig. 2.3). Higher trophic level organisms are not included, meaning that the complex interactions taking place within and across trophic levels are not accounted for. Furthermore, several biological processes are simplified in this model by the use of parameterizations. For instance the production of $CaCO_3$ is linked to NPP by a fixed ratio, and $CaCO_3$ dissolves at a constant rate throughout the water column and in the sediments, as the model does not represent calcifying organisms.

Phytoplankton productivity in our model is limited by light and nitrogen, but the model does not include a limitation by iron, silicate or phosphorus. Iron limitation is most important in so-called high-nutrient, low-chlorophyll zones, where the supply of iron to the euphotic zone is limited and the control by grazers is high (Martin, 1992). A study by Hutchins et al. (1998) highlights that within the CalCS there are regions with varying degrees of iron limitation. More specifically, Bruland et al. (2001) found that between Monterey Bay and Point Reyes, where the continental shelf is broad enough to allow upwelled waters to come into contact with iron-rich sediments, iron supplies are abundant and can lead to diatom blooms drawing down much of the upwelled nitrate and other nutrients. To the south of Monterey Bay off the Big Sur coast on the other hand, iron supplies are limited due to much of the upwelling taking place offshore of the continental shelf. To account for iron limitation of phytoplankton, the model would need to include an iron cycle, which would help to improve the representation of varying degrees of phytoplankton productivity within the CalCS.

Furthermore, nitrogen (N_2) fixation by diazotrophs is not implemented in our model. A study by Hamersley et al. (2011) showed however that N_2 fixation does exist in the Southern California Bight. Including N_2 fixation in our model could thus help improve the representation of the pCO_2 seasonal cycle in the southern CalCS, as has been alluded to by Leinweber et al. (2005).

From these examples it becomes clear that by using a simple biogeochemical model such as NPZD, we are able to simulate the basic biogeochemical processes between the individual nitrate and carbon pools, however this model is clearly not sufficient for the representation of more complex ecosystem processes. Fiechter et al. (2014) for instance used ROMS coupled to the North Pacific Ecosystem Model for Understanding Regional Oceanography (NEMURO) model, which includes multiple zooplankton and phytoplankton classes and several limiting macronutrients. In the light of climate change, which is projected to have an impact these organisms and on the relative abundance of nutrients, an upgrade to a more complex model should be considered.

Riverine input

Presently, our simulations do not include a parameterization for riverine input or an explicit mod-

eling thereof along the US West Coast. We currently only apply a temperature and salinity restoring with a relaxation timescale of three months on the model's surface heat and freshwater input fluxes, which allows for seasonal variations of temperature and salinity to be accounted for and thus implicitly includes a signal from larger rivers such as the Columbia River (Hauri et al., 2013b). However, although this restoring procedure likely improves the mean state of temperature and salinity, it cannot account for any short-term, intense temperature and salinity signals associated with the natural variability of riverine discharge. Another factor impeding the implicit resolution of riverine input via surface restoring is the coarse resolution of the temperature and salinity data: in the case of the climatological simulations, temperature and salinity are derived from the World Ocean Atlas 2005 (WOA05), which has a horizontal resolution of $1^\circ \times 1^\circ$, whereas in the hindcast simulations, the temperature and salinity restoring is based on data from ERA-Interim with a horizontal resolution of $\sim$79 km (see Table 2.2 in Chapter 2). Both resolutions are too coarse to accurately resolve rivers mouths and hence the riverine input of temperature, salinity or nutrients is likely only seen as a very reduced signal in the forcing data's grid boxes which are in the immediate proximity of larger rivers. Any signals from rivers along the US West Coast that are smaller than the Columbia River are likely not even felt by our surface restoring.

Riverine input has an impact on the biogeochemistry of coastal waters, by altering the concentrations of DIC, Alk and nutrients such as nitrate and iron, and by changing the freshwater content and temperature of waters in the proximity of the river mouth. This contribution is especially important during the rainy season, when riverine outflow is more intense. As riverine waters have a different DIC-to-Alk ratio and are usually more acidic than the surrounding coastal ocean waters (Salisbury et al., 2008), the local degree of ocean acidification can be significantly altered by including the influence of riverine input. Hauri et al. (2013b) concluded that their modeled pH and Ω_{arag} were not accurately represented in the vicinity of the Columbia River mouth, due to their model not including riverine input. In addition, eutrophication of coastal waters due to enhanced riverine input of nutrients (Cai et al., 2011) and rainfall in higher latitudes (Nohara et al., 2006) are expected to increase in the future. Thus the relative importance of riverine input and the upwelling of nutrients will vary with climate change. Therefore, accounting for riverine input along the US West Coast, especially from large rivers such as the Columbia River, would be an important addition to our model's boundary forcing.

6.3 Outlook and suggestions for future research

In this PhD thesis, I have quantified the past and present seasonal to interannual variability in $p\mathrm{CO}_2$ and air–sea CO_2 fluxes and determined trends in ocean acidification over the last three decades in the CalCS. The results from this thesis immediately raise various questions which could be addressed in future extensions of my work based on the ROMS setup for the CalCS. In the following, I highlight the most pressing questions and elucidate how to go about answering

them.

Future simulations under different climate change scenarios

The analyses done for this thesis are based either on climatological simulations, representative of the current, mean state of the CalCS, or on hindcast simulations from 1979 to 2012, which give insight into past interannual to decadal variability and trends over the last few decades. One obvious extension of my work would be to run a set of future simulations of the CalCS of the 21st century with ROMS and to investigate the following questions:

- Will coastal upwelling and the supply of DIC and nutrients to the surface ocean intensify, or will upper-ocean warming and increased stratification prevail, leading to reduced vertical mixing and less nutrients and DIC at the surface under global warming?
- How will the nutrient supply to the CalCS change in the future and what are the driving mechanisms behind these possible changes? Will changes in stratification dominate trends in nutrient supply and biological productivity or are changes in the advection or enrichment of source waters more important?
- What are the overall implications of the above questions for oceanic pCO_2 and air–sea CO_2 fluxes? Will the CalCS remain a neutral system in terms of air–sea CO_2 fluxes or will there be a shift towards overall carbon uptake or outgassing?
- How will ocean acidification progress over the 21st century? Do our results from Chapter 4 also hold for the present century, i.e. that an increase in wind-induced upwelling accelerates local ocean acidification along the coast? Or are there non-linearities in the carbonate system at play, which complicate a prognosis of how ocean acidification in the CalCS will evolve in the future based solely on results from our hindcast simulations?

To address the above questions, I propose to force ROMS at the atmospheric and lateral boundaries with anomalies from simulations over the 21st century from Earth System Models (ESM) of the Coupled Model Intercomparison Project 5 (CMIP5) under different climate change scenarios. The anomalies would be computed to a reference time period and added to climatological lateral boundary conditions as was done for the hindcast simulations in Chapters 4 and 5 using CCSM output (Graven et al., 2012). Specifically, the following steps would need to be pursued to account for uncertainties between the individual CMIP5 model simulations and between different scenarios and to include the effect of internal variability within each simulation (following the approach of Hawkins and Sutton, 2009):

- **Model uncertainty:** Force ROMS with output from all CMIP5 models which include a representation of the oceanic carbon cycle. By using output from multiple models to force

ROMS, we can generate a range of possible future trends in ocean acidification and air–sea CO_2 fluxes in the CalCS. From this, we can determine whether the the multi-model mean trends over the 21st century are statistically significantly different from zero.

- **Scenario uncertainty:** Force ROMS with output from simulations following two of the four available Representative Concentration Pathway (RCP) emission scenarios (Cubasch et al., 2013), namely RCP 8.5 (business-as-usual emission scenario) and RCP 2.6 (peak-and-decline emission scenario). This will allow us to determine a range of possible trends in response to different rates of increase in atmospheric CO_2.

- **Internal variability:** Use multi-member ensemble output from one of the CMIP5 models (e.g., a 30-member ensemble simulation of the GFDL ESM2M; Dunne et al., 2012, 2013) to force ROMS in order to constrain the variability intrinsic to the climate system arising from slightly perturbed initial conditions.

In Chapter 4 we draw attention to the fact that on average, ESMs have major difficulties in simulating coastal upwelling (Fig. B.1), due in part to their coarse resolution in the ocean and in part to a misrepresentation of upwelling-favorable winds. This underestimation of the response of coastal winds to increasing atmospheric CO_2 and surface warming could explain why Rykaczewski and Dunne (2010) model only a limited change in upwelling, and highlights the importance of using a highly resolved regional oceanic model such as ROMS to accurately simulate the upwelling dynamics in the CalCS. One caveat remains however, namely the underestimation of trends in alongshore winds in the CMIP5 models as shown in Fig. B.1. Several previous studies have highlighted that the modeling of upwelling in the CalCS is sensitive to the resolution of the wind forcing product (e.g., Capet et al., 2004; Bakun et al., 2010; Song et al., 2011; Fiechter et al., 2014, see Section 6.2). An underestimation of trends in upwelling-favorable winds would have major implications for trends in ocean acidification, in biological productivity and in the air–sea CO_2 fluxes. One option would be to pick individual CMIP5 models which are more successful in reproducing alongshore winds than the multimodel mean to force ROMS. However, this would not allow us to constrain our trends through the analysis of the multi-model variability. Given the fact that global ESM simulations with integrated carbon cycles at higher resolutions than 0.5°–1° in the CalCS region are currently unavailable, the above approach using multiple CMIP5 models currently seems the most judicious choice. Due to limitations in computational resources of running a large ensemble of simulations, time slice experiments with end-of-21st-century forcing from CMIP5 models constitute a feasible alternative to full transient simulations.

A further, but computationally more expensive, alternative is the coupling of ROMS to a regional atmospheric model, such as COSMO (Consortium for Small-scale Modeling) or WRF (Weather Research and Forecasting Model). ROMS and the atmospheric regional model would be forced laterally by the output from the oceanic and atmospheric components, respectively, of the global ESM from CMIP5. Within the domain, ROMS and the regional atmospheric model would

be free to exchange flux and state information, thus allowing for ocean-atmosphere feedbacks to take place. Such feedbacks include for instance changes in sea surface temperature due to global warming or intensification of upwelling affecting the overlying air temperature, which could additionally alter the thermal land-sea gradient and impact coastal upwelling.

Analysis of high-frequency variability

In Chapters 4 and 5, we focused on the analysis of interannual variability and long-term trends from hindcast simulations over the time period 1979–2012. Given that our hindcast simulations are forced with daily atmospheric values, this offers the possibility of additionally analyzing high-frequency events on subseasonal timescales.

In Chapter 5 we showed that the high frequency ($<$ 1 year) signal of air–sea CO_2 fluxes accounts for a substantial fraction of the total variability of these fluxes (Fig. 5.1). Furthermore, Fig. 5.1 reveals that the variability of the high-frequency signal is amplified during summer months and during extreme events in the climate system on interannual timescales. A study on the North Atlantic basin demonstrates that the North Atlantic Oscillation (NAO) has an impact on the carbon cycle on subannual timescales (Keller et al., 2012). While the basin-wide net air–sea CO_2 flux is little affected by the NAO variability, there exist non-linearities that can locally reduce the carbon sink during NAO negative phases. Along the same lines, the intensity and frequency of anomalous states of Pacific modes of variability might impact the long-term behavior of the CalCS carbon cycle, giving rise to the following questions:

- Do short-term, intense upwelling events have a substantial impact on the long-term mean CO_2 source/sink behavior of the CalCS?
- What are the mechanisms behind the increase in the magnitude of short-term variability on seasonal and interannual timescales?

To follow up on analyses done by Hauri et al. (2013a), an investigation of aragonite undersaturation events in our hindcast simulation would allow for the quantification of past changes in the frequency, intensity and duration of short-term events under fully forced conditions. In addition to the stressor ocean acidification, this includes the possibility of investigating the effect of other transiently evolving stressors, such as the expansion of oxygen minimum zones, surface ocean warming and changes in primary production (Bopp et al., 2013).

Comparison of the CalCS to other EBUS in terms of long-term trends and interannual variability of the upper ocean carbon cycle.

In this PhD thesis, the CalCS served as a case study for the other three EBUS. However, the response to the increase in anthropogenic CO_2 and to changes in multiple stressors related to climate

change is not necessarily expected to be consistent among the EBUS. A study by Lachkar (2014) highlighted the opposing effect of an intensification of upwelling-favorable winds in the CalCS and in the Canary Current System. In the CalCS, a doubling of alongshore wind stress resulted in a tripling of the volume of waters undersaturated with respect to aragonite. In the Canary Current System on the other hand, this wind intensification led to a disappearance of undersaturation. This difference in the responses of the two EBUS was found to be a consequence of the relative importance of upwelling and biological production in each system. These results highlight the importance of conducting comparative studies on other EBUS under the same experimental design as the ones done in this thesis.

Therefore, I suggest to run hindcast simulations for the Canary and Humboldt Current System - the two systems which are currently most studied in our research group - that are analogous to the simulations we conducted for Chapters 4 and 5 to address the following questions:

- Do all EBUS react consistently to the increase in atmospheric CO_2?
- Do the other EBUS also experience a change in wind-induced upwelling, and if yes, how does this affect ocean acidification in those regions?
- Is there a surface ocean cooling in the other EBUS over the last three decades? How does this affect the vertical oceanic structure of these regions and the supply of nutrients to the surface?
- How did primary productivity change over the last few decades in the other EBUS? What are the potential implications of such changes for local commercial fisheries that are dependent on a thriving ecosystem?

These are just a few of the many questions that could be addressed in a comparative study of these three EBUS. Ideally, future simulations as described above, would be conducted for the Canary and Humboldt Current System as well, in order to compare past and future changes in their carbon cycles and biogeochemistry.

6.4 Final remarks

The work done in this PhD thesis highlights the necessity of further modeling work on the carbon cycle in the CalCS and in other EBUS and the need for a strengthening of the observational network, particularly in the nearshore 100 km, where we have shown that the temporal and spatial variability of carbon fluxes requires a denser sampling frequency. Further it suggests that collaborations between the observational and modeling communities should be continued or strengthened in the future, in order to most accurately capture the multitude of temporal variability modes of

carbon fluxes over the whole CalCS domain. Finally, I hope that the work done for this PhD thesis will inspire a future continuation of regional oceanic modeling of the carbon cycle in EBUS, which we have demonstrated to be particularly vulnerable to the myriad ways in which climate change can affect these regions. The maintenance of a healthy coastal ecosystem is of utmost importance for the future success of regional and global communities that are dependent on marine resources. This should suffice as a motivation for immediate action to continuously monitor and reduce anthropogenic impacts on coastal upwelling ecosystems and invest in methods of sustainable resource harvesting.

Appendix A

Supplementary material to Chapter 3

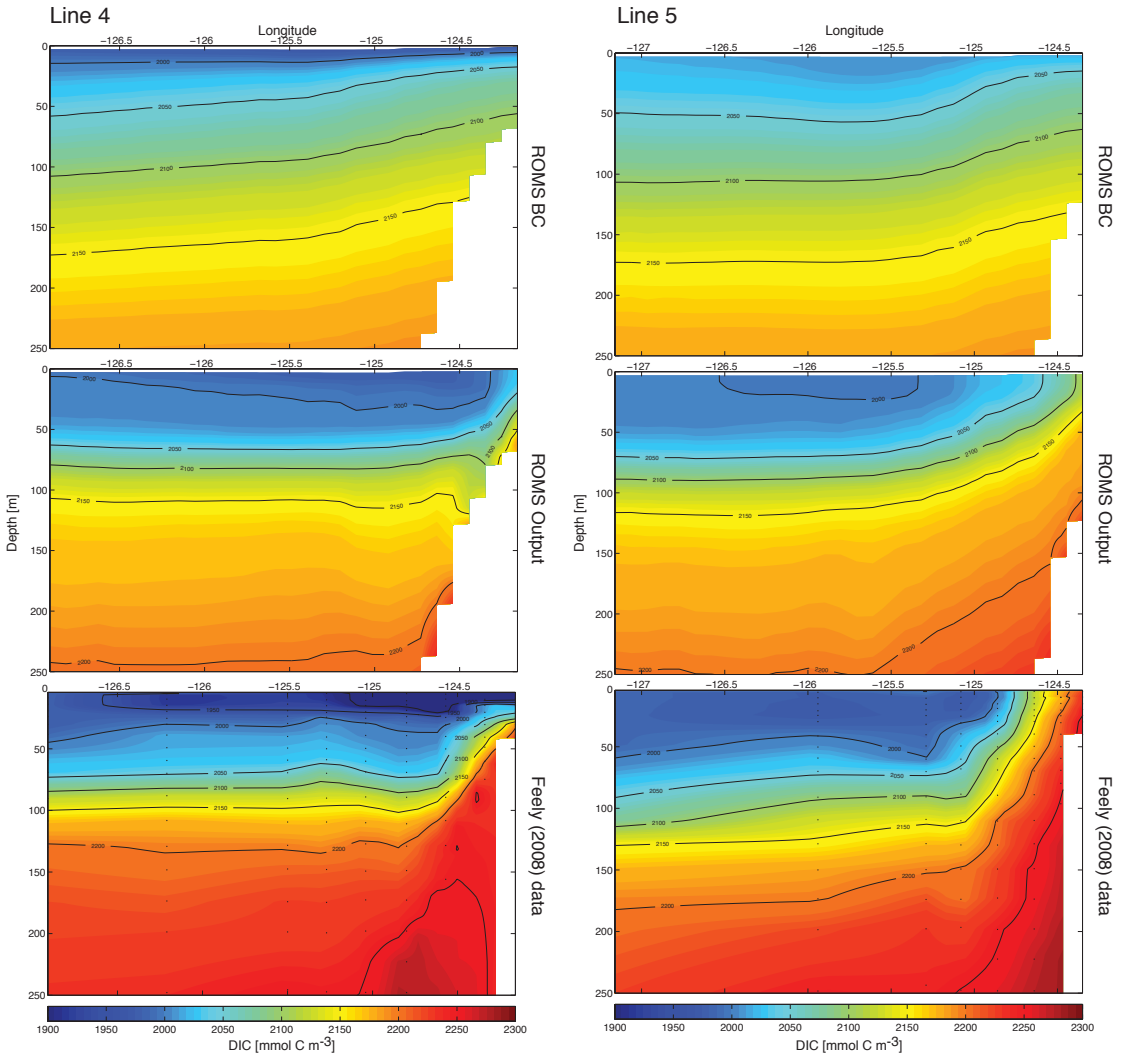

Figure A.1 Vertical sections of DIC from the GLODAP climatology, used to force ROMS at its lateral boundaries (top panels; averaged over May and June), modeled ROMS output (center panels, 7-year averages over May and June) and from Feely et al. (2008) transect lines 4 and 5, sampled during a cruise in May and June 2007 (bottom panels). The data from GLODAP and ROMS output were sampled in the same location as the observations to be comparable. The black dots in the bottom panels are sample locations from the Feely et al. (2008) cruise.

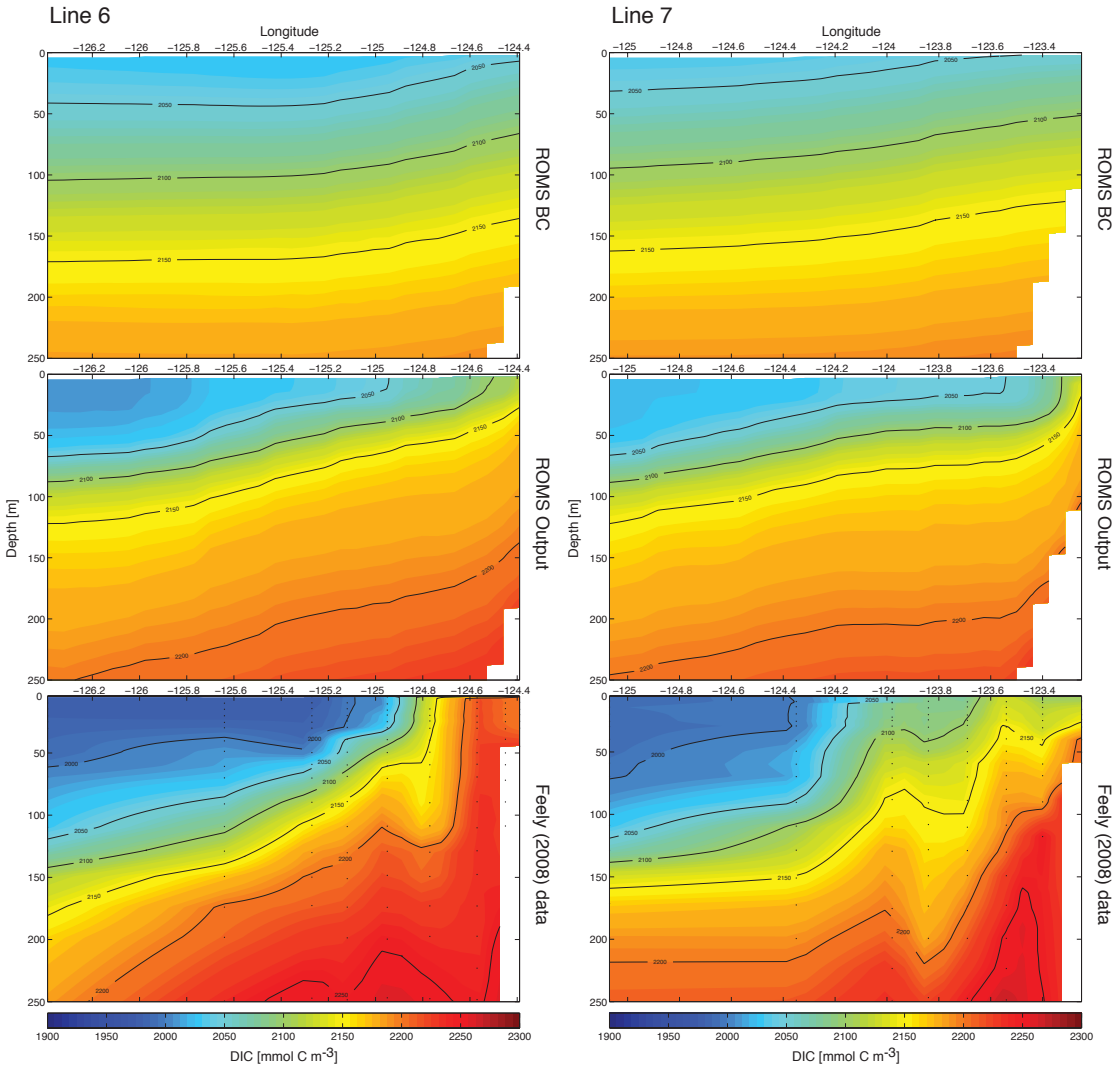

Figure A.2 Vertical sections of DIC from the GLODAP climatology, used to force ROMS at its lateral boundaries (top panels; averaged over May and June), modeled ROMS output (center panels, 7-year averages over May and June) and from Feely et al. (2008) transect lines 6 and 7, sampled during a cruise in May and June 2007 (bottom panels). The data from GLODAP and ROMS output were sampled in the same location as the observations to be comparable. The black dots in the bottom panels are sample locations from the Feely et al. (2008) cruise.

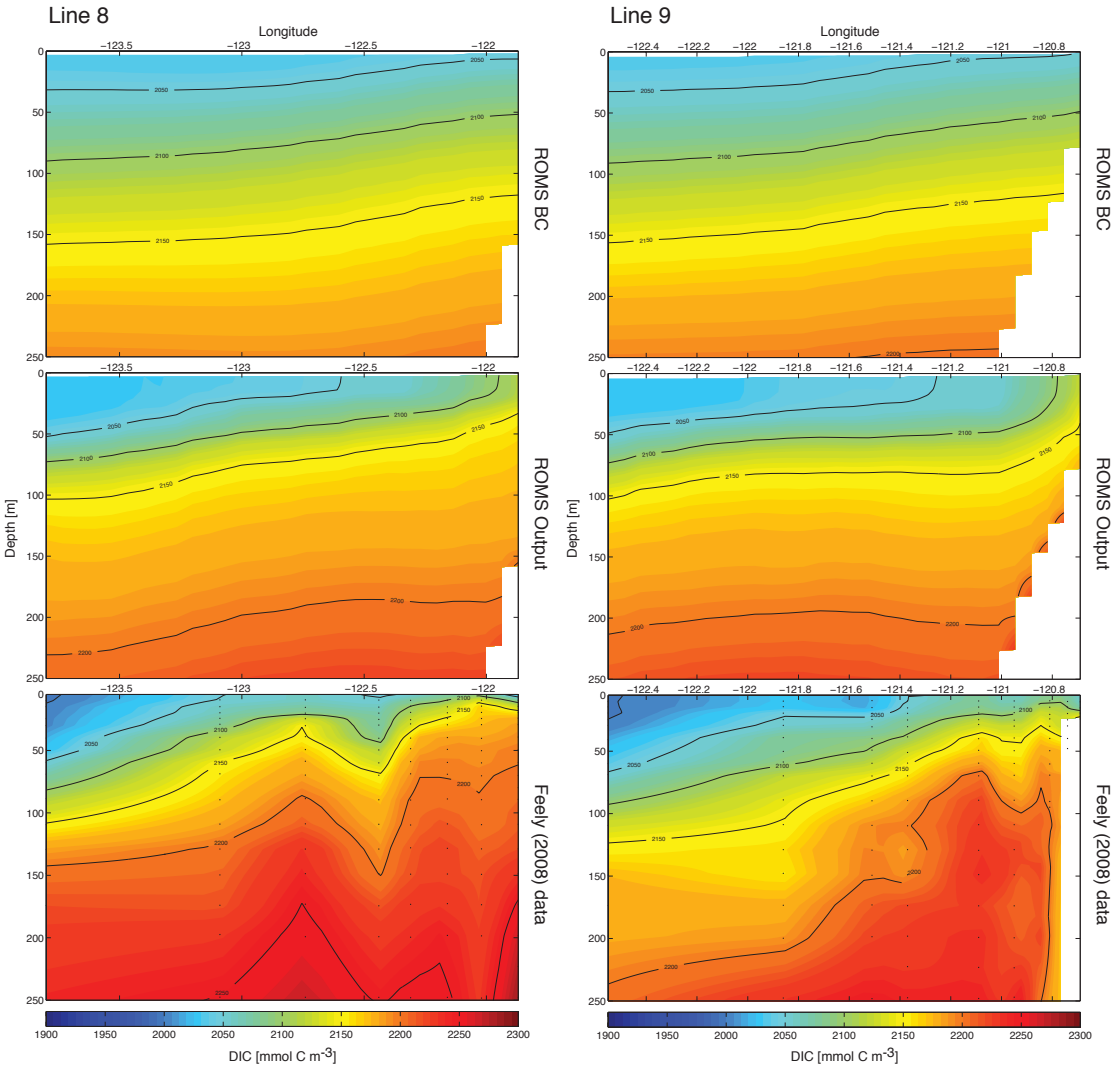

Figure A.3 Vertical sections of DIC from the GLODAP climatology, used to force ROMS at its lateral boundaries (top panels; averaged over May and June), modeled ROMS output (center panels, 7-year averages over May and June) and from Feely et al. (2008) transect lines 8 and 9, sampled during a cruise in May and June 2007 (bottom panels). The data from GLODAP and ROMS output were sampled in the same location as the observations to be comparable. The black dots in the bottom panels are sample locations from the Feely et al. (2008) cruise.

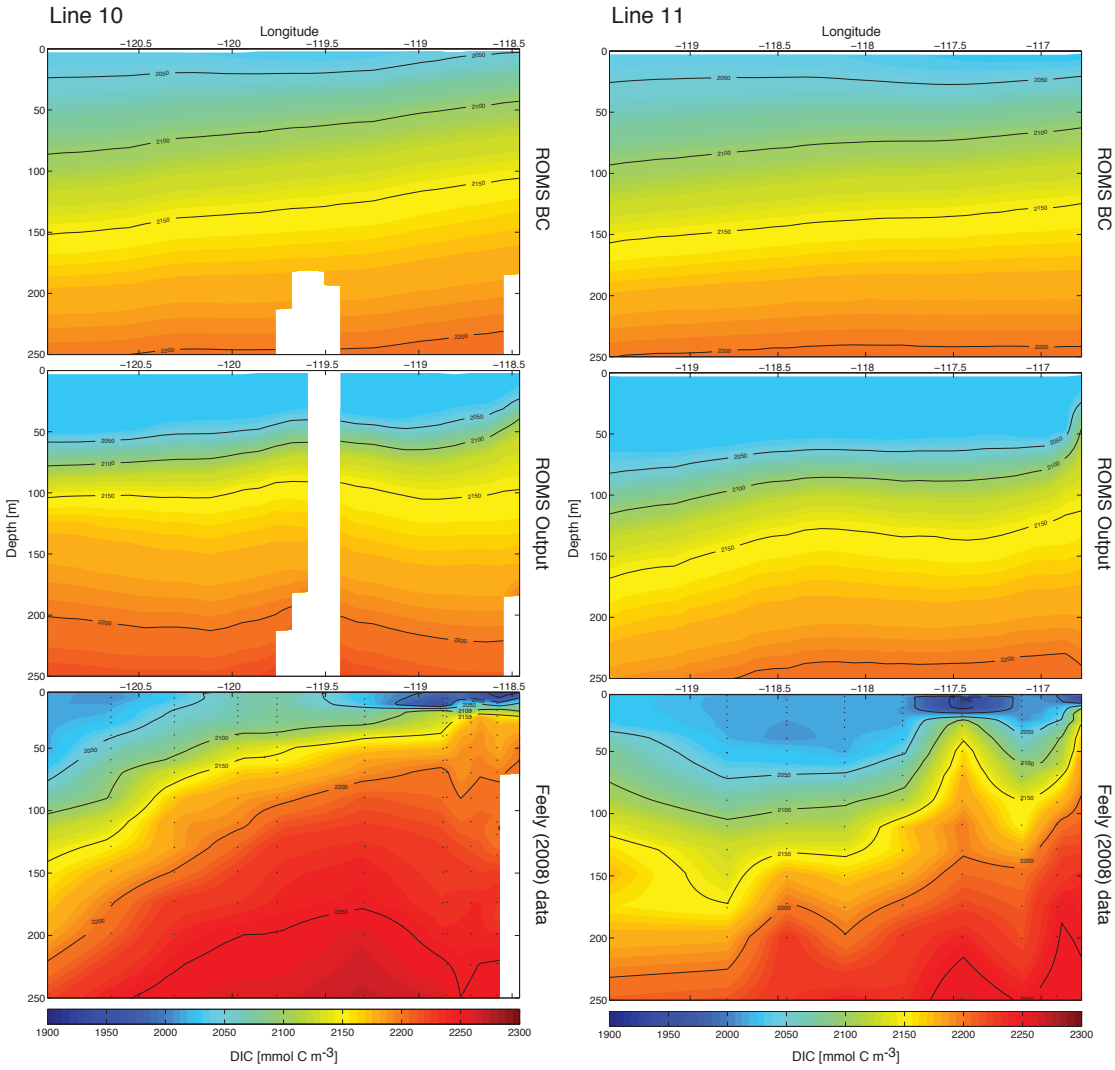

Figure A.4 Vertical sections of DIC from the GLODAP climatology, used to force ROMS at its lateral boundaries (top panels; averaged over May and June), modeled ROMS output (center panels, 7-year averages over May and June) and from Feely et al. (2008) transect lines 10 and 11, sampled during a cruise in May and June 2007 (bottom panels). The data from GLODAP and ROMS output were sampled in the same location as the observations to be comparable. The black dots in the bottom panels are sample locations from the Feely et al. (2008) cruise.

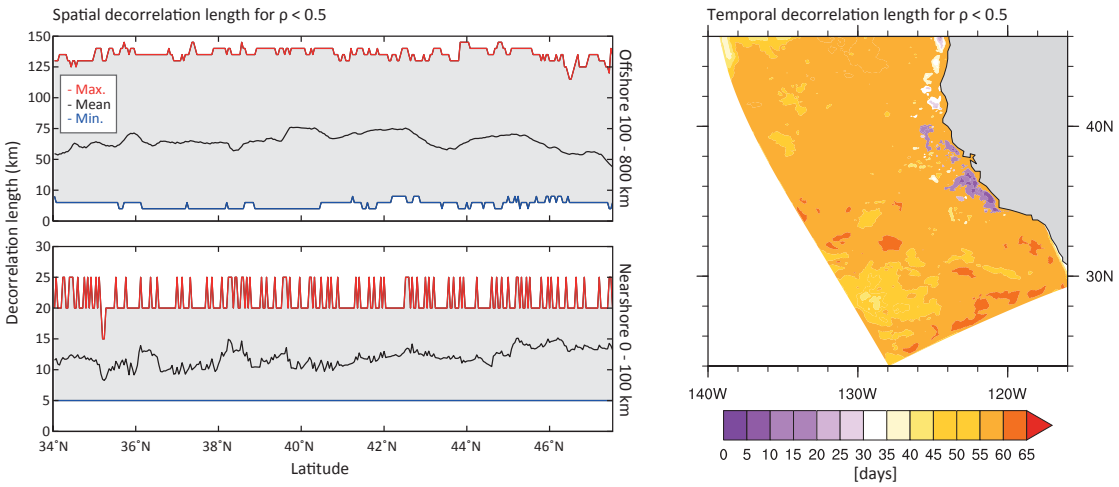

Figure A.5 Spatial and temporal decorrelation length scales computed for 2-day averaged pCO_2 output from a climatological simulation from Turi et al. (2014a). The spatial decorrelation length scales (given in km) were computed for all grid boxes in the offshore direction as a function of latitude for a nearshore 0–100 km and an offshore 100–800 km region separately (see contour lines in Fig. 3.1). The temporal correlation length scales (given in days) were calculated for 2-day averaged model output for every grid box. Both spatial and temporal decorrelation length scales are defined as the length scale (in km or days) at which the correlation coefficient drops below a value of 0.5.

Appendix B

Supplementary material to Chapter 4

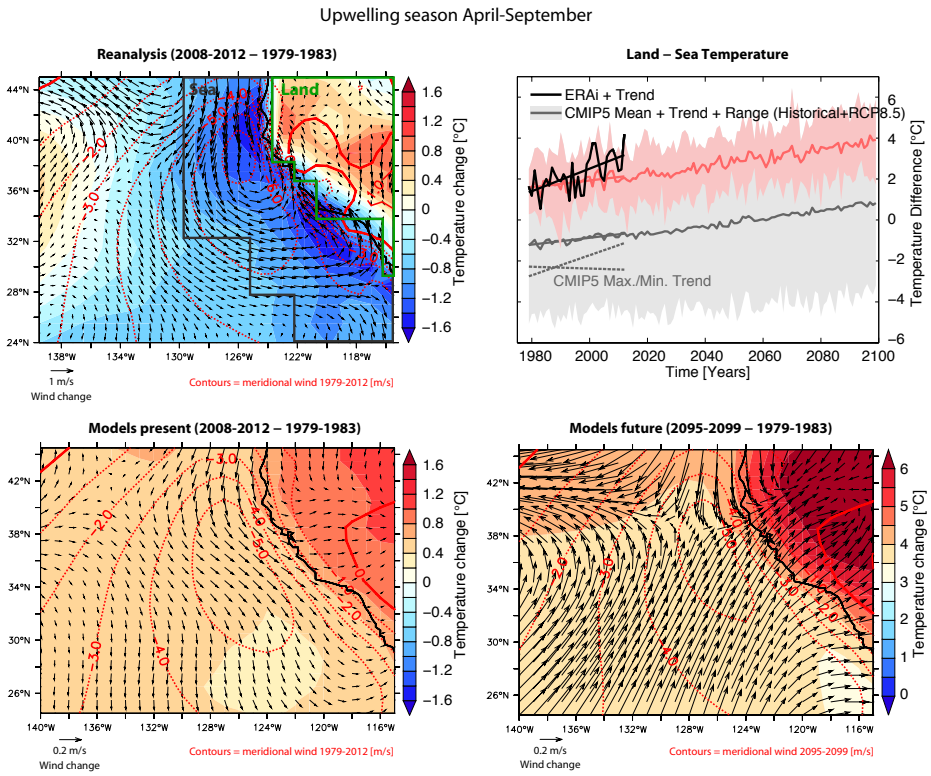

Figure B.1 Current and future changes in the CalCS during the upwelling season (April-September). (Top left) ERA-Interim anomalies in surface air temperature (shading) and in surface winds (vectors), calculated as 2008-2012 minus 1979-1983. Contours give the mean meridional winds from 1979 to 2012. (Bottom left) As in (Top left) but for the multi-model mean of available CMIP5 models. Note the different vector reference lengths. (Bottom right) As in (Bottom left) but for anomalies calculated as 2095-2099 minus 1979-1983. Note the different colorbars. (Top right) Time series of the land-sea temperature difference, averaged over the boxes indicated in (Top left). Red indicates models that have a mean positive land-sea temperature difference during 1979–2012, in agreement with the ERA-Interim reanalysis (9 out of 33 models).

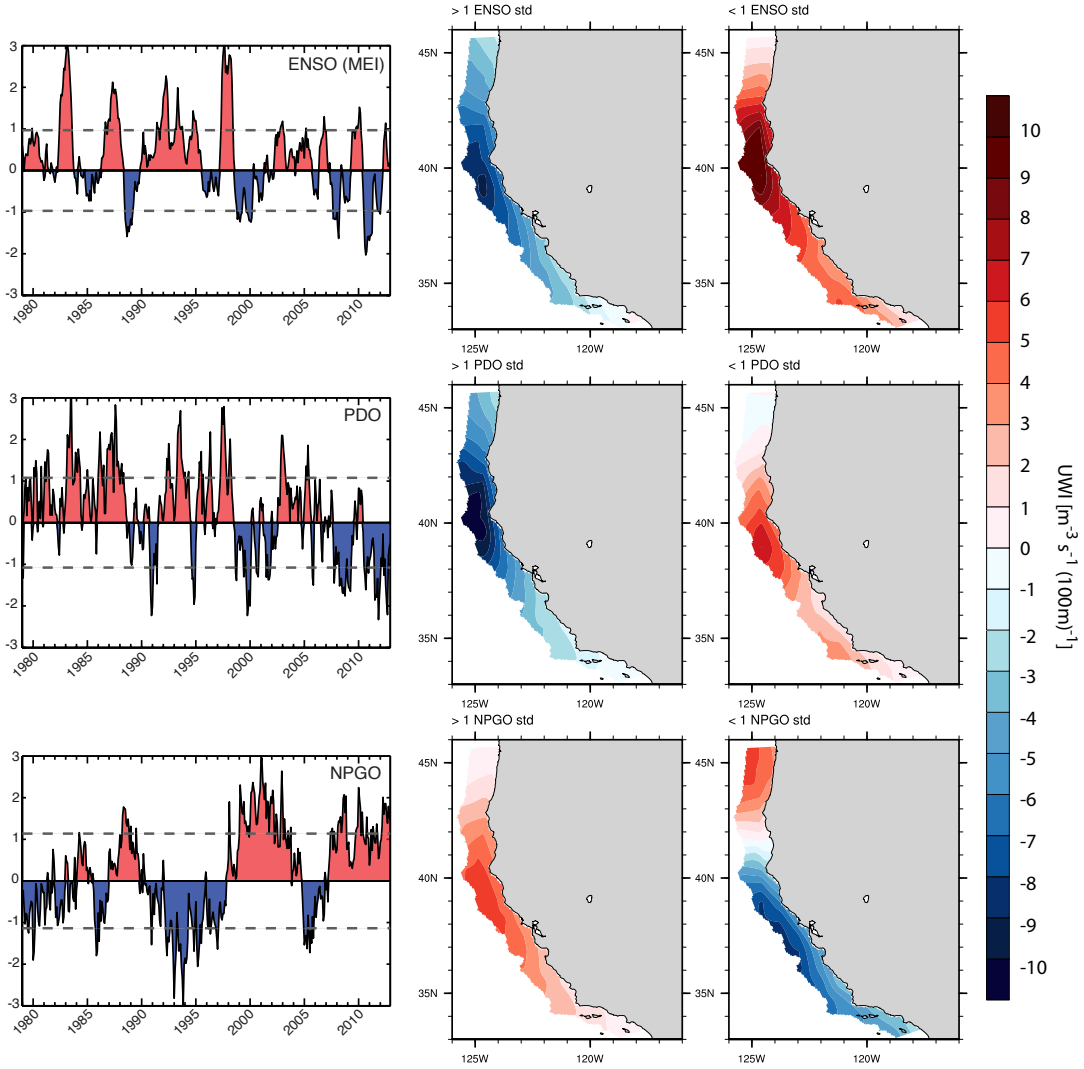

Figure B.2 Extreme year composite analysis of upwelling index (UWI) with ENSO (MEI: Multivariate ENSO Index; top row), PDO (center row) and NPGO (bottom row) and the respective climate indices time series from 1979 to 2012 (left column). Years were considered as extreme if three consecutive months in one year exceeded the ± 1 standard deviation threshold (dashed lines in the left column). Red shaded areas in the left column represent positive phases of the respective variability mode, while blue areas correspond to negative phases. The UWI was computed from the alongshore wind stress component of the ERA-Interim wind forcing and integrated for increments of 100 m along the coast (as calculated in Macias et al., 2012). The UWI represents the magnitude of offshore (positive values) or onshore (negative values) water transport.

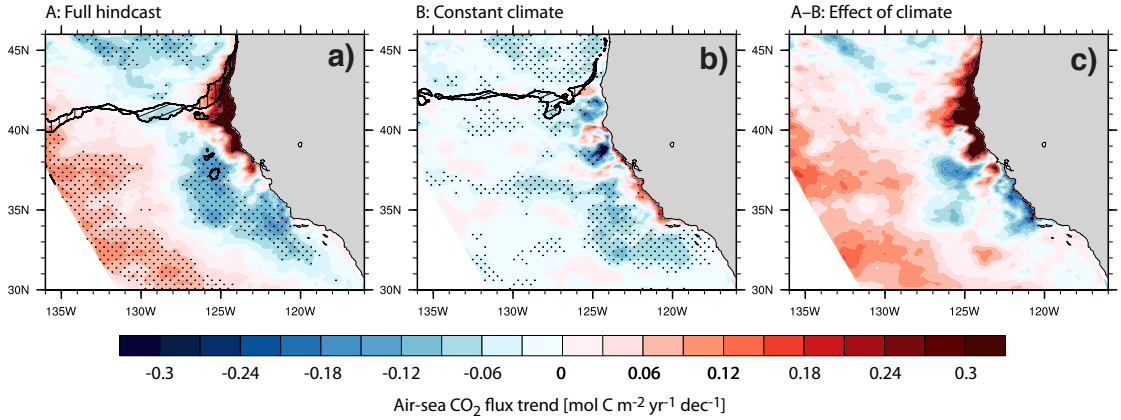

Figure B.3 Changes per decade in air–sea CO_2 fluxes from 1979 to 2012 for **(a)** the HCast and **(b)** the CClim simulations, calculated as the least squares linear trends of the data. Panel **(c)** is the difference between the HCast and the CClim trends (HCast–CClim). The black stippling indicates trends that are significant at the 95% significance level (calculated as the p-value from a Student's t-test; not calculated for panel **(c)**). The vertical and slanted shading indicates areas which experienced a sign change over the 34 simulation years.

Appendix C

Supplementary material to Chapter 5

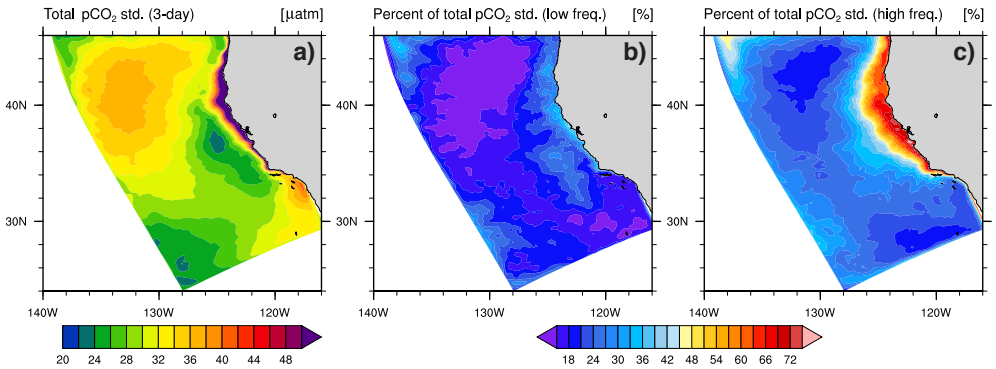

Figure C.1 Comparison of pCO_2 standard deviations computed from **(a)** 3-day averages, **(b)** from the low-frequency and **(c)** from the high-frequency component of these 3-day averages. The low- and high-frequency signals were computed from deseasonalized 3-day averages by filtering them with a fast Fourier transform (FFT) filter, using a cutoff frequency of one year. Any linear trends in pCO_2 were removed prior to the FFT analysis.

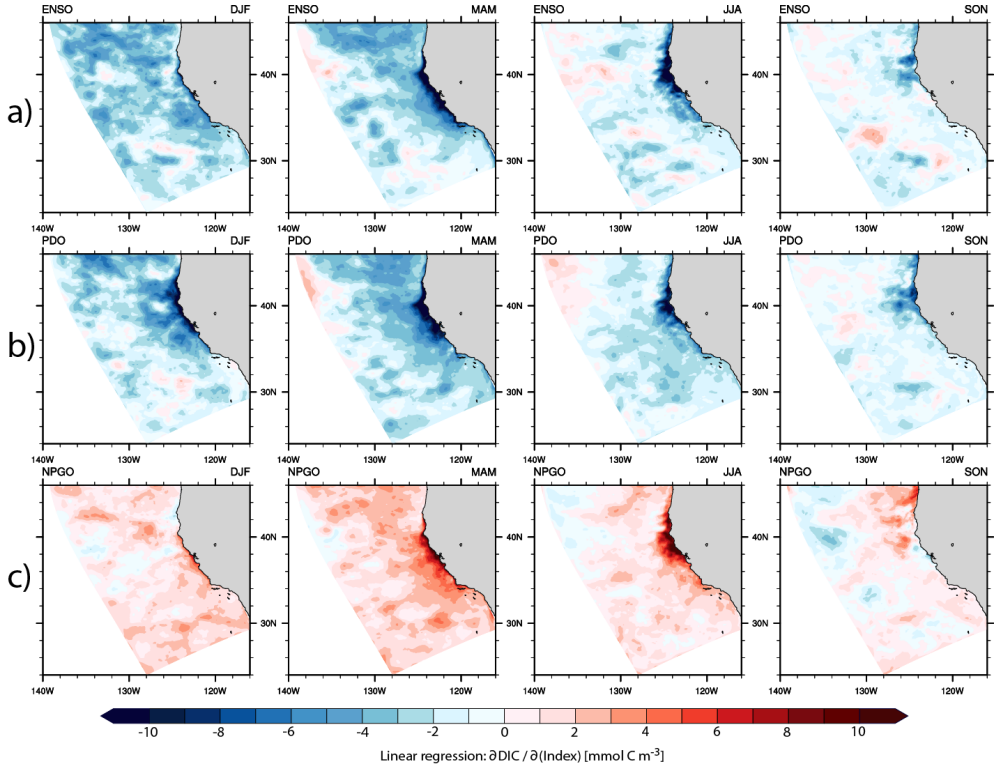

Figure C.2 Sensitivity of surface ocean dissolved inorganic carbon (DIC) to per unit index changes in **(a)** ENSO, **(b)** PDO and **(c)** NPGO, calculated as the linear regression slopes of individual seasons on an annual basis.

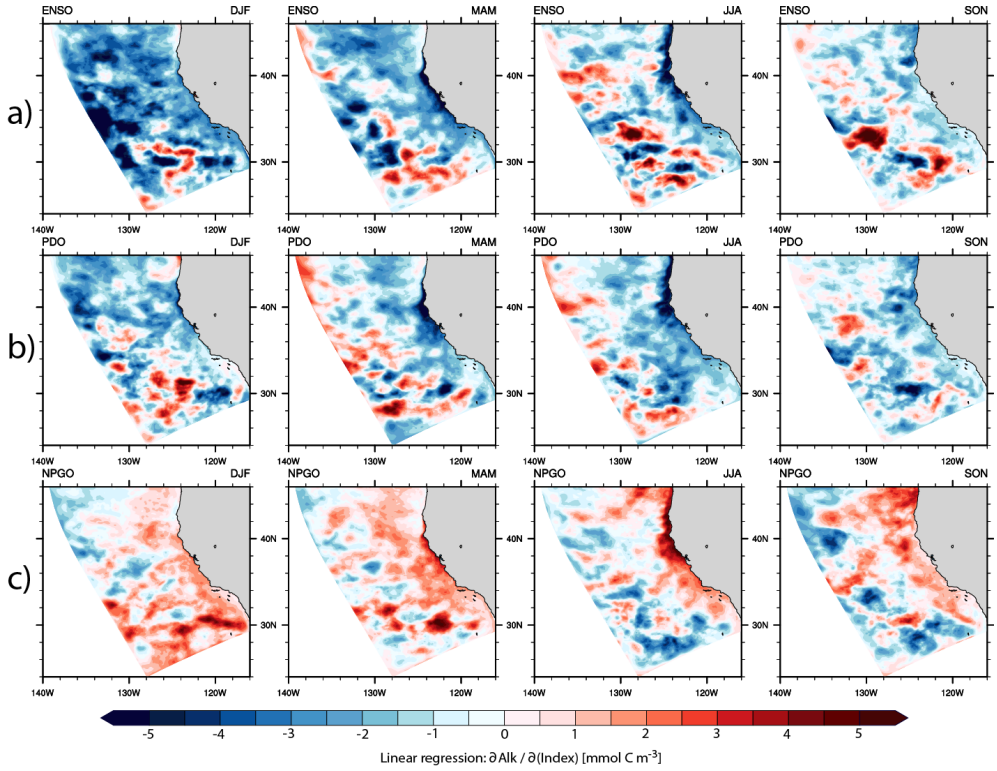

Figure C.3 Sensitivity of surface ocean alkalinity (Alk) to per unit index changes in **(a)** ENSO, **(b)** PDO and **(c)** NPGO, calculated as the linear regression slopes of individual seasons on an annual basis.

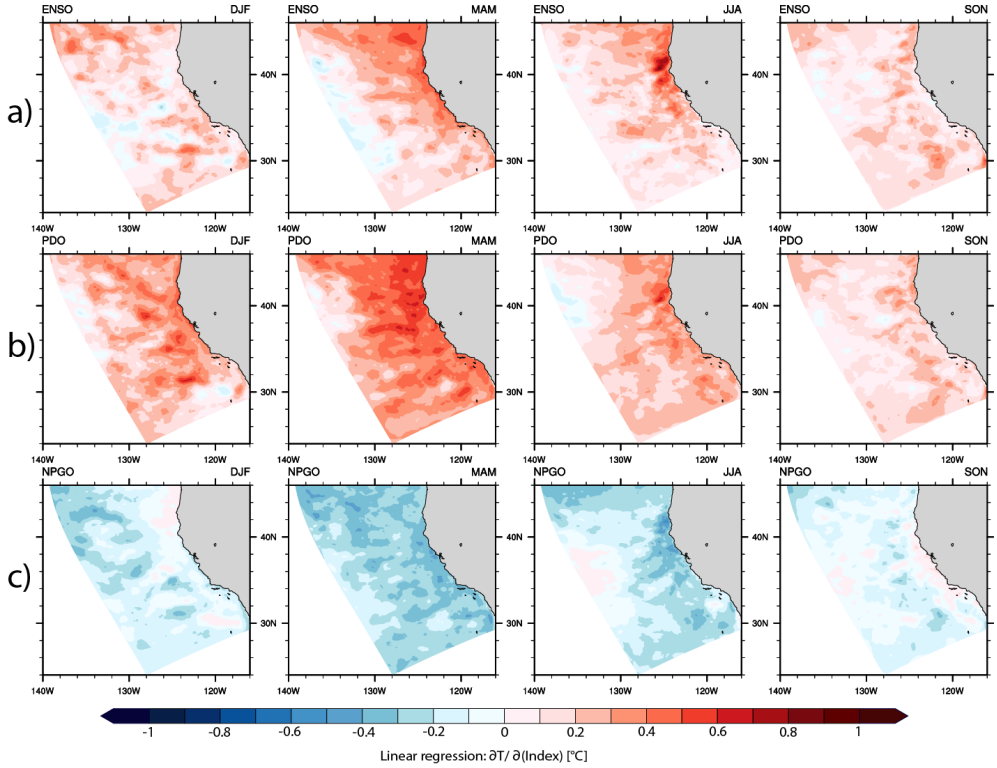

Figure C.4 Sensitivity of surface ocean temperature (T) to per unit index changes in **(a)** ENSO, **(b)** PDO and **(c)** NPGO, calculated as the linear regression slopes of individual seasons on an annual basis.

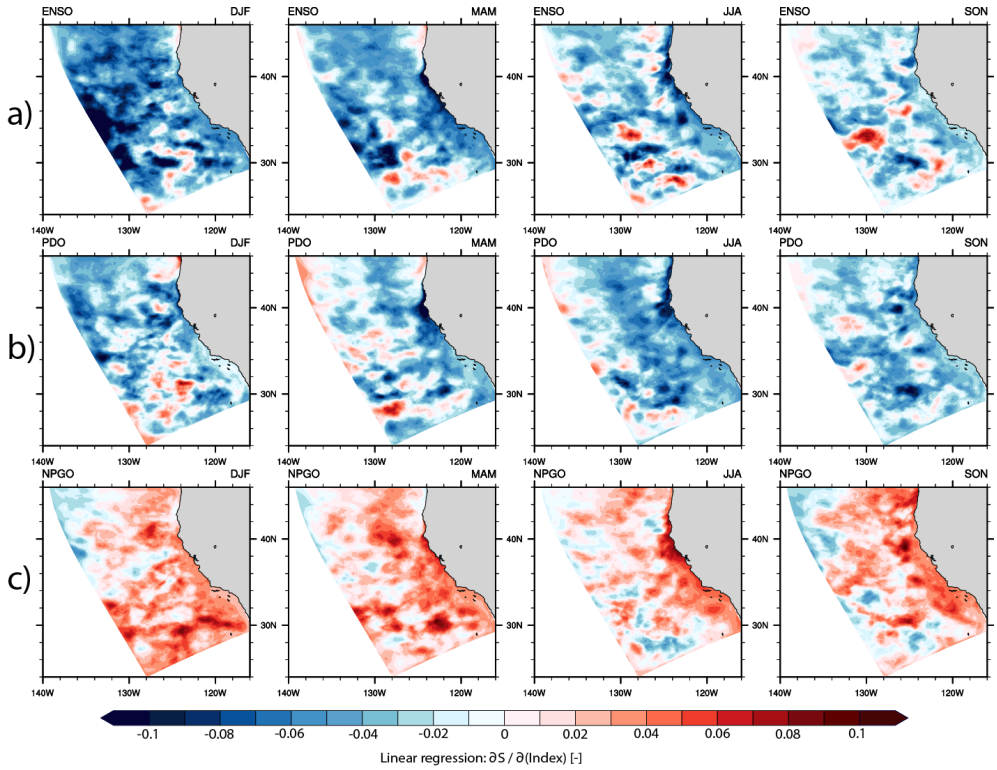

Figure C.5 Sensitivity of surface ocean salinity (S) to per unit index changes in **(a)** ENSO, **(b)** PDO and **(c)** NPGO, calculated as the linear regression slopes of individual seasons on an annual basis.

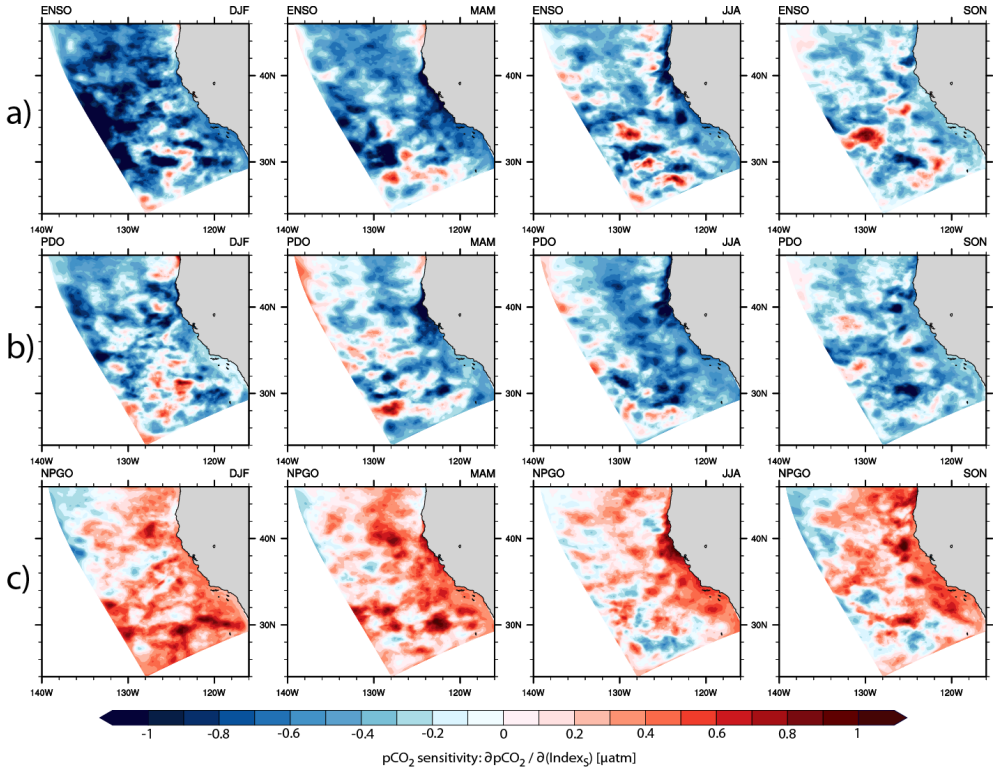

Figure C.6 Sensitivity of pCO_2 to surface ocean salinity (S) fluctuations induced by changes in **(a)** ENSO, **(b)** PDO and **(c)** NPGO (last term of Eq. 5.1).

List of Figures

List of Tables

Bibliography

Antonov, J. I., Locarnini, R. A., Boyer, T. P., Mishonov, A. V., and Garcia, H. E. (2006). World Ocean Atlas 2005, Volume 2: Salinity. In Levitus, S., editor, *NOAA Atlas NESDIS 62*, page 182. U.S. Government Printing Office, Washington, D.C.

Ashok, K. and Yamagata, T. (2009). The El Niño with a difference. *Nature*, 461:481–484.

Bakun, A. (1990). Global climate change and intensification of coastal ocean upwelling. *Science*, 247(4939):198–201.

Bakun, A., Field, D. B., Redondo-Rodriguez, A., and Weeks, S. J. (2010). Greenhouse gas, upwelling-favorable winds, and the future of coastal ocean upwelling ecosystems. *Global Change Biology*, 16(4):1213–1228.

Barber, R. T. and Chavez, F. P. (1983). Biological Consequences of El Niño. *Science*, 222(4629):1203–1210.

Barnier, B., Siefridt, L., and Marchesiello, P. (1995). Thermal forcing for a global ocean circulation model using a three-year climatology of ECMWF analyses. *Journal of Marine Systems*, 6(4):363–380.

Bauer, J. E., Cai, W.-J., Raymond, P. A., Bianchi, T. S., Hopkinson, C. S., and Regnier, P. A. G. (2013). The changing carbon cycle of the coastal ocean. *Nature*, 504:61–70.

Beckmann, A. and Haidvogel, D. (1993). Numerical Simulation of Flow around a Tall Isolated Seamount. Part I: Problem Formulation and Model Accuracy. *Journal of Physical Oceanography*, 23(8):1736–1753.

Bednarsek, N., Feely, R., Reum, J., Peterson, B., Menkel, J., Alin, S., and Hales, B. (2014). Limacina helicina shell dissolution as an indicator of declining habitat suitability owing to ocean acidification in the California Current Ecosystem. *Proceedings of the Royal Society B*, 281(1785):20140123.

Bograd, S. J., Castro, C. G., Di Lorenzo, E., Palacios, D. M., Bailey, H., Gilly, W., and Chavez, F. P. (2008). Oxygen declines and the shoaling of the hypoxic boundary in the California Current. *Geophysical Research Letters*, 35:L12607.

Bograd, S. J. and Lynn, R. J. (2001). Physical-biological coupling in the California Current during the 1997-99 E1 Niño-La Niña cycle. *Geophysical Research Letters*, 28(2):275–278.

Bograd, S. J. and Lynn, R. J. (2003). Long-term variability in the Southern California Current System. *Deep Sea Research Part II: Topical Studies in Oceanography*, 50:2355–2370.

Bograd, S. J., Schroeder, I., Sarkar, N., Qiu, X., Sydeman, W. J., and Schwing, F. B. (2009). Phenology of coastal upwelling in the California Current. *Geophysical Research Letters*, 36(1):L01602.

Bopp, L., Resplandy, L., Orr, J. C., Doney, S. C., Dunne, J. P., Gehlen, M., Halloran, P., Heinze, C., Ilyina, T., Séférian, R., Tjiputra, J., and Vichi, M. (2013). Multiple stressors of ocean ecosystems in the 21st century: projections with CMIP5 models. *Biogeosciences*, 10:6225–6245.

Borges, A. (2005). Do we have enough pieces of the jigsaw to integrate CO_2 fluxes in the coastal ocean? *Estuaries and Coasts*, 28(1):3–27.

Borges, A., Delille, B., and Frankignoulle, M. (2005). Budgeting sinks and sources of CO_2 in the coastal ocean: Diversity of ecosystems counts. *Geophysical Research Letters*, 32(14):L14601.

Borges, A., Schiettecatte, L.-S., Abril, G., Delille, B., and Gazeau, F. (2006). Carbon dioxide in European coastal waters. *Estuarine, Coastal and Shelf Science*, 70(3):375–387.

Boyd, P., Doney, S., Strzepek, R., Dusenberry, J., Lindsay, K., Fung, I., Zealand, N., Hole, W., Dynamics, G., and Science, P. (2008). Climate-mediated changes to mixed-layer properties in the Southern Ocean: assessing the phytoplankton response. *Biogeosciences*, 5:847–864.

Brown, E., Colling, A., Park, D., Phillips, J., Rothery, D., and Wright, J. (2001). Other Major Current Systems. In *Ocean Circulation*, chapter 5, pages 143–189. Butterworth-Heinemann, Oxford.

Bruland, K. W., Rue, E. L., and Smith, G. J. (2001). Iron and macronutrients in California coastal upwelling regimes: Implications for diatom blooms. *Limnology and Oceanography*, 46(7):1661–1674.

Cai, W.-J. (2011). Estuarine and Coastal Ocean Carbon Paradox: CO_2 Sinks or Sites of Terrestrial Carbon Incineration? *Annual Review of Marine Science*, 3:123–145.

Cai, W.-J. and Dai, M. (2004). Comment on "Enhanced open ocean storage of CO_2 from shelf sea pumping". *Science*, 306:1477c.

Cai, W.-J., Dai, M., and Wang, Y. (2006). Air-sea exchange of carbon dioxide in ocean margins: A province-based synthesis. *Geophysical Research Letters*, 33(12):L12603.

Cai, W.-J., Hu, X., Huang, W.-J., Murrell, M. C., Lehrter, J. C., Lohrenz, S. E., Chou, W.-C., Zhai, W., Hollibaugh, J. T., Wang, Y., Zhao, P., Guo, X., Gundersen, K., Dai, M., and Gong, G.-C. (2011). Acidification of subsurface coastal waters enhanced by eutrophication. *Nature Geoscience*, 4(11):766–770.

Cai, W.-J. and Wang, Y. (1998). The chemistry, fluxes, and sources of carbon dioxide in the estuarine waters of the Satilla and Altamaha Rivers, Georgia. *Limnology and Oceanography*, 43(4):657–668.

Capet, X., Colas, F., Penven, P., Marchesiello, P., and McWilliams, J. C. (2008). Eddies in eastern boundary subtropical upwelling systems. *Ocean modeling in an Eddying regime, Geophysical monograph series*, 177:1–18.

Capet, X. J., Marchesiello, P., and McWilliams, J. C. (2004). Upwelling response to coastal wind profiles. *Geophysical Research Letters*, 31(13):L13311.

Capone, D. G. and Hutchins, D. A. (2013). Microbial biogeochemistry of coastal upwelling regimes in a changing ocean. *Nature Geoscience*, 6(9):711–717.

Chaigneau, A., Eldin, G., and Dewitte, B. (2009). Eddy activity in the four major upwelling systems from satellite altimetry (1992-2007). *Progress In Oceanography*, 83(1-4):117–123.

Chan, F., Barth, J. A., Lubchenco, J., Kirincich, A., Weeks, H., Peterson, W. T., and Menge, B. A. (2008). Emergence of anoxia in the California Current large marine ecosystem. *Science*, 319(5865):920.

Chassignet, E. and Verron, J. (2006). *Ocean Weather Forecasting: An Integrated View of Oceanography*. Springer, Dordrecht, Netherlands.

Chavez, F. P. (1999). Biological and Chemical Response of the Equatorial Pacific Ocean to the 1997-98 El Niño. *Science*, 286(5447):2126–2131.

Chavez, F. P. and Messié, M. (2009). A comparison of Eastern Boundary Upwelling Ecosystems. *Progress In Oceanography*, 83(1-4):80–96.

Chavez, F. P., Pennington, J., Castro, C., Ryan, J., Michisaki, R. P., Schlining, B., Walz, P., Buck, K., McFadyen, A., and Collins, C. (2002). Biological and chemical consequences of the 1997-1998 El Niño in central California waters. *Progress in Oceanography*, 54(1-4):205–232.

Chavez, F. P., Ryan, J., Lluch-Cota, S. E., and Ñiquen C, M. (2003). From Anchovies to Sardines and Back: Multidecadal Change in the Pacific Ocean. *Science*, 299(5604):217–221.

Chavez, F. P., Takahashi, T., Cai, W.-J., Friederich, G., Hales, B., Wanninkhof, R., and Feely, R. A. (2007). Coastal Oceans. In King, A., Dilling, L., Zimmerman, G., Fairman, D., Houghton, R., Marland, G., Rose, A., and Wilbanks, T., editors, *The First State of the Carbon*

Cycle Report (SOCCR): The North American Carbon Budget and Implications for the Global Carbon Cycle. A Report by the U.S. Climate Change Science Program and the Subcommittee on Global Change Research, chapter 15, pages 157–166. National Oceanic and Atmospheric Administration, National Climatic Data Center, Asheville, NC, USA.

Checkley Jr., D. M. and Barth, J. A. (2009). Patterns and processes in the California Current System. *Progress In Oceanography*, 83(1-4):49–64.

Chelton, D. B., DeSzoeke, R. A., Schlax, M. G., El Naggar, K., and Siwertz, N. (1998). Geographical Variability of the First Baroclinic Rossby Radius of Deformation. *Journal of Physical Oceanography*, 28(3):433–460.

Chen, C.-T. A. and Borges, A. V. (2009). Reconciling opposing views on carbon cycling in the coastal ocean: Continental shelves as sinks and near-shore ecosystems as sources of atmospheric CO_2. *Deep Sea Research Part II: Topical Studies in Oceanography*, 56(8-10):578–590.

Chepurin, G., Carton, J., and Dee, D. (2005). Forecast Model Bias Correction in Ocean Data Assimilation. *Monthly Weather Review*, 133:1328–1342.

Chhak, K. and Di Lorenzo, E. (2007). Decadal variations in the California Current upwelling cells. *Geophysical Research Letters*, 34(14):L14604.

Chhak, K. C., DiLorenzo, E., Schneider, N., and Cummins, P. F. (2009). Forcing of Low-Frequency Ocean Variability in the Northeast Pacific. *Journal of Climate*, 22(5):1255–1276.

Ciais, P., Sabine, C., Bala, G., Bopp, L., Brovkin, V., Canadell, J., Chhabra, A., DeFries, R., Galloway, J., Heimann, M., Jones, C., Le Quéré, C., Myneni, R., Piao, S., and Thornton, P. (2013). Carbon and Other Biogeochemical Cycles. In Stocker, T., Qin, D., Plattner, G.-K., Tignor, M., Allen, S., Boschung, J., Nauels, A., Xia, Y., Bex, V., and Midgley, P., editors, *Climate Change 2013: The Physical Science Basis. Contribution of Working Group I to the Fifth Assessment Report of the Intergovernmental Panel on Climate Change*. Cambridge University Press, Cambridge, United Kingdom and New York, NY, USA.

Clarke, A. J. (2014). El Niño physics and El Niño predictability. *Annual Review of Marine Science*, 6:79–99.

Collins, C., Pennington, J., Castro, C., Rago, T., and Chavez, F. P. (2003). The California Current system off Monterey, California: physical and biological coupling. *Deep Sea Research Part II: Topical Studies in Oceanography*, 50(14-16):2389–2404.

Collins, W., Bitz, C., Blackmon, M., Bonan, G., Bretherton, C., Carton, J., Chang, P., Doney, S., Hack, J., Henderson, T., Kiehl, J., Large, W., McKenna, D., Santer, B., and Smith, R. (2006). The Community Climate System Model Version 3 (CCSM3). *Journal of Climate*, 19(11):2122–2143.

Conway, T. J., Tans, P. P., Waterman, L. S., Thoning, K. W., Kitzis, D. R., Masarie, K. A., and Zhang, N. (1994). Evidence for interannual variability of the carbon cycle from the National Oceanic and Atmospheric Administration/Climate Monitoring and Diagnostics Laboratory Global Air Sampling Network. *Journal of Geophysical Research*, 99(D11):22,831–22,855.

Cooley, S. R. and Doney, S. C. (2009). Anticipating ocean acidifications economic consequences for commercial fisheries. *Environmental Research Letters*, 4(2):024007.

Cubasch, U., Wuebbles, D., Chen, D., Facchini, M., Frame, D., Mahowald, N., and Winther, J.-G. (2013). Introduction. In Stocker, T., Qin, D., Plattner, G.-K., Tignor, M., Allen, S., Boschung, J., Nauels, A., Xia, Y., Bex, V., and Midgley, P., editors, *Climate Change 2013: The Physical Science Basis. Contribution of Working Group I to the Fifth Assessment Report of the Intergovernmental Panel on Climate Change*. Cambridge, United Kingdom and New York, NY, USA.

da Silva, A., Young, C., and Levitus, S. (1994). Atlas of surface marine data 1994, Volume 1: Algorithms and Procedures. NOAA Atlas NESDIS 6. Technical report, U.S. Gov. Printing Office, Washington, DC.

Dee, D., Uppala, S., Simmons, A., Berrisford, P., Poli, P., Kobayashi, S., Andrae, U., Balmaseda, M., Balsamo, G., Bauer, P., Bechtold, P., Beljaars, A., van de Berg, L., Bidlot, J., Bormann, N., Delsol, C., Dragani, R., Fuentes, M., Geer, A., Haimberger, L., Healy, S., Hersbach, H., Hólm, E., Isaksen, L., Kållberg, P., Köhler, M., Matricardi, M., McNally, A., Monge-Sanz, B., Morcrette, J.-J., Park, B.-K., Peubey, C., de Rosnay, P., Tavolato, C., Thépaut, J.-N., and Vitart, F. (2011). The ERA-Interim reanalysis: configuration and performance of the data assimilation system. *Quarterly Journal of the Royal Meteorological Society*, 137(656):553–597.

Demarcq, H. (2009). Trends in primary production, sea surface temperature and wind in upwelling systems (1998-2007). *Progress in Oceanography*, 83(1-4):376–385.

Denman, K. L., Brasseur, G., Chidthaisong, A., Ciais, P., Cox, P., Dickinson, R., Hauglustaine, D., Heinze, C., Holland, E., Jacob, D., Lohmann, U., Ramachandran, S., da Silva Dias, P. L., Wofsy, S. C., and Zhang, C. (2007). Couplings Between Changes in the Climate System and Biogeochemistry. In Solomon, S., Qin, D., Manning, M., Chen, Z., Marquis, M., Averyt, K., Tignor, M., and Miller, H., editors, *Climate Change 2007: The Physical Science Basis. Contribution of Working Group I to the Fourth Assessment Report of the Intergovernmental Panel on Climate Change*, pages 499–587. Cambridge University Press, Cambridge, United Kingdom and New York, NY, USA.

Di Lorenzo, E., Cobb, K. M., Furtado, J. C., Schneider, N., Anderson, B. T., Bracco, A., Alexander, M. A., and Vimont, D. J. (2010). Central Pacific El Niño and decadal climate change in the North Pacific Ocean. *Nature Geoscience*, 3(11):762–765.

Di Lorenzo, E., Fiechter, J., Schneider, N., Bracco, A., Miller, A. J., Franks, P. J. S., Bograd, S. J., Moore, A. M., Thomas, A. C., Crawford, W., Peña, A., and Hermann, A. J. (2009). Nutrient and salinity decadal variations in the central and eastern North Pacific. *Geophysical Research Letters*, 36:L14601.

Di Lorenzo, E., Miller, A. J., Schneider, N., and McWilliams, J. C. (2005). The Warming of the California Current System: Dynamics and Ecosystem Implications. *Journal of Physical Oceanography*, 35(3):336–362.

Di Lorenzo, E., Schneider, N., Cobb, K., Franks, P., Chhak, K., Miller, A. J., McWilliams, J. C., Bograd, S. J., Arango, H., Curchitser, E., Powell, T., and Rivière, P. (2008). North Pacific Gyre Oscillation links ocean climate and ecosystem change. *Geophysical Research Letters*, 35(8):1–6.

Dickson, A. G. and Millero, F. J. (1987). A comparison of the equilibrium constants for the dissociation of carbonic acid in seawater media. *Deep-Sea Research Part I: Oceanographic Research Papers*, 34(10):1733–1743.

Diffenbaugh, N. S., Snyder, M. A., and Sloan, L. C. (2004). Could CO_2-induced land-cover feedbacks alter near-shore upwelling regimes? *PNAS*, 101(1):27–32.

Doney, S. C., Fabry, V. J., Feely, R. A., and Kleypas, J. A. (2009a). Ocean Acidification: The Other CO_2 Problem. *Annual Review of Marine Science*, 1:169–192.

Doney, S. C., Lima, I., Feely, R. A., Glover, D. M., Lindsay, K., Mahowald, N., Moore, J. K., and Wanninkhof, R. (2009b). Mechanisms governing interannual variability in upper-ocean inorganic carbon system and air-sea CO_2 fluxes: Physical climate and atmospheric dust. *Deep Sea Research Part II: Topical Studies in Oceanography*, 56(8-10):640–655.

Doney, S. C., Mahowald, N., Lima, I., Feely, R. A., Mackenzie, F. T., Lamarque, J.-F., and Rasch, P. J. (2007). Impact of anthropogenic atmospheric nitrogen and sulfur deposition on ocean acidification and the inorganic carbon system. *PNAS*, 104(37):14580–14585.

Dunne, J. P., John, J. G., Adcroft, A. J., Griffies, S. M., Hallberg, R. W., Shevliakova, E., Stouffer, R. J., Cooke, W., Dunne, K. a., Harrison, M. J., Krasting, J. P., Malyshev, S. L., Milly, P. C. D., Phillipps, P. J., Sentman, L. T., Samuels, B. L., Spelman, M. J., Winton, M., Wittenberg, A. T., and Zadeh, N. (2012). GFDLs ESM2 Global Coupled Climate-Carbon Earth System Models. Part I: Physical Formulation and Baseline Simulation Characteristics. *Journal of Climate*, 25(19):6646–6665.

Dunne, J. P., John, J. G., Shevliakova, E., Stouffer, R. J., Krasting, J. P., Malyshev, S. L., Milly, P. C. D., Sentman, L. T., Adcroft, A. J., Cooke, W., Dunne, K. a., Griffies, S. M., Hallberg, R. W., Harrison, M. J., Levy, H., Wittenberg, A. T., Phillips, P. J., and Zadeh, N. (2013). GFDLs ESM2 Global Coupled ClimateCarbon Earth System Models. Part II: Carbon System Formulation and Baseline Simulation Characteristics. *Journal of Climate*, 26(7):2247–2267.

Emerson, S. and Hedges, J. (2008). The Global Carbon Cycle: Interactions Between the Atmosphere and Ocean. In *Chemical Oceanography and the Marine Carbon Cycle*. Cambridge University Press.

England, M. H., McGregor, S., Spence, P., Meehl, G. A., Timmermann, A., Cai, W., Gupta, A. S., McPhaden, M. J., Purich, A., and Santoso, A. (2014). Recent intensification of wind-driven circulation in the Pacific and the ongoing warming hiatus. *Nature Climate Change*, 4:222–227.

Eppley, R. W. and Peterson, B. J. (1979). Particulate organic matter flux and planktonic new production in the deep ocean. *Nature*, 282:677–680.

Evans, W., Hales, B., and Strutton, P. G. (2011). Seasonal cycle of surface ocean pCO_2 on the Oregon shelf. *Journal of Geophysical Research*, 116(C5):C05012.

Fabry, V. J., Seibel, B. A., Feely, R. A., and Orr, J. C. (2008). Impacts of ocean acidification on marine fauna and ecosystem processes. *ICES Journal of Marine Science*, 65:414–432.

Fassbender, A. J., Sabine, C. L., Feely, R. A., Langdon, C., and Mordy, C. W. (2011). Inorganic carbon dynamics during northern California coastal upwelling. *Continental Shelf Research*, 31(11):1180–1192.

Feely, R. A., Doney, S. C., and Cooley, S. R. (2009). Ocean Acidification: Present Conditions and Future Changes in a High-CO_2 World. *Oceanography*, 22(4):36–47.

Feely, R. A., Sabine, C. L., Hernandez-Ayon, J. M., Ianson, D., and Hales, B. (2008). Evidence for Upwelling of Corrosive "Acidified" Water onto the Continental Shelf. *Science*, 320(5882):1490–1492.

Feely, R. A., Sabine, C. L., Lee, K., Berelson, W., Kleypas, J., Fabry, V. J., and Millero, F. J. (2004). Impact of anthropogenic CO_2 on the $CaCO_3$ system in the oceans. *Science*, 305(5682):362–366.

Fiechter, J., Curchitser, E. N., Edwards, C. A., Chai, F., Goebel, N. L., and Chavez, F. P. (2014). Air-sea CO_2 fluxes in the California Current: Impacts of model resolution and coastal topography. *Global Biogeochemical Cycles*, 28(4):371–385.

Frankignoulle, M., Abril, G., Borges, A., Bourge, I., Canon, C., Delille, B., Libert, E., and Théate, J.-M. (1998). Carbon Dioxide Emission from European Estuaries. *Science*, 282(5388):434–436.

Fréon, P., Barange, M., and Arístegui, J. (2009). Eastern Boundary Upwelling Ecosystems: Integrative and comparative approaches. *Progress In Oceanography*, 83(1-4):1–14.

Friederich, G., Walz, P., Burczynski, M., and Chavez, F. P. (2002). Inorganic carbon in the central California upwelling system during the 1997-1999 El Niño-La Niña event. *Progress in Oceanography*, 54(1-4):185–203.

Frischknecht, M., Münnich, M., and Gruber, N. (2014). Remote versus Local Influence of ENSO on the California Current System (submitted to Journal of Geophysical Research).

Frölicher, T. (2009). *Ensemble Modeling of the Coupled Carbon Cycle-Climate System*. Inauguraldissertation, Universität Bern.

Furtado, J. C., Di Lorenzo, E., Anderson, B. T., and Schneider, N. (2011). Linkages between the North Pacific Oscillation and central tropical Pacific SSTs at low frequencies. *Climate Dynamics*, 39(12):2833–2846.

Garcia, H. E., Locarnini, R. A., Boyer, T. P., and Antonov, J. I. (2006a). World Ocean Atlas 2005, Volume 3: Dissolved Oxygen, Apparent Oxygen Utilization, and Oxygen Saturation. In Levitus, S., editor, *NOAA Atlas NESDIS 63*, page 342. U.S. Government Printing Office, Washington, D.C.

Garcia, H. E., Locarnini, R. A., Boyer, T. P., and Antonov, J. I. (2006b). World Ocean Atlas 2005, Volume 4: Nutrients (phosphate, nitrate, silicate). In Levitus, S., editor, *NOAA Atlas NESDIS 64*, page 396. U.S. Government Printing Office, Washington, D.C.

García-Reyes, M. and Largier, J. (2010). Observations of increased wind-driven coastal upwelling off central California. *Journal of Geophysical Research*, 115:C04011.

Gent, P., Bryan, F., Danabasoglu, G., Lindsay, K., Tsumumne, D., Hecht, M., and Doney, S. (2006). Ocean Chlorofluorocarbon and Heat Uptake during the Twentieth Century in the CCSM3. *Journal of Climate*, 19(11):2366–2381.

GLOBALVIEW-CO2 (2013). Cooperative Global Atmospheric Data Integration Project. 2013, updated annually. Multi-laboratory compilation of synchronized and gap-filled atmospheric carbon dioxide records for the period 1979-2012.

Graven, H. D., Gruber, N., Key, R., Khatiwala, S., and Giraud, X. (2012). Changing controls on oceanic radiocarbon: New insights on shallow-to-deep ocean exchange and anthropogenic CO_2 uptake. *Journal of Geophysical Research*, 117:C10005.

Gregor, L. and Monteiro, P. M. (2013). Is the southern Benguela a significant regional sink of CO_2? *South African Journal of Science*, 109(5/6):1–5.

Gruber, N., Frenzel, H., Doney, S. C., Marchesiello, P., McWilliams, J. C., Moisan, J. R., Oram, J. J., Plattner, G.-K., and Stolzenbach, K. D. (2006). Eddy-resolving simulation of plankton ecosystem dynamics in the California Current System. *Deep-Sea Research Part I: Oceanographic Research Papers*, 53(9):1483–1516.

Gruber, N., Gloor, M., Mikaloff Fletcher, S. E., Doney, S. C., Dutkiewicz, S., Follows, M. J., Gerber, M., Jacobson, A. R., Joos, F., Lindsay, K., Menemenlis, D., Mouchet, A., Müller, S. A., Sarmiento, J. L., and Takahashi, T. (2009). Oceanic sources, sinks, and transport of atmospheric CO_2. *Global Biogeochemical Cycles*, 23(1):GB1005.

Gruber, N., Hauri, C., Lachkar, Z., Loher, D., Frölicher, T. L., and Plattner, G.-K. (2012). Rapid Progression of Ocean Acidification in the California Current System. *Science*, 337(6091):220–223.

Gruber, N., Lachkar, Z., Frenzel, H., Marchesiello, P., Münnich, M., McWilliams, J. C., Nagai, T., and Plattner, G.-K. (2011). Eddy-induced reduction of biological production in eastern boundary upwelling systems. *Nature Geoscience*, 4(11):787–792.

Gruber, N. and Sarmiento, J. L. (2002). Biogeochemical/Physical Interactions in Elemental Cycles. In Robinson, A. R., McCarthy, J. J., and Rothschild, B., editors, *THE SEA: Biological-Physical Interactions in the Oceans*, volume 12, pages 337–399. John Wiley and Sons, volume 12 edition.

Gutknecht, E., Dadou, I., Le Vu, B., Cambon, G., Sudre, J., Garçon, V., Machu, E., Rixen, T., Kock, A., Flohr, A., Paulmier, A., and Lavik, G. (2011). Nitrogen transfers and air-sea N_2O fluxes in the upwelling off Namibia within the oxygen minimum zone: a 3-D model approach. *Biogeosciences Discussions*, 8(2):3537–3618.

Hales, B., Strutton, P. G., Saraceno, M., Letelier, R., Takahashi, T., Feely, R. A., Sabine, C., and Chavez, F. (2012). Satellite-based prediction of pCO_2 in coastal waters of the eastern North Pacific. *Progress in Oceanography*, 103:1–15.

Hales, B., Takahashi, T., and Bandstra, L. (2005). Atmospheric CO_2 uptake by a coastal upwelling system. *Global Biogeochemical Cycles*, 19(1):GB1009.

Hamersley, M., Turk, K., Leinweber, A., Gruber, N., Zehr, J., Gunderson, T., and Capone, D. (2011). Nitrogen fixation within the water column associated with two hypoxic basins in the Southern California Bight. *Aquatic Microbial Ecology*, 63(2):193–205.

Hauri, C., Gruber, N., McDonnell, A. M. P., and Vogt, M. (2013a). The intensity, duration, and severity of low aragonite saturation state events on the California continental shelf. *Geophysical Research Letters*, 40(13):3424–3428.

Hauri, C., Gruber, N., Plattner, G.-K., Alin, S., Feely, R. A., Hales, B., and Wheeler, P. A. (2009). Ocean acidification in the California Current System. *Oceanography*, 22(4):60–71.

Hauri, C., Gruber, N., Vogt, M., Doney, S. C., Feely, R. A., Lachkar, Z., Leinweber, A., McDonnell, A., Münnich, M., and Plattner, G.-K. (2013b). Spatiotemporal variability and long-term trends of ocean acidification in the California Current System. *Biogeosciences*, 10:193–216.

Hawkins, E. and Sutton, R. (2009). The Potential to Narrow Uncertainty in Regional Climate Predictions. *Bulletin of the American Meteorological Society*, 90(8):1095–1107.

Henson, S. A., Sarmiento, J. L., Dunne, J. P., Bopp, L., Lima, I., Doney, S. C., John, J., and Beaulieu, C. (2010). Detection of anthropogenic climate change in satellite records of ocean chlorophyll and productivity. *Biogeosciences*, 7(2):621–640.

Hickey, B. (1979). The California Current system-hypotheses and facts. *Progress in Oceanography*, 2(8):191–279.

Hood, R. R., Bates, N. R., Capone, D. G., and Olson, D. B. (2001). Modeling the effect of nitrogen fixation on carbon and nitrogen fluxes at BATS. *Deep-Sea Research Part II: Topical Studies in Oceanography*, 48:1609–1648.

Hutchins, D., DiTullio, G., Zhang, Y., and Bruland, K. W. (1998). An iron limitation mosaic in the California upwelling regime. *Limnology and Oceanography*, 43(6):1037–1054.

Huyer, A. (1983). Coastal upwelling in the California Current system. *Progress in Oceanography*, 12(3):259–284.

Huyer, A., Smith, R., and Fleischbein, J. (2002). The coastal ocean off Oregon and northern California during the 1997-8 El Niño. *Progress in Oceanography*, 54:311–341.

Jackett, D. and McDougall, T. (1995). Minimal Adjustment of Hydrographic Profiles to Achieve Static Stability. *Journal of Atmospheric and Oceanic Technology*, 12(2):381–389.

Jin, X., Gruber, N., Dunne, J. P., Sarmiento, J. L., and Armstrong, R. A. (2006). Diagnosing the contribution of phytoplankton functional groups to the production and export of particulate organic carbon, $CaCO_3$, and opal from global nutrient and alkalinity distributions. *Global Biogeochemical Cycles*, 20(2):GB2015.

Jones, S., Le Quéré, C., and Rödenbeck, C. (2012). Autocorrelation characteristics of surface ocean pCO_2 and air-sea CO_2 fluxes. *Global Biogeochemical Cycles*, 26(2):GB2042.

Kahru, M., Kudela, R., Manzano-Sarabia, M., and Mitchell, B. G. (2009). Trends in primary production in the California Current detected with satellite data. *Journal of Geophysical Research*, 114(C2):C02004.

Kahru, M., Kudela, R. M., Manzano-Sarabia, M., and Mitchell, B. G. (2012). Trends in the surface chlorophyll of the California Current: Merging data from multiple ocean color satellites. *Deep Sea Research Part II: Topical Studies in Oceanography*, 77-80:89–98.

Keller, K., Joos, F., Raible, C., Cocco, V., Frölicher, T. L., Dunne, J. P., Gehlen, M., Bopp, L., Orr, J. C., Tjiputra, J., Heinze, C., Segschneider, J., Roy, T., and Metzl, N. (2012). Variability of the ocean carbon cycle in response to the North Atlantic Oscillation. *Tellus B*, 1:1–25.

Keller, K. M., Joos, F., and Raible, C. C. (2013). Time of Emergence of trends in ocean biogeochemistry. *Biogeosciences Discussions*, 10(11):18065–18092.

Key, R. M., Kozyr, A., Sabine, C. L., Lee, K., Wanninkhof, R., Bullister, J. L., Feely, R. A., Millero, F. J., Mordy, C., and Peng, T.-H. (2004). A global ocean carbon climatology: Results from Global Data Analysis Project (GLODAP). *Global Biogeochemical Cycles*, 18(4):GB4031.

King, J. R., Agostini, V. N., Harvey, C. J., McFarlane, G. A., Foreman, M. G., Overland, J. E., Di Lorenzo, E., Bond, N. A., and Aydin, K. Y. (2011). Climate forcing and the California Current ecosystem. *ICES Journal of Marine Science*, 68(6):1199–1216.

Kleypas, J., Buddemeier, R., Archer, D., Gattuso, J.-P., Langdon, C., and Opdyke, B. (1999). Geochemical Consequences of Increased Atmospheric Carbon Dioxide on Coral Reefs. *Science*, 284(5411):118–120.

Kleypas, J., Feely, R. A., Fabry, V. J., Langdon, C., Sabine, C. L., and Robbins, L. (2006). Impacts of Ocean Acidification on Coral Reefs and Other Marine Calcifiers: A Guide for Future Research. Technical report, A report from a workshop held 18-20 April 2005, sponsored by the NSF, NOAA, and the U.S. Geological Survey, St. Petersburg, Florida, USA.

Komhyr, W., Gammon, R., Harris, T., Waterman, L. S., Conway, T., Taylor, W., and Thoning, K. (1985). Global Atmospheric Distribution and Variations From 1968-1982 NOAA/GMCC CO_2 Flask Sample Data. *Journal of Geophysical Research*, 90(D3):5567–5596.

Koslow, J., Goericke, R., Lara-Lopez, A., and Watson, W. (2011). Impact of declining intermediate-water oxygen on deepwater fishes in the California Current. *Marine Ecology Progress Series*, 436:207–218.

Lachkar, Z. (2014). Effects of upwelling increase on ocean acidification in the California and Canary Current systems. *Geophysical Research Letters*, 41(1):90–95.

Lachkar, Z. and Gruber, N. (2011). What controls biological production in coastal upwelling systems? Insights from a comparative modeling study. *Biogeosciences*, 8:2961–2976.

Lachkar, Z. and Gruber, N. (2012). A comparative study of biological production in eastern boundary upwelling systems using an artificial neural network. *Biogeosciences*, 9(1):293–308.

Lachkar, Z. and Gruber, N. (2013). Response of biological production and air-sea CO_2 fluxes to upwelling intensification in the California and Canary Current Systems. *Journal of Marine Systems*, 109-110:149–160.

Large, W., McWilliams, J., and Doney, S. (1994). Oceanic vertical mixing: A review and a model with a nonlocal boundary layer parameterization. *Reviews of Geophysics*, 32(4):363–403.

Large, W. G. and Yeager, S. G. (2004). Diurnal to Decadal Global Forcing For Ocean and Sea-Ice Models: The Data Sets and Flux Climatologies. Technical report, NCAR/TN-460+STR, National Center for Atmospheric Research, Boulder, Colorado.

Laruelle, G. G., Dürr, H. H., Slomp, C. P., and Borges, A. V. (2010). Evaluation of sinks and sources of CO_2 in the global coastal ocean using a spatially-explicit typology of estuaries and continental shelves. *Geophysical Research Letters*, 37(15):L15607.

Lavaniegos, B. E. and Ohman, M. D. (2007). Coherence of long-term variations of zooplankton in two sectors of the California Current System. *Progress in Oceanography*, 75(1):42–69.

Le Quéré, C. (2009). Closing the global budget for CO_2. *Global Change*, 74:28–31.

Le Quéré, C., Andres, R. J., Boden, T., Conway, T., Houghton, R. A., House, J. I., Marland, G., Peters, G. P., van der Werf, G. R., Ahlström, A., Andrew, R. M., Bopp, L., Canadell, J. G., Ciais, P., Doney, S. C., Enright, C., Friedlingstein, P., Huntingford, C., Jain, A. K., Jourdain, C., Kato, E., Keeling, R. F., Klein Goldewijk, K., Levis, S., Levy, P., Lomas, M., Poulter, B., Raupach, M. R., Schwinger, J., Sitch, S., Stocker, B. D., Viovy, N., Zaehle, S., and Zeng, N. (2013). The global carbon budget 1959-2011. *Earth System Science Data*, 5(1):165–185.

Lee, K. (2001). Global net community production estimated from the annual cycle of surface water total dissolved inorganic carbon. *Limnology and Oceanography*, 46(6):1287–1297.

Lee, K., Tong, L. T., Millero, F. J., Sabine, C. L., Dickson, A. G., Goyet, C., Park, G.-H., Wanninkhof, R., Feely, R. A., and Key, R. M. (2006). Global relationships of total alkalinity with salinity and temperature in surface waters of the world's oceans. *Geophysical Research Letters*, 33(19):L19605.

Leinweber, A. and Gruber, N. (2013). Variability and trends of ocean acidification in the Southern California Current System: A timeseries from Santa Monica Bay. *Journal of Geophysical Research: Oceans*, 118:3622–3633.

Leinweber, A., Gruber, N., Frenzel, H., Friederich, G., and Chavez, F. P. (2009). Diurnal carbon cycling in the surface ocean and lower atmosphere of Santa Monica Bay, California. *Geophysical Research Letters*, 36(8):L08601.

Leinweber, A., Neumann, T., and Schneider, B. (2005). The role of N_2-fixation to simulate the pCO_2 observations from the Baltic Sea. *Biogeosciences Discussions*, 2:609–636.

Liu, K.-K., Atkinson, L., Chen, C. A., Gao, S., Hall, J., MacDonald, R., Talaue-McManus, L., and Quiñones, R. (2000). Exploring Continental Margin Carbon Fluxes on a Global Scale. *Eos Transactions, AGU*, 81(52):641–644.

Liu, K.-K., Atkinson, L., Quiñones, R., and Talaue-McManus, L. (2010). Biogeochemistry of continental margins in a global context. In Liu, K.-K., Atkinson, L., Quiñones, R., and Talaue-McManus, L., editors, *Carbon and Nutrient Fluxes in Continental Margins. Global Change - The IGBP Series*, pages 3–24. Springer Berlin Heidelberg, Berlin.

Locarnini, R. A., Mishonov, A. V., Antonov, J. I., Boyer, T. P., and Garcia, H. E. (2006). World Ocean Atlas 2005, Volume 1: Temperature. In Levitus, S., editor, *NOAA Atlas NESDIS 61*, page 182. U.S. Government Printing Office, Washington, D.C.

Loucaides, S., Tyrrell, T., Achterberg, E. P., Torres, R., Nightingale, P. D., Kitidis, V., Serret, P., Woodward, M., and Robinson, C. (2012). Biological and physical forcing of carbonate chemistry in an upwelling filament off northwest Africa: Results from a Lagrangian study. *Global Biogeochemical Cycles*, 26(3):GB3008.

Lovenduski, N. S., Gruber, N., Doney, S. C., and Lima, I. D. (2007). Enhanced CO_2 outgassing in the Southern Ocean from a positive phase of the Southern Annular Mode. *Global Biogeochemical Cycles*, 21(2):GB2026.

Macias, D., Landry, M. R., Gershunov, A., Miller, A. J., and Franks, P. J. S. (2012). Climatic control of upwelling variability along the western North-American coast. *PloS one*, 7(1):e30436.

Mackas, D., Strub, P., Thomas, A., and Montecino, V. (2006). Eastern Ocean Boundaries Pan-Regional Overview. In Robinson, A. and Brink, K., editors, *The Sea*, pages 21–29. Harvard University Press.

Mackenzie, F., Andersson, A., Lerman, A., and Ver, L. (2005). Boundary exchanges in the global coastal margin: Implications for the organic and inorganic carbon cycles. In Robinson, A. and Brink, K., editors, *The Sea*, pages 193–225. Harvard University Press.

Manning, A. and Keeling, R. (2006). Global oceanic and land biotic carbon sinks from the Scripps atmospheric oxygen flask sampling network. *Tellus B*, 58(2):95–116.

Mantua, N. J. and Hare, S. R. (2002). The Pacific Decadal Oscillation. *Journal of Oceanography*, 58:35–44.

Mantua, N. J., Hare, S. R., Zhang, Y., Wallace, J. M., and Francis, R. C. (1997). A Pacific Interdecadal Climate Oscillation with Impacts on Salmon Production. *Bulletin of the American Meteorological Society*, 78(6):1069–1079.

Marchesiello, P., McWilliams, J. C., and Shchepetkin, A. (2003). Equilibrium structure and dynamics of the California Current System. *Journal of Physical Oceanography*, 33(4):753–783.

Marchesiello, P., McWilliams, J. C., and Shchepetkin, A. F. (2001). Open boundary conditions for long-term integration of regional oceanic models. *Ocean Modelling*, 3(1-2):1–20.

Martin, J. (1992). Iron as a Limiting Factor in Oceanic Productivity. In Falkowski, P. and Woodhead, A., editors, *Primary Productivity and Biogeochemical Cycles in the Sea*, pages 123–137. Springer US.

Martiny, A. C., Pham, C. T., Primeau, F. W., Vrugt, J. A., Moore, J. K., Levin, S. A., and Lomas, M. W. (2013). Strong latitudinal patterns in the elemental ratios of marine plankton and organic matter. *Nature Geoscience*, 6(4):279–283.

Masson-Delmotte, V., Schulz, M., Abe-Ouchi, A., Beer, J., Ganopolski, A., González Rouco, J., Jansen, E., Lambeck, K., Luterbacher, J., Naish, T., Osborn, T., Otto-Bliesner, B., Quinn, T., Ramesh, R., Rojas, M., Shao, X., and Timmermann, A. (2013). Information from Paleoclimate Archives. In Stocker, T., Qin, D., Plattner, G.-K., Tignor, M., Allen, S., Boschung, J., Nauels, A., Xia, Y., Bex, V., and Midgley, P., editors, *Climate Change 2013: The Physical Science Basis. Contribution of Working Group I to the Fifth Assessment Report of the Intergovernmental Panel on Climate Change*. Cambridge University Press, Cambridge, United Kingdom and New York, NY, USA.

McGowan, J., Cayan, D., and Dorman, L. (1998). Climate-Ocean Variability and Ecosystem Response in the Northeast Pacific. *Science*, 281(5374):210–217.

McGowan, J. A., Bograd, S. J., Lynn, R. J., and Miller, A. J. (2003). The biological response to the 1977 regime shift in the California Current. *Deep-Sea Research Part II: Topical Studies in Oceanography*, 50(14-16):2567–2582.

McNeil, B. I., Matear, R. J., Key, R. M., Bullister, J. L., and Sarmiento, J. L. (2003). Anthropogenic CO2 uptake by the ocean based on the global chlorofluorocarbon data set. *Science*, 299(5604):235–239.

Mearns, L. O., Arritt, R., Biner, S., Bukovsky, M. S., McGinnis, S., Sain, S., Caya, D., Correia Jr., J., Flory, D., Gutowski, W., Takle, E. S., Jones, R., Leung, R., Moufouma-Okia, W., McDaniel, L., Nunes, A. M., Qian, Y., Roads, J., Sloan, L., and Snyder, M. (2012). The North American Regional Climate Change Assessment Program: Overview of Phase I Results. *Bulletin of the American Meteorological Society*, 93(9):1337–1362.

Mehrbach, C., Culberson, C., Hawley, J., and Pytkowicz, R. (1973). Measurement of the apparent dissociation constants of carbonic acid in seawater at atmospheric pressure. *Limnology and Oceanography*, 18(6):897–907.

Mendelssohn, R. and Schwing, F. (2002). Common and uncommon trends in SST and wind stress in the California and Peru - Chile current systems. *Progress in Oceanography*, 53(196):141–162.

Mikaloff Fletcher, S. E., Gruber, N., Jacobson, A. R., Doney, S. C., Dutkiewicz, S., Gerber, M., Follows, M., Joos, F., Lindsay, K., Menemenlis, D., Mouchet, A., Müller, S. A., and Sarmiento, J. L. (2006). Inverse estimates of anthropogenic CO_2 uptake, transport, and storage by the ocean. *Global Biogeochemical Cycles*, 20(2):GB2002.

Millero, F. J. (1995). Thermodynamics of the carbon dioxide system in the oceans. *Geochimica et Cosmochimica Acta*, 59(4):661–677.

Mucci, A. (1983). The solubility of calcite and aragonite in seawater at various salinities, temperatures, and one atmosphere total pressure. *American Journal of Science*, 283:780–799.

Muller-Karger, F. E., Varela, R., Thunell, R., Luerssen, R., Hu, C., and Walsh, J. J. (2005). The importance of continental margins in the global carbon cycle. *Geophysical Research Letters*, 32(1):L01602.

Murnane, R., Sarmiento, J. L., and Le Quéré, C. (1999). Spatial distribution of air-sea CO_2 fluxes and the interhemispheric transport of carbon by the oceans. *Global Biogeochemical Cycles*, 13(2):287–305.

Nagai, T., Gruber, N., Frenzel, H., McWilliams, J. C., and Plattner, G.-K. (2014). Dominant role of eddies in offshore transport in the California Current System (submitted to Journal of Geophysical Research: Oceans).

Narayan, N., Paul, a., Mulitza, S., and Schulz, M. (2010). Trends in coastal upwelling intensity during the late 20th century. *Ocean Science*, 6(3):815–823.

Nohara, D., Kitoh, A., Hosaka, M., and Oki, T. (2006). Impact of Climate Change on River Discharge Projected by Multimodel Ensemble. *Journal of Hydrometeorology*, 7:1076–1089.

Orr, J. C., Fabry, V. J., Aumont, O., Bopp, L., Doney, S. C., Feely, R. A., Gnanadesikan, A., Gruber, N., Ishida, A., Joos, F., Key, R. M., Lindsay, K., Maier-Reimer, E., Matear, R., Monfray, P., Mouchet, A., Najjar, R. G., Plattner, G.-K., Rodgers, K. B., Sabine, C. L., Sarmiento, J. L., Schlitzer, R., Slater, R. D., Totterdell, I. J., Weirig, M.-F., Yamanaka, Y., and Yool, A. (2005). Anthropogenic ocean acidification over the twenty-first century and its impact on calcifying organisms. *Nature*, 437(7059):681–686.

Palacios, D., Bograd, S. J., and Mendelssohn, R. (2004). Long-term and seasonal trends in stratification in the California Current, 1950–1993. *Journal of Geophysical Research*, 109(C10016):1–12.

Pauly, D. and Christensen, V. (1995). Primary production required to sustain global fisheries. *Nature*, 374:255–257.

Pennington, J., Castro, C., Collins, C., Evans, W., Friederich, G., Michisaki, R., and Chavez, F. (2010). The Northern and Central California Coastal Upwelling System. In Liu, K.-K., Atkinson, L., Quiñones, R., and Talaue-McManus, L., editors, *Carbon and Nutrient Fluxes in Continental Margins. Global Change - The IGBP Series*, pages 29–44. Springer Berlin Heidelberg.

Pfeil, B., Olsen, A., Bakker, D. C. E., Hankin, S., Koyuk, H., Kozyr, A., Malczyk, J., Manke, A., Metzl, N., Sabine, C. L., Akl, J., Alin, S. R., Bates, N., Bellerby, R. G. J., Borges, A., Boutin, J., Brown, P. J., Cai, W.-J., Chavez, F. P., Chen, A., Cosca, C., Fassbender, A. J., Feely, R., González-Dávila, M., Goyet, C., Hales, B., Hardman-Mountford, N., Heinze, C., Hood, M., Hoppema, M., Hunt, C. W., Hydes, D., Ishii, M., Johannessen, T., Jones, S. D., Key, R. M., Körtzinger, A., Landschützer, P., Lauvset, S. K., Lefèvre, N., Lenton, A., Lourantou, A.,

Merlivat, L., Midorikawa, T., Mintrop, L., Miyazaki, C., Murata, A., Nakadate, A., Nakano, Y., Nakaoka, S., Nojiri, Y., Omar, A. M., Padin, X. A., Park, G.-H., Paterson, K., Perez, F. F., Pierrot, D., Poisson, A., Ríos, A. F., Santana-Casiano, J. M., Salisbury, J., Sarma, V. V. S. S., Schlitzer, R., Schneider, B., Schuster, U., Sieger, R., Skjelvan, I., Steinhoff, T., Suzuki, T., Takahashi, T., Tedesco, K., Telszewski, M., Thomas, H., Tilbrook, B., Tjiputra, J., Vandemark, D., Veness, T., Wanninkhof, R., Watson, A. J., Weiss, R., Wong, C. S., and Yoshikawa-Inoue, H. (2013). A uniform, quality controlled Surface Ocean CO_2 Atlas (SOCAT). *Earth System Science Data*, 5:125–143.

Plattner, G.-K., Gruber, N., Frenzel, H., and McWilliams, J. C. (2005). Decoupling marine export production from new production. *Geophysical Research Letters*, 32(11):L11612.

Raymond, P. A., Caraco, N. F., and Cole, J. J. (1997). Carbon Dioxide Concentration and Atmospheric Flux in the Hudson River. *Estuaries*, 20(2):381–390.

Redfield, A., Ketchum, B., and Richards, F. (1963). The influence of organisms on the composition of seawater. In Hill, M., editor, *THE SEA: Ideas and Observations on Progress in the Study of the Sea*, pages 26–77. Wiley Interscience, New York, USA.

Regnier, P., Friedlingstein, P., Ciais, P., Mackenzie, F. T., Gruber, N., Janssens, I. A., Laruelle, G. G., Lauerwald, R., Luyssaert, S., Andersson, A. J., Arndt, S., Arnosti, C., Borges, A. V., Dale, A. W., Gallego-Sala, A., Goddéris, Y., Goossens, N., Hartmann, J., Heinze, C., Ilyina, T., Joos, F., LaRowe, D. E., Leifeld, J., Meysman, F. J. R., Munhoven, G., Raymond, P. A., Spahni, R., Suntharalingam, P., and Thullner, M. (2013). Anthropogenic perturbation of the carbon fluxes from land to ocean. *Nature Geoscience*, 6:597–607.

Rhein, M., Rintoul, S., Aoki, S., Campos, E., Chambers, D., Feely, R., Gulev, S., Johnson, G., Josey, S., Kostianoy, A., Mauritzen, C., Roemmich, D., L.D., T., and Wang, F. (2013). Observations: Ocean. In Stocker, T., Qin, D., Plattner, G.-K., Tignor, M., Allen, S., Boschung, J., Nauels, A., Xia, Y., Bex, V., and Midgley, P., editors, *Climate Change 2013: The Physical Science Basis. Contribution of Working Group I to the Fifth Assessment Report of the Intergovernmental Panel on Climate Change*. Cambridge University Press, Cambridge, United Kingdom and New York, NY, USA.

Rio, M.-H. and Hernandez, F. (2004). A mean dynamic topography computed over the world ocean from altimetry, in situ measurements, and a geoid model. *Journal of Geophysical Research*, 109:C12032.

Risien, C. M. and Chelton, D. B. (2008). A Global Climatology of Surface Wind and Wind Stress Fields from Eight Years of QuikSCAT Scatterometer Data. *Journal of Physical Oceanography*, 38(11):2379–2413.

Roemmich, D. and McGowan, J. (1995). Climatic Warming and the Decline of Zooplankton in the California Current. *Science*, 267(5202):1324–1326.

Rykaczewski, R. R. and Dunne, J. (2010). Enhanced nutrient supply to the California Current Ecosystem with global warming and increased stratification in an earth system model. *Geophysical Research Letters*, 37(L21606).

Sabine, C. L., Feely, R. A., Gruber, N., Key, R. M., Lee, K., Bullister, J. L., Wanninkhof, R., Wong, C. S., Wallace, D. W., Tilbrook, B., Millero, F. J., Peng, T.-H., Kozyr, A., Ono, T., and Rios, A. F. (2004). The oceanic sink for anthropogenic CO_2. *Science*, 305(5682):367–371.

Salisbury, J., Green, M., Hunt, C., and Campbell, J. (2008). Coastal Acidification by Rivers: A Threat to Shellfish? *Eos Transactions, AGU*, 89(50):513–528.

Sarmiento, J. L., Dunne, J., Gnanadesikan, A., Key, R. M., Matsumoto, K., and Slater, R. (2002). A new estimate of the $CaCO_3$ to organic carbon export ratio. *Global Biogeochemical Cycles*, 16(4):1107.

Sarmiento, J. L. and Gruber, N. (2006). *Ocean Biogeochemical Dynamics*. Princeton University Press, Princeton, New Jersey, USA.

Schmittner, A., Gruber, N., Mix, A., Key, R., Tagliabue, A., and Westberry, T. (2013). Biology and air-sea gas exchange controls on the distribution of carbon isotope ratios (δ^{13}C) in the ocean. *Biogeosciences*, 10(9):5793–5816.

Schwing, F. B. and Mendelssohn, R. (1997). Increased coastal upwelling in the California Current System. *Journal of Geophysical Research*, 102(C2):3421–3438.

Seo, H., Brink, K. H., Dorman, C. E., Koracin, D., and Edwards, C. a. (2012). What determines the spatial pattern in summer upwelling trends on the U.S. West Coast? *Journal of Geophysical Research*, 117:C08012.

Shchepetkin, A. F. and McWilliams, J. C. (1998). Quasi-Monotone Advection Schemes Based on Explicit Locally Adaptive Dissipation. *Monthly Weather Review*, 126(6):1541–1580.

Shchepetkin, A. F. and McWilliams, J. C. (2005). The regional oceanic modeling system (ROMS): a split-explicit, free-surface, topography-following-coordinate oceanic model. *Ocean Modelling*, 9(4):347–404.

Smith, R., Jones, P., Briegleb, B., Bryan, F., Danabasoglu, G., Dennis, J., Dukowicz, J., Eden, C., Fox-Kemper, B., Gent, P., Hecht, M., Jayne, S., Jochum, M., Large, W., Lindsay, K., Maltrud, M., Norton, N., Peacock, S., Vertenstein, M., and Yeager, S. (2010). The Parallel Ocean Program (POP) Reference Manual. Technical report, Tech. Rep. LAUR-10-01853, Los Alamos National Laboratory, Los Alamos, NM, USA.

Smith, W. and Sandwell, D. (1997). Global Sea Floor Topography from Satellite Altimetry and Ship Depth Soundings. *Science*, 277(5334):1956–1962.

Snyder, M. A., Sloan, L. C., Diffenbaugh, N. S., and Bell, J. L. (2003). Future climate change and upwelling in the California Current. *Geophysical Research Letters*, 30(15):1823.

Song, H., Miller, A. J., Cornuelle, B. D., and Di Lorenzo, E. (2011). Changes in upwelling and its water sources in the California Current System driven by different wind forcing. *Dynamics of Atmospheres and Oceans*, 52:170–191.

Soto, C. G. (2002). The potential impacts of global climate change on marine protected areas. *Reviews in Fish Biology and Fisheries*, 11:181–195.

Stramma, L., Johnson, G. C., Sprintall, J., and Mohrholz, V. (2008). Expanding oxygen-minimum zones in the tropical oceans. *Science*, 320(5876):655–658.

Tabata, S. (1975). The general circulation of the Pacific Ocean and a brief account of the oceanographic structure of the north pacific ocean Part I-circulation and volume transports. *Atmosphere*, 13(4):133–168.

Takahashi, T., Sutherland, S., and Kozyr, A. (2013). Global ocean surface water partial pressure of CO_2 database: Measurements performed during 1957-2012 (Version 2012). ORNL/CDIAC-160, NDP-088(V2012). *Carbon Dioxide Information Analysis Center, Oak Ridge National Laboratory, U.S. Department of Energy, Oak Ridge, Tennessee*.

Takahashi, T., Sutherland, S. C., Feely, R. A., and Wanninkhof, R. (2006). Decadal change of the surface water pCO_2 in the North Pacific: A synthesis of 35 years of observations. *Journal of Geophysical Research*, 111(C7):C07S05.

Takahashi, T., Sutherland, S. C., Wanninkhof, R., Sweeney, C., Feely, R. A., Chipman, D. W., Hales, B., Friederich, G., Chavez, F., Sabine, C., Watson, A., Bakker, D. C., Schuster, U., Metzl, N., Yoshikawa-Inoue, H., Ishii, M., Midorikawa, T., Nojiri, Y., Körtzinger, A., Steinhoff, T., Hoppema, M., Olafsson, J., Arnarson, T. S., Tilbrook, B., Johannessen, T., Olsen, A., Bellerby, R., Wong, C., Delille, B., Bates, N., and de Baar, H. J. (2009). Climatological mean and decadal change in surface ocean pCO_2, and net sea-air CO_2 flux over the global oceans. *Deep-Sea Research Part II: Topical Studies in Oceanography*, 56(8-10):554–577.

Taylor, K. E. (2001). Summarizing multiple aspects of model performance in a single diagram. *Journal of Geophysical Research*, 106(D7):7183–7192.

Taylor, K. E., Stouffer, R. J., and Meehl, G. A. (2012). An Overview of CMIP5 and the Experiment Design. *Bulletin of the American Meteorological Society*, 93(4):485–498.

Thomas, H., Bozec, Y., Elkalay, K., and de Baar, H. J. W. (2004). Enhanced open ocean storage of CO_2 from shelf sea pumping. *Science*, 304:1005–1008.

Toggweiler, J. R., Murnane, R., Carson, S., Gnanadesikan, A., and Sarmiento, J. L. (2003). Representation of the carbon cycle in box models and GCMs, 2. Organic pump. *Global Biogeochemical Cycles*, 17(1):1027.

Tsunogai, S., Watanabe, S., and Sato, T. (1999). Is there a "continental shelf pump" for the absorption of atmospheric CO_2? *Tellus*, 51(3):701–712.

Turi, G., Lachkar, Z., and Gruber, N. (2014a). Spatiotemporal variability and drivers of pCO_2 and air-sea CO_2 fluxes in the California Current System: an eddy-resolving modeling study. *Biogeosciences*, 11(3):671–690.

Turi, G., Lachkar, Z., Matthias, M., Gruber, N., and Loher, D. (2014b). Recent climatic changes enhance ongoing ocean acidification in the California Current System. *(in prep.)*.

Turi, G., Lachkar, Z., Münnich, M., Loher, D., and Gruber, N. (2014c). High interannual variability of air-sea CO_2 fluxes in the California Current System. *(in prep.)*.

Volk, T. and Hoffert, M. I. (1985). Ocean carbon pumps: Analysis of relative strengths and efficiencies in ocean-driven atmospheric CO_2 changes. In Sundquist, E. T. and Broecker, W. S., editors, *The Carbon Cycle and Atmospheric CO_2: Natural Variations Archean to Present, Geophysical Monograph Series*, volume 32, pages 99–110. Washington, D.C.

Walker, G. (1924). Correlation in seasonal variations of weather, IX: A further study of world weather. *Memoirs of the India Meteorological Department*, 14:275–332.

Walsh, J. J. (1988). *On the Nature of Continental Shelves*. Academic Press, New York, USA.

Wanninkhof, R. (1992). Relationship Between Wind Speed and Gas Exchange Over the Ocean. *Journal of Geophysical Research*, 97(C5):7373–7382.

Wanninkhof, R., Asher, W. E., Ho, D. T., Sweeney, C., and McGillis, W. R. (2009). Advances in Quantifying Air-Sea Gas Exchange and Environmental Forcing. *Annual Reviews of Marine Science*, 1:213–244.

Wanninkhof, R., Park, G. H., Takahashi, T., Sweeney, C., Feely, R., Nojiri, Y., Gruber, N., Doney, S. C., McKinley, G. A., Lenton, A., Le Quéré, C., Heinze, C., Schwinger, J., Graven, H., and Khatiwala, S. (2013). Global ocean carbon uptake: magnitude, variability and trends. *Biogeosciences*, 10:1983–2000.

Weiss, R. F. (1974). Carbon dioxide in water and seawater: the solubility of a non-ideal gas. *Marine Chemistry*, 2(3):203–215.

Wolter, K. and Timlin, M. S. (1993). Monitoring ENSO in COADS with a seasonally adjusted principal component index. Proceedings of the 17th Climate Diagnostics Workshop.

Wolter, K. and Timlin, M. S. (1998). Measuring the strength of ENSO events: How does 1997/98 rank? *Weather*, 53:315–324.

Wolter, K. and Timlin, M. S. (2011). El Niño/Southern Oscillation behaviour since 1871 as diagnosed in an extended multivariate ENSO index (MEI.ext). *International Journal of Climatology*, 31:1074–1087.

Yeh, S.-W., Kug, J.-S., Dewitte, B., Kwon, M.-H., Kirtman, B. P., and Jin, F.-F. (2009). El Niño in a changing climate. *Nature*, 461:511–514.

Zwiers, F. and von Storch, H. (1995). Taking Serial Correlation into Account in Tests of the Mean. *Journal of Climate*, 8(2):336–351.